Project 09-793

Development of Adaptive Model Refinement (AMoR) for Multiphysics and Multifidelity Problems

Integrated University Programs

Dr. Paul Turinsky
North Carolina State University

Keith Bradley, Technical POC

National Nuclear Security Administration

NEUP Grant CFP-09-793

Development of Adaptive Model Refinement (AMoR) for Multiphysics and Multifidelity Problems

Final Report

Principle Investigator: Paul Turinsky

Research Associates:
Ross Hays
Jaesok Heo

Research Assistants:
Robert Dacus
Sterling Scatterfield
Jason Andrus
Philip Marquis
B. Ellen Aldridge

September 2, 2014

Abstract

This project investigated the development and utilization of Adaptive Model Refinement (AMoR) for nuclear systems simulation applications. AMoR refers to utilization of several models of physical phenomena which differ in prediction fidelity. If the highest fidelity model is judged to always provide or exceeded the desired fidelity, than if one can determine the difference in a Quantity of Interest (QoI) between the highest fidelity model and lower fidelity models, one could utilize the fidelity model that would just provide the magnitude of the QoI desired. Assuming lower fidelity models require less computational resources, in this manner computational efficiency can be realized provided the QoI value can be accurately and efficiently evaluated. This work utilized Generalized Perturbation Theory (GPT) to evaluate the QoI, by convoluting the GPT solution with the residual of the highest fidelity model determined using the solution from lower fidelity models. Specifically, a reactor core neutronics problem and thermal-hydraulics problem were studied to develop and utilize AMoR. The highest fidelity neutronics model was based upon the 3D space-time, two-group, nodal diffusion equations as solved in the NESTLE computer code. Added to the NESTLE code was the ability to determine the time-dependent GPT neutron flux. The lower fidelity neutronics model was based upon the point kinetics equations along with utilization of a prolongation operator to determine the 3D space-time, two-group flux. The highest fidelity thermal-hydraulics model was based upon the space-time equations governing fluid flow in a closed channel around a heat generating fuel rod. The Homogenous Equilibrium Mixture (HEM) model was used for the fluid and Finite Difference Method was applied to both the coolant and fuel pin energy conservation equations. The lower fidelity thermal-hydraulic model was based upon the same equations as used for the highest fidelity model but now with coarse spatial meshing, corrected somewhat by employing effective fuel heat conduction values. The effectiveness of switching between the highest fidelity model and lower fidelity model as a function of time was assessed using the neutronics problem. Based upon work completed to date, one concludes that the time switching is effective in annealing out differences between the highest and lower fidelity solutions. The effectiveness of using a lower fidelity GPT solution, along with a prolongation operator, to estimate the QoI was also assessed. The utilization of a lower fidelity GPT solution was done in an attempt to avoid the high computational burden associated with solving for the highest fidelity GPT solution. Based upon work completed to date, one concludes that the lower fidelity adjoint solution is not sufficiently accurate with regard to estimating the QoI; however, a formulation has been revealed that may provide a path for addressing this shortcoming.

Table of Contents

Overview

To further enhance simulation capabilities, whether it is of a nuclear power system or nuclear fuel assembly, the inclusion of high fidelity models of different physics phenomena coupled together in a tight fashion will be required. One of the challenges of accomplishing this is to do it in such a way that a given level of computational fidelity can be obtained without over burdening the computer resources that are available to end users. If all of the modeling of the physics is accomplished by using highly detailed models, it is doubtful that available computer resources would be able to complete typical design and safety analysis tasks. To overcome this limitation, multifidelity approaches have been proposed and to a limited extent pursued. [Note, within the context of the work proposed, multiscale models can be thought of as one class of multifidelity models.] If a multifidelity model approach is to be utilized, there must be the capability to determine the differences of the collection of fidelities for different physics models that are being employed so that higher-fidelity physics models can be called upon when necessary to satisfy stated accuracy requirements. For transient applications, one would expect the fidelity for each physics model to change with time. The work completed developed the capability to determine the differences in predicted values of Quantities of Interest (QoI) due to model introduced errors for the collection of fidelity-level models currently being employed, and automatically change this collection of fidelity-level models as necessary to just meet stated accuracy requirements. In this manner the minimum multiphysics and multifidelity modeling computational resources is expended to meet a stated set of accuracy requirements as controlled by differences caused by model introduced errors. More concisely, an Adaptive Model Refinement (AMoR) capability has been investigated for usage in modeling nuclear systems.

Work Completed

The milestones as originally planned are presented in Table I.

Table I. Original milestones

Milestone
1. Task 1.a Development of Multifidelity Neutronics Models
2. Issue Annual Report
3. Task 1.b Development of AMoR for Neutronics Models
4. Issue Annual Report
5. Task 2. Development of Multiphysics Models
6. Task 3. Development of AMoR for Multiphysics Models
7. Issue Final Report

As noted in Table I, model development and AMoR tasks were divided into those focusing on neutronics and subsequently on multiphysics. The neutronics model development included the following subtasks:

- establishing a PWR core model for an operating reactor in a reload cycle for the nodal diffusion code NESTLE to obtain the higher fidelity 3D space-time flux solution,
- adding time-dependent Generalized Adjoint Capability (GPT) to NESTLE,
- adding the capability to determine the residual of the nodal diffusion equations based upon the prolongated point kinetic equations forward flux solution and convoluting it with the GPT flux to obtain the QoI,
- adding the capability to generate point kinetic parameters and prolongation operators utilizing NESTLE, and
- development of a point kinetics equations solver code and utilization of prolongation operators to construct the lower fidelity 3D space-time dependent flux .

The multiphysics model development included the following subtasks:

- development of a single closed channel thermal-hydraulic model of the coolant and fuel pin using the Homogenous Equilibrium Mixture (HEM) fluids model and the Finite Difference Method (FDM) to establish the higher-fidelity computer code to determine the time-space dependent coolant and fuel temperatures,
- generation, using the higher fidelity thermal-hydraulic model, of effective thermal conductivities for the fuel to be used in the lower fidelity model based upon using a coarser spatial mesh and the associated prolongation operator,
- development of a time-dependent GPT solver code for the thermal-hydraulic model, one solver based upon the mathematical adjoint and another solver based upon the physical adjoint, and
- addition of the capability to determine the residual of the thermal-hydraulic equations based upon the prolongated lower-fidelity forward coolant and fuel temperature solution and convoluting it with the GPT fuel and coolant temperatures to obtain the QoI.

These capabilities were subsequently utilized to obtain higher and lower fidelity solutions for the neutronics and thermal-hydraulic problems.

For the neutronics problem the focus was on having determined the Quantity of Interest (QoI), whether the differences of the lower and higher fidelity solution could be annealed out by switching periodically with time from the lower to the higher fidelity solution for a short span of time. The higher fidelity GPT solution was used to determine the QoI. Switching with time between the higher and lower fidelity solutions, including regeneration of the prolongation operator, was completed using the prolongated point kinetic equations solution as the initial conditions for NESTLE when branching occurred. The conclusion from the study so far completed is that the strategy of switching between the lower and higher fidelity solution as directed by the magnitude of the QoI can be effective, implying lower fidelity solution differences with the higher fidelity solution can be periodically annealed out.

For the thermal-hydraulic problem the focus was on exploring the usage of the lower fidelity GPT solution to estimate the QoI. Since more computational effort is required to determine the higher fidelity GPT solution [N(N+1)/2 versus N time steps solved for], for AMoR to be computationally efficient a lower fidelity GPT solution must be such that the QoI interest can be estimated sufficiently accurate. This was assessed by convoluting the lower fidelity GPT coolant and fuel temperature solution with the residual of the higher fidelity thermal-hydraulic equations using the prolongated lower fidelity, forward solution. As noted earlier, this was done utilizing adjoint operators based upon both the mathematical and physical adjoints, in addition to an analytic adjoint that enabled code verification. The conclusion from the study so far completed is that no prolongated lower fidelity GPT solution has been found that approximates the QoI with sufficient accuracy. However, a formulation has been revealed that indicates exactly what QoI the prolongated lower fidelity GPT solution is determining, which we believe can be utilized to determine a lower fidelity adjoint operator and/or prolongation operator that will improve the accuracy of the estimated QoI.

Organization of Report

In Section A of this report, the neutronics results are presented in the fashion of the master's thesis of Mr. Sterling Scatterfield. His work builds upon earlier work of Mr. Jason Andrus and is being continued by Ms. B Ellen Eldridge. In Section B of this report, the thermal-hydraulics results are presented in the fashion of the master's thesis of Mr. Trip Dacus. His work builds upon earlier work of Mr. Philip Marquis and is being continued by Mr. Dacus, but not focused on the GPT solution of two-phase fluid flow utilizing Computational Fluid Dynamics (CFD). Finally, Section C presents the derivation of the time dependent GPT equations that have been programed into the NESTLE code by Post Docs Dr. Jaesok Heo and Dr. Ross Hays. Ms. Eldridge is continuing this work utilizing the NESTLE code's GPT capability.

Section A

Neutronics Results

ABSTRACT

SATTERFIELD, STERLING JUSTIN. The Application of Adaptive Model Refinement to Nuclear Reactor Core Simulation. (Under the direction of Paul Turinsky.)

Nuclear reactor design is a complex, iterative process consisting of the integration of multiple independent system designs, resulting in near constant redesign requiring more simulations. The nature of this processes is perpetually driving designers to improve the time/accuracy ratio of reactor simulations to help ensure the achievement of the best possible solution. The application of advanced simulation techniques is used by designers to improve their simulation capabilities. These techniques revolve around two basic approaches, one of which is to integrate multiple simulation models to create a hybrid model with the hopes of yielding higher fidelity solutions faster; This is the aspiration of Adaptive Model Refinement (AMoR). This work is a proof of concept for the application of the AMoR method to nuclear reactor neutron simulation, specifically the integration of NESTLE [1], a few-group diffusion simulator, with a point reactor kinetics solver (PKE-Solver).

The basis for this approach is grounded in the Quasi-Static method [7] [8], expanding on the concept of the separability of the flux into amplitude-flux shape-functions [6]. Using this idea, a formulation for the separation of the flux and precursor concentrations into amplitude-spatial factors was created. The relationship between these factors allowed for the calculation of the spatial factors by NESTLE, the higher fidelity model, and the calculation of the amplitude factors by the PKE-Solver, the lower fidelity model, resulting in a projected 3-D model. Multiple error metrics were developed to asses the fidelity of this projected model.

Two AMoR approaches were evaluated in this research. One approach involved the creation of a steady-state library containing the shape-factors, which were used in real-time with the PKE-Solver to generate the projected model. This approach resulted in a maximum locally normalized flux and precursor concentration error of roughly 12 - 30% and 60 - 65%, respectively, for the transients simulated. A 2 second transient test case and a 120 second transient test case were evaluated. The second approach, involved updating the shape-factors from the higher fidelity model, in real time, when the error of the projected model was deemed too large. For the 2 second transient case, 8 shape-factor updates were required, using a PKE-Solver time-step size of 0.01 seconds, to maintain a maximum flux error of 25%. For the 120 second transient case, only 4 updates were required, using a PKE-Solver time-step size of 0.30 seconds, to maintain a maximum flux error of 10%.

The Application of Adaptive Model Refinement to Nuclear Reactor Core Simulation

by
Sterling Justin Satterfield

A thesis submitted to the Graduate Faculty of
North Carolina State University
in partial fulfillment of the
requirements for the Degree of
Master of Science

Nuclear Engineering

Raleigh, North Carolina

2013

APPROVED BY:

Dmitriy Anistratov	Ilse Ipsen

Paul Turinsky
Chair of Advisory Committee

DEDICATION

This work is dedicated to my parents. Without their sincere support I would have certainly never accomplished as much as I have in my lifetime.

BIOGRAPHY

Sterling Satterfield is originally from the small West Texas town of Midland. He is the youngest of five children of Mr. Johnny Satterfield and Mrs. Jeannie Satterfield. After receiving degrees in Mechanical Engineering and Mathematics from the University of Texas of the Permian Basin in 2011, he moved to Raleigh, North Carolina to pursue a master's degree in Nuclear Engineering.

ACKNOWLEDGEMENTS

The completion of this project would not have been possible without the assistance of a great many people. First, I would like to thank my advisor, Dr. Paul Turinsky, for his patients and guidance while over seeing my work through the last two years. I would also like to thank my friend Ross Hays of the Nuclear Engineering Department for the considerable amount of advice and assistance he has provided me throughout this time. As well, I would like to thank Hermine Kabbendjian for her hard work and advice over the last two years.

In addition, I would like to thank my friends, family, and girlfriend, Karen Compton, for keeping me grounded during my time in North Carolina.

I would also like to thank Dr. Wright, Dr. Nelson, Mr. Cameron, as well as countless others of the University of Texas at the Permian Basin without whom I would have never made it this far in my academic career.

As well I would like to thank my long time friend and mentor David Cox for making the time to feed my scientific, engineering, and business interest and for the sound advice and guidance he has provided me throughout my college career.

The last person I would like to thank is Mrs. Karen Sullivan. Without her subtle suggestion to enter the regional science fair, my life would have been drastically different.

Finally, I would like to acknowledge the DOE, CASL, and the Dean's Grant which without their financial support this work would have never been made possible.

TABLE OF CONTENTS

LIST OF TABLES

LIST OF FIGURES

Chapter 1

Introduction

Nuclear reactor design is a complex process involving the evaluation of many technical parameters. In addition, most of these design parameters have interdependencies which are not easily evaluated by designers. As a result, multiple reactor simulation codes are used to validate a reactor design before a design can be constructed.

In general, reactor simulations are non-trivial and require significant resources to provide a solution. To ensure that the design space is adequately explored, simulations are repeatedly solved under varying conditions. This repetitive solution analysis can quickly drive up cost and time required for reactor design. Also, it is important to note that not all simulation solutions provide the same detail or resolution. Thus the design processes consists of many trade-offs resulting in varied financial consequences. These economic consequences fuel the motivation to continually increase current simulation capabilities to optimize reactor design; in short, pushing designers to find better designs, faster and cheaper.

For simulation purposes the nuclear reactor is divided into multiple independent systems. Each of these systems are simulated and validated separately, then the results are integrated to create the final design. From this description it is easy to understand how the design process can be plagued with seemingly constant re-designs, requiring more simulations. The division of the reactor into multiple systems is simply because simulating an entire reactor with a single, multi-physics code, is beyond the current state of the art, though there are teams of researchers attempting to address this issue such as CASL[1]. Thus, designers have a multi-facade problem consisting of limited computational capabilities, multi-physics coupling, and independent system simulations.

This research aims to address one piece of this complicated design process, the independent

[1]CASL is the **C**onsortium for **A**dvanced **S**imulation of **L**ight water reactors. CASL's mission is to "Provide coupled, higher-fidelity, usable modeling and simulation capabilities needed to address light water reactor operational and safety performance-defining phenomena.

systems simulation; more specifically, the reactor core design process. Reactor core design is a large, active area of research primarily concerned with controlling the reactor power distribution and reactivity. The behavior of the reactor core is studied by simulating the interactions of neutrons with materials, this is known as neutron transport simulation.

Neutron transport simulations are divided into two main methods, deterministic and stochastic. In short, stochastic methods utilize random variables, in a systematic manner, to evaluate a design. This research does not focus on stochastic methods but rather deterministic methods. The deterministic method attempts to solve the Boltzmann transport equation while minimizing the necessary computer resources and maximizing the level of solution accuracy. The goal of this research is to determine the applicability of an advanced modeling technique, Adaptive Model Refinement, to deterministic neutron transport simulations.

1.1 Deterministic Simulation Techniques

1.1.1 Overview

The deterministic approach utilizes the Boltzmann transport equation which expresses an inventory balance of all neutrons in the phase space. The Boltzmann equation was developed circa 1800 to describe the kinetic gas theory. This equation was adapted to explain neutron transport in 1940 and in this form is known as the *neutron transport equation* [2]. Following, is the transport equation using standard notation, Eq. 1.1.

$$\frac{1}{v}\frac{\partial\,\psi(\vec{r},\mathbf{\Omega},E,t)}{\partial t} + \mathbf{\Omega}\cdot\vec{\nabla}\psi(\vec{r},\mathbf{\Omega},E,t) + \Sigma_t(\vec{r},E,t)\psi(\vec{r},\mathbf{\Omega},E,t) = \int_{4\pi} d\mathbf{\Omega}' \int_0^\infty dE'\,\Sigma_s(\vec{r},\mathbf{\Omega}'\rightarrow\mathbf{\Omega},E'\rightarrow E,t)\psi(\vec{r},\mathbf{\Omega}',E',t) + \frac{\boldsymbol{\chi}(\vec{r},E,t)}{4\pi}\int_{4\pi} d\mathbf{\Omega}' \int_0^\infty dE'\,\nu_f(\vec{r},E',t)\Sigma_f(\vec{r},E',t)\psi(\vec{r},\mathbf{\Omega}',E',t) + Q(\vec{r},\mathbf{\Omega},E,t) \quad (1.1)$$

Note that delayed neutrons are ignored in writing this equation.

Numerical approaches to solving the transport equation are widely used for general geometries, as analytic solutions are only known for few simplistic geometric arrangements. In general solving the transport equation is a formidable task and because of this several approximation techniques have been developed. The ultimate goal of this research is to extended current transport simulation capabilities by implementing an advanced modeling technique. For this proof of concept study the advanced technique has been applied to diffusion and point kinetics simulations, which approximate the transport equation.

The diffusion equation basis is founded through the assumption that the flux is linearly

anisotropic[2]. Following this, assuming that the neutron source is isotropic[3] and that the rate of change of the current density is much smaller than the other terms of the equation[4], results in the formulation of Fick's law in terms of the neutron current density[5]. From all of these assumptions, the diffusion approximation of the neutron transport equation arises and can be concisely presented using standard notation as the *energy dependent diffusion equation* [2]. Following, is the energy dependent diffusion equation using standard notation, Eq. 1.2 .

$$\frac{1}{v(E)}\frac{\partial\phi(\vec{r},E,t)}{\partial t} - \nabla\cdot D(\vec{r},E,t)\nabla\phi(\vec{r},E,t) + \Sigma_t(\vec{r},E,t)\phi(\vec{r},E,t) = \int_0^\infty dE'\,\Sigma_s(\vec{r},E'\to E,t)\phi(\vec{r},E',t) + \boldsymbol{\chi}(\vec{r},E,t)\int_0^\infty dE'\,\nu_f(\vec{r},E',t)\Sigma_f(\vec{r},E',t)\psi(\vec{r},E',t) + Q(\vec{r},E,t) \quad (1.2)$$

The point kinetic equations are a further simplification of the diffusion equation. Though, before the point kinetic equations can be formulated the diffusion equation must be modified to account for delayed neutron effects[6]. The source term in the diffusion equation must also include terms which account for the contributions of delayed neutrons. Accompanying this substitution, the precursor concentration balance equations are introduced[7]. The point kinetic treatment is based upon expressing both the flux and precursor concentrations as a product of time dependent amplitude functions and slowly time varying spatial shape functions. Using adjoint perturbation theory and applying a likewise treatment for the adjoint functions, the point kinetic equations [2] for the amplitude functions are obtained without approximation. Following, are the set of equations which make up the point reactor kinetics equations using standard notation, Eq. 1.3 and Eq. 1.4.

$$\frac{dn(t)}{dt} = \frac{k(t)(1-\beta(t))-1}{l}n(t) + \sum_{i=1}^{I}\lambda_i C_i(t), \quad (1.3)$$

$$\frac{dC_i(t)}{dt} = \beta_i(t)\frac{k(t)}{l(t)}n(t) - \lambda_i C_i(t), \qquad i=1,\ldots,I \quad (1.4)$$

It is common practice to assume that the spatial shape functions equations' time derivative

[2]The linearly anisotropic assumption implies that the angular flux is weakly dependent on angle.

[3]A isotropic neutron source implies: $Q(\vec{r},\boldsymbol{\Omega},E,t) = \frac{1}{4\pi}Q(\vec{r},E,t)$

[4]Assuming that the derivative is negligibly small in comparison, implies that the rate of current density variation with respect to time is much slower than the collision frequency, $v(E)\Sigma_t(\vec{r},E)$.

[5]Fick's law formulated in terms of the neutron current density: $J(\vec{r},E,t) = -D(\vec{r},E)\nabla\phi(\vec{r},E,t)$

[6]To account for delayed neutrons, the fission source is modified:
$S_f(\vec{r},t) = (1-\beta)\int_0^\infty dE\,\nu_f(\vec{r},E,t)\Sigma_f(\vec{r},E,t)\phi(\vec{r},E,t)$

[7]The precursor concentration balance equations:
$\frac{\partial C_i(\vec{r},t)}{\partial t} = -\lambda_i C_i(\vec{r},t) + \beta_i(t)\int_0^\infty dE\,\nu_f(\vec{r},E,t)\Sigma_f(\vec{r},E,t)\phi(\vec{t},E,t)$

can be ignored, implying a quasi steady state exists, achieved mathematically by casting as an eigenvalue equations. Note that the spatial shape equations still have time dependence through the time dependence of cross-sections. The time dependence of the point kinetic parameters, i.e. $k(t)$, $\beta(t)$, $\beta_i(t)$, and $l(t)$, originate since they are given by inner products involving not only cross-sections but also the forward and adjoint spatial shape functions.

For the purposes of this research, the diffusion equation will be solved by the NESTLE code and the point kinetics equations will be solved by a point kinetics solver simply referred to as the PKE-Solver.

1.1.2 NESTLE

The code name NESTLE stands for **N**odal **E**igenvalue, **S**teady-state, **T**ransient, **L**e core **E**valuator. NESTLE was developed using FORTRAN 77. As the title implies, NESTLE is capable of solving the eigenvalue, eigenvalue adjoint, external fixed-source steady-state, and external fixed-source transient or eigenvalue initiated transient problems. The code solves the few-group neutron diffusion equation using the Nodal Expansion Method (NEM) and supports hexagonal and Cartesian geometries. When evaluating a transient case, delayed neutrons are accounted for utilizing the standard multi-group precursor concentration equations. Also, criticality or power level searches can be performed when analyzing steady-state eigenvalue or steady-state external fixed-source problems, respectively. In addition, NESTLE contains an impressive arsenal of features not needed for this proof of concept study [1].

For the steady-state cases NESTLE solves the multi-group steady-state fixed-source diffusion equation [1]. To accommodate the use of a numerical method the diffusion equation is discretized using the finite difference method. To minimize finite difference errors, spatial coupling coefficients are corrected using a nodal expansion method. Following, is the modified diffusion equation using standard multi-group notation, Eq. 1.5, where from now on spatial $\vec{r}$ and time t dependence is suppressed.

$$\begin{aligned} -\nabla \cdot D_g \nabla \phi_g + \Sigma_{t_g} \phi_g &= \sum_{g'=1}^{G} \Sigma_{s_{g,g'}} \phi_{g'} + \boldsymbol{\chi}_g \sum_{g'=1}^{G} \nu_{g'} \Sigma_{f_{g'}} \phi_{g'} + Q_{ext_g} \\ g &= 1, \ldots, G \end{aligned} \tag{1.5}$$

When solving the transient problem under external fixed-source conditions the multi-group diffusion equation is adapted to account for the delayed neutrons [1]. The equation is modified in the same way the equation is changed for point reactor kinetics. The following is the adapted multi-group equation using standard notation, Eq. 1.6 and Eq. 1.7.

$$\frac{1}{v_g}\frac{\partial \phi_g}{\partial t} - \nabla \cdot D_g \nabla \phi_g + \Sigma_{t_g}\phi_g = \sum_{g'=1}^{G} \Sigma_{s_{g,g'}}\phi_{g'} + (1-\beta)\,\boldsymbol{\chi}_g^{(p)} \sum_{g'=1}^{G} \nu_{g'}\,\Sigma_{f_{g'}}\phi_{g'} + \sum_{i=1}^{I^{(D)}} \boldsymbol{\chi}_{gi}^{(D)} \lambda_i\, C_i + Q_{ext_g} \tag{1.6}$$

and

$$\frac{\partial C_i}{\partial t} = \beta_i \sum_{g=1}^{G} \nu_g\,\Sigma_{f_g}\phi_g - \lambda_i C_i, \qquad i = 1, \ldots, I^{(D)} \tag{1.7}$$

To accommodate the eigenvalue initiated transient problem the equation is slightly altered by setting $Q_{ext_g} = 0$ and replacing $\nu_g\,\Sigma_{f_g}$ with $(\nu_g\,\Sigma_{f_g})/k$ [1].

1.1.3 PKE-Solver

The point kinetics equations solver (PKE-solver) consist of a simple matrix solver which evaluates the point kinetic equations with input parameters generated by NESTLE. It is advantageous to modify the point kinetic equations slightly to utilize two new terms, ρ and Λ, which represent *reactivity* and *mean neutron generation time*, respectively. Reactivity is formulated in the following manner,

$$\rho(t) = \frac{k(t) - 1}{k(t)},$$

and mean neutron generation time, the mean generation time between the birth of a neutron and the subsequent absorption, is defined simply by

$$\Lambda = \frac{l}{k}.$$

Applying these formulations to the standard point kinetic equations yields the most convenient form of the equations, (Eq. 1.8).

$$\begin{aligned} \frac{dn}{dt} &= \frac{\rho - \beta}{\Lambda} n + \sum_{i=1}^{I} \lambda_i C_i, \\ \frac{dC_i}{dt} &= \frac{\beta_i}{\Lambda} n - \lambda_i C_i, \qquad i = 1, \ldots, I. \end{aligned} \tag{1.8}$$

This form of the point reactor kinetic equations is known as the conventional form [2].

1.2 Advanced Simulation Techniques

1.2.1 Overview

Due to the complexity of nuclear reactors the desired simulation fidelity is currently out of reach for designers. This creates a level of uncertainty in many aspects of reactor design. This uncertainty is generally accommodated by increasing safety margins, resulting in increased financial burden. For this reason, reactor simulation is a constantly evolving field of research.

To help overcome the formidable challenges accompanying reactor simulation, many advanced simulation approaches have been and continue to be researched. Advanced modeling techniques can take many forms but most techniques revolve around two central ideas. One method is to integrate multiple simulation models to create a hybrid model with the hopes of yielding higher fidelity solutions faster. The second central idea attempts to couple multiple physics phenomena into a single code, called multi-physics coupling, with the intentions of producing similar fidelity results faster. For this study, the first approach was investigated further by combining a diffusion code and point reactor kinetics code to create a type of hybrid model, with the goal of producing higher fidelity results faster; though, the speed at which these results can be calculated was not investigated during this demonstration of concept.

The approach being evaluated in this study has a well known and very similar 'sister' technique, adaptive mesh refinement (AMR). AMR is an advanced simulation technique which is used to vary the resolution of numerical schemes. When a numerical method is applied to a problem the dimensions of the problem are often broken into discrete regions or 'cells', typically for neutron diffusion calculations in a repeating fashion, creating a grid or 'mesh'. Assuming the numerical scheme is well behaved, the resolution of the solution is dependent upon the grid spacing. From this point forward, when describing the problem space only the spatial dimensions will be discussed for simplicity.

In general, the simulation of a realistic problem involves regions of the problem space which have differing requirements for grid spacing to supply a solution of acceptable fidelity. To take advantage of this disparity AMR is applied. When using AMR the spatial mesh is varied to provide higher resolution where needed and lower resolution where acceptable. This allows the user to find the solution to a problem using differing resolutions while still providing the same accuracy as simulating with a higher cell count uniform grid, thus improving the time/accuracy ratio. Adaptive Model Refinement (AMoR) is similar in that it allows the user to adjust the solution method to best fit the varying complexity of the problem space, but differs in that instead of varying the resolution, the model fidelity is varied by switching between physics models.

1.2.2 Adaptive Model Refinement

The goal AMoR is to develop the capability to determine which physics model, given physics models of differing fidelity, to utilized to provide a solution with the desired level of fidelity while requiring minimum computational resources. Applying this to steady-state problems would entail a single selection. Considering this selection in terms of multi-fidelity, not unlike multi-grid, would correspond to the height of a V cycle, in that higher-fidelity models are associated with traversing up the V. In contrast to the steady-state application, applying this method to time-dependent problems would require the switching between models of differing fidelity as one model advances in time. The foundation of this approach is grounded in what is known as the quasi-static method of reactor kinetics. The past success of this method demonstrates the applicability of neutron flux reconstruction techniques with loosely coupled systems, resulting in an improved time/accuracy ratio [11].

The eventual goal of this research is to utilize an adjoint method to determine the fidelity of the specific physics model and thus act as a guide to determine which physics model will produce results with the desired fidelity at minimum computational expense. Since the adjoint method is still under development, the fidelity of models produced during this study were determined by comparing the AMoR results with the higher fidelity solution, which was solved in advance.

The switching between physics models requires projection and restriction operator capabilities. When considering these operators in terms of several physics models of differing fidelities, their interpreted meaning should not be limited to only discretized spatial-energy group projection mappings but also be viewed as restriction operators generating lower-fidelity models from higher-fidelity models. This interpretation yields insight into the AMoR's ability to utilize physics models of differing fidelity to produce a single solution of acceptable fidelity.

For the purposes of this research, the AMoR method was studied utilizing NESTLE, a 3-D, two-group, space-time solution calculated by the nodal form of the neutron diffusion equations, as the higher-fidelity model and the PKE-Solver, a point reactor kinetics equation solver, as the lower fidelity model. The projection operator involves mapping the point kinetics flux to a 3-D, two group flux and the precursor group concentrations to a 3-D precursor group concentrations. The restriction operator will involve determining the point kinetic parameters from the 3-D flux and precursor group concentrations.

1.2.3 Quasi-static Diffusion

The quasi-static approach of reactor kinetics was first introduced by Henry roughly fifty-five years ago [7] [8]. This approach was created to address the questionable results produced when applying point reactor kinetics equations. The approach developed by Henry factors the neutron

flux into 'amplitude' and 'shape' functions, Eq. 1.9.

$$\phi(\vec{r}, E, t) = T(t)\psi(\vec{r}, E, t) \tag{1.9}$$

The amplitude function, $T(t)$, is solely dependent upon time and provides the determining information regarding changes in reactor power, where as the shape function, $\psi(\vec{r}, E, \mathbf{\Omega}, t)$, describes the time-dependence of the power distribution. This factorization is done by demanding that the spatial weighted integral of the shape function be time independent. This assures that the shape function varies slower with time than the amplitude function, allowing larger time-steps to be taken for the shape function versus the amplitude function. For the so called 'adiabatic' approach, the shape function is assumed independent of time. For reactor dynamics the adiabatic approach yields much better results when compared with point kinetics alone [12]; though, when compared with full space-time calculations the differences were significant for certain transients [9]. A short time later it was demonstrated that the error of this approach could be minimized by applying a nonlinear coupling between amplitude and shape functions [10]; This approach is referred to as 'quasi-static'. This method was further developed by not setting to zero the shape function time derivative [11], resulting in the present day form of the quasi-static scheme, commonly referred to as the 'Improved Quasi-static Method', (IQM).

The IQM is utilized by solving the point reactor kinetic parameters using the shape function equation on a macro-time-step, Δt, and applying these parameters to the amplitude function equations, i.e. the point reactor kinetic equations, solved on a micro-time-step, δt, and then after $n = \Delta t/\delta t$ time steps switching back to solve the amplitude function equations [5]. As a result of the nonlinear treatment, there exist problems of such complexity that the convergence of the iterative method can take longer than the time needed to find a solution by the most suitable implicit numerical algorithm [3].

As opposed to applying the coupled amplitude-shape function approach used by the IQM, it is possible to develop an alternative method applying a coupled amplitude-flux shape function approach [6]. In this approach the flux is factored into 'amplitude' and 'flux' functions, Eq. 1.10.

$$\phi(\vec{r}, E, t) = T(t)\hat{\phi}(\vec{r}, E, t) \tag{1.10}$$

The resulting integration scheme is linear, as opposed to the non-linear IQM scheme, and as a result is much easier to implement. This scheme is known as the 'Predictor-Corrector Quasi-static Method' (PCQM) [4].

The application of the AMoR method is most similar to the PCQM, in that the flux is factored into amplitude-flux shape functions. In addition to this factorization, the precursor concentrations are also factored into amplitude-precursor shape functions. The primary differ-

ence between the IQM/PCQM and the AMoR approach is the treatment of the macro-time-step, Δt; the AMoR method does not use a constant value for Δt. The overall goal of the AMoR method is such that Δt is not assumed and is instead determined, during the simulation with time by the adjoint method. Though the adjoint method is not used in this research as it is still under development, the macro-time-step is defined by the discrepancies between the projected model and the higher fidelity solution.

Chapter 2

Methodology

2.1 Adaptive Model Refinement Method Formulation

The application of the AMoR method requires the development of shape-factors for the flux and precursor group concentrations. The values are calculated by NESTLE and used by the PKE-Solver to create the projected 3-D model. Speaking in terms of the IQM method, the macro-time-step, at which the shape-factor values are calculated, is dependent upon the formulation of the specific AMoR approach. As discussed above, the discrepancies between the higher fidelity model and the projected result indicates when physics model switching is needed. In addition to this approach, a steady-state library approach was also developed to explore the possibilities of a predetermined macro-time-step using a AMoR scheme and is discussed in detail in section 2.2.1 *Organization of the Steady-state Library.*

2.1.1 Output from NESTLE

Specific to this research, NESTLE solved the 2-neutron energy group, 6-precursor group, nodal diffusion equation. The core geometry consisted of a quarter core slice of a Westinghouse 4-loop, 3,311 MWt, PWR. The specific geometric inputs, material inputs, and cross-section data were from a sample data set[1]. Specific reductions in complexity were assumed[2] in this research to simplify the problem and help demonstrate the concept. The unaltered NESTLE v5.2.1 outputs some of the needed values for the AMoR method, such as the scalar flux,

$$\phi(\vec{r}, E, t) \rightarrow \phi_{g,m}(t),$$

[1]The data set was sampled from the McGuire Nuclear Station, Unit 1, Cycle 13.

[2]The specific assumptions are turning off the Xenon and Samarium options and not using the thermal-hydraulic feedback option.

the precursor group concentration,

$$C_i(\vec{r},t) \rightarrow C_{i,m}(t),$$

and the neutron velocity,

$$v(\vec{r},E,t) \rightarrow v_{g,m}(t),$$

where g is the neutron energy group ranging $g = 1, 2$, i is the precursor group ranging $i = 1, \ldots, 6$, and n is the spatial node ranging $m = 1, \ldots, M$.

Modifications to NESTLE were needed to adapt the code for use with the AMoR method. The energy dependent neutron density is calculated as,

$$n_{g,m}(t) = \frac{\phi_{g,m}(t)}{v_{g,m}(t)}.$$

Let the initial energy dependent neutron density be denoted by $n_{g,m}(0)$.

In addition the volume average neutron density, the energy dependent volume averaged scalar flux, the volume averaged scalar flux, the volume average precursor group concentration values, and the volume averaged neutron velocity values are needed. Note that any volume averaged values are only averaged over the fuel containing volume of the core and not the entirety of the geometric core. The volume calculations are limited to this region because the PKE-Solver is only capable of approximating the fueled region of the core. The volume averaged neutron density is formulated as,

$$\langle n(t) \rangle = \frac{\int_V dV \int_0^\infty dE\, n(\vec{r},E,t)}{\int_V dV} = \frac{\sum_{m=1}^{M} \sum_{g=1}^{2} n_{g,m}(t) V_m}{\sum_{m=1}^{M} V_m},$$

where V_m is the volume of node m and V is the total volume of the fueled region of the core. Let the initial volume averaged neutron density be denoted by $\langle n(0) \rangle$. Also, allow the normalized volume averaged neutron density to be defined as $\langle \bar{n}(t) \rangle$, such that,

$$\langle \bar{n}(t) \rangle = \frac{\langle n(t) \rangle}{\langle n(0) \rangle}. \tag{2.1}$$

The energy dependent volume averaged scalar flux is calculated by,

$$\langle \phi_g(t) \rangle = \frac{\int_V dV \int_{E_{g-1}}^{E_g} dE\, \phi(\vec{r},E,t)}{\int_V dV} = \frac{\sum_{m=1}^{M} \phi_{g,m}(t) V_m}{\sum_{m=1}^{M} V_m}. \tag{2.2}$$

The volume averaged scalar flux is formulated as,

$$\langle \phi(t) \rangle = \frac{\int_V dV \int_0^\infty dE\, \phi(\vec{r}, E, t)}{\int_V dV} = \frac{\sum_{m=1}^M \sum_{g=1}^2 \phi_{g,m}(t) V_m}{\sum_{m=1}^M V_m}.$$

The volume averaged precursor group concentration is calculated by,

$$\langle C_i(t) \rangle = \frac{\int_V C_i(\vec{r}, t) dV}{\int_V dV} = \frac{\sum_{m=1}^M C_{i,m}(t) V_m}{\sum_{m=1}^M V_m}. \tag{2.3}$$

Let the initial volume averaged precursor group concentrations be denoted by $\langle C_i(0) \rangle$. Also, allow the normalized volume averaged precursor group concentration to be defined as $\langle \bar{C}_i(t) \rangle$, such that,

$$\langle \bar{C}_i(t) \rangle = \frac{\langle C_i(t) \rangle}{\langle C_i(0) \rangle}. \tag{2.4}$$

The volume averaged neutron velocity is formulated as,

$$\langle v(t) \rangle = \frac{\langle \phi(t) \rangle}{\langle n(t) \rangle}. \tag{2.5}$$

Before the shape-factor values can be formulated one additional value is needed, this factor is referred to as the flux energy partition function, $\langle f_g^{(\phi)}(t) \rangle$, and is calculated by,

$$\langle f_g^{(\phi)}(t) \rangle = \frac{\langle \phi_g(t) \rangle}{\langle \phi(t) \rangle}. \tag{2.6}$$

2.1.2 Shape-factor Formulation

The scalar flux and precursor group concentration shape-factors can be formulated simply in terms of the nodal value divided by the volume averaged value. Thus the scalar flux shape-factor, $S_{g,m}^{(\phi)}(t)$, can be calculated by,

$$S_{g,m}^{(\phi)}(t) = \frac{\phi_{g,m}(t)}{\langle \phi_g(t) \rangle}, \tag{2.7}$$

and the precursor group concentration shape-factor, $S_{i,m}^{(C)}(t)$, can be calculated by,

$$S_{i,m}^{(C)}(t) = \frac{C_{i,m}(t)}{\langle C_i(t) \rangle}. \tag{2.8}$$

From these factors the scalar flux and precursor group concentration values can be broken down from their 3-D form into their amplitude-shape form. The scalar flux can be factored using the following,

$$\phi_{g,m}(t) = S_{g,m}^{(\phi)}(t) \langle f_g^{(\phi)}(t) \rangle \langle v(t) \rangle \langle \bar{n}(t) \rangle \langle n(0) \rangle. \tag{2.9}$$

The precursor group concentration can be factored using the following,

$$C_{i,m}(t) = S_{i,m}^{(C)}(t)\langle \bar{C}_i(t)\rangle\langle C_i(0)\rangle. \tag{2.10}$$

2.1.3 Output from the PKE-Solver

The PKE-Solver evaluates the point reactor kinetics equations utilizing 6-precursor group concentrations. The point kinetic input parameters, i.e. beta values, reactivity, etc., are provided by NESTLE v5.2.1 under steady-state conditions. The PKE-Solver outputs the approximate normalized core averaged neutron density, $\langle \bar{\tilde{n}}(t)\rangle$, and the approximate normalized core averaged precursor group concentration, $\langle \bar{\tilde{C}}_i(t)\rangle$.

2.1.4 Formulation of the Projected Model

Using the outputs from NESTLE and PKE-Solver it is now possible to create an approximation of the 3-D flux and precursor group concentrations. This approximation is referred to as the *Projected Model*. Recall equation Eq. 2.9 and replace the normalized volume averaged neutron density, $\langle \bar{n}(t)\rangle$, with the PKE-Solver approximate normalized volume averaged neutron density, $\langle \bar{\tilde{n}}(t)\rangle$. This substitution produces the approximate, or projected 3-D flux[3], $\tilde{\phi}_{g,m}(t)$.

$$\tilde{\phi}_{g,m}(t) = S_{g,m}^{(\phi)}(t)\langle f_g^{(\phi)}(t)\rangle\langle v(t)\rangle\langle \bar{\tilde{n}}(t)\rangle\langle n(0)\rangle \tag{2.11}$$

Recall equation Eq. 2.10 and replace the normalized volume averaged precursor group concentrations, $\langle \bar{C}_i(t)\rangle$, with the PKE-Solver calculated approximate normalized volume averaged precursor group concentrations, $\langle \bar{\tilde{C}}_i(t)\rangle$. This substitution results in the projected 3-D precursor group concentrations[4], $\tilde{C}_{i,m}(t)$.

$$\tilde{C}_{i,m}(t) = S_{i,m}^{(C)}(t)\langle \bar{\tilde{C}}_i(t)\rangle\langle C_i(0)\rangle \tag{2.12}$$

2.1.5 Formulation of Verification Calculations

To ensure that the AMoR method was implemented correctly, verification calculations were developed. These equations specifically ensure that the projected model is calculated correctly along with the locally normalized error calculations for the flux and precursor group concentrations. For verification purposes the shape-factor values for both flux and precursor group concentrations are updated at each time-step, as well as the flux energy partition function and

[3]Due to the initialization of the shape-factors and the relatively low computational cost of solving a steady-state problem with NESTLE, $\langle n(0)\rangle$ is always obtainable.

[4]Due to the initialization of the shape-factors and the relatively low computational cost of solving a steady-state problem with NESTLE, $\langle C_i(0)\rangle$ is always obtainable.

the volume averaged neutron velocity. Updating these factors makes it possible to find a relationship between the locally normalized error calculations and the normalized volume averaged calculations.

For the flux values, consider the locally normalized error equation between the NESTLE calculated 3-D flux and the projected 3-D flux,

$$\varepsilon_{flux,g,m}(t) = \frac{\phi_{g,m}(t) - \tilde{\phi}_{g,m}(t)}{\phi_{g,m}(t)}.$$

Recall Eq. 2.11 and applying this to the locally normalized error equation results in the following,

$$\varepsilon_{flux,g,m}(t) = \frac{\phi_{g,m}(t) - \frac{\phi_{g,m}(t)}{\langle\phi_g(t)\rangle}\frac{\langle\phi_g(t)\rangle}{\langle\phi(t)\rangle}\langle v(t)\rangle\langle n(0)\rangle\langle\bar{\tilde{n}}(t)\rangle}{\phi_{g,n}(t)} = 1 - \frac{\langle v(t)\rangle\langle n(0)\rangle\langle\bar{\tilde{n}}(t)\rangle}{\langle\phi(t)\rangle}.$$

From this form, a relationship between the two error equations can be reached by applying Eq. 2.1 and Eq. 2.5, such that,

$$\varepsilon_{flux,g,m}(t) = \frac{\langle n(t)\rangle - \langle n(0)\rangle\langle\bar{\tilde{n}}(t)\rangle}{\langle n(t)\rangle} = \frac{\langle\bar{n}(t)\rangle - \langle\bar{\tilde{n}}(t)\rangle}{\langle\bar{n}(t)\rangle}.$$

A formal relationship between the locally normalized flux error, $\varepsilon_{flux,g,m}(t)$, and the normalized volume averaged neutron density error, $\varepsilon_{den}(t)$, has been obtained.

$$\varepsilon_{den}(t) = \frac{\langle\bar{n}(t)\rangle - \langle\bar{\tilde{n}}(t)\rangle}{\langle\bar{n}(t)\rangle} = \varepsilon_{flux,g,m}(t) = \frac{\phi_{g,m}(t) - \tilde{\phi}_{g,m}(t)}{\phi_{g,m}(t)} \tag{2.13}$$

Using the error relationship (Eq. 2.13) the flux projection calculations can be verified by ensuring that the locally normalized flux error values, $\varepsilon_{flux,g,m}(t)$, do not differ from the normalized volume averaged neutron density error values, $\varepsilon_{den}(t)$, by more than single precision[5] machine error, ε_{mach}[6], which is approximately 10^{-7}; This can be expressed as,

$$-\varepsilon_{mach} \leqslant \left(\varepsilon_{flux,g,m}(t) - \varepsilon_{den}(t)\right) \leqslant \varepsilon_{mach}.$$

For the precursor group concentrations, consider the locally normalized error equation between the NESTLE calculated 3-D precursor group concentrations and the projected 3-D pre-

[5]Single precision calculations were performed because NESTLE was coded using FORTRAN 77 which is a single precision code language by default.

[6]Note that the value denoted as ε_{mach} is not strictly the single precision machine error value, which is variable. The value is actually on the order of the single precision machine error as more than one calculation is performed.

cursor group concentrations,

$$\varepsilon_{prec,i,m}(t) = \frac{C_{i,m}(t) - \tilde{C}_{i,m}(t)}{C_{i,m}(t)}.$$

Recall Eq. 2.12 and applying this to the locally normalized error equation results in the following,

$$\varepsilon_{prec,i,m}(t) = \frac{C_{i,m}(t) - \frac{C_{i,m}(t)}{\langle C_i(t)\rangle}\langle C_i(0)\rangle\langle\bar{\tilde{C}}_i(t)\rangle}{C_{i,m}(t)} = 1 - \frac{\langle C_i(0)\rangle\langle\bar{\tilde{C}}_i(t)\rangle}{\langle C_i(t)\rangle}.$$

From this form, a relationship between the two error equations can be reached by applying Eq. 2.4, such that,

$$\varepsilon_{prec,i,m}(t) = \frac{\langle C_i(t)\rangle - \langle C_i(0)\rangle\langle\bar{\tilde{C}}_i(t)\rangle}{\langle C_i(t)\rangle} = \frac{\langle \bar{C}_i(t)\rangle - \langle\bar{\tilde{C}}_i(t)\rangle}{\langle \bar{C}_i(t)\rangle}.$$

A formal relationship between the locally normalized precursor group concentrations error, $\varepsilon_{prec,i,m}(t)$, and the normalized volume averaged precursor group concentrations error, $\varepsilon_{prec,i}(t)$, has been reached.

$$\varepsilon_{prec,i}(t) = \frac{\langle \bar{C}_i(t)\rangle - \langle\bar{\tilde{C}}_i(t)\rangle}{\langle \bar{C}_i(t)\rangle} = \varepsilon_{prec,i,m}(t) = \frac{C_{i,m}(t) - \tilde{C}_{i,m}(t)}{C_{i,m}(t)} \tag{2.14}$$

Using the error relationship (Eq. 2.14) the precursor group concentration projection calculations can be verified by ensuring that the locally normalized precursor group concentration error values, $\varepsilon_{prec,i,m}(t)$, do not differ from the normalized volume averaged precursor group concentrations error values, $\varepsilon_{prec,i}(t)$, by more than the single precision machine error, ε_{mach}; This can be expressed as,

$$-\varepsilon_{mach} \leqslant \left(\varepsilon_{prec,i,m}(t) - \varepsilon_{prec,i}(t)\right) \leqslant \varepsilon_{mach}.$$

2.1.6 Formulation of Error Calculations

To determine the fidelity of the projected model, a set of error equations were developed. The calculations were developed specifically for use with a steady-state library data set but are also applicable to updated transient values. To formulate the error equations the steady-sate values must be determined using the steady-state library data set. The library is arranged such that the needed quantities are identified by rod position. Thus, using the current rod position of the PKE-Solver, $x(t)$, the corresponding values from the data set can be obtained. This brings about two cases;

Case 1: No interpolation

One case is when the PKE-Solver rod position equals a library archived rod position, i.e. $x(t) = x_k^{ss}$ for some $k = 1, \ldots, K$. When this occurs, the archived steady-state values are the needed values and no interpolation is required. Thus, from the data entry corresponding to the steady-state rod position, $x_{k(t)}^{ss}$, the approximated flux shape-factor is denoted by,

$$\tilde{S}_{g,m}^{(\phi)}(t) = S_{g,m,k(t)}^{(\phi),ss},$$

and the approximate precursor group concentration shape-factor is defined as,

$$\tilde{S}_{i,m}^{(C)}(t) = S_{i,m,k(t)}^{(C),ss}.$$

In addition, the flux energy partition function is obtained as,

$$\langle \tilde{f}_g^{(\phi)}(t) \rangle = \langle f_{g,k(t)}^{(\phi),ss} \rangle,$$

and the volume averaged neutron velocity is denoted by,

$$\langle \tilde{v}(t) \rangle = \langle v_{k(t)}^{ss} \rangle.$$

Case 2: Interpolation

Another case to consider is when the PKE-Solver rod position lies between two archived data entries and the values are found by linearly interpolating the entries. From the data set's upper rod position entry the upper flux shape-factor, flux energy partition function, volume averaged neutron velocity, and precursor group concentrations shape-factor are obtained and denoted with $\widehat{k}(t)$. Using the data set's lower rod position entry the factors are obtained and denoted with $\breve{k}(t)$ [7].

Once the upper and lower values have been retrieved the interpolated values can be determined as follows.
The approximate flux shape-factor:

$$\tilde{S}_{g,m}^{(\phi)}(t) = \left[\frac{S_{g,m,\widehat{k}(t)}^{(\phi),ss} - S_{g,m,\breve{k}(t)}^{(\phi),ss}}{x_{\widehat{k}(t)}^{ss} - x_{\breve{k}(t)}^{ss}} \left(x(t) - x_{\breve{k}(t)}^{ss} \right) \right] + S_{g,m,\breve{k}(t)}^{(\phi),ss}$$

[7] The designation of the rod position $\widehat{k}(t)$ and $\breve{k}(t)$ are not to be confused with the multiplication factor k described in Chapter 1. There is no significant relationship between the two variables.

The approximate flux energy partition function:

$$\langle \tilde{f}_g^{(\phi)}(t) \rangle = \left[\frac{\langle f_{g,\hat{k}(t)}^{(\phi),ss} \rangle - \langle f_{g,\check{k}(t)}^{(\phi),ss} \rangle}{x_{\hat{k}(t)}^{ss} - x_{\check{k}(t)}^{ss}} \big(x(t) - x_{\check{k}(t)}^{ss} \big) \right] + \langle f_{g,\check{k}(t)}^{(\phi),ss} \rangle$$

The approximate volume averaged neutron velocity:

$$\langle \tilde{v}(t) \rangle = \left[\frac{\langle v_{\hat{k}(t)}^{ss} \rangle - \langle v_{\check{k}(t)}^{ss} \rangle}{x_{\hat{k}(t)}^{ss} - x_{\check{k}(t)}^{ss}} \big(x(t) - x_{\check{k}(t)}^{ss} \big) \right] + \langle v_{\check{k}(t)}^{ss} \rangle$$

The approximate precursor group concentration shape-factor:

$$\tilde{S}_{i,m}^{(C)} = \left[\frac{S_{i,m,\hat{k}(t)}^{(C),ss} - S_{i,m,\check{k}(t)}^{(C),ss}}{x_{\hat{k}(t)}^{ss} - x_{\check{k}(t)}^{ss}} \big(x(t) - x_{\check{k}(t)}^{ss} \big) \right] + S_{i,m,\check{k}(t)}^{(C),ss}$$

Using these factors with the PKE-Solver calculated approximate normalized volume averaged neutron density and approximate normalized volume averaged precursor group concentrations, the projected model can be constructed. Applying Eq. 2.11 yields the approximate projected 3-D flux.

$$\tilde{\phi}_{g,m}(t) = \tilde{S}_{g,m}^{(\phi)}(t) \langle \tilde{f}_g^{(\phi)}(t) \rangle \langle \tilde{v}(t) \rangle \langle n(0) \rangle \langle \bar{\tilde{n}}(t) \rangle \tag{2.15}$$

Applying Eq. 2.12 results in the approximate projected 3-D precursor group concentrations.

$$\tilde{C}_{i,m}(t) = \tilde{S}_{i,m}^{(C)}(t) \langle C_i(0) \rangle \langle \bar{\tilde{C}}_i(t) \rangle \tag{2.16}$$

Once the approximate projected model values (Eq. 2.15 and Eq. 2.16) have been calculated it is possible to formulate various error metrics. For the flux values the following metrics can be formulated:
Energy group dependent, locally normalized L-1 error at the maximum flux position or the maximum flux error position:

$$\varepsilon_{1,flux,local,g} = \left[\left(\frac{\phi_{g,m^*}(t) - \tilde{\phi}_{g,m^*}(t)}{\phi_{g,m^*}(t)} \right) : m^* = \left(\arg\max_m [\phi_{g,m}(t)] \; or \; \arg\max_m \frac{|\phi_{g,m}(t) - \tilde{\phi}_{g,m}(t)|}{\phi_{g,m}(t)} \right) \right] \tag{2.17}$$

Locally normalized L-1 error at the maximum flux position or the maximum flux error position:

$$\varepsilon_{1,flux,local,total} = \left[\left(\frac{\phi_{m*}(t) - \tilde{\phi}_{m*}(t)}{\phi_{m*}(t)} \right) : m^* = \left(\arg\max_m [\phi_m(t)] \; or \; \arg\max_m \frac{|\phi_m(t) - \tilde{\phi}_m(t)|}{\phi_m(t)} \right) \right]$$

Energy group dependent average normalized L-1 error at the maximum flux position or the maximum flux error position:

$$\varepsilon_{1,flux,avg,g} = \left[\left(\frac{\phi_{g,m*}(t) - \tilde{\phi}_{g,m*}(t)}{\langle \phi_g(t) \rangle} \right) : m^* = \left(\arg\max_m [\phi_{g,m}(t)] \; or \; \arg\max_m \frac{|\phi_{g,m}(t) - \tilde{\phi}_{g,m}(t)|}{\langle \phi_g(t) \rangle} \right) \right] \quad (2.18)$$

Average normalized L-1 error at the maximum flux position or the maximum flux error position:

$$\varepsilon_{1,flux,avg,total} = \left[\left(\frac{\phi_{m*}(t) - \tilde{\phi}_{m*}(t)}{\langle \phi(t) \rangle} \right) : m^* = \left(\arg\max_m [\phi_m(t)] \; or \; \arg\max_m \frac{|\phi_m(t) - \tilde{\phi}_m(t)|}{\langle \phi(t) \rangle} \right) \right]$$

Energy group dependent volume weighted L-2 error[8]:

$$\varepsilon_{2,flux,g} = \sqrt{\frac{\sum_{m=1}^{M} \left[\left(\phi_{g,m}(t) - \tilde{\phi}_{g,m}(t) \right)^2 \Delta z_m \right]}{M_{xy} Z}} \frac{1}{\langle \phi_g(t) \rangle}$$

where Δz_m is the height of the m^{th} node, Z is the total height of the reactor, and m_{xy} is the number of nodes in a single XY-plane. Note, that the XY-grid is uniform though the height of each Z-plane differs. Thus, to volume weight the error of each node, a single node need only be multiplied by the height of the node, Δz_m. The relationship between the number of nodes in a single XY-plane and the total number of nodes, M, can be represented by,

$$M_{xy} = \frac{M}{M_z},$$

[8]The L-2 error describes the overall/average error of the projected model, where as the L-1 errors only describe a single node within the projected model.

where M_z is the number of Z-planes. From this it is clear that,

$$Z = \frac{1}{M_{xy}} \sum_{m=1}^{M} \Delta z_m.$$

Volume weighted L-2 error:

$$\varepsilon_{2,flux,total} = \sqrt{\frac{\sum_{m=1}^{M} \left[\left(\phi_m(t) - \tilde{\phi}_m(t) \right)^2 \Delta z_m \right]}{M_{xy} Z}} \frac{1}{\langle \phi(t) \rangle}$$

For the precursor group concentration values the following metrics can be formulated: Locally normalized L-1 error at the maximum precursor group concentration position or the maximum precursor group concentration error position:

$$\varepsilon_{1,pre,local,i} = \left[\left(\frac{C_{i,m^*}(t) - \tilde{C}_{i,m^*}(t)}{C_{i,m^*}(t)} \right) : m^* = \left(\arg\max_m [C_{i,m}(t)] \; or \; \arg\max_m \frac{|C_{i,m}(t) - \tilde{C}_{i,m}(t)|}{C_{i,m}(t)} \right) \right] \quad (2.19)$$

Averaged normalized L-1 error at the maximum precursor group concentration position or the maximum precursor group concentration error position:

$$\varepsilon_{1,pre,avg,i} = \left[\left(\frac{C_{i,m^*}(t) - \tilde{C}_{i,m^*}(t)}{\langle C_i(t) \rangle} \right) : m^* = \left(\arg\max_m [C_{i,m}(t)] \; or \; \arg\max_m \frac{|C_{i,m}(t) - \tilde{C}_{i,m}(t)|}{\langle C_i(t) \rangle} \right) \right] \quad (2.20)$$

Volume weighted L-2 error:

$$\varepsilon_{2,pre,i} = \sqrt{\frac{\sum_{m=1}^{M} \left[\left(C_{i,m}(t) - \tilde{C}_{i,m}(t) \right)^2 \Delta z_m \right]}{M_{xy} Z}} \frac{1}{\langle C_i(t) \rangle}$$

2.1.7 Component Error Analysis

To understand and assess the performance of the projected model, it is important to analysis the error equations to determine the sources of the error. This analysis was performed for the group dependent locally normalized and average normalized error calculations.

Flux Component Error Analysis

The energy group dependent locally normalized L-1 error at the maximum flux position or maximum flux error position, Eq. 2.17, can be combined with the approximate projected 3-D flux, Eq. 2.15, to produce the following (only considering the error term for notational simplicity),

$$\left(\frac{\phi_{g,m*}(t)-\tilde{\phi}_{g,m*}(t)}{\phi_{g,m*}(t)}\right)=\left(\frac{\phi_{g,m*}(t)-\tilde{S}^{(\phi)}_{g,m*}(t)\langle\tilde{f}^{(\phi)}_{g}(t)\rangle\langle\tilde{v}(t)\rangle\langle n(0)\rangle\langle\bar{\tilde{n}}(t)\rangle}{\phi_{g,m*}(t)}\right). \tag{2.21}$$

Notice that the approximate flux shape-factor, approximate flux energy partition function, approximate volume averaged neutron velocity, and PKE-Solver calculated normalized volume averaged neutron density factors can be reformulated into the following:

$$\begin{aligned}
\tilde{S}^{(\phi)}_{g,m}(t) &= S^{(\phi)}_{g,m}(t)-\Delta S^{(\phi)}_{g,m}(t) && (2.22)\\
\langle\tilde{f}^{(\phi)}_{g}(t)\rangle &= \langle f^{(\phi)}_{g}(t)\rangle-\Delta\langle f^{(\phi)}_{g}(t)\rangle && (2.23)\\
\langle\tilde{v}(t)\rangle &= \langle v(t)\rangle-\Delta\langle v(t)\rangle && (2.24)\\
\langle\bar{\tilde{n}}(t)\rangle &= \langle\bar{n}(t)\rangle-\Delta\langle\bar{n}(t)\rangle && (2.25)
\end{aligned}$$

where the first terms are the exact values and the Δ terms are the difference between the exact terms and approximate terms.

Applying Eq. 2.22 - Eq. 2.25 to the right-hand-side of Eq. 2.21 results in:

$$\left(\phi_{g,m*}(t)-\left[\left(S^{(\phi)}_{g,m*}(t)-\Delta S^{(\phi)}_{g,m*}(t)\right)\left(\langle f^{(\phi)}_{g}(t)\rangle-\Delta\langle f^{(\phi)}_{g}(t)\rangle\right)\right.\right.$$
$$\left.\left.\left(\langle v(t)\rangle-\Delta\langle v(t)\rangle\right)\langle n(0)\rangle\left(\langle\bar{n}(t)\rangle-\Delta\langle\bar{n}(t)\rangle\right)\right]\right)\frac{1}{\phi_{g,m*}(t)} \tag{2.26}$$

Expansion of the multi-factor term in Eq. 2.26 provides the following equation[9]:

$$\left[S^{(\phi)}_{g,m*}(t)\langle f^{(\phi)}_{g}(t)\rangle\langle v(t)\rangle\langle n(0)\rangle\langle\bar{n}(t)\rangle-\Delta S^{(\phi)}_{g,m*}(t)\langle f^{(\phi)}_{g}(t)\rangle\langle v(t)\rangle\langle n(0)\rangle\langle\bar{n}(t)\rangle-\right.$$
$$S^{(\phi)}_{g,m*}(t)\Delta\langle f^{(\phi)}_{g}(t)\rangle\langle v(t)\rangle\langle n(0)\rangle\langle\bar{n}(t)\rangle-S^{(\phi)}_{g,m*}(t)\langle f^{(\phi)}_{g}(t)\rangle\Delta\langle v(t)\rangle\langle n(0)\rangle\langle\bar{n}(t)\rangle-$$
$$\left.S^{(\phi)}_{g,m*}(t)\langle f^{(\phi)}_{g}(t)\rangle\langle v(t)\rangle\langle n(0)\rangle\Delta\langle\bar{n}(t)\rangle-\mathcal{O}(\Delta^2)\right] \tag{2.27}$$

Considering the terms independently and using Eq. 2.22 - Eq. 2.25, and Eq. 2.9 where applicable yields valuable insight.

[9]Note there are no bounds placed on the magnitude of the second order terms denoted, $\mathcal{O}(\Delta^2)$.

1st Term:

$$S^{(\phi)}_{g,m*}(t)\,\langle f^{(\phi)}_g(t)\rangle\langle v(t)\rangle\langle n(0)\rangle\langle \bar{n}(t)\rangle = \phi_{g,m*}(t) \tag{2.28}$$

2nd Term:

$$\Delta S^{(\phi)}_{g,m*}(t)\,\langle f^{(\phi)}_g(t)\rangle\langle v(t)\rangle\langle n(0)\rangle\langle \bar{n}(t)\rangle = \left(S^{(\phi)}_{g,m*}(t) - \tilde{S}^{(\phi)}_{g,m*}(t)\right)\langle f^{(\phi)}_g(t)\rangle\langle v(t)\rangle\langle n(0)\rangle\langle \bar{n}(t)\rangle \tag{2.29}$$

3rd Term:

$$S^{(\phi)}_{g,m*}(t)\,\Delta\langle f^{(\phi)}_g(t)\rangle\langle v(t)\rangle\langle n(0)\rangle\langle \bar{n}(t)\rangle = S^{(\phi)}_{g,m*}(t)\left(\langle f^{(\phi)}_g(t)\rangle - \langle \tilde{f}^{(\phi)}_g(t)\rangle\right)\langle v(t)\rangle\langle n(0)\rangle\langle \bar{n}(t)\rangle \tag{2.30}$$

4th Term:

$$S^{(\phi)}_{g,m*}(t)\,\langle f^{(\phi)}_g(t)\rangle\Delta\langle v(t)\rangle\langle n(0)\rangle\langle \bar{n}(t)\rangle = S^{(\phi)}_{g,m*}(t)\,\langle f^{(\phi)}_g(t)\rangle\left(\langle v(t)\rangle - \langle \tilde{v}(t)\rangle\right)\langle n(0)\rangle\langle \bar{n}(t)\rangle \tag{2.31}$$

5th Term:

$$S^{(\phi)}_{g,m*}(t)\,\langle f^{(\phi)}_g(t)\rangle\langle v(t)\rangle\langle n(0)\rangle\Delta\langle \bar{n}(t)\rangle = S^{(\phi)}_{g,m*}(t)\,\langle f^{(\phi)}_g(t)\rangle\langle v(t)\rangle\langle n(0)\rangle\left(\langle \bar{n}(t)\rangle - \langle \bar{\tilde{n}}(t)\rangle\right) \tag{2.32}$$

Recall Eq. 2.26 and apply the relationships obtained from Eq. 2.28 - Eq. 2.32 to obtain the following;

$$\left(\frac{\left(S^{(\phi)}_{g,m*}(t) - \tilde{S}^{(\phi)}_{g,m*}(t)\right)}{S^{(\phi)}_{g,m*}(t)} + \frac{\left(\langle f^{(\phi)}_g(t)\rangle - \langle \tilde{f}^{(\phi)}_g(t)\rangle\right)}{\langle f^{(\phi)}_g(t)\rangle} + \frac{\left(\langle v(t)\rangle - \langle \tilde{v}(t)\rangle\right)}{\langle v(t)\rangle} + \frac{\left(\langle \bar{n}(t)\rangle - \langle \bar{\tilde{n}}(t)\rangle\right)}{\langle \bar{n}(t)\rangle} + \mathcal{O}(\Delta^2)\right) \tag{2.33}$$

Let the following definitions hold.
Flux shape-factor error:

$$\varepsilon_{\tilde{S}^{(\phi)}_{g,m*}(t)} = \frac{\left(S^{(\phi)}_{g,m*}(t) - \tilde{S}^{(\phi)}_{g,m*}(t)\right)}{S^{(\phi)}_{g,m*}(t)} \tag{2.34}$$

Flux energy partition function error:

$$\varepsilon_{\langle \tilde{f}^{(\phi)}_{g}(t)\rangle} = \frac{\left(\langle f^{(\phi)}_{g}(t)\rangle - \langle \tilde{f}^{(\phi)}_{g}(t)\rangle\right)}{\langle f^{(\phi)}_{g}(t)\rangle} \tag{2.35}$$

Volume averaged neutron velocity error:

$$\varepsilon_{\langle \tilde{v}(t)\rangle} = \frac{\left(\langle v(t)\rangle - \langle \tilde{v}(t)\rangle\right)}{\langle v(t)\rangle} \tag{2.36}$$

Normalized volume averaged neutron density error:

$$\varepsilon_{\langle \tilde{\bar{n}}(t)\rangle} = \frac{\left(\langle \bar{n}(t)\rangle - \langle \tilde{\bar{n}}(t)\rangle\right)}{\langle \bar{n}(t)\rangle} \tag{2.37}$$

Thus Eq. 2.17 can be reformulated by applying Eq. 2.34 - Eq. 2.37 to Eq. 2.33 resulting in,

$$\varepsilon_{1,flux,local,g} = \left(\varepsilon_{\tilde{S}^{(\phi)}_{g,m*}(t)} + \varepsilon_{\langle \tilde{f}^{(\phi)}_{g}(t)\rangle} + \varepsilon_{\langle \tilde{v}(t)\rangle} + \varepsilon_{\langle \tilde{\bar{n}}(t)\rangle} + \mathcal{O}(\Delta^2)\right) \tag{2.38}$$

where m^* is defined in Figure 2.17.

The energy group dependent average normalized L-1 error at the maximum flux position or the maximum flux error position, Eq. 2.18, can be combined with the approximate projected 3-D flux, Eq. 2.15, to produce the following (only considering the error term for notational simplicity),

$$\left(\frac{\phi_{g,m*}(t) - \tilde{\phi}_{g,m*}(t)}{\langle \phi_g(t)\rangle}\right) = \left(\frac{\phi_{g,m*}(t) - \tilde{S}^{(\phi)}_{g,m*}(t)\langle \tilde{f}^{(\phi)}_{g}(t)\rangle\langle \tilde{v}(t)\rangle\langle n(0)\rangle\langle \tilde{\bar{n}}(t)\rangle}{\langle \phi_g(t)\rangle}\right). \tag{2.39}$$

Applying Eq. 2.22 - Eq. 2.25 to the right-hand-side of Eq. 2.21 results in:

$$\Bigg(\phi_{g,m^*}(t) - \Bigg[\Big(S^{(\phi)}_{g,m^*}(t) - \Delta S^{(\phi)}_{g,m^*}(t)\Big)\Big(\langle f^{(\phi)}_g(t)\rangle - \Delta\langle f^{(\phi)}_g(t)\rangle\Big) \\ \Big(\langle v(t)\rangle - \Delta\langle v(t)\rangle\Big)\langle n(0)\rangle\Big(\langle \bar{n}(t)\rangle - \Delta\langle \bar{n}(t)\rangle\Big)\Bigg]\Bigg)\frac{1}{\langle \phi_g(t)\rangle} \quad (2.40)$$

Recall the energy dependent volume averaged flux, Eq. 2.2, and apply this to the approximate projected 3-D flux, Eq. 2.15, to yield,

$$\langle \tilde{\phi}_g(t)\rangle = \langle \tilde{S}^{(\phi)}_g(t)\rangle\langle \tilde{f}^{(\phi)}_g(t)\rangle\langle \tilde{v}(t)\rangle\langle n(0)\rangle\langle \bar{\tilde{n}}(t)\rangle, \quad (2.41)$$

where the volume averaged flux shape-factor is defined as,

$$\langle S^{(\phi)}_g(t)\rangle = \frac{\sum_{m=1}^{M} S^{(\phi)}_{g,m}(t)V_m}{\sum_{m=1}^{M} V_m}. \quad (2.42)$$

Recall the definition of the flux shape-factor, Eq. 2.7, and the definition of the energy dependent volume averaged flux, Eq. 2.2; Apply these definitions to Eq. 2.42 yielding,

$$\langle S^{(\phi)}_g(t)\rangle = \frac{1}{\langle \phi_g(t)\rangle}\frac{\sum_{m=1}^{M} \phi_{g,m}(t)V_m}{\sum_{m=1}^{M} V_m} = 1. \quad (2.43)$$

Apply Eq. 2.28 - Eq. 2.32, Eq. 2.41, and Eq. 2.43 to Eq. 2.40 resulting in the following equation.

$$S^{(\phi)}_{g,m^*}(t)\Bigg(\frac{\Big(S^{(\phi)}_{g,m^*}(t) - \tilde{S}^{(\phi)}_{g,m^*}(t)\Big)}{S^{(\phi)}_{g,m^*}(t)} + \frac{\Big(\langle f^{(\phi)}_g(t)\rangle - \langle \tilde{f}^{(\phi)}_g(t)\rangle\Big)}{\langle f^{(\phi)}_g(t)\rangle} + \\ \frac{\Big(\langle v(t)\rangle - \langle \tilde{v}(t)\rangle\Big)}{\langle v(t)\rangle} + \frac{\Big(\langle \bar{n}(t)\rangle - \langle \bar{\tilde{n}}(t)\rangle\Big)}{\langle \bar{n}(t)\rangle} + \mathcal{O}(\Delta^2)\Bigg) \quad (2.44)$$

Thus Eq. 2.18 can be reformulated by applying Eq. 2.34 - Eq. 2.37 to Eq. 2.44 yielding,

$$\varepsilon_{1,flux,average,g} = \Bigg(S^{(\phi)}_{g,m^*}(t)\Big(\varepsilon_{\tilde{S}^{(\phi)}_{g,m^*}(t)} + \varepsilon_{\langle \tilde{f}^{(\phi)}_g(t)\rangle} + \varepsilon_{\langle \tilde{v}(t)\rangle} + \varepsilon_{\langle \bar{\tilde{n}}(t)\rangle}\Big) + \mathcal{O}(\Delta^2)\Bigg) \quad (2.45)$$

where m^* is defined by Eq. 2.18.

Precursor Group Concentration Component Error Analysis

The locally normalized L-1 error at the maximum precursor group concentration position or the maximum precursor group concentration error position, Eq. 2.19, can be combined with the approximate projected 3-D precursor group concentrations, Eq. 2.16, to produce the following (only consider the error term for notational simplicity),

$$\left(\frac{C_{i,m^*}(t) - \tilde{C}_{i,m^*}(t)}{C_{i,m^*}(t)}\right) = \left(\frac{C_{i,m^*}(t) - \tilde{S}^{(C)}_{i,m^*}(t)\,\langle C_i(0)\rangle\langle\bar{\tilde{C}}_i(t)\rangle}{C_{i,m^*}(t)}\right). \tag{2.46}$$

Notice that the approximate precursor shape-factor and the PKE-Solver calculated normalized volume averaged precursor group concentration factors can be reformulated into the following:

$$\tilde{S}^{(C)}_{i,m}(t) = S^{(C)}_{i,m}(t) - \Delta S^{(C)}_{i,m}(t) \tag{2.47}$$

$$\langle\bar{\tilde{C}}_i(t)\rangle = \langle\bar{C}_i(t)\rangle - \Delta\langle\bar{C}_i(t)\rangle \tag{2.48}$$

where the first terms are the exact values and the Δ terms are the difference between the exact values and the approximate values.

Applying Eq. 2.47 and Eq. 2.48 to the right hand side of Eq. 2.46 results in:

$$\left(C_{i,m^*}(t) - \left(S^{(C)}_{i,m^*}(t) - \Delta S^{(C)}_{i,m^*}(t)\right)\langle C_i(0)\rangle\left(\langle\bar{C}_i(t)\rangle - \Delta\langle\bar{C}_i(t)\rangle\right)\right)\frac{1}{C_{i,m^*}(t)} \tag{2.49}$$

Expansion of the multi-factor term in Eq. 2.49 provides the following equation:

$$\Bigg[S^{(C)}_{i,m^*}(t)\,\langle C_i(0)\rangle\langle\bar{C}_i(t)\rangle - \Delta S^{(C)}_{i,m^*}(t)\,\langle C_i(0)\rangle\langle\bar{C}_i(t)\rangle - S^{(C)}_{i,m^*}(t)\,\langle C_i(0)\rangle\Delta\langle\bar{C}_i(t)\rangle + \mathcal{O}(\Delta^2)\Bigg] \tag{2.50}$$

Considering the terms of Eq. 2.50 independently and using Eq. 2.47, Eq. 2.48, and Eq. 2.10 where applicable yields valuable insight.

1st Term:

$$S^{(C)}_{i,m^*}(t)\,\langle C_i(0)\rangle\langle\bar{C}_i(t)\rangle = C_{i,m^*}(t) \tag{2.51}$$

2nd Term:

$$\Delta S^{(C)}_{i,m^*}(t)\,\langle C_i(0)\rangle\langle\bar{C}_i(t)\rangle = \left(S^{(C)}_{i,m^*}(t) - \tilde{S}^{(C)}_{i,m^*}(t)\right)\langle C_i(0)\rangle\langle\bar{C}_i(t)\rangle \tag{2.52}$$

3rd Term:

$$S^{(C)}_{i,m^*}(t)\,\langle C_i(0)\rangle\Delta\langle\bar{C}_i(t)\rangle = S^{(C)}_{i,m^*}(t)\,\langle C_i(0)\rangle\left(\langle\bar{C}_i(t)\rangle - \langle\bar{\tilde{C}}_i(t)\rangle\right) \tag{2.53}$$

Apply the relationships obtained from Eq. 2.51 - Eq. 2.53 to Eq. 2.49 resulting in;

$$\left(\frac{\left(S^{(C)}_{i,m*}(t) - \tilde{S}^{(C)}_{i,m*}(t) \right)}{S^{(C)}_{i,m*}(t)} + \frac{\left(\langle \bar{C}_i(t) \rangle - \langle \bar{\tilde{C}}_i(t) \rangle \right)}{\langle \bar{C}_i(t) \rangle} + \mathcal{O}(\Delta^2) \right) \tag{2.54}$$

Let the following definitions hold.
Precursor group concentration shape-factor error:

$$\varepsilon_{\tilde{S}^{(C)}_{i,m*}(t)} = \frac{\left(S^{(C)}_{i,m*}(t) - \tilde{S}^{(C)}_{i,m*}(t) \right)}{S^{(C)}_{i,m*}(t)} \tag{2.55}$$

Normalized volume averaged precursor group concentration error:

$$\varepsilon_{\langle \bar{\tilde{C}}_i(t) \rangle} = \frac{\left(\langle \bar{C}_i(t) \rangle - \langle \bar{\tilde{C}}_i(t) \rangle \right)}{\langle \bar{C}_i(t) \rangle} \tag{2.56}$$

Thus Eq. 2.19 can be refomulated by applying Eq. 2.55 and Eq. 2.56 to Eq. 2.54 yielding,

$$\varepsilon_{1,pre,local,i} = \left(\varepsilon_{\tilde{S}^{(C)}_{i,m*}(t)} + \varepsilon_{\langle \bar{\tilde{C}}_i(t) \rangle} + \mathcal{O}(\Delta^2) \right) \tag{2.57}$$

where m^* is defined by Eq. 2.19.

The average normalized L-1 error at the maximum precursor group concentration position or the maximum precursor group concentration error position, Eq. 2.20, can be combined with the approximate projected 3-D precursor group concentration, Eq. 2.16, to produce the following (only consider the error term for notational simplicity),

$$\left(\frac{C_{i,m*}(t) - \tilde{C}_{i,m*}(t)}{\langle C_i(t) \rangle} \right) = \left(\frac{C_{i,m*}(t) - \tilde{S}^{(C)}_{i,m*}(t) \langle C_i(0) \rangle \langle \bar{\tilde{C}}_i(t) \rangle}{\langle C_i(t) \rangle} \right). \tag{2.58}$$

Applying Eq. 2.47 and Eq. 2.48 to the right hand side of Eq. 2.58 results in:

$$\left(C_{i,m*}(t) - \left(S^{(C)}_{i,m*}(t) - \Delta S^{(C)}_{i,m*}(t) \right) \langle C_i(0) \rangle \left(\langle \bar{C}_i(t) \rangle - \Delta \langle \bar{C}_i(t) \rangle \right) \right) \frac{1}{\langle C_i(t) \rangle} \tag{2.59}$$

Recall the volume averaged precursor concentration, Eq. 2.3, and apply this to the approximate projected 3-D precursor group concentration, Eq. 2.16, to yield,

$$\langle \tilde{C}_i(t) \rangle = \langle \tilde{S}^{(C)}_i(t) \rangle \langle C_i(0) \rangle \langle \bar{\tilde{C}}_i(t) \rangle, \tag{2.60}$$

where the volume averaged precursor group concentration shape-factor is defined as,

$$\langle S_i^{(C)}(t)\rangle = \frac{\sum_{m=1}^{M} S_{i,m}^{(C)}(t)V_m}{\sum_{m=1}^{M} V_m}. \tag{2.61}$$

Recall the definition of the precursor group concentration shape-factor, Eq. 2.8, and the definition of the volume averaged precursor group concentration, Eq. 2.3; Apply these definitions to Eq. 2.61 yielding,

$$\langle S_i^{(C)}(t)\rangle = \frac{1}{\langle C_i(t)\rangle}\frac{\sum_{m=1}^{M} C_{i,m}(t)V_m}{\sum_{m=1}^{M} V_m} = 1. \tag{2.62}$$

Apply Eq. 2.51 - Eq. 2.53, Eq. 2.60, and Eq. 2.62 to Eq. 2.59 resulting in the following equation.

$$S_{i,m^*}^{(C)}(t)\left(\frac{\left(S_{i,m^*}^{(C)}(t) - \tilde{S}_{i,m^*}^{(C)}(t)\right)}{S_{i,m^*}^{(C)}(t)} + \frac{\left(\langle \bar{C}_i(t)\rangle - \langle \bar{\tilde{C}}_i(t)\rangle\right)}{\langle \bar{C}_i(t)\rangle} + \mathcal{O}(\Delta^2)\right) \tag{2.63}$$

Thus Eq. 2.20 can be reformulated by applying Eq. 2.55 and Eq. 2.56 to Eq. 2.63 yielding,

$$\varepsilon_{1,pre,avg,i} = \left(S_{i,m^*}^{(C)}(t)\left(\varepsilon_{\tilde{S}_{i,m^*}^{(C)}(t)} + \varepsilon_{\langle \bar{\tilde{C}}_i(t)\rangle}\right) + \mathcal{O}(\Delta^2)\right) \tag{2.64}$$

where m^* is defined by Eq. 2.20.

2.1.8 NESTLE Restart Error Analysis

When using the AMoR model switching approach, the projected model results are input into NESTLE. The code is then restarted, with the belief that NESTLE will anneal out the introduced error. This claim is based on the following argument:

Let the time-space discretized equation, Eq. 1.6, be represented by the following form,

$$\bar{\bar{A}}_t\bar{\phi}_t = \bar{\bar{B}}_t\bar{\phi}_{t-1}. \tag{2.65}$$

This representation (Eq. 2.65) will be referred to as the exact solution, where $\bar{\bar{A}}_t$ operates on $\bar{\phi}_t$, $\bar{\bar{B}}_t$ operates on $\bar{\phi}_{t-1}$, and $\bar{\phi}_t$ is the flux at time-step t and $t-1$. The operator $\bar{\bar{A}}_t$ is the loss operator associated with the left hand side of Eq. 1.6 and the operator $\bar{\bar{B}}_t$ is the production operator associated with the right hand side of Eq. 1.6.

Note that the flux produced by the projected model is an approximation of the exact flux

and can be expressed as,

$$\bar{\phi}_t = \bar{\tilde{\phi}}_t + \bar{\varepsilon}_t \tag{2.66}$$

where $\bar{\varepsilon}_t$ is the error between the exact flux, $\bar{\phi}_t$, and projected flux, $\bar{\tilde{\phi}}_t$.

Substituting Eq. 2.66, into the time-space discretized equation, Eq. 2.65, yields,

$$\bar{\bar{A}}_t(\bar{\tilde{\phi}}_t + \bar{\varepsilon}_t) = \bar{\bar{B}}_t(\bar{\tilde{\phi}}_{t-1} + \bar{\varepsilon}_{t-1}), \tag{2.67}$$

which can be rearranged into,

$$\bar{\bar{A}}_t\bar{\varepsilon}_t = \bar{\bar{B}}_t\bar{\varepsilon}_{t-1} + (\bar{\bar{B}}_t\bar{\tilde{\phi}}_{t-1} - \bar{\bar{A}}_t\bar{\tilde{\phi}}_t). \tag{2.68}$$

Let the residual, $\bar{r}_t$, be defined as $(\bar{\bar{B}}_t\bar{\tilde{\phi}}_{t-1} - \bar{\bar{A}}_t\bar{\tilde{\phi}}_t)$, such that Eq. 2.68 can be expressed in the following form,

$$\bar{\bar{A}}_t\bar{\varepsilon}_t = \bar{\bar{B}}_t\bar{\varepsilon}_{t-1} + \bar{r}_t. \tag{2.69}$$

Note that Eq. 2.69 does not directly lend insight into the error at time-step t, denoted by $\bar{\varepsilon}_t$, because the error at time-step $t-1$, denoted as $\bar{\varepsilon}_{t-1}$, is unknown. Though, continuing this argument further does provide insight into the previously made claim. Pressing forward, by rearranging[10] Eq. 2.69, the error at time-step t can be expressed as,

$$\bar{\varepsilon}_t = \bar{\bar{A}}_t^{-1}\,(\bar{\bar{B}}_t\bar{\varepsilon}_{t-1} + \bar{r}_t). \tag{2.70}$$

Given the general nature of Eq. 2.70, the error for time-step $t+1$ can be represented by,

$$\bar{\varepsilon}_{t+1} = \bar{\bar{A}}_{t+1}^{-1}\,(\bar{\bar{B}}_{t+1}\bar{\varepsilon}_t + \bar{r}_{t+1}) \tag{2.71}$$

and combining Eq. 2.70 and Eq. 2.71 yields an expression for the error at time-step $t+1$, in terms of $\bar{\varepsilon}_{t-1}$,

$$\bar{\varepsilon}_{t+1} = \bar{\bar{A}}_{t+1}^{-1}\Big(\bar{\bar{B}}_{t+1}\left[\bar{\bar{A}}_t^{-1}\,(\bar{\bar{B}}_t\bar{\varepsilon}_{t-1} + \bar{r}_t)\right] + \bar{r}_{t+1}\Big). \tag{2.72}$$

Expanding out terms in Eq. 2.72.

$$\bar{\varepsilon}_{t+1} = \big(\bar{\bar{A}}_{t+1}^{-1}\,\bar{\bar{B}}_{t+1}\big)\big(\bar{\bar{A}}_t^{-1}\,\bar{\bar{B}}_t\big)\bar{\varepsilon}_{t-1} + (\bar{\bar{A}}_{t+1}^{-1}\,\bar{\bar{B}}_{t+1})\bar{\bar{A}}_t^{-1}\,\bar{r}_{t+1} + \bar{\bar{A}}_{t+1}\bar{r}_{t+1} \tag{2.73}$$

Notice that the general basis provided by Eq. 2.73 can be extended to time-step $t+2$ rather

[10] Given the physics of the system, matrix $\bar{\bar{A}}_t$ is invertible. See the NESTLE manual for further explanation [1].

easily,

$$\bar{\varepsilon}_{t+2} = (\bar{\bar{A}}_{t+2}^{-1}\,\bar{\bar{B}}_{t+2})(\bar{\bar{A}}_{t+1}^{-1}\,\bar{\bar{B}}_{t+1})(\bar{\bar{A}}_{t}^{-1}\,\bar{\bar{B}}_{t})\bar{\varepsilon}_{t-1} + (\bar{\bar{A}}_{t+2}^{-1}\,\bar{\bar{B}}_{t+2})(\bar{\bar{A}}_{t+1}^{-1}\bar{\bar{B}}_{t+1})\bar{\bar{A}}_{t}^{-1}\bar{r}_t + (\bar{\bar{A}}_{t+2}^{-1}\,\bar{\bar{B}}_{t+2})\bar{\bar{A}}_{t+1}^{-1}\,\bar{r}_{t+1} + \bar{\bar{A}}_{t+2}^{-1}\,\bar{r}_{t+2} \quad (2.74)$$

and thus generally extended to time-step $t+j$,

$$\bar{\varepsilon}_{t+j} = \left[\prod_{j'=0}^{j} \bar{\bar{A}}_{t+j'}^{-1}\bar{\bar{B}}_{t+j'}\right]\bar{\varepsilon}_{t-1} + \sum_{t'=t}^{t+j}\left[\prod_{j'=(t'-t+1)}^{j}\left(\bar{\bar{A}}_{t+j'}^{-1}\,\bar{\bar{B}}_{t+j'}\right)\right]\bar{\bar{A}}_{t'}^{-1}\bar{r}_{t'} = \left[\prod_{j'=0}^{j}\bar{\bar{C}}_{t+j'}\right]\bar{\varepsilon}_{t-1} + \sum_{t'=t}^{t+j}\left[\prod_{j'=(t'-t+1)}^{j}\bar{\bar{C}}_{t+j'}\right]\bar{\bar{A}}_{t'}^{-1}\bar{r}_{t'} \quad (2.75)$$

where $\bar{\bar{C}}_{t+j'}$ is defined simply as the product of $\bar{\bar{A}}_{t+j'}^{-1}\,\bar{\bar{B}}_{t+j'}$. Note that when $j' > j$ the product term equals one[11].

Assuming the operators $\bar{\bar{A}}$ and $\bar{\bar{B}}$ have no dependence on time implies that $\bar{\bar{C}}$ also has no time dependence. The eigenvalue problem associated with $\bar{\bar{C}}$ is given by,

$$\bar{\bar{C}}\bar{\psi}_p = \lambda_p\bar{\psi}_p \qquad \text{for } p = 1, 2, \ldots. \quad (2.76)$$

Assume the spectrum of λ_p is discrete and $\{\bar{\psi}_p\}$ forms a complete basis. Then we can express $\bar{\varepsilon}$ and $\bar{r}$ as follows,

$$\bar{\varepsilon}_{t-1} = \sum_p c_p^{(\varepsilon_{t-1})}\,\bar{\psi}_p \quad (2.77)$$

and

$$\bar{\bar{A}}_t^{-1}\,\bar{r}_t = \sum_p c_p^{(A_t^{-1}\,r_t)}\,\bar{\psi}_p. \quad (2.78)$$

where c_p denotes the coefficients for the expansion in terms of the eigenvector. Thus Eq. 2.76 terms involving multiples of $\bar{\bar{C}}$ operating on a vector can be written as follows,

$$\left[\prod_{j'=0}^{j}\bar{\bar{C}}_{t+j'}\right]\bar{\varepsilon}_{t-1} = \sum_p c_p^{(\varepsilon_{t-1})}\,(\lambda_p)^{j+1}\,\bar{\psi}_p \quad (2.79)$$

and

$$\left[\prod_{j'=(t'-t+1)}^{j}\bar{\bar{C}}_{t+j'}\right]\bar{\bar{A}}_{t'}^{-1}\bar{r}_{t'} = \sum_p c_p^{(A_t^{-1}r_t)}\,(\lambda_p)^j\,\bar{\psi}_p. \quad (2.80)$$

Denoted by σ_1 is the spectral radius of C, i.e. the largest absolute eigenvalue. It follows,

[11] This case occurs when $t' = t + j$, thus $j' = (t' - t + 1) = (t + j - t + 1) = j + 1$ which is larger than j.

that as long as $\sigma_1 < 1$ is true[12], the term involving $\bar{\varepsilon}_{t-1}$ will approach zero as $j \to \infty$. Also the terms involving $\bar{r}_t$ will approach zero, as will other time-step values, when time step $t' \ll t + j$. For time-step values where $t' \approx t + j$ there will not be much damping.

But as j advances these terms will be dampened implying $|\bar{\varepsilon}_{t+j}|$ gets smaller, which in turn implies $|\bar{r}_{t+j}|$ gets smaller. This supports a continuing decrease in magnitude of the error. Numerical experiments will be used to observe the actual behavior of $\{\bar{r}_{t'}\}$.

2.2 Adaptive Model Refinement Organization

The organization of the AMoR method is dependent upon the approach. As mentioned previously, two approaches were implemented in this research; One approach involving the use of a steady state library and a second approach utilizing active model switching. In both approaches the point kinetic parameters[13] are calculated by NESTLE beforehand under steady-state conditions. Both approaches begin with NESTLE calculated shape-factors to create the projected 3-D model. From this point forward, when mentioning the input of the NESTLE calculated factors for the projected model these will simply be referred to as the *shape-factors* even though they include the flux shape-factors, the precursor group concentration shape-factors, the average neutron velocity, the flux energy partition function, the initial volume averaged neutron density, and the initial volume averaged precursor group concentrations.

2.2.1 Organization of the Steady-state Library Approach

When using the steady-state library approach, NESTLE is used, before the beginning of the transient, to calculate the input point kinetic parameters and to generate a library of factors needed for the projected model. As with the point kinetic parameters, the steady-state library values are evaluated under steady-state conditions for various rod positions, starting with all rods out (ARO) and ending with one (actually a grouping of rods) rod fully inserted.

At the beginning of the transient, the PKE-Solver starts by reading in the point kinetic parameters and the ARO shape-factors. The PKE-Solver then initiates the transient and calculates the projected model at the end of the first time-step. This is done by slightly inserting the rod using the same insertion speed, solving the PKE, determining the shape-factors for this position by linear interpolation, and using these results in the projected model. This continues until the rod is fully inserted. While the PKE-Solver is executing the transient the error between

[12]This is surely true for the steady-state case based on the physics of the system. See the NESTLE manual for further explanation [1]

[13]The specific point kinetic parameters input are current rod position, calculated static bank worth, average neutron lifetime,average neutron velocity, precursor group yield fractions or beta values, and precursor group decay constants or lambda values. These values are calculated under steady-state conditions for various rod positions starting with all rods out (ARO) and ending with one rod fully inserted.

the projected model, i.e. the lower fidelity model, and the NESTLE output solution, i.e. the higher fidelity model, is calculated.

This method was primarily developed to gain insight into the behavior of the point kinetics solution relative to the diffusion solution and to set a baseline error to compare with the active model switching approach. It is obvious that there is at least one short coming with this approach compared to the active model switching approach; The steady-state library does not account for transient effects on the shape-profile. In short, the precursor values are in equilibrium with the rod position which is not the case during transients.

2.2.2 Organization of the Active Model Switching Approach

For the active model switching approach, NESTLE is used, before the beginning of the transient, to calculate the input point kinetic parameters and to generate the needed shape-factor values for the projected model. As opposed to the steady-state conditions the point kinetic parameters and the shape-factor values are calculated under transient conditions for various rod positions. This is accomplished by initializing the transient under steady-state conditions and then recording the ARO shape-factors. Next the rod is quickly inserted[14] producing shape-factor values which account for the prompt neutron shape-profile effects but do not account for the precursor equilibrium effects, which is an advantage over the steady-state approach.

The calculation proceeds as for the steady-state library approach, except when the error is deemed too large the PKE-Solver is paused. Let this point in the transient be denoted as time τ.

Once the PKE-Solver is paused the projected 3-D flux and precursor group concentration values are output from three two-steps[15] prior, let this be denoted by $\tau - 2\Delta t$. The earlier values are used because the current values posses larger amounts of error. These flux and precursor group concentration values are then utilized to restart NESTLE. The restart begins at $\tau - 2\Delta t$ and is advanced to time τ using a much smaller time-step than the PKE-Solver time-step. This slow marching is believed to anneal out some of the error introduced by the PKE-Solver and the short comings of the projected model. Once time τ is reached the shape-factor values are output. Then NESTLE quickly inserts the rods, producing shape-factor values for the remainder of the transient. These new outputs are transferred to the PKE-Solver and replace the old shape-factor values. The PKE-Solver is then un-paused and advanced forward. This process continues until a single rod is fully inserted.

This method has its advantages, namely the incorporation of precursor transient behavior

[14] In this case *quickly inserted* means that the time-step is at least 1000x smaller than the smallest decay constant (approximately 1/3 sec). The entire insertion transient last roughly two thousandths of a second.

[15] The two time-steps prior was assumed for this research but in the future this value can be investigated to find some formulation to indicate the most ideal value.

into the shape-profile. Though this approach also has draw backs, most prominently the increase complexity stemming from the selection of the number of time-steps prior to the current time τ needed to provide acceptable values to restart NESTLE and also determining the time-step size for the NESTLE restart and quick rod insertion. In this research these values were assumed and not investigated to find the optimal values.

Chapter 3

Results

The motivation behind this work is to investigate the implementation of AMoR methods and to gauge the accuracy of the resulting projected 3-D model. In this chapter the finding of this research will be presented. Namely, the results of the error metrics applied to the two AMoR approaches developed and outlined in Chapter 2.

3.1 Testing Environment

This research was conducted on a standard desktop computer running Windows XP 64-bit. The codes used for this research are NESTLE v5.2.1 [1] and a simple PKE-Solver which were modified to accommodate the AMoR approaches. The codes were compiled and executed with Microsoft Visual Studios 2005 using the Intel FORTRAN compiler.

3.2 Test Cases

The cases executed for this work consist of NESTLE inputs from a sample data set. The data is from the McGuire Nuclear Station, Unit 1 on fuel cycle 13. This reactor is a 3,311 MWt 4-loop Westinghouse PWR. The simulation entails a quarter-core, Cartesian geometry with a cyclic radial interior boundary condition and zero flux boundary conditions on the radial exterior, Z-plane top, and Z-plane bottom. The core consist of 28 Z-planes made up of 18X18 node, XY-planes. Materials do not fill the entire 18X18 XY-plane as the shape of the core is not strictly square. The fueled region of the core consist of the inner 26 Z-planes and a restricted selection of the 18X18 XY-planes. The NESTLE Xenon and Samarium options are turned off, as is the thermal-hydraulic feedback option. A soluble boron level of 1899.83ppm was used along with a constant coolant inlet temperature of $555.50^{\circ}F$ and a constant coolant mass flow rate of 1,439,284.5 lb/(ft^2 sec).

All transient cases began at the ARO position and ended with a single rod bundle fully inserted over varying transient durations. Two temporal cases were considered for this research; A fast rod insertion transient with a duration of 2 seconds and a slow rod insertion transient with a duration of 120 seconds. The AMoR approaches were applied under differing precursor conditions. For the verification calculations and the steady-state library approach, the transients were performed with fully active precursor calculations but for the active model switching approach the precursor β_i values, or the fraction of all fission neutrons emitted per fission in a precursor group, were set to value of 0.0001[1]. This assumption was applied to limit the precursor influence on the calculations because when executing the active model switching approach their values are highly erroneous. Minimizing the precursor's effects allows for the analysis of this method's ability to perform prompt neutron calculations without interference from the precursor concentrations which makes the results look more like the hybrid method to be discussed later.

The volume averaged neutron density and volume averaged precursor group concentrations behave nearly identical for the verification calculations and the steady-state library approach; the only variant being, the number of transient data outputs provided from the exact solution, though this makes a very minor difference in the average behavior.

[1]The value of 0.0001 was used because exactly zero is problematic for computational reasons. At this small of a value the precursor contributions are negligible.

For the 2 second transient, the exact transient solution contained 40 printouts. The general behavior of the volume averaged neutron density and the volume averaged precursor group concentrations can be viewed in Figure 3.1 and Figure 3.2 - Figure 3.7, respectively. These figures contain the NESTLE and PKE-Solver solutions side-by-side to illustrate that both the higher and lower fidelity models produce similarly behaving average solutions. The radial and axial relative power distributions for the 2 second transient, 10 data records are displayed in Table A.1 - Table A.22.

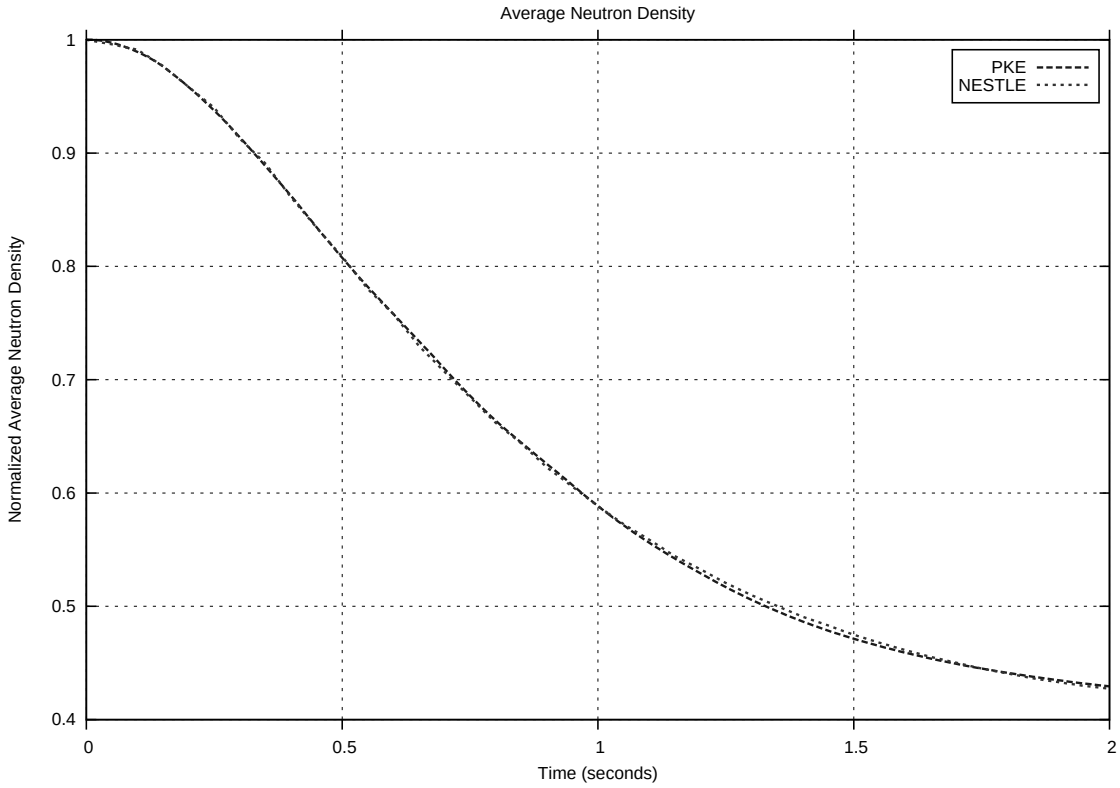

Figure 3.1: Normalzied Volume Averaged Neutron Density

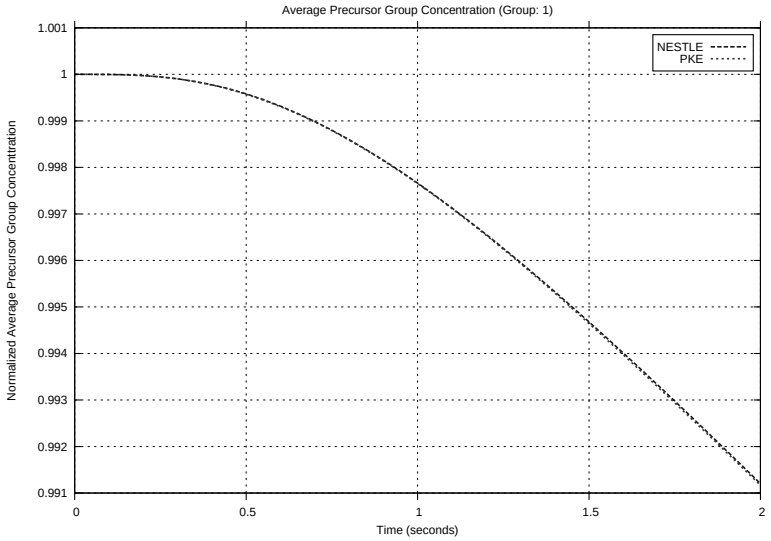

Figure 3.2: Normalized Volume Averaged Precursor Concentration (Group: 1)

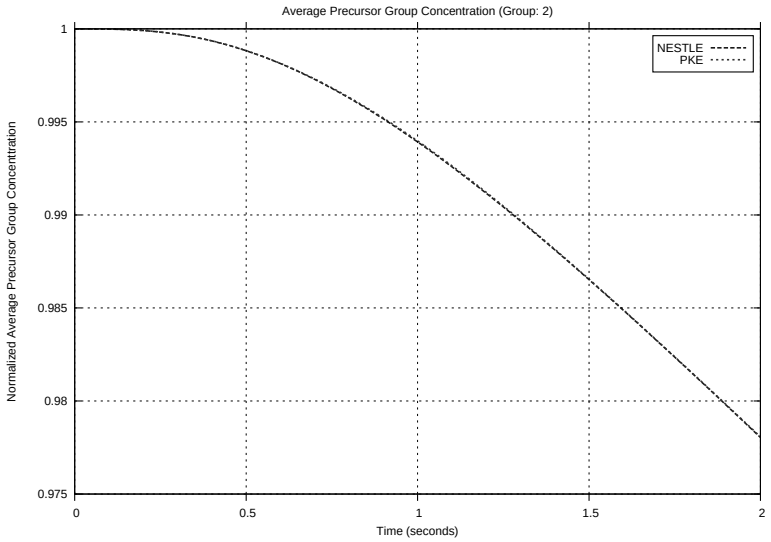

Figure 3.3: Normalized Volume Averaged Precursor Concentration (Group: 2)

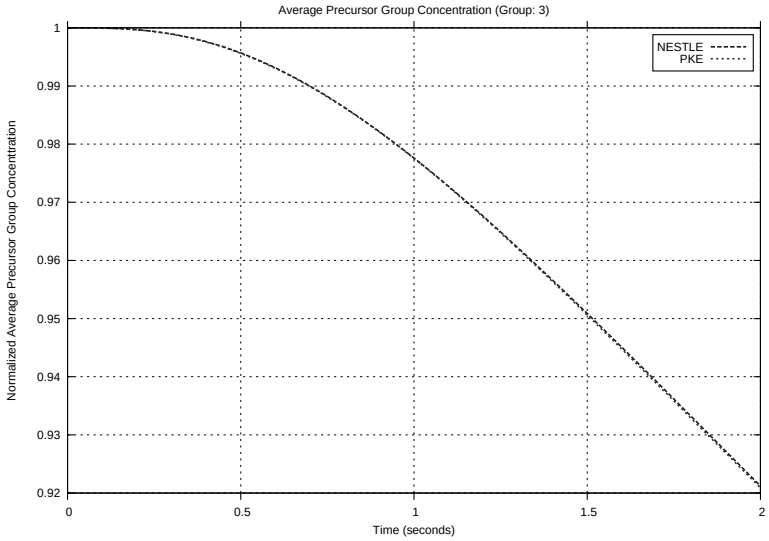

Figure 3.4: Normalized Volume Averaged Precursor Concentration (Group: 3)

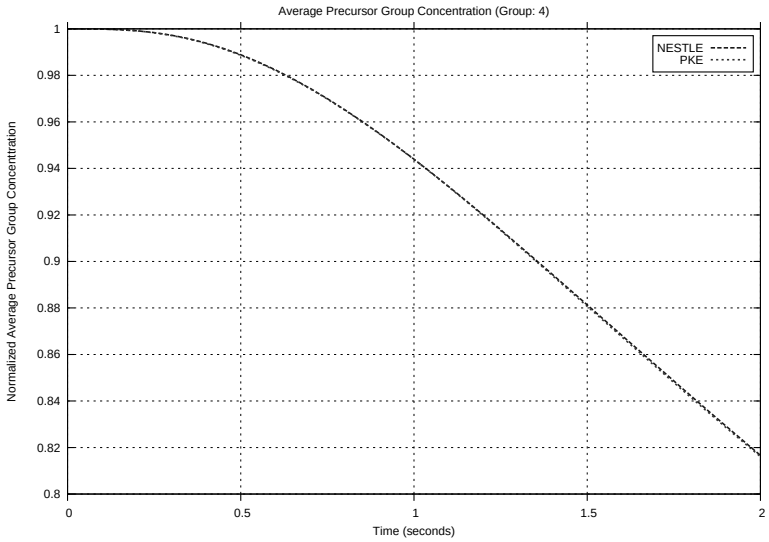

Figure 3.5: Normalized Volume Averaged Precursor Concentration (Group: 4)

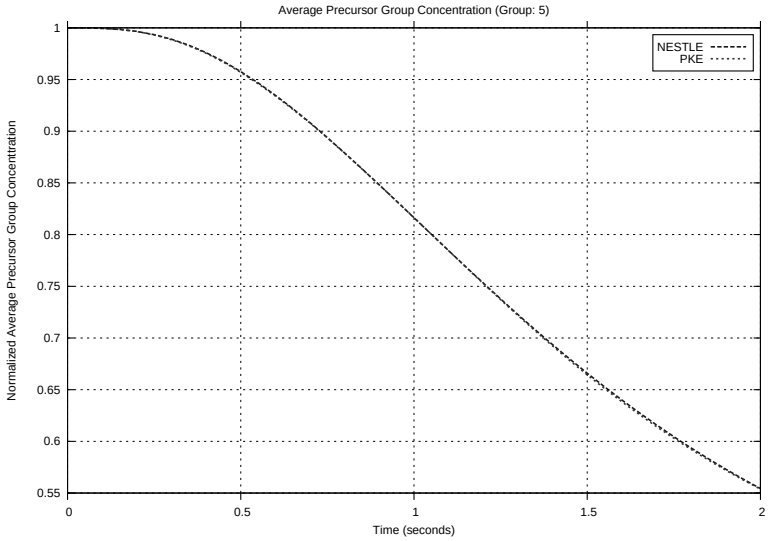

Figure 3.6: Normalized Volume Averaged Precursor Concentration (Group: 5)

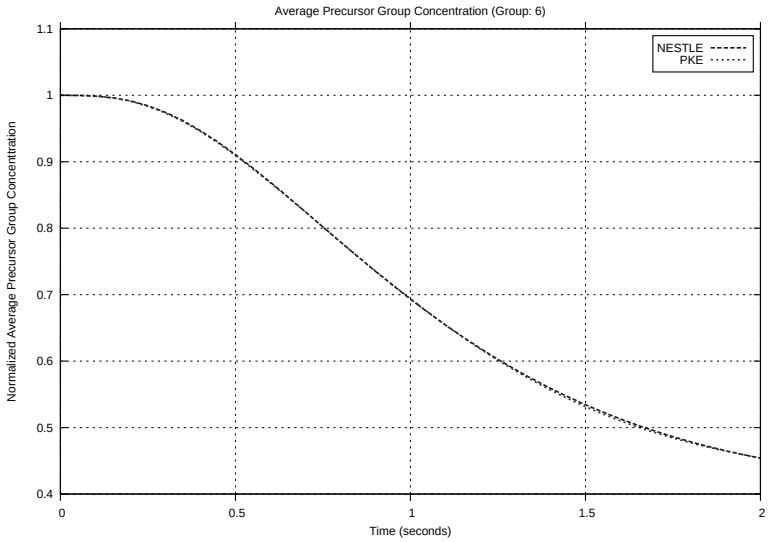

Figure 3.7: Normalized Volume Averaged Precursor Concentration (Group: 6)

Like wise, for the 120 second transient, the exact transient solution contained 40 printouts. The general behavior of the volume averaged neutron density and the volume averaged precursor group concentrations can be viewed in Figure 3.8 and Figure 3.9 - Figure 3.14, respectively. The figures display the NESTLE and PKE-Solver solutions side-by-side to illustrate that the higher fidelity and lower fidelity models produce similarly behaving average solutions. The radial and axial relative power distributions for the 120 second transient, 10 data records are displayed in Table A.23 - Table A.44.

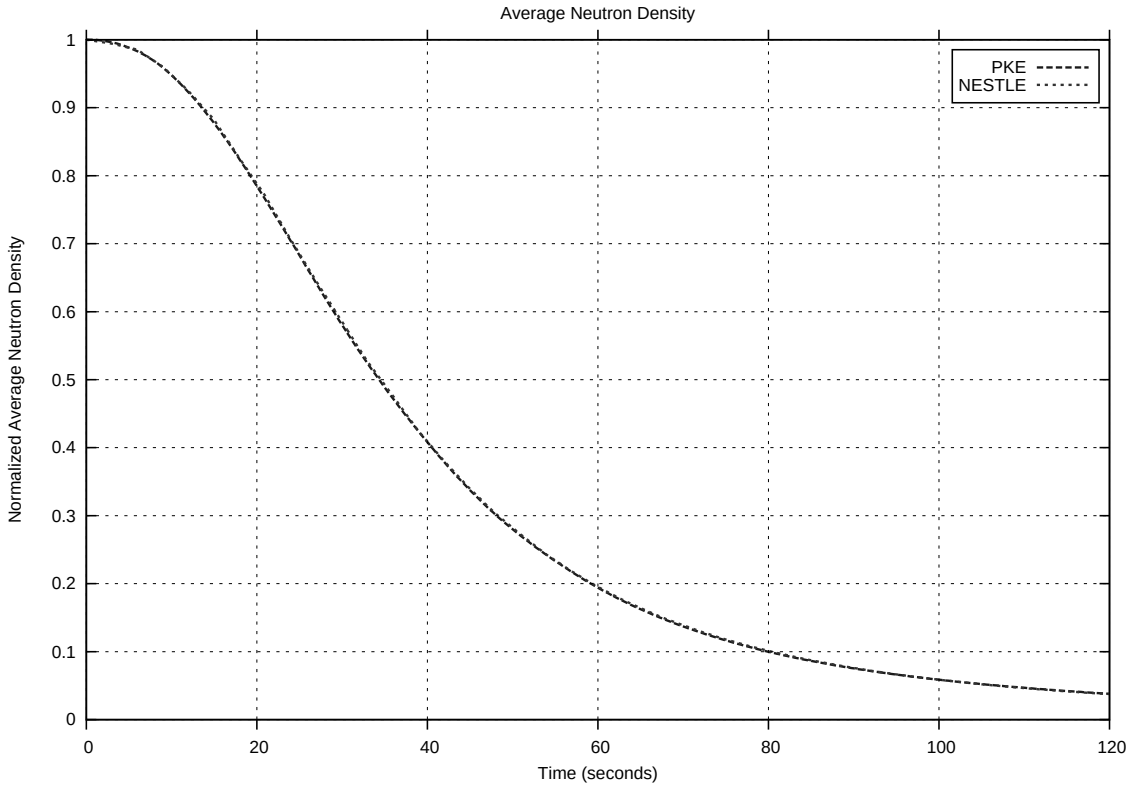

Figure 3.8: Normalzied Volume Averaged Neutron Density

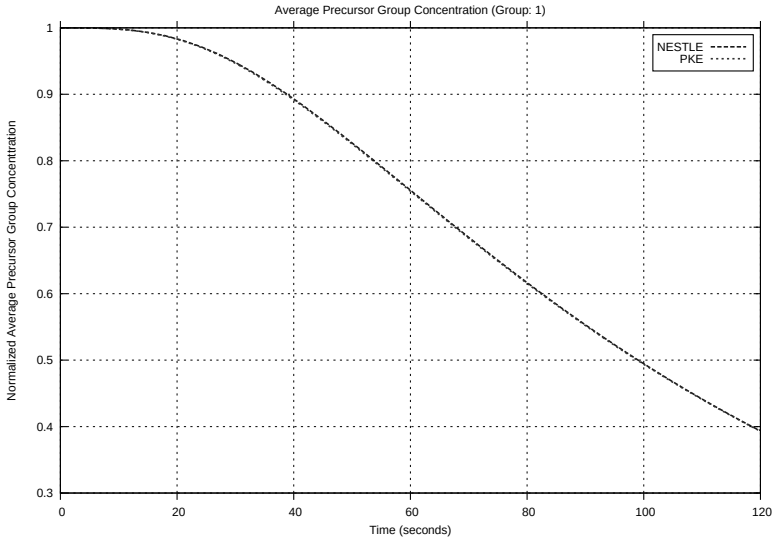

Figure 3.9: Normalized Volume Averaged Precursor Concentration (Group: 1)

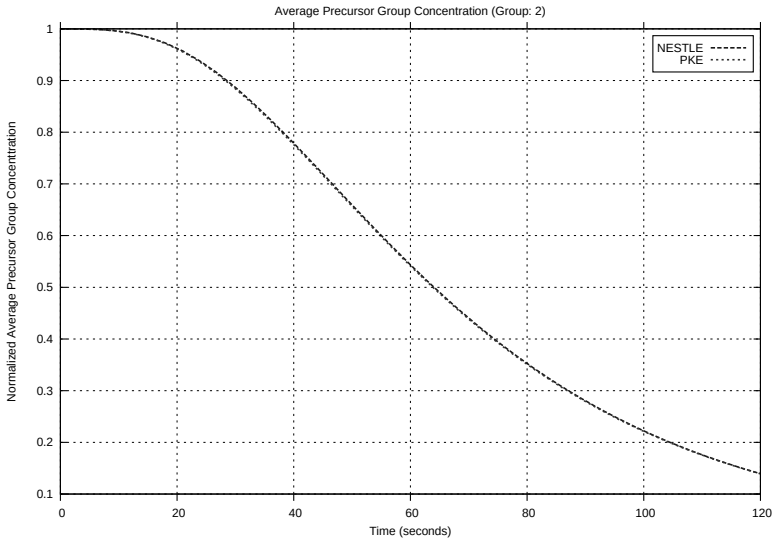

Figure 3.10: Normalized Volume Averaged Precursor Concentration (Group: 2)

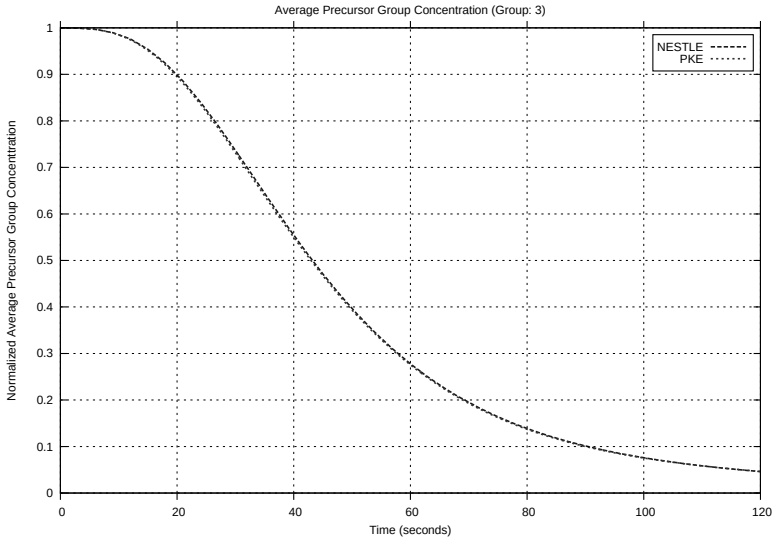

Figure 3.11: Normalized Volume Averaged Precursor Concentration (Group: 3)

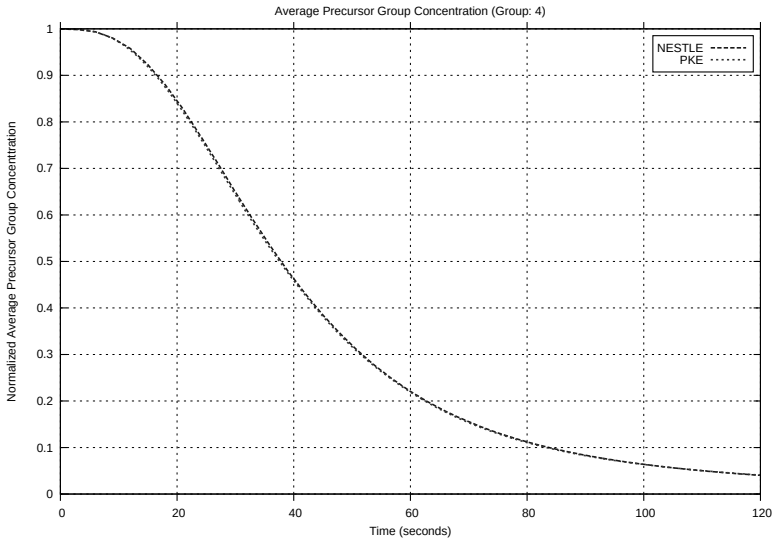

Figure 3.12: Normalized Volume Averaged Precursor Concentration (Group: 4)

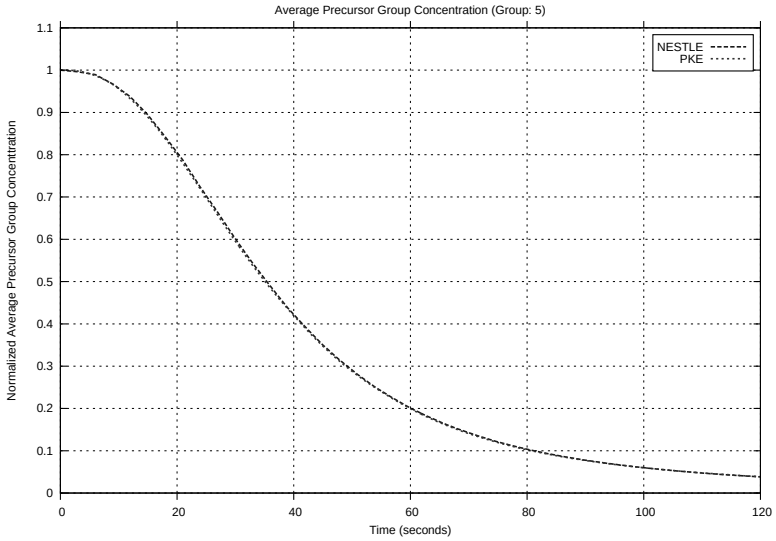

Figure 3.13: Normalized Volume Averaged Precursor Concentration (Group: 5)

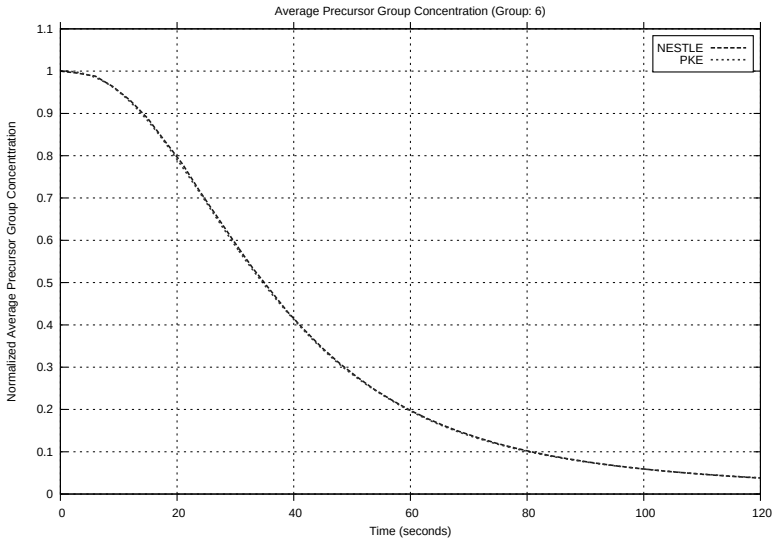

Figure 3.14: Normalized Volume Averaged Precursor Concentration (Group: 6)

The volume averaged neutron density and volume averaged precursor group concentrations behavior for the active model switching approach differs significantly from the verification calculations and the steady-state library approach. This difference stems from the assumption applied to the precursor β_i values.

For the 2 second and the 120 second transient, the exact transient solution contained 40 printouts. The general behavior of the volume averaged neutron density for the 2 second case and the 120 second case can be viewed in Figure 3.15 and Figure 3.16, respectively. The volume averaged precursor group concentration behavior has been omitted due to the assumption applied to this approach. Like the steady-state library approach, the NESTLE and PKE-Solver solutions are shown side-by-side to demonstrate that the higher and lower fidelity solutions produce very similarly behaving average solutions. The radial and axial relative power distributions for the 2 second transient, 40 data records are displayed in Table A.45 - Table A.66 and the radial and axial relative power distributions for the 120 second transient, 40 data records are displayed in Table A.67 - Table A.88. They indicate a substantial change in both the core average and radially integrated relative power (flux) distributions, implying a severe test for the AMoR methods examples.

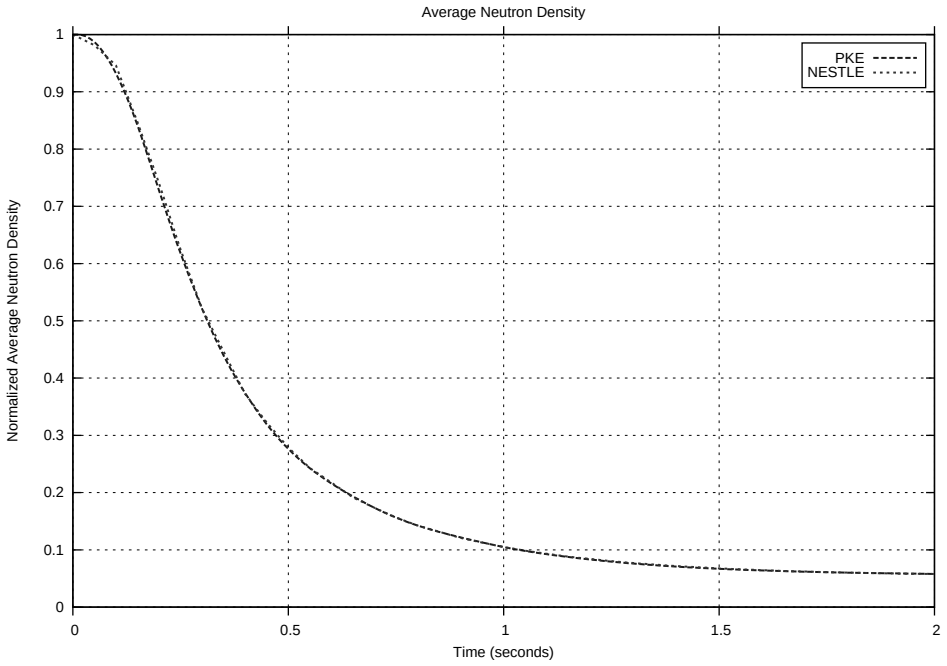

Figure 3.15: Normalzied Volume Averaged Neutron Density

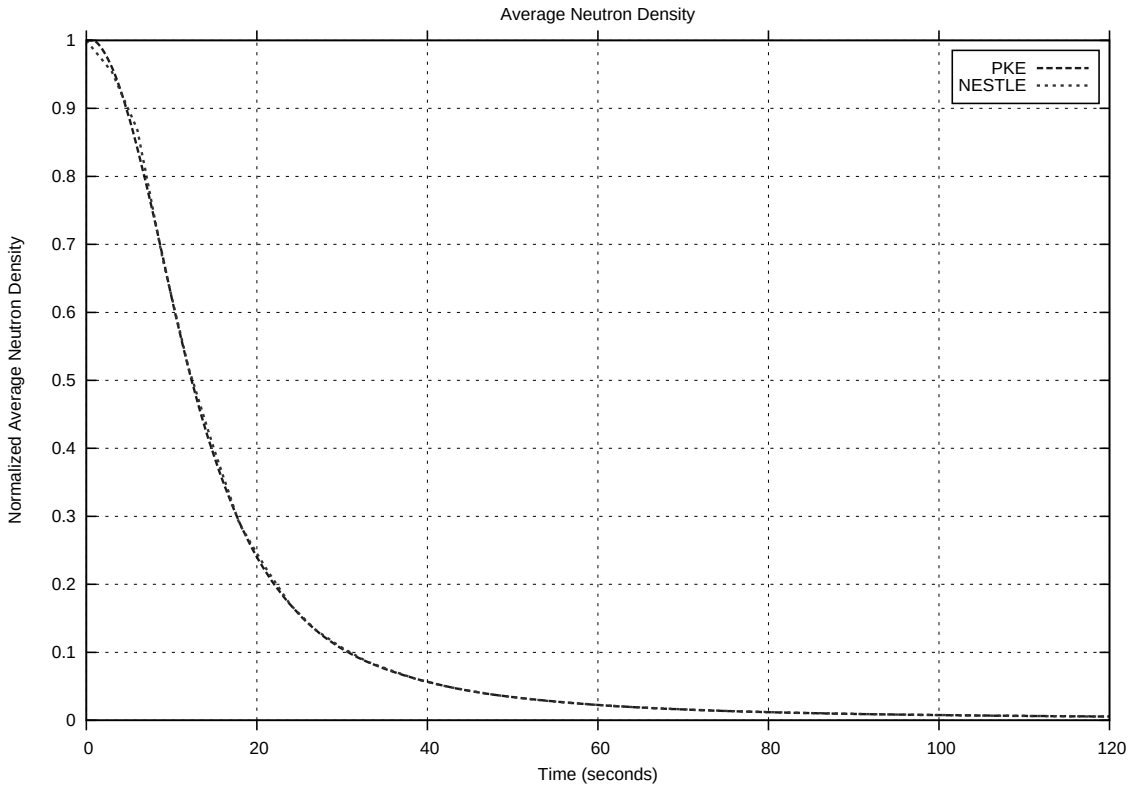

Figure 3.16: Normalzied Volume Averaged Neutron Density

3.3 Verification Calculation Results

As described in Chapter 2, the verification of the projection calculations can be preformed by using the NESTLE calculated transient data to also provide the actual transient, time-dependent shape-factor values for the projection calculations, as opposed to using one of the AMoR approaches outlined previously. Two transient cases performed for the verification analysis entailed a 2 second rod insertion transient and a 120 second rod insertion transient.

For the 2 second transient, NESTLE was executed with a time-step of 0.002 seconds. Every 25 time-steps or 0.05 seconds the transient and shape-factor data were recorded, resulting in 40 data points. The PKE-Solver was executed using a time-step of 0.02 seconds and the error results were output every time-step.

For the 120 second transient, NESTLE was executed with a time-step of 0.12 seconds. The transient and shape-factor data were recorded every 25 time-steps or 3.0 seconds, resulting in 40 data points.The PKE-Solver was executed using a time-step of 1.20 seconds and the error results were output every time-step.

The 2 second transient case is described by Figure 3.17 and Figure 3.18. The 120 second transient case results can be observed by Figure 3.19 and Figure 3.20.

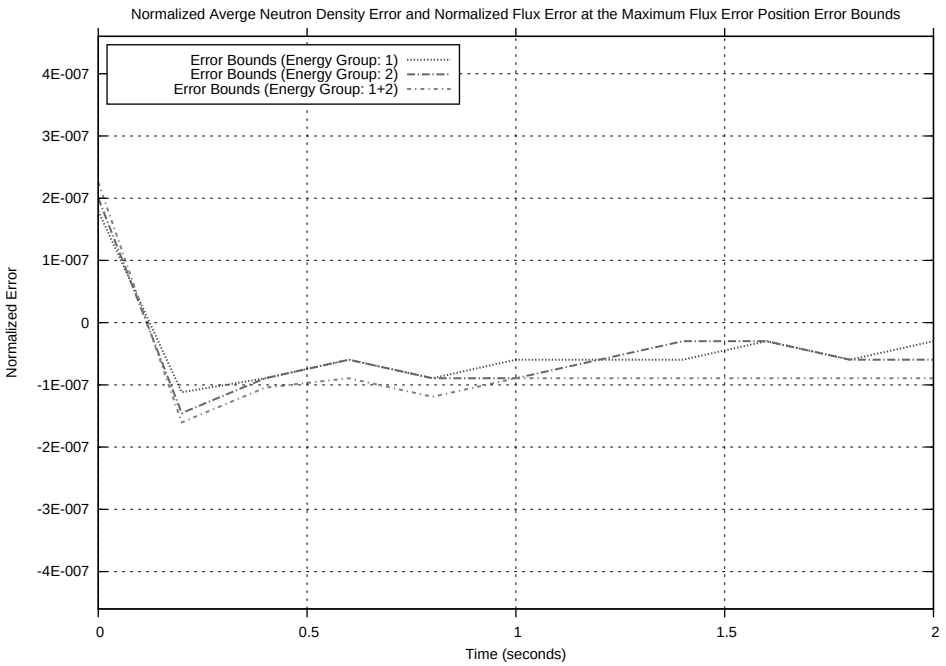

Figure 3.17: Error Bounds of the Normalized Volume Averaged Neutron Density Error and Locally Normalized Nodal Flux Error at the Maximum Flux Error Position (2 Second Case)

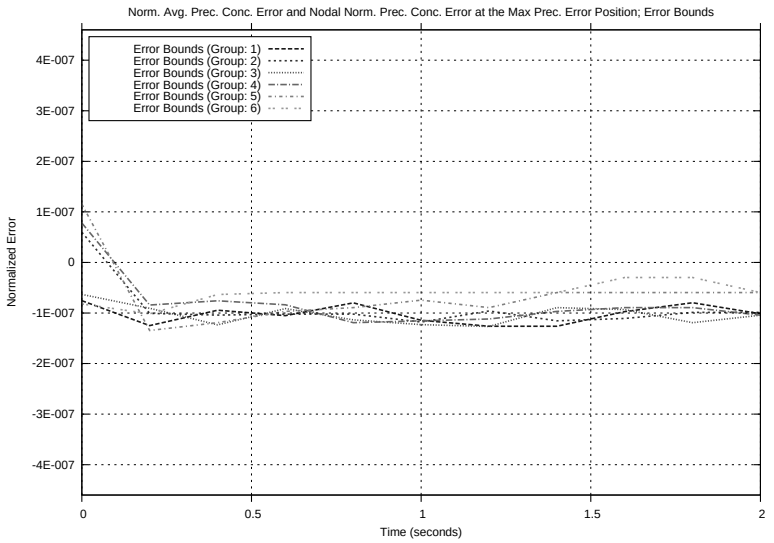

Figure 3.18: Error Bounds of the Normalized Volume Averaged Precursor Group Concentration Error and the Locally Normalized Nodal Precursor Group Concentration Error at the Maximum Precursor Group Concentration Error Position (2 Second Case)

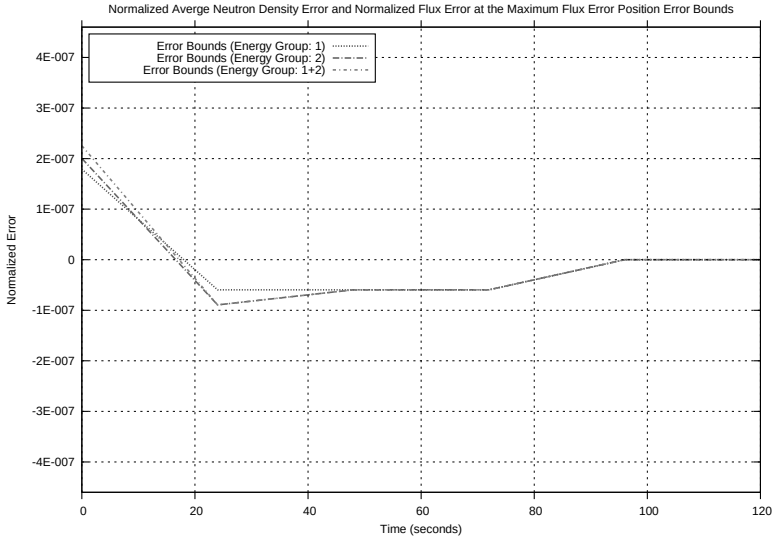

Figure 3.19: Error Bounds of the Normalized Volume Averaged Neutron Density Error and Locally Normalized Nodal Flux Error at the Maximum Flux Error Position (120 Second Case)

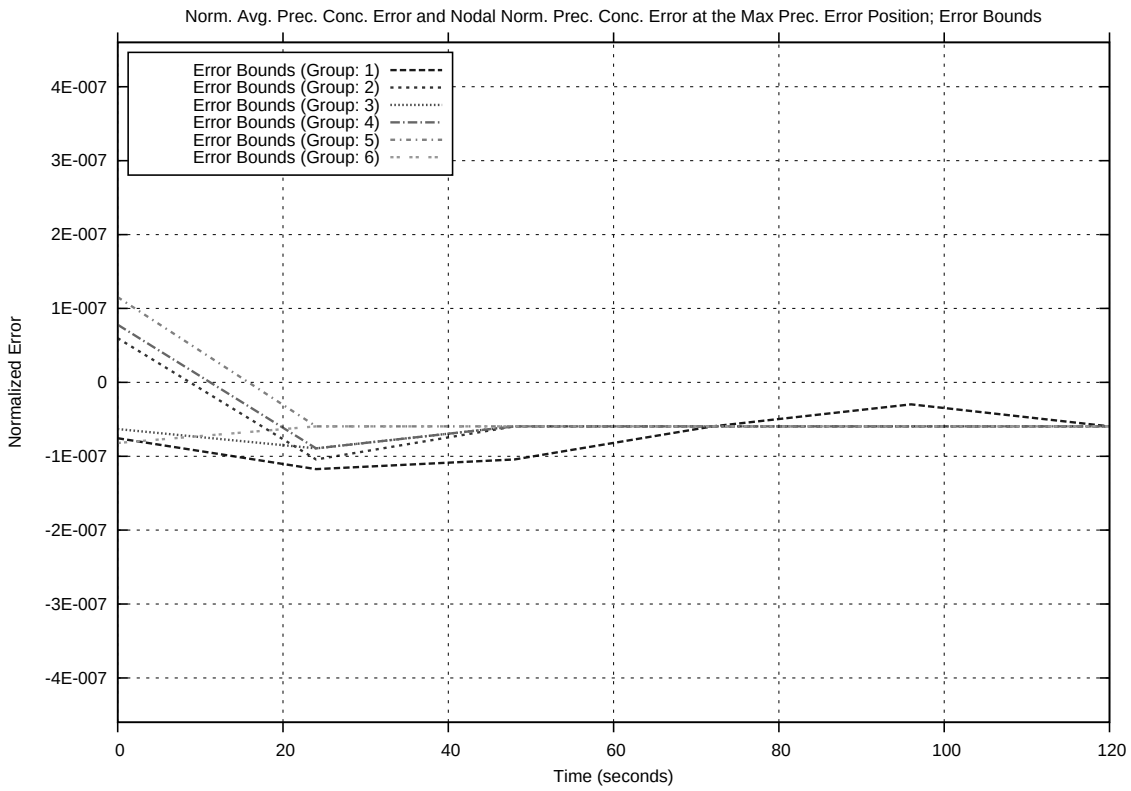

Figure 3.20: Error Bounds of the Normalized Volume Averaged Precursor Group Concentration Error and the Locally Normalized Nodal Precursor Group Concentration Error at the Maximum Precursor Group Concentration Error Position (120 Second Case)

Figure 3.17 and Figure 3.19 clearly demonstrate that the projection flux calculations for the 2 second and 120 second transient are within the single precision machine error bounds. From Figure 3.18 and Figure 3.20 it is clear that the projection precursor group concentration calculations for the 2 second and 120 second transient are within the single precision machine error bounds. Given these results, it is reasonable to believe that the projection calculations have been implemented correctly.

3.4 Steady-State Library Results

As described in Chapter 2, the steady-state library approach involves the use of a data library consisting of steady-state, equilibrium conditions entries at various rod positions, beginning with ARO and ending with one rod fully inserted. For this work, two steady-state libraries were created containing either 10 steady-state entries or 25 steady-state entries. As with the verification results, a fast transient, duration of 2 seconds, and a slow transient, duration 120 seconds, were used for the exact solutions. Each transient case was evaluated with either 10 data outputs or with 40 data outputs. The use of multiple steady-state library sizes and multiple exact transient solutions output intervals, provides insight into the effects of the linear interpolation on both the shape-factors and the exact solution.

2 Second Transient, 10 Steady-State Data Points, 10 Transient Data Points

For the 2 second transient utilizing the 10 entry steady-state library and the 10 data output exact solution, the following results were obtained regarding the flux error and precursor error equations developed in Chapter 2 (See section 2.1.6). The flux error at the maximum flux position and maximum flux error position, locally and averaged normalized results, can be viewed in Figure 3.21-Figure 3.24. Also the L-2 flux error is displayed in Figure 3.25. The precursor group concentration error at the maximum precursor group concentration position and the maximum precursor group concentration error position, locally and averaged normalized results, can be viewed in Figure 3.26 - Figure 3.29. As well, the L-2 precursor group concentration error can be observed in Figure 3.30. In addition, the flux and precursor group concentration error and error component values are located in Appendix-B.

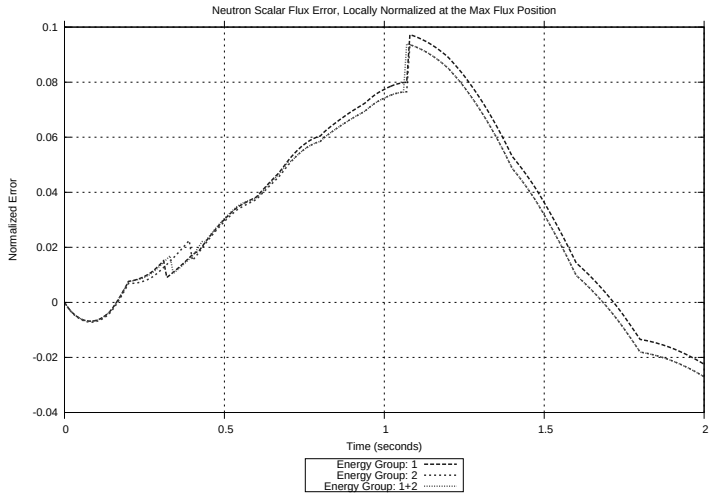

Figure 3.21: Locally Normalized Flux Error at the Maximum Flux Position (10 SS, 10 Trans)

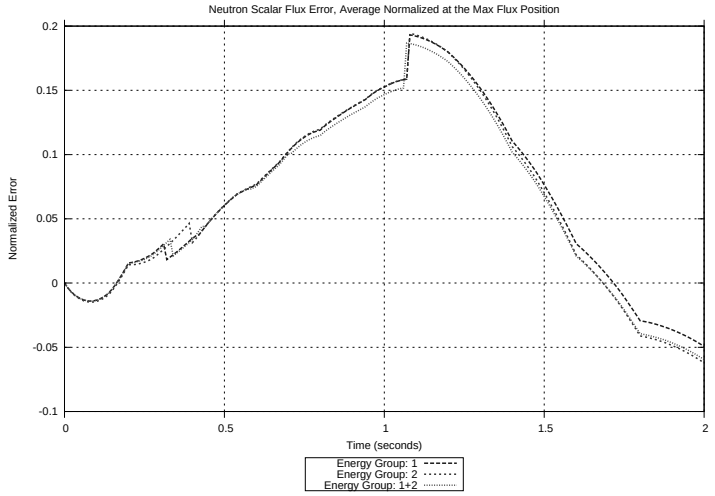

Figure 3.22: Average Normalized Flux Error at the Maximum Flux Position (10 SS, 10 Trans)

Comparing the locally normalized error (Figure 3.21) with the volume averaged normalized error (Figure 3.22), it is clear that the average normalization results in a larger error value. This is obviously because the average value must be less than the maximum value, resulting in a higher error from the normalization.

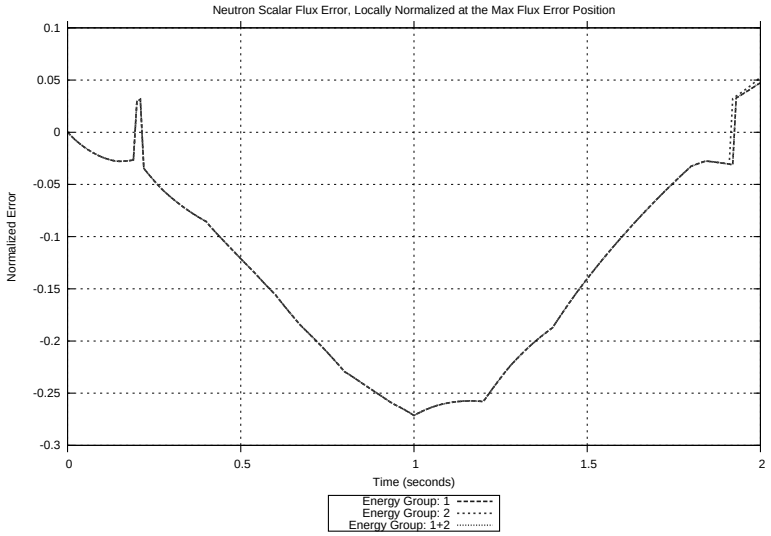

Figure 3.23: Locally Normalized Flux Error at the Maximum Flux Error Position (10 SS, 10 Trans)

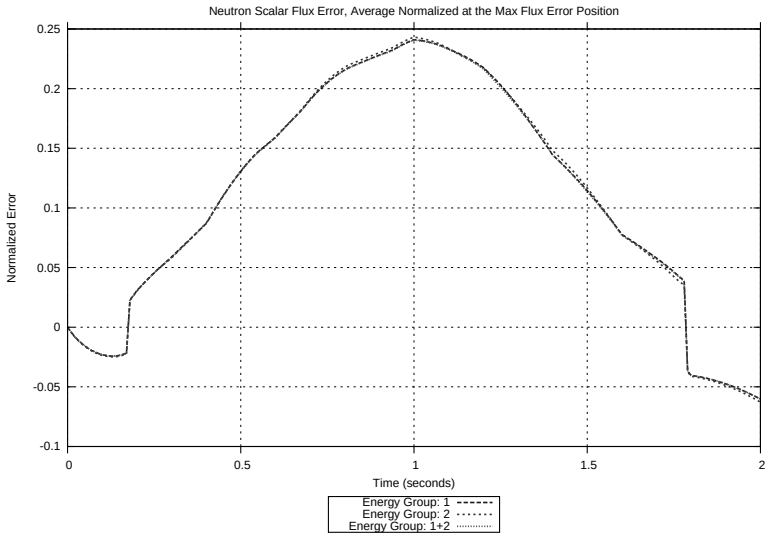

Figure 3.24: Average Normalized Flux Error at the Maximum Flux Error Position (10 SS, 10 Trans)

Note the differences in behavior between the flux locally normalized maximum error (Figure 3.23) and the flux averaged normalized maximum error (Figure 3.24). These difference are

possible because the locally normalized and average normalized maximum error may not occur at the same position. Let the maximum flux difference occurs at a single node n_{diff} where the following expression holds true.

$$n_{diff} := \arg\max_{n} |\phi_{g,n}(t) - \tilde{\phi}_{g,n}(t)|.$$

The position of n_{diff} may or may not satisfy the conditions of the locally and averaged normalized maximum error; such that the flux locally normalized maximum error occurs at node n_{loc} and the flux average normalized maximum error is obtained at position n_{avg}, where the flux locally normalized maximum error position is defined as

$$n_{loc} := \arg\max_{n} \frac{|\phi_{g,n}(t) - \tilde{\phi}_{g,n}(t)|}{\phi_{g,n}(t)}$$

and the flux average normalized maximum error position is defined as

$$n_{avg} := \arg\max_{n} \frac{|\phi_{g,n}(t) - \tilde{\phi}_{g,n}(t)|}{\langle \phi_g(t) \rangle}.$$

To further illustrate consider the following numerical example. Let the flux locally normalized maximum error be equal to the following,

$$\varepsilon_{flx,local} = \frac{2.0 \times 10^{14} - 6.0 \times 10^{14}}{2.0 \times 10^{14}} = \frac{-4.0 \times 10^{14}}{2.0 \times 10^{14}} = -2.0$$

where $\phi_{n_{loc}}(t) = 2.0 \times 10^{14}$ and $\tilde{\phi}_{n_{loc}}(t) = 6.0 \times 10^{14}$. Let the flux average normalized maximum error be equal to the following,

$$\varepsilon_{flx,avg} = \frac{1.5 \times 10^{15} - 2.5 \times 10^{15}}{1.0 \times 10^{15}} = \frac{-1.0 \times 10^{15}}{1.0 \times 10^{15}} = -1.0$$

where $\phi_{n_{avg}}(t) = 1.5 \times 10^{15}$, $\tilde{\phi}_{n_{avg}} = 2.5 \times 10^{15}$, and $\langle \phi \rangle = 1.0 \times 10^{15}$. Also, let the maximum flux difference be defined as,

$$0.1 \times 10^{15} - 1.35 \times 10^{15} = -1.25 \times 10^{15}$$

where $\phi_{n_{diff}} = 0.1 \times 10^{15}$ and $\tilde{\phi}_{n_{diff}} = 1.35 \times 10^{15}$.

In this example, the flux locally normalized, the flux average normalized, and the flux difference maximums all occur at different positions. The example displays how the locally normalized maximum error value provides consideration to the large magnitude and small magnitude flux nodes, on a node by node basis. The downside to this is that the information

yielded may only involve small magnitude nodes which are of less interest since the associated power level will be low and not that limiting. On the other hand, the average normalized maximum error value provides insight into the node which has the largest difference relative to the volume averaged value, which is likely to be biased toward large magnitude flux nodes and therefore of more interest due to the associated higher power levels. As for the flux maximum difference, this error metric only provides information regarding the node with the largest absolute difference. The difficultly of formulating an all encompassing error metric is now clear and to some degree can be contributed to the fact that the flux values span across multiple orders of magnitude.

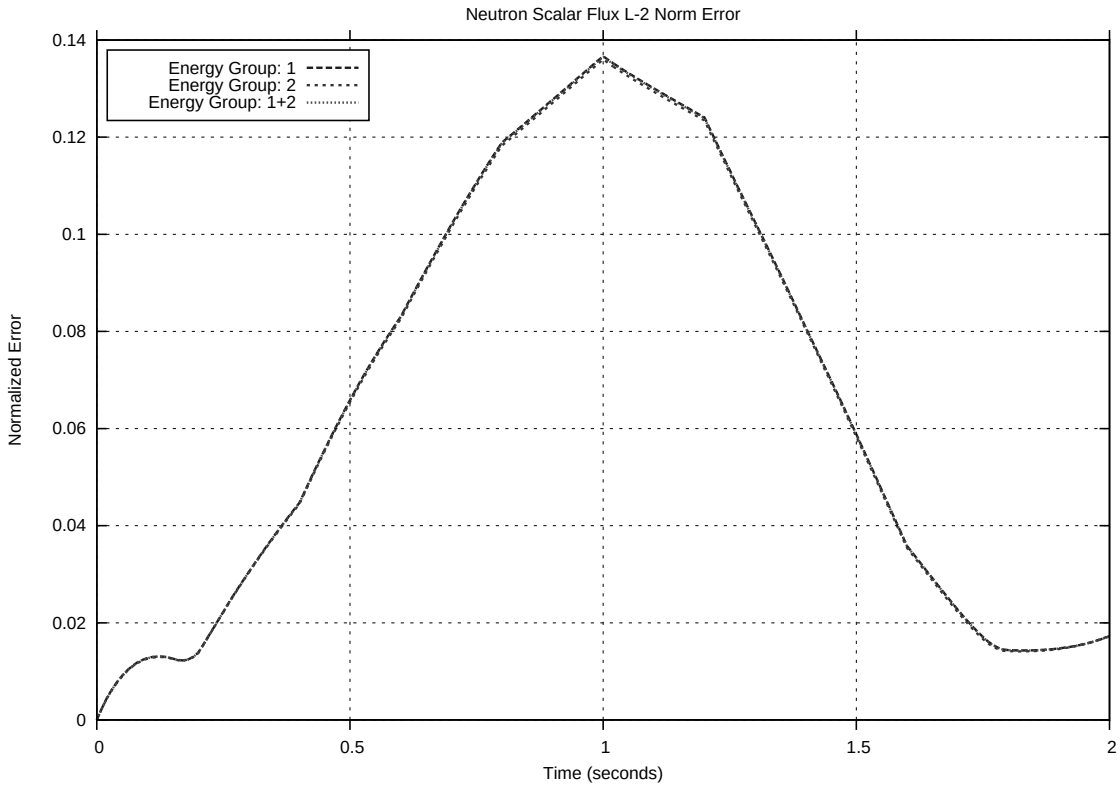

Figure 3.25: Flux L2-Error (10 SS, 10 Trans)

Note that even though the flux maximum error is relatively large (see Figure 3.23 and Figure 3.24), the flux L2 error is roughly half the maximum (Figure 3.25).

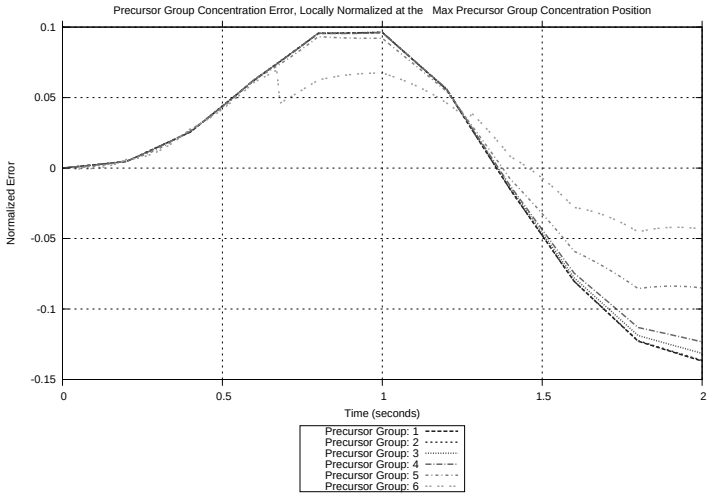

Figure 3.26: Locally Normalized Precursor Group Concentration Error at the Maximum Precursor Group Concentration Position (10 SS, 10 Trans)

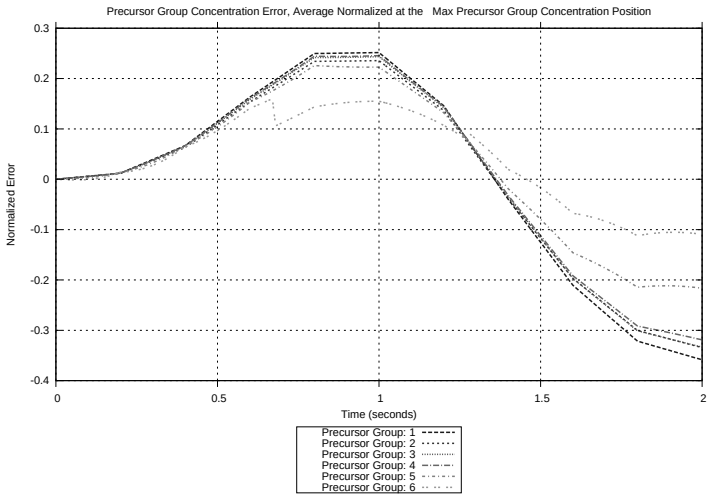

Figure 3.27: Average Normalized Precursor Group Concentration Error at the Maximum Precursor Group Concentration Position (10 SS, 10 Trans)

As with the flux errors at the maximum flux position, notice the increase in error magnitude between the locally normalized (Figure 3.26) versus average normalized error values (Figure 3.27).

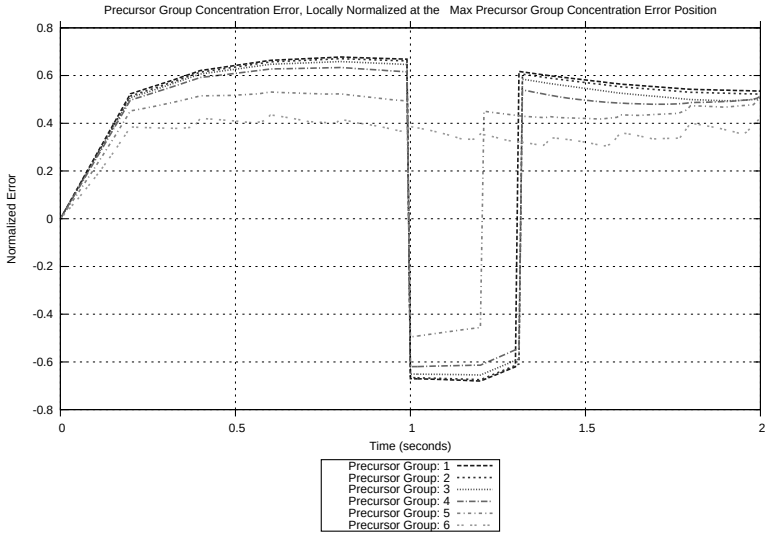

Figure 3.28: Locally Normalized Precursor Group Concentration Error at the Maximum Precursor Group Concentration Error Position (10 SS, 10 Trans)

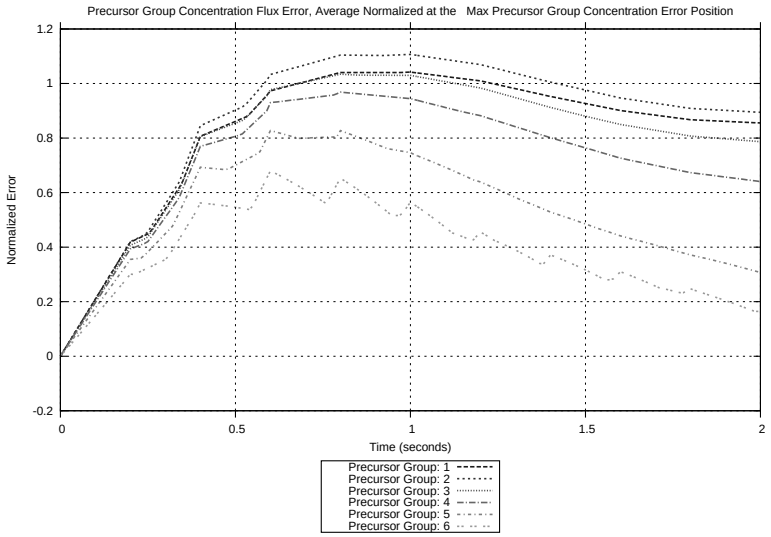

Figure 3.29: Average Normalized Precursor Group Concentration Error at the Maximum Precursor Group Concentration Error Position (10 SS, 10 Trans)

Notice the magnitude of the error in Figure 3.28 and Figure 3.29. The error is very large because of the precursor values reaching equilibrium in the steady-state cases used to deter-

mine the point reactor kinetic parameters and shape-factor values. This behavior is then passed through the shape-factor values to the projected model, resulting in erroneous projected precursor group concentrations.

Also, note the difference in behavior between the precursor group concentration locally normalized and averaged normalized maximum error, Figure 3.28 and Figure 3.29, respectively; specifically at roughly time equal to 1 second. The ability for Figure 3.28 to display negative values while Figure 3.29 displays positive values is because of the capability of the precursor group concentration locally normalized and averaged normalized maximum error values to not occur at the same positions, as discussed previously for the flux locally normalized and average normalized maximum error values (Figure 3.23 and Figure 3.24). The jump at about 1.0 and 1.3 seconds in Figure 3.28 occurs because the location of the spatial location of the maximum error is based upon the absolute error; whereas, the error plotted in this figure is the "signed" error. So when spatial location shifts at these two times, shifting between positive and negative errors are occurring. If the absolute error were plotted the curve would be smooth.

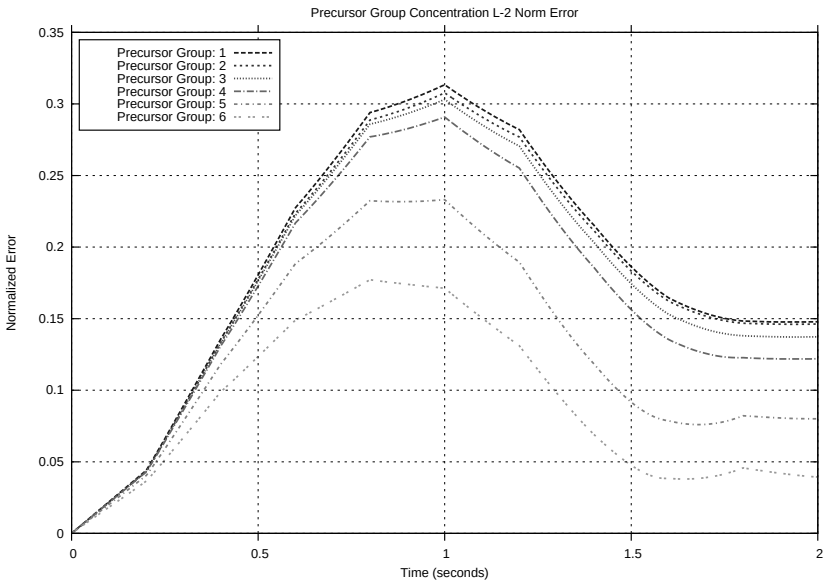

Figure 3.30: Precursor Group Concentration L2-Error (10 SS, 10 Trans)

The same behavior displayed by the flux L2-Error Figure 3.25, such that the maximum error values are relatively large but the L2-Error values are smaller, is also exhibited in the precursor group concentrations maximum error, see Figure 3.28 and Figure 3.29 compared with Figure 3.30.

2 Second Transient, 10 Steady-State Data Points, 40 Transient Data Points

For the 2 second transient utilizing the 10 entry steady-state library and the 40 data output exact solution, the following results were obtained regarding the flux error and precursor error equations. The locally normalized flux error at the maximum flux position and the maximum flux error position have been supplied in Figure 3.31 and Figure 3.32. Also, the locally normalized precursor group concentration error at the maximum precursor group concentration position and the maximum precursor group concentration error position are given in Figure 3.35 and Figure 3.36. Appendix-B contains the flux and precursor average normalized errors along with the L2-error values.

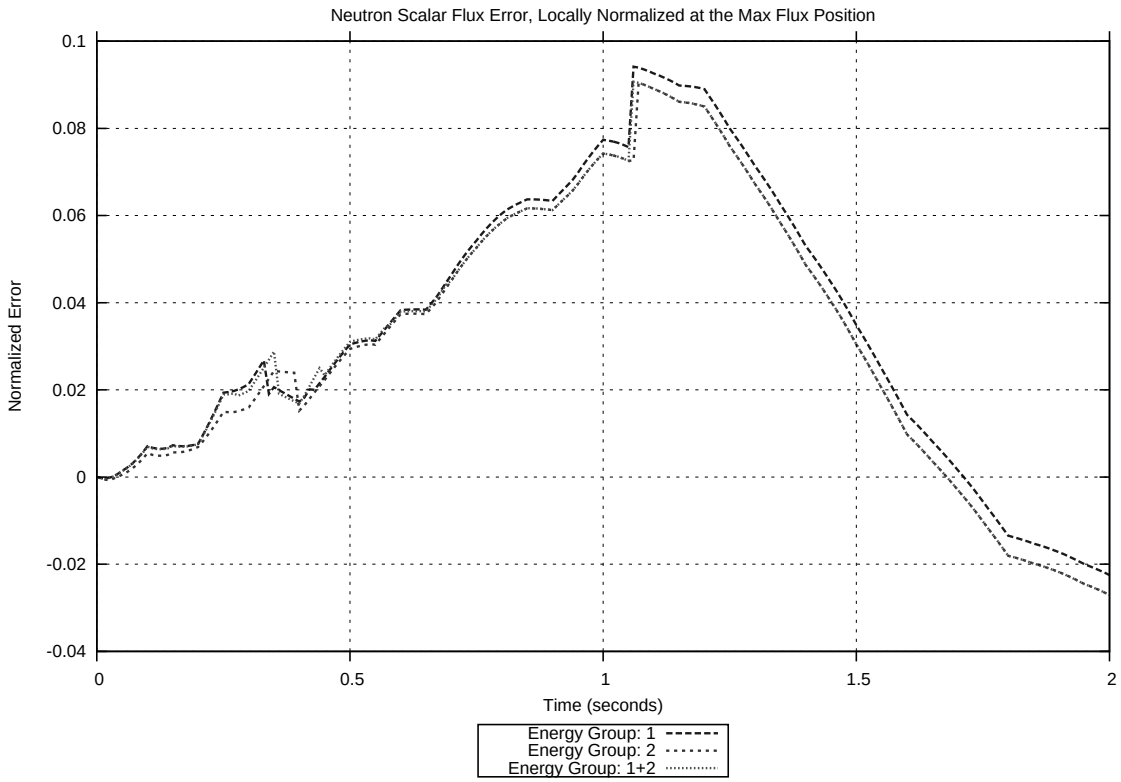

Figure 3.31: Locally Normalized Flux Error at the Maximum Flux Position (10 SS, 40 Trans)

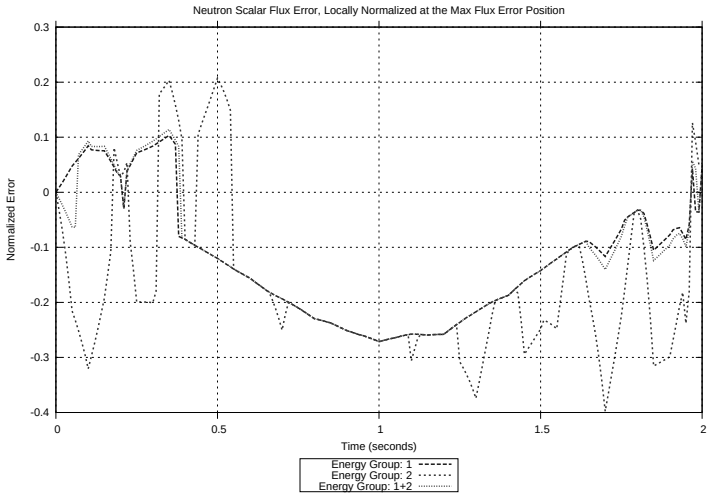

Figure 3.32: Locally Normalized Flux Error at the Maximum Flux Error Position (10 SS, 40 Trans)

Contrasting Figure 3.32 with Figure 3.23 the behavior displayed may appear erratic. This is due in part to the fact that Figure 3.23 is displaying the true error values and not the absolute error values, resulting in some flipping across the axis, as previously explained. Taking the absolute value of the error paints a slightly less erratic picture (Figure 3.33).

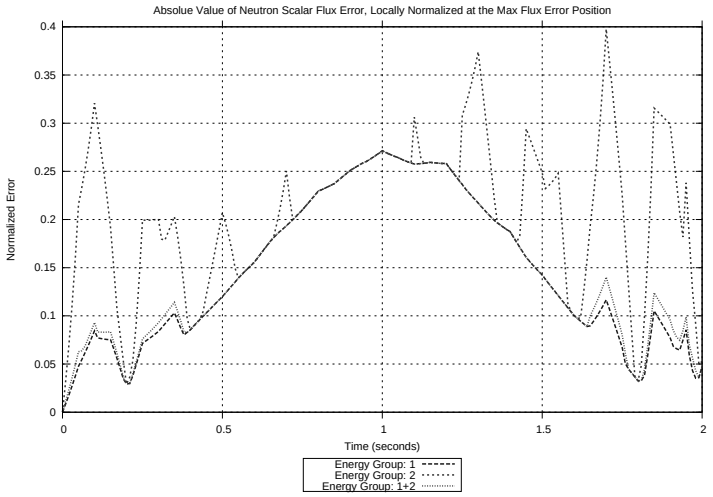

Figure 3.33: Absolute Value of the Locally Normalized Flux Error at the Maximum Flux Error Position (10 SS, 40 Trans)

The spikes that occur throughout the plot are attributed to errors introduced from the shape-factor values and are predominantly evident in group: 2, see Figure 3.34.

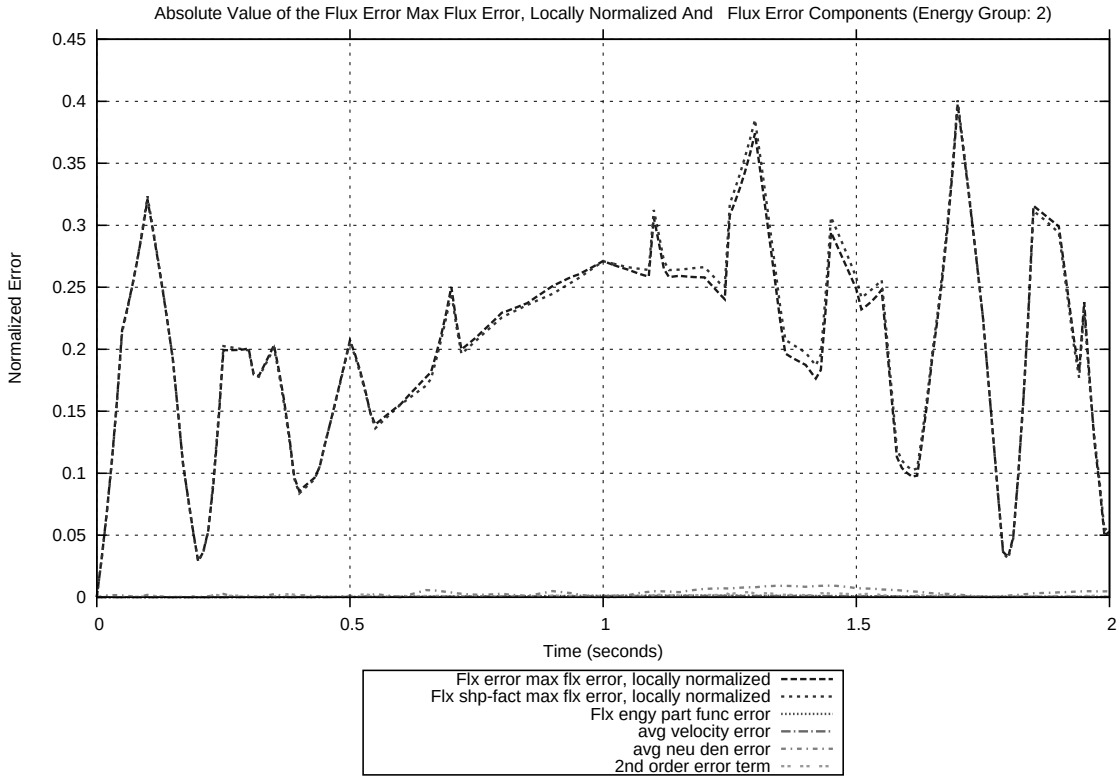

Figure 3.34: Absolute Value of the Locally Normalized Flux Error and Error Components at the Maximum Flux Error Position (10 SS, 40 Trans, Group: 2)

At this time the cause of these spikes are believed to stem from interpolation errors and differences between the equilibrium conditions experienced by the steady-state data library and the transient conditions experienced by the NESTLE transient solution. It is clear that the errors originate with the shape-factors and are then past on to the projected model. This behavior is not evident in Figure 3.23 when the transient and steady-state data was recorded on the same rod intervals, i.e. 10 steady-state data points recorded on the same regular intervals as the 10 transient data points were recorded. The behavior is also found in Figure 3.32, Figure 3.38, and Figure 3.42 where the data output intervals do not align, i.e. 10 transient data records versus 40 transient data records. In addition, note that the average neutron density error plays a very minor role in the component error.

Also, note that the extreme behavior is limited to flux group 2, the thermal group. As

the rod is stepped into the core, the absorption cross-section values at nodes where the rod is inserted fluctuate widely for the thermal group, thus this group is heavily influenced by the rod insertion relative to the fast group, group 1. Also, the larger cross-section values for the thermal group, relative to the fast group, result in a small mean free path, or average lifetime; this makes interpolation difficult under spatially dynamic conditions. In addition the spikes appear to occur on a slightly irregular interval. This behavior is believed to stem from the interpolation error and occurs slightly irregular because the Z-planes do not have a uniform height. The Z-plane heights affect when the rod tip effects are felt by the shape-factors, resulting in highly erroneous values for some interpolation calculations.

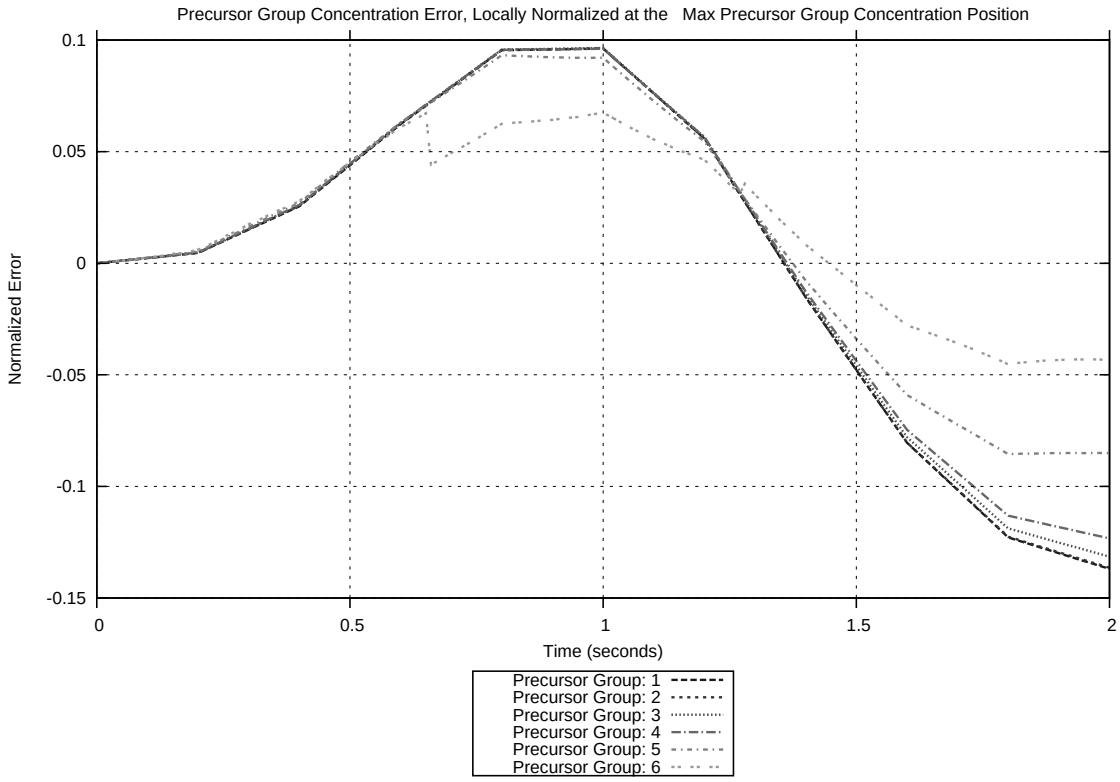

Figure 3.35: Locally Normalized Precursor Group Concentration Error at the Maximum Precursor Group Concentration Position (10 SS, 40 Trans)

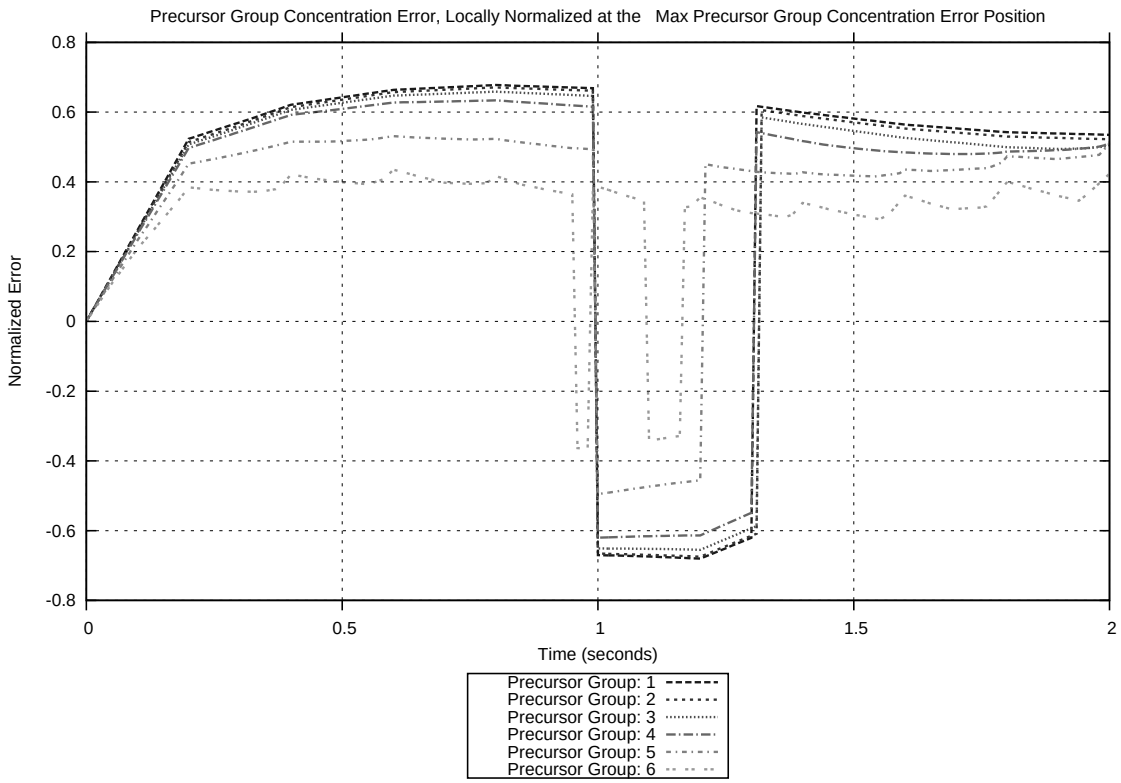

Figure 3.36: Locally Normalized Precursor Group Concentration Error at the Maximum Precursor Group Concentration Error Position (10 SS, 40 Trans)

Note, that the error in Figure 3.35 is located at the maximum precursor group concentration position and in Figure 3.36 is located at the precursor group concentration locally normalized maximum error position, which are not necessarily located at the same node; hence, their difference in appearance.

2 Second Transient, 25 Steady-State Data Points, 10 Transient Data Points

For the 2 second transient utilizing the 25 entry steady-state library and the 10 data output exact solution, the following results were obtained regarding the flux error and precursor error equations. The locally normalized flux error at the maximum flux position and the maximum flux error position have been supplied in Figure 3.37 and Figure 3.38. Also, the locally normalized precursor group concentration error at the maximum precursor group concentration position and the maximum precursor group concentration error position are given in Figure 3.39 and Figure 3.40. Appendix-B contains the flux and precursor average normalized errors along with the L2-error values.

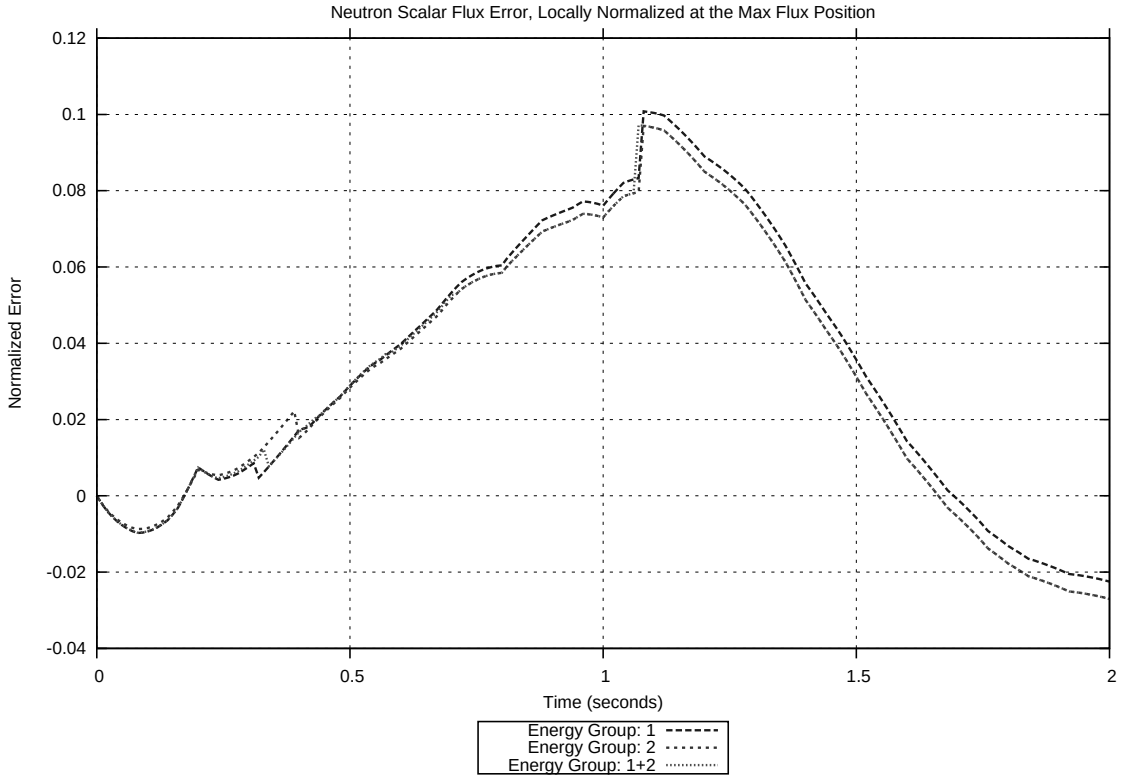

Figure 3.37: Locally Normalized Flux Error at the Maximum Flux Position (25 SS, 10 Trans)

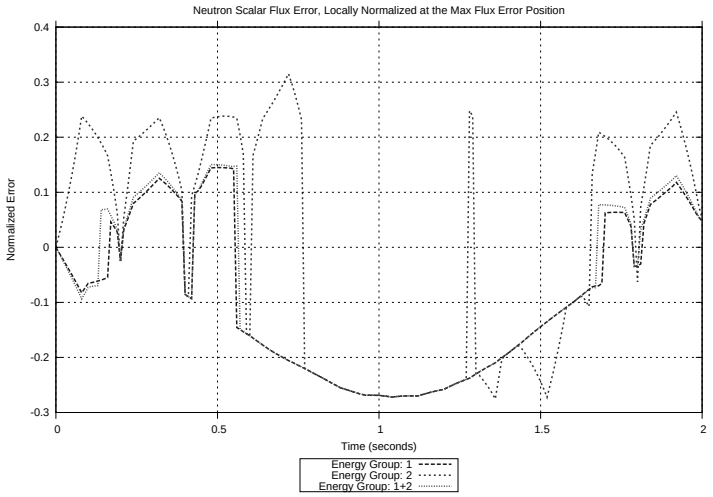

Figure 3.38: Locally Normalized Flux Error at the Maximum Flux Error Position (25 SS, 10 Trans)

The erratic behavior displayed in Figure 3.38 is believed to be caused by the same factors explaining the behavior of Figure 3.32.

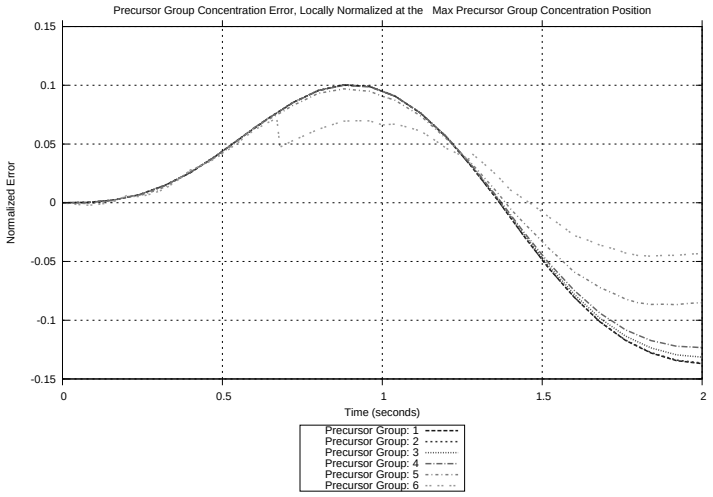

Figure 3.39: Locally Normalized Precursor Group Concentration Error at the Maximum Precursor Group Concentration Position (25 SS, 10 Trans)

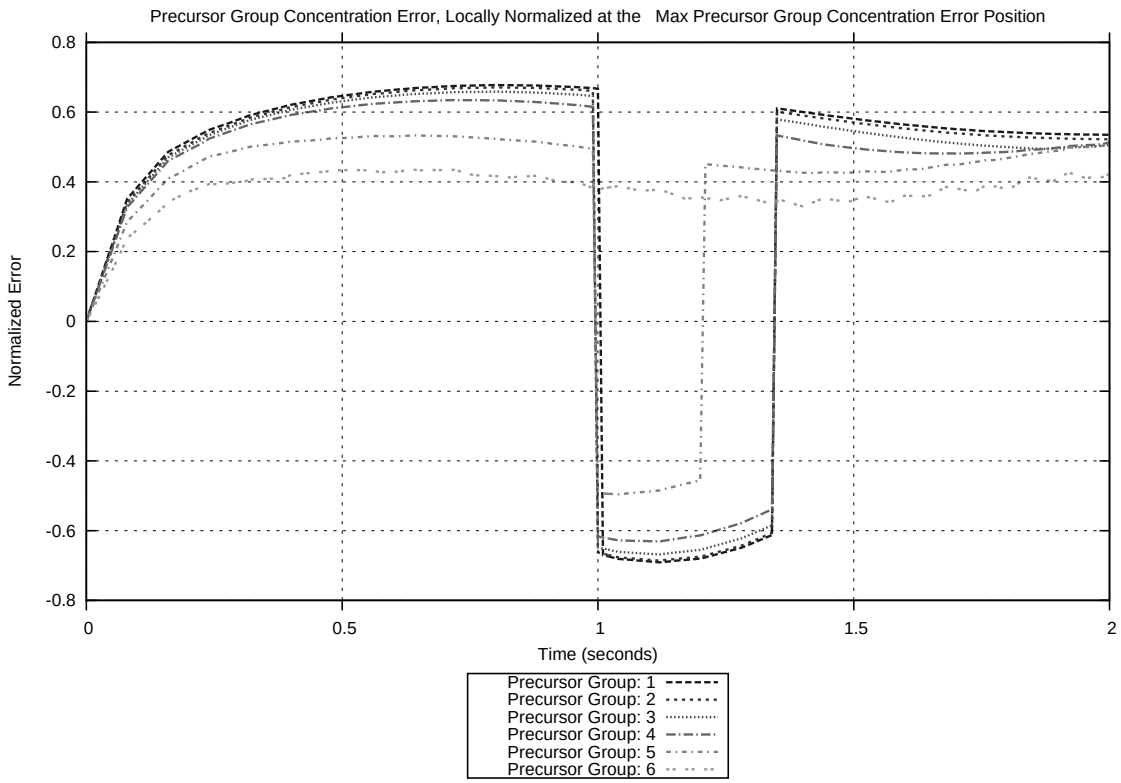

Figure 3.40: Locally Normalized Precursor Group Concentration Error at the Maximum Precursor Group Concentration Error Position (25 SS, 10 Trans)

Likewise, Figure 3.39 displays the error at the maximum precursor group concentration position; whereas, Figure 3.40 represents the error at the precursor group concentration locally normalized maximum error position, hence their differences.

2 Second Transient, 25 Steady-State Data Points, 40 Transient Data Points

For the 2 second transient utilizing the 25 entry steady-state library and the 40 data output exact solution, the following results were obtained regarding the flux error and precursor error equations. The locally normalized flux error at the maximum flux position and the maximum flux error position have been supplied in Figure 3.41 and Figure 3.42. Also, the locally normalized precursor group concentration error at the maximum precursor group concentration position and the maximum precursor group concentration error position are given in Figure 3.43 and Figure 3.44. Appendix-B contains the flux and precursor average normalized errors along with the L2-error values.

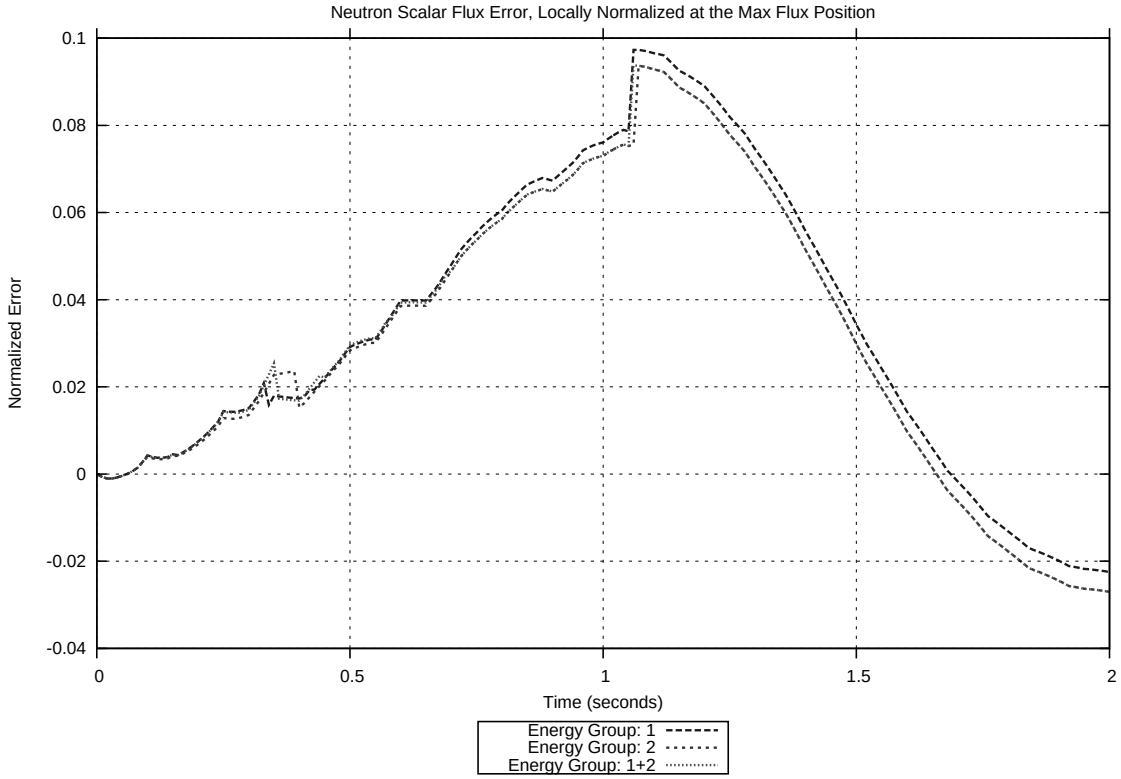

Figure 3.41: Locally Normalized Flux Error at the Maximum Flux Position (25 SS, 40 Trans)

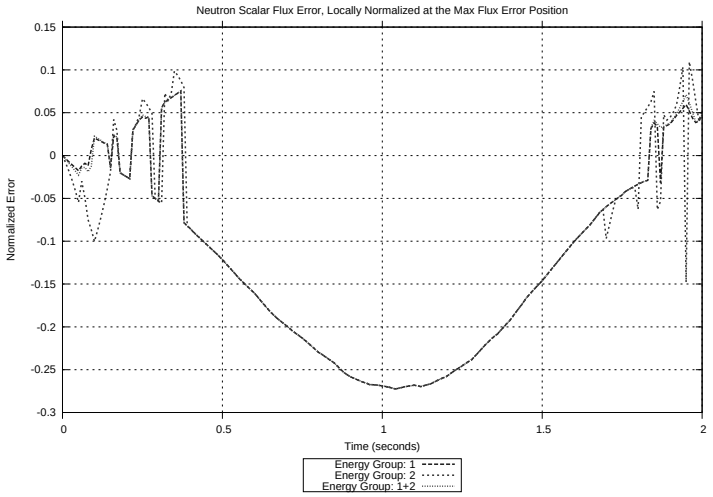

Figure 3.42: Locally Normalized Flux Error at the Maximum Flux Error Position (25 SS, 40 Trans)

Again, the behavior presented in Figure 3.42 is believed to be caused by the same factors influencing the behavior of Figure 3.32; though, comparing Figure 3.42 with Figure 3.23, the overall behavior is similar.

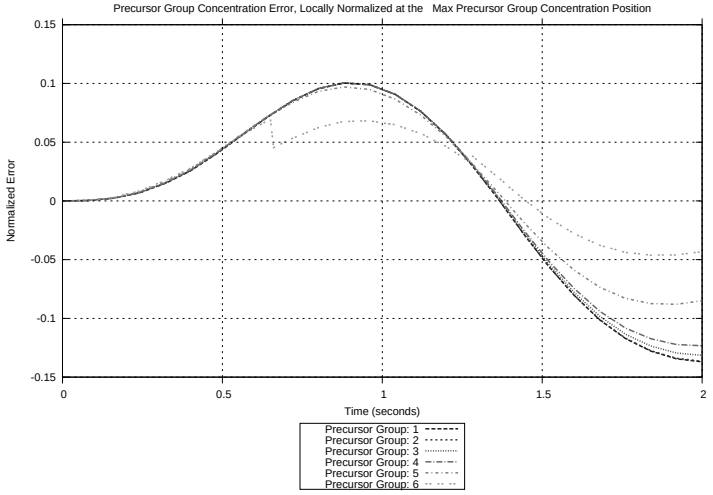

Figure 3.43: Locally Normalized Precursor Group Concentration Error at the Maximum Precursor Group Concentration Position (25 SS, 40 Trans)

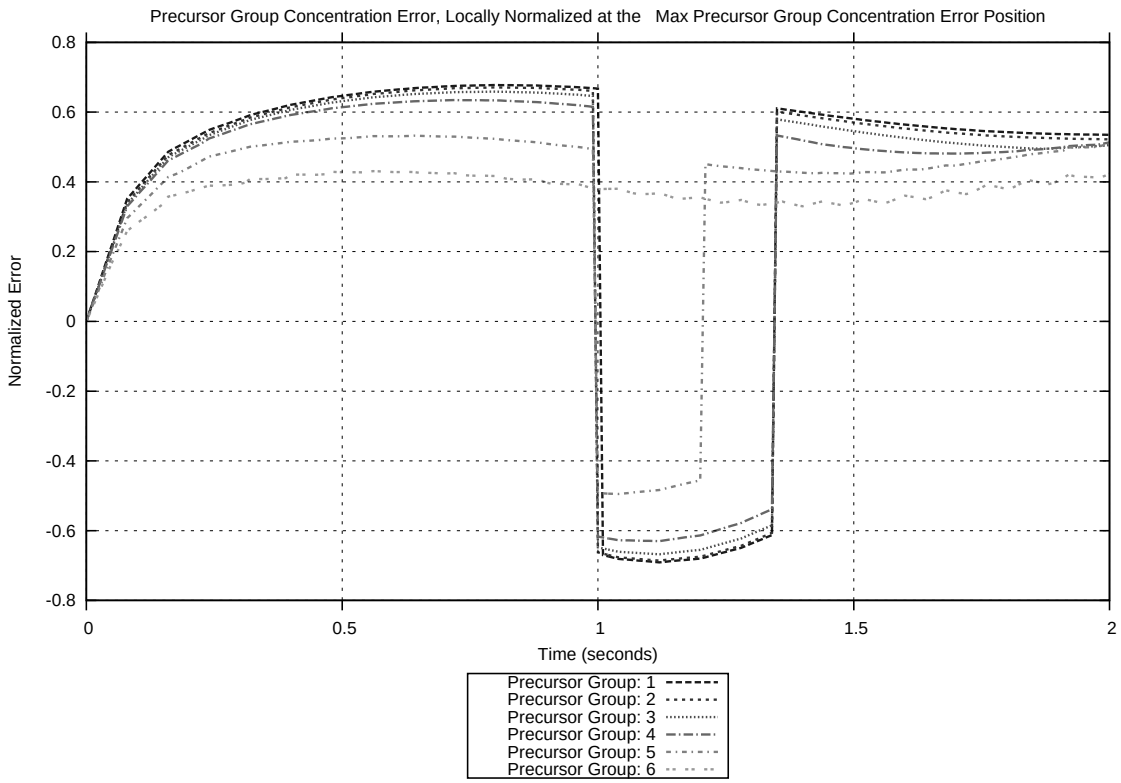

Figure 3.44: Locally Normalized Precursor Group Concentration Error at the Maximum Precursor Group Concentration Error Position (25 SS, 40 Trans)

As well, the differences between Figure 3.43 and Figure 3.44 are attributed to the ability of the maximum precursor group concentration position and the precursor group concentration locally normalized maximum error position to not coincide.

Also, notice the small ridges present in precursor group 6 in Figure 3.36 and compare with Figure 3.44. These small variations are believed to also be the results of interpolation effects from the differing number of steady-state data points used. Again, comparing the ridges present in precursor group 6 in Figure 3.40 with Figure 3.44, it is apparent that the differing number of transient data points also has bearing on these effects. Including Figure 3.28 and comparing with Figure 3.44, it is apparent that both the number of steady-state data records and the number of transient data records affects the small ridges present in precursor group 6.

120 Second Transient, 10 Steady-State Data Points, 10 Transient Data Points

For the 120 second transient utilizing the 10 entry steady-state library and the 10 data output exact solution, the following results were obtained regarding the flux error and precursor error equations. The locally normalized flux error at the maximum flux position and the maximum flux error position have been supplied in Figure 3.45 and Figure 3.46. Also, the locally normalized precursor group concentration error at the maximum precursor group concentration position and the maximum precursor group concentration error position are given in Figure 3.48 and Figure 3.49. Appendix-B contains the flux and precursor average normalized errors along with the L2-error values.

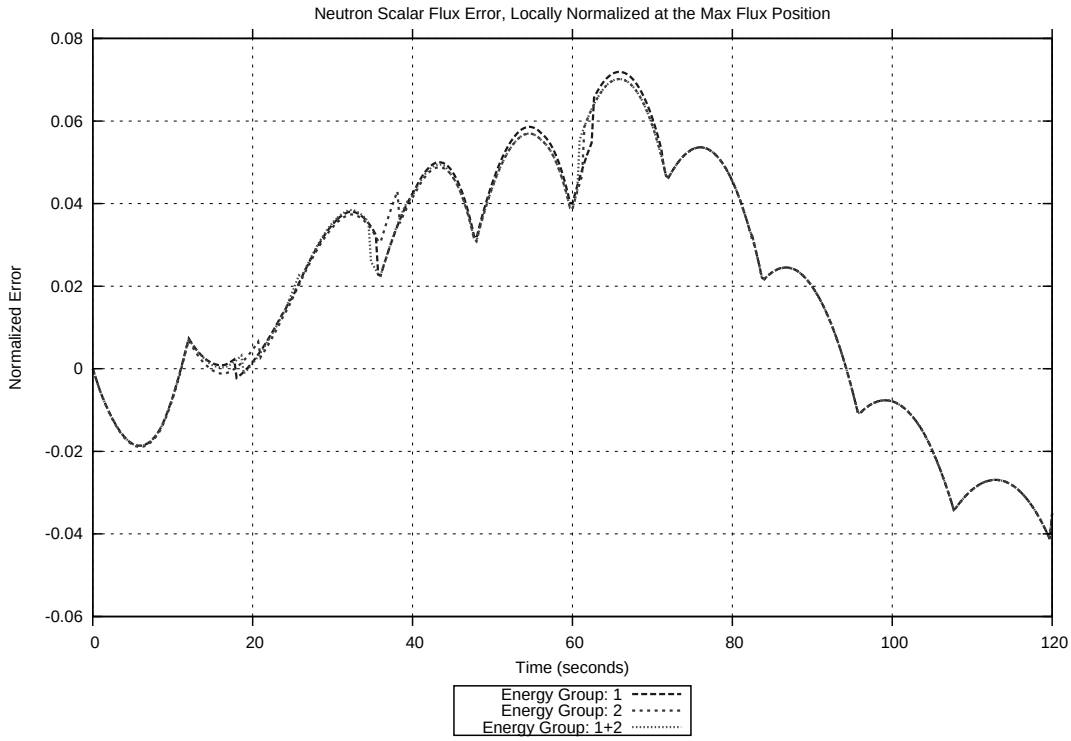

Figure 3.45: Locally Normalized Flux Error at the Maximum Flux Position (10 SS, 10 Trans)

Contrasting Figure 3.21 with Figure 3.45, it is apparent that the 120 second transient maintains lower flux locally normalized maximum flux position error values than the 2 second transient. This is believed to be a results of the longer transient time, which is better approximated by the steady-state cases than is the 2 second transient. Again the ridges are believed to be caused by interpolation.

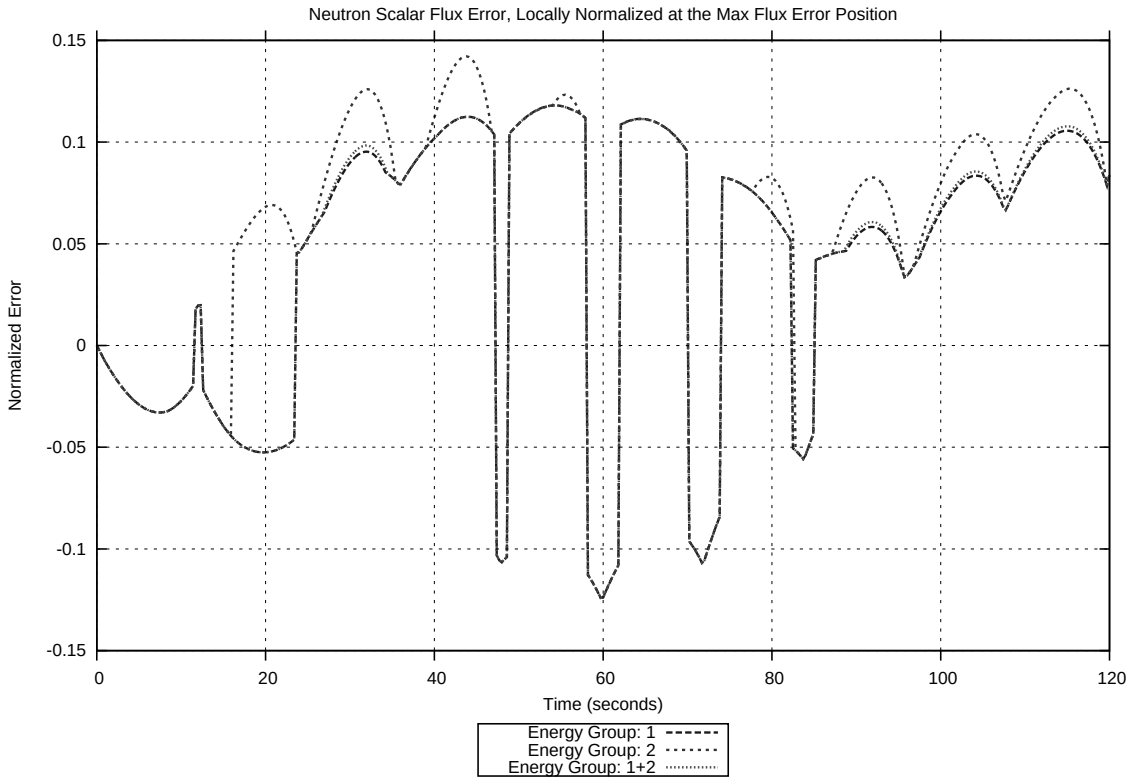

Figure 3.46: Locally Normalized Flux Error at the Maximum Flux Error Position (10 SS, 10 Trans)

Notice the seemingly erratic behavior of Figure 3.46 as compared to Figure 3.23. If the absolute error were plotted instead of the "signed" error the curve would be much smoother. It is apparent that the overall error values are smaller in comparison to the 2 second transient, by almost half. This occurs even though the volume averaged neutron density error is much more significant in the case of the 120 second transient, as seen in Figure 3.47.

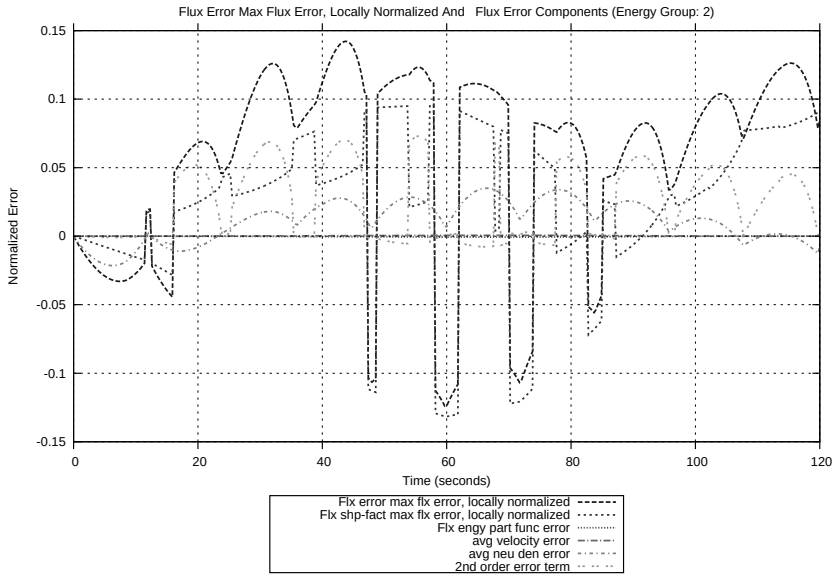

Figure 3.47: Locally Normalized Flux Error and Error Components at the Maximum Flux Error Position (10 SS, 10 Trans, Group: 2)

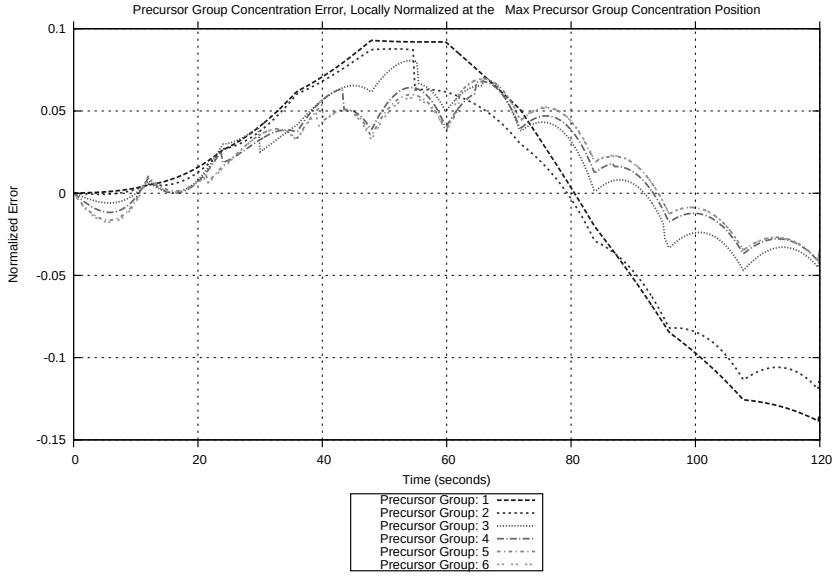

Figure 3.48: Locally Normalized Precursor Group Concentration Error at the Maximum Precursor Group Concentration Position (10 SS, 10 Trans)

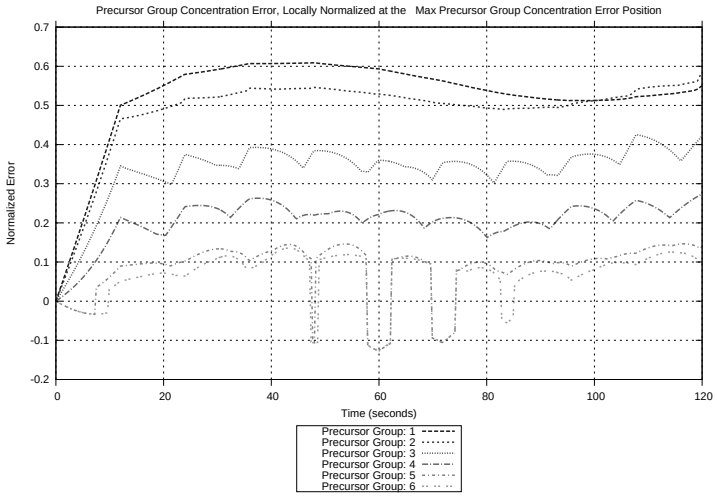

Figure 3.49: Locally Normalized Precursor Group Concentration Error at the Maximum Precursor Group Concentration Error Position (10 SS, 10 Trans)

As with the flux locally normalized maximum error Figure 3.46, the precursor group 6 displays less smoothness in comparison to group 1, group 2, group 3, and group 4. Some insight as to the source of this discrepancy can be gleaned from viewing the component error analysis for these groups. Again, the jumps are due to error sign switching when location of the absolute maximum occurs.

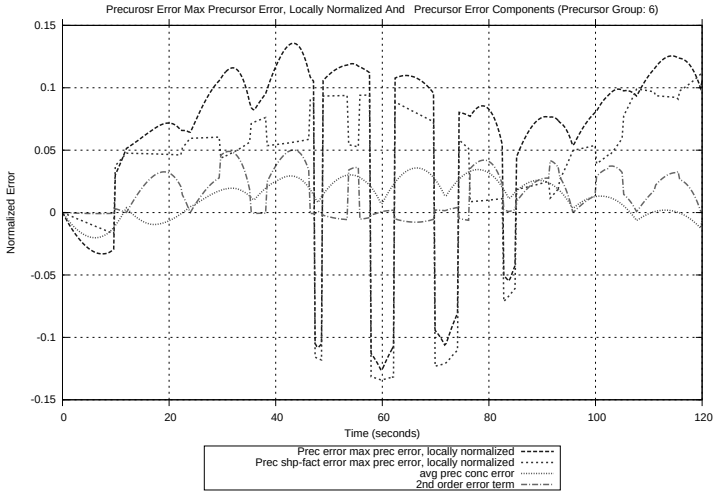

Figure 3.50: Locally Normalized Precursor Group Concentration Error at the Maximum Precursor Group Concentration Error Position (10 SS, 10 Trans, Group 6)

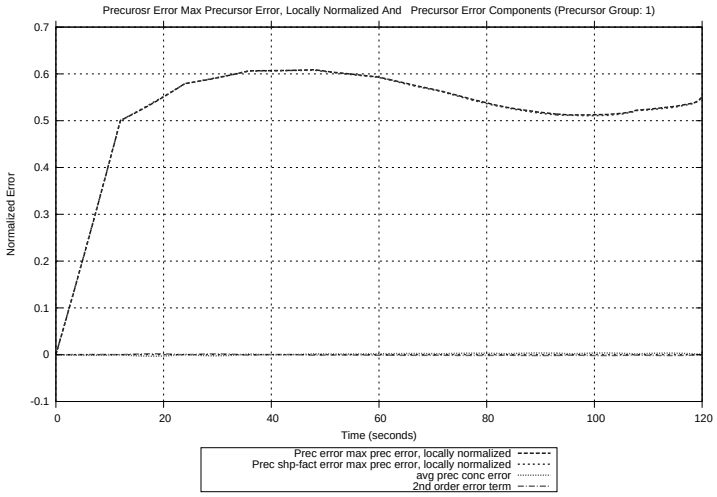

Figure 3.51: Locally Normalized Precursor Group Concentration Error and Error Components at the Maximum Precursor Group Concentration Error Position (10 SS, 10 Trans, Group 1)

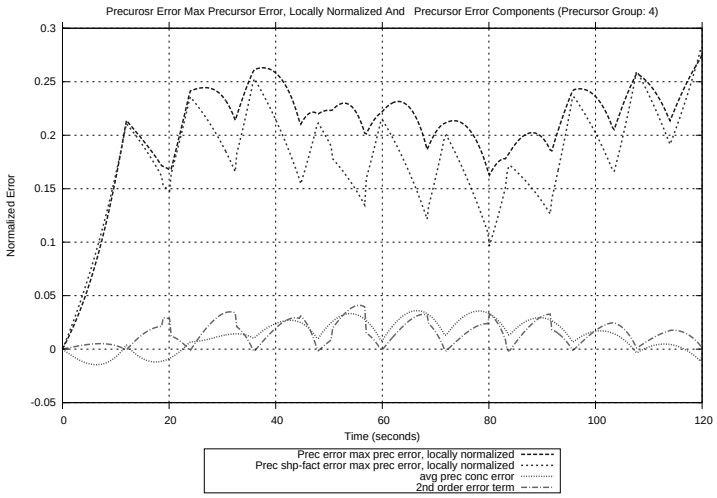

Figure 3.52: Locally Normalized Precursor Group Concentration Error and Error Components at the Maximum Precursor Group Concentration Error Position (10 SS, 10 Trans, Group 4)

It is clear from Figure 3.50, Figure 3.51, and Figure 3.52 that the behavior becomes less smooth as the volume averaged precursor group concentration error becomes more significant.

120 Second Transient, 10 Steady-State Data Points, 40 Transient Data Points

For the 120 second transient utilizing the 10 entry steady-state library and the 40 data output exact solution, the following results were obtained regarding the flux error and precursor error equations. The locally normalized flux error at the maximum flux position and the maximum flux error position have been supplied in Figure 3.53 and Figure 3.54. Also, the locally normalized precursor group concentration error at the maximum precursor group concentration position and the maximum precursor group concentration error position are given in Figure 3.55 and Figure 3.56. Appendix-B contains the flux and precursor average normalized errors along with the L2-error values.

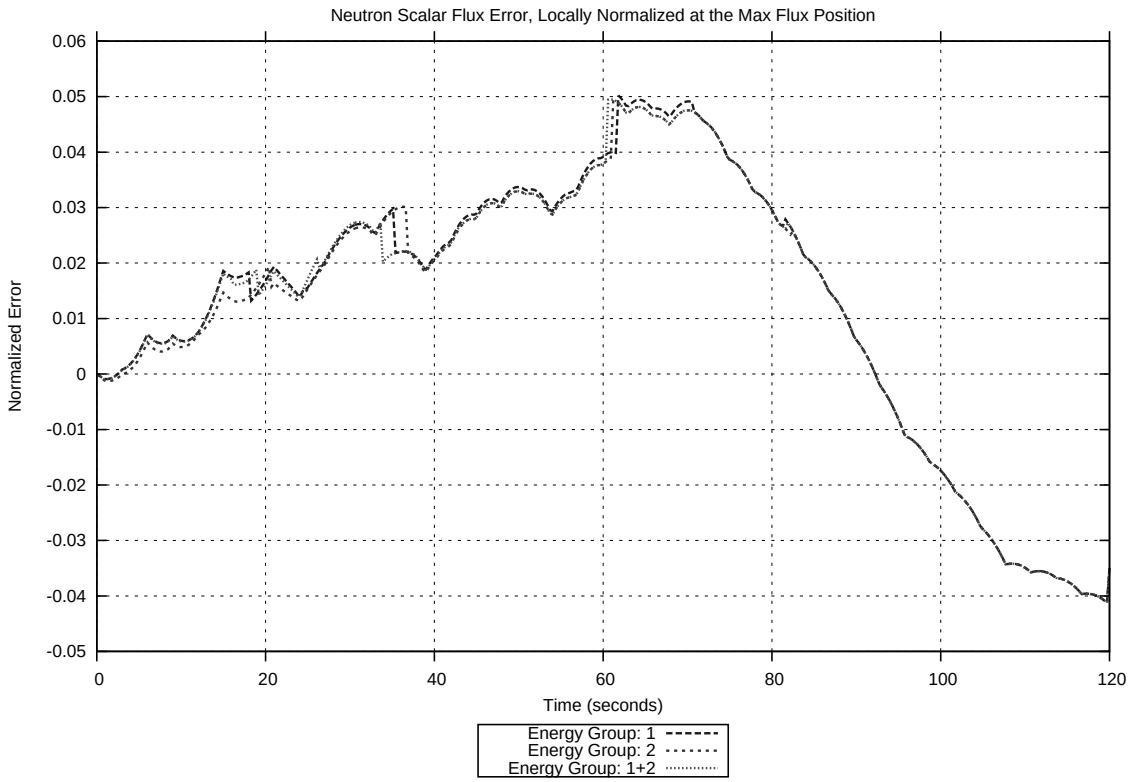

Figure 3.53: Locally Normalized Flux Error at the Maximum Flux Position (10 SS, 40 Trans)

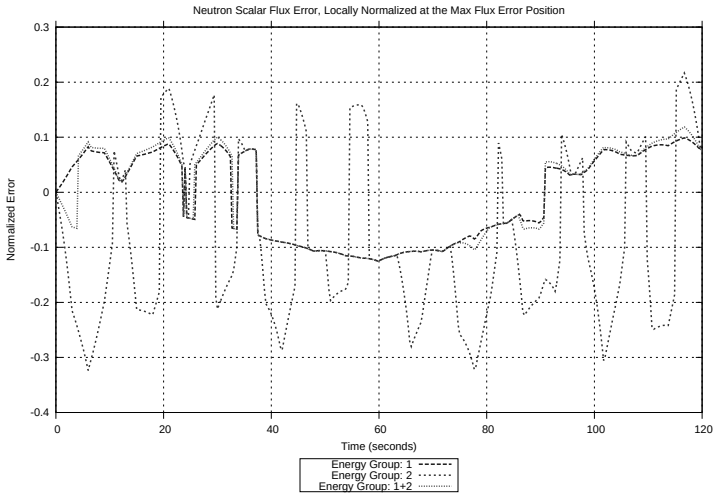

Figure 3.54: Locally Normalized Flux Error at the Maximum Flux Error Position (10 SS, 40 Trans)

The description for the distinct behavior of Figure 3.54 is the same as the argument made for Figure 3.46.

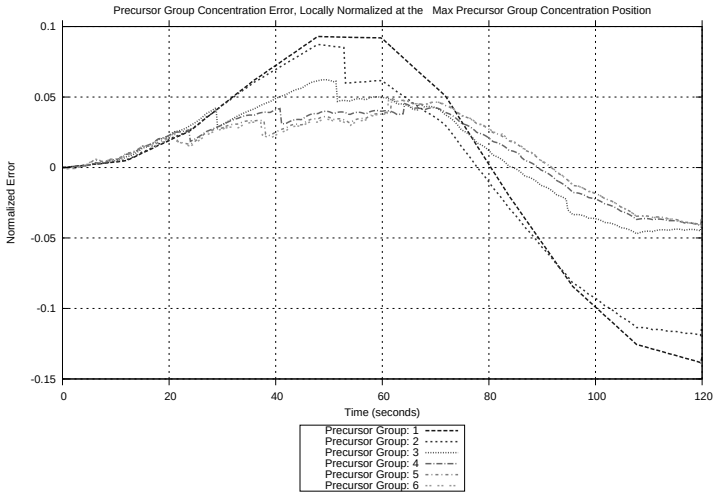

Figure 3.55: Locally Normalized Precursor Group Concentration Error at the Maximum Precursor Group Concentration Position (10 SS, 40 Trans)

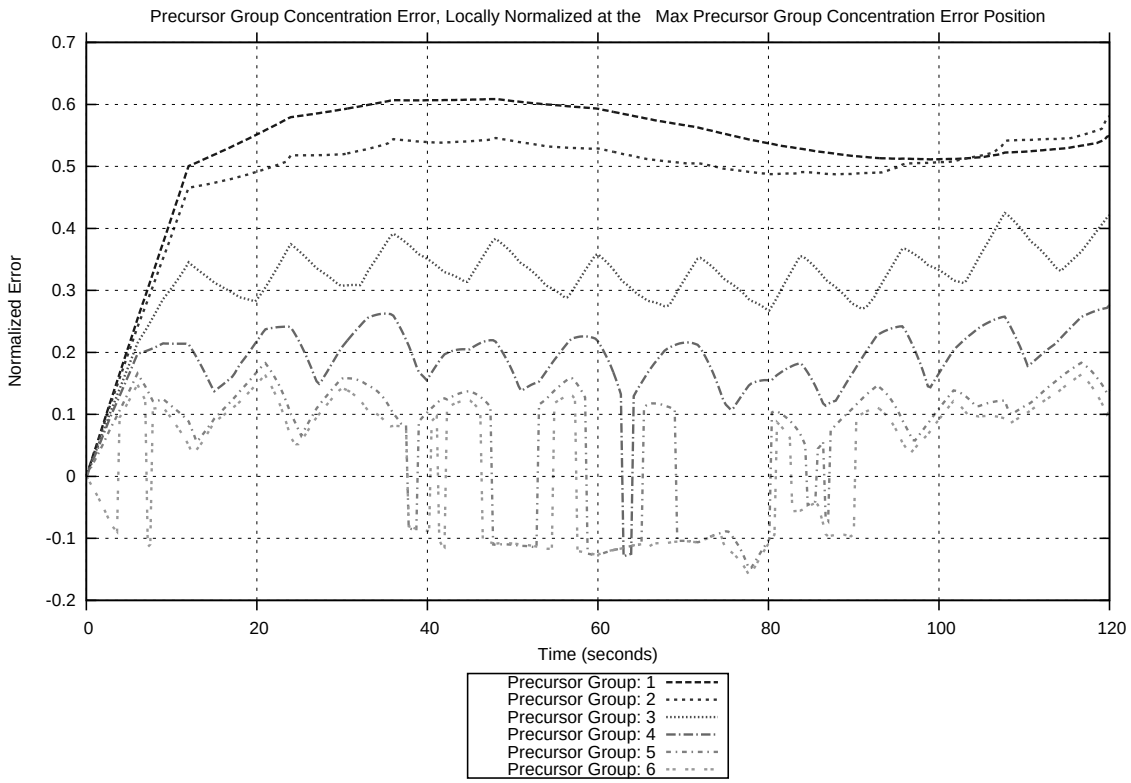

Figure 3.56: Locally Normalized Precursor Group Concentration Error at the Maximum Precursor Group Concentration Error Position (10 SS, 40 Trans)

As well, see the argument characterizing the behavior for Figure 3.49 to describe the trends seen in Figure 3.56.

120 Second Transient, 25 Steady-State Data Points, 10 Transient Data Points

For the 120 second transient utilizing the 25 entry steady-state library and the 10 data output exact solution, the following results were obtained regarding the flux error and precursor error equations. The locally normalized flux error at the maximum flux position and the maximum flux error position have been supplied in Figure 3.57 and Figure 3.58. Also, the locally normalized precursor group concentration error at the maximum precursor group concentration position and the maximum precursor group concentration error position are given in Figure 3.59 and Figure 3.60. Appendix-B contains the flux and precursor average normalized errors along with the L2-error values.

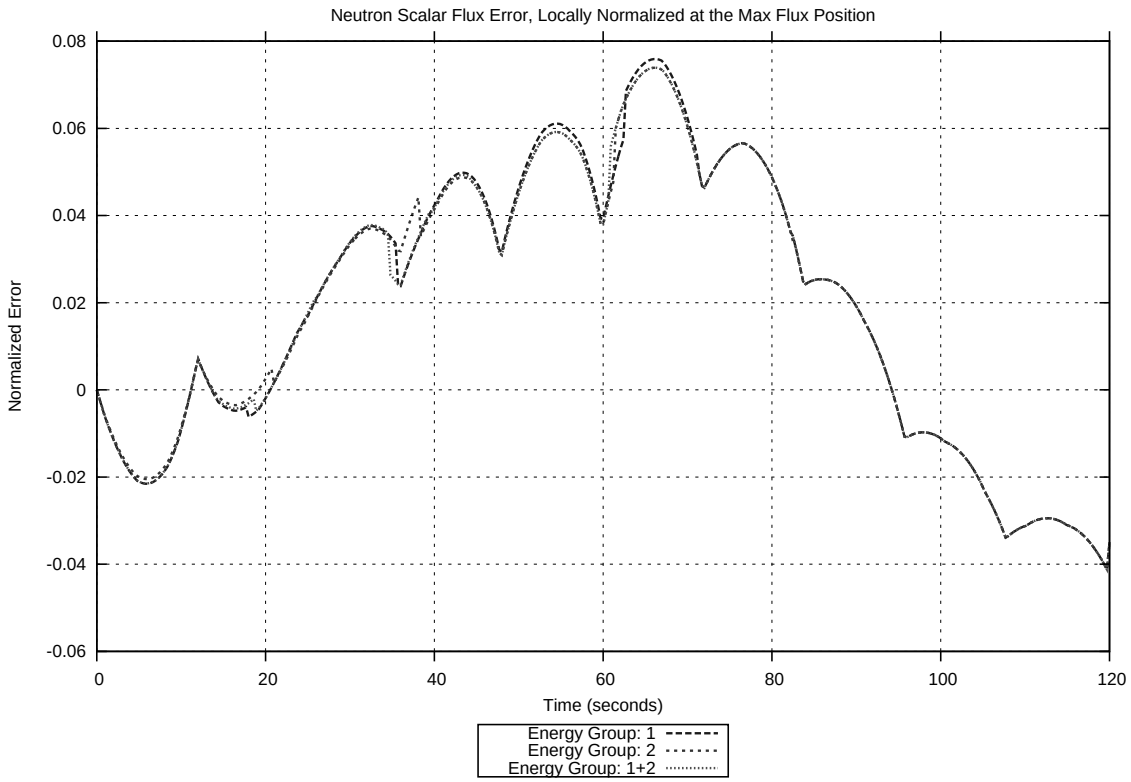

Figure 3.57: Locally Normalized Flux Error at the Maximum Flux Position (25 SS, 10 Trans)

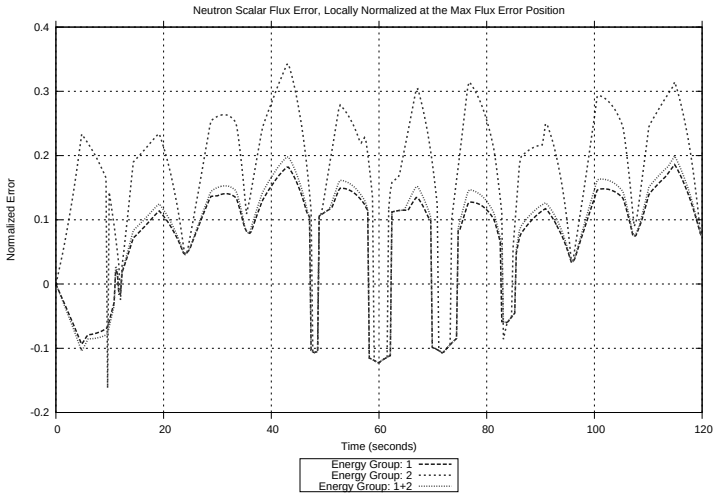

Figure 3.58: Locally Normalized Flux Error at the Maximum Flux Error Position (25 SS, 10 Trans)

Again, see the argument made for Figure 3.46 to describe the behavior of Figure 3.58.

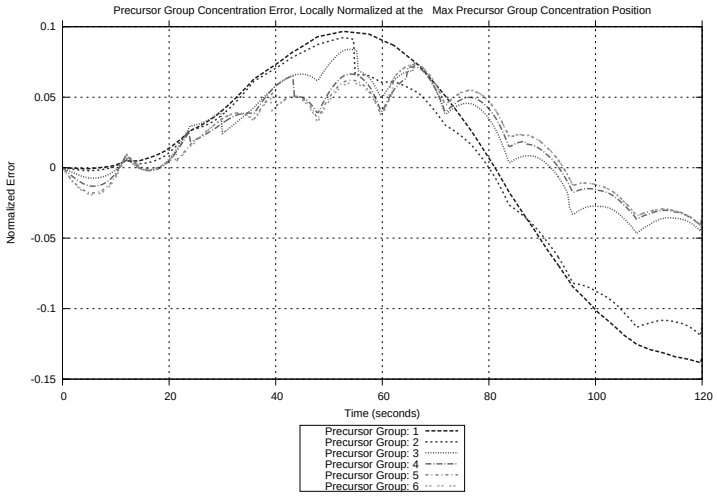

Figure 3.59: Locally Normalized Precursor Group Concentration Error at the Maximum Precursor Group Concentration Position (25 SS, 10 Trans)

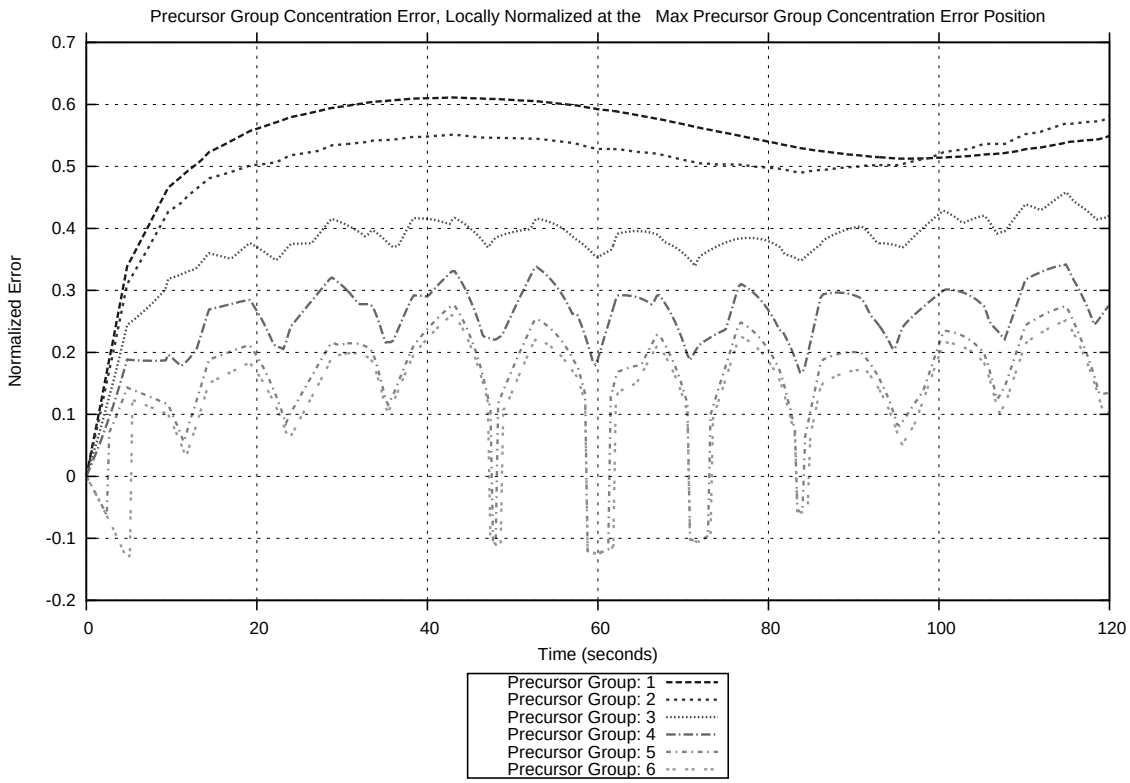

Figure 3.60: Locally Normalized Precursor Group Concentration Error at the Maximum Precursor Group Concentration Error Position (25 SS, 10 Trans)

As well, see the description for the behavior of Figure 3.49 to describe Figure 3.60.

120 Second Transient, 25 Steady-State Data Points, 40 Transient Data Points

For the 120 second transient utilizing the 25 entry steady-state library and the 40 data output exact solution, the following results were obtained regarding the flux error and precursor error equations. The locally normalized flux error at the maximum flux position and the maximum flux error position have been supplied in Figure 3.61 and Figure 3.62. Also, the locally normalized precursor group concentration error at the maximum precursor group concentration position and the maximum precursor group concentration error position are given in Figure 3.63 and Figure 3.64. Appendix-B contains the flux and precursor average normalized errors along with the L2-error values.

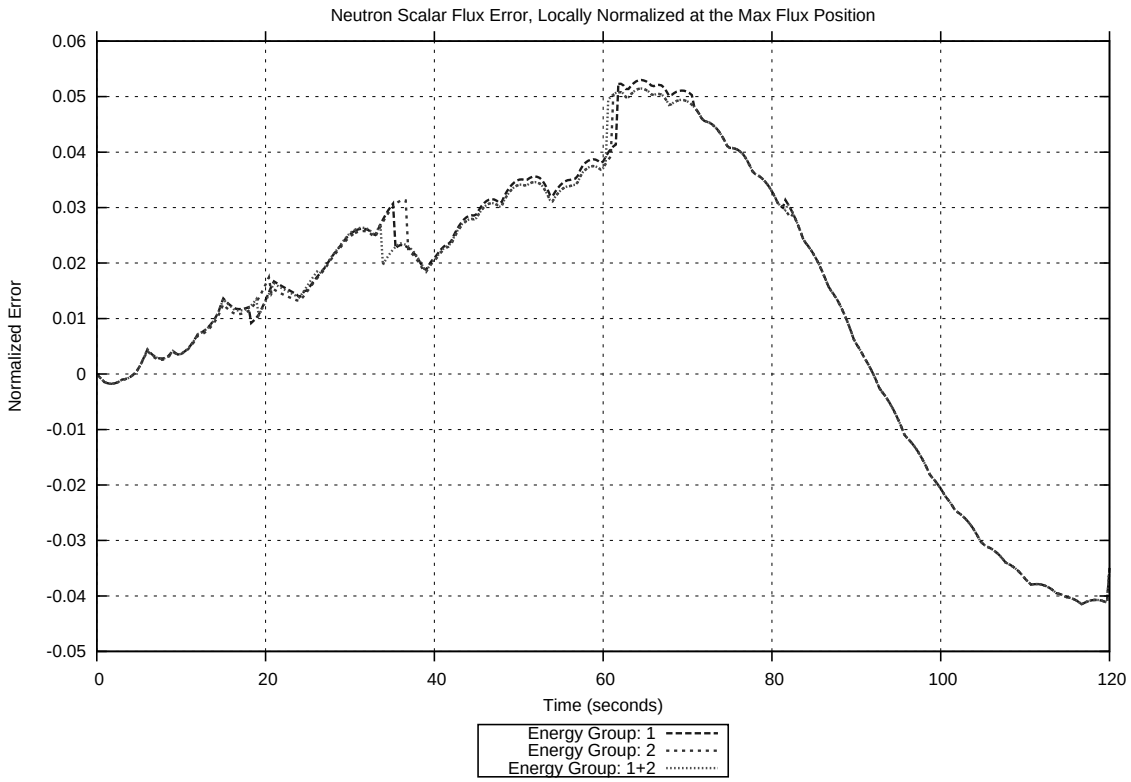

Figure 3.61: Locally Normalized Flux Error at the Maximum Flux Position (25 SS, 40 Trans)

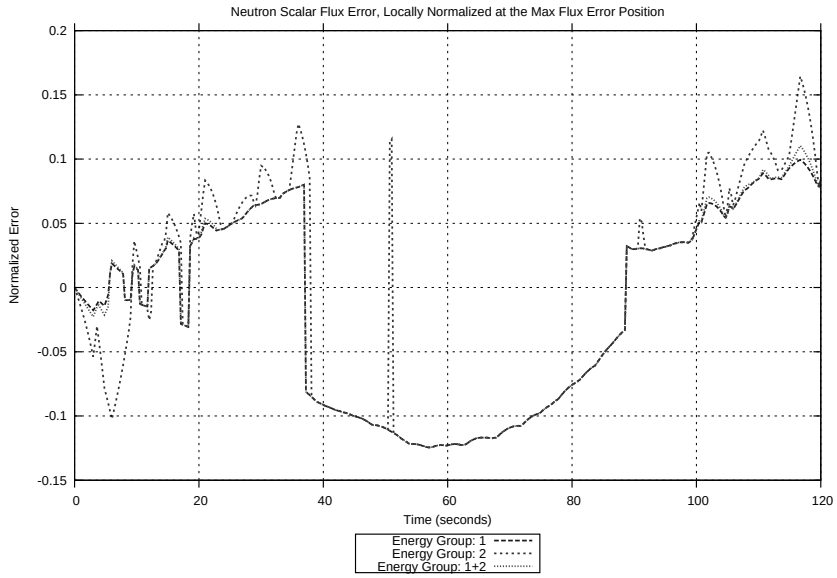

Figure 3.62: Locally Normalized Flux Error at the Maximum Flux Error Position (25 SS, 40 Trans)

Once again, see the argument made for Figure 3.46 to describe the behavior of Figure 3.62.

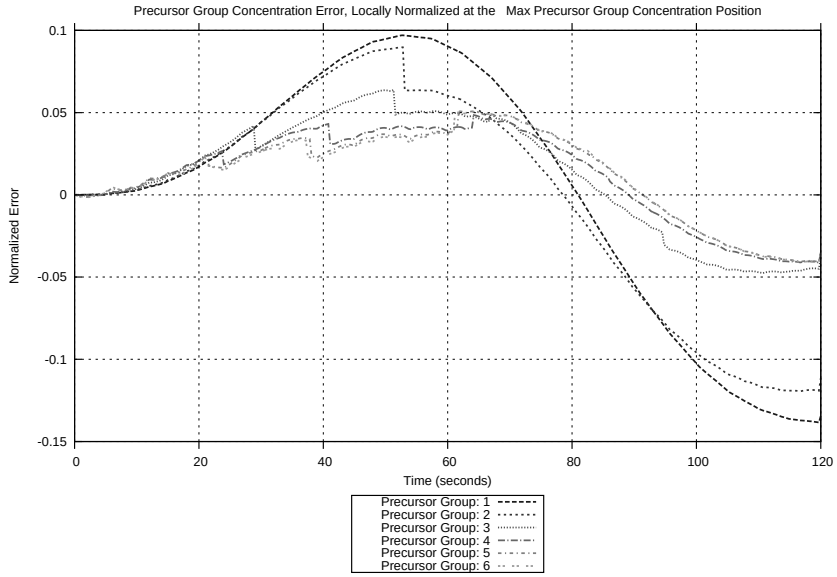

Figure 3.63: Locally Normalized Precursor Group Concentration Error at the Maximum Precursor Group Concentration Position (25 SS, 40 Trans)

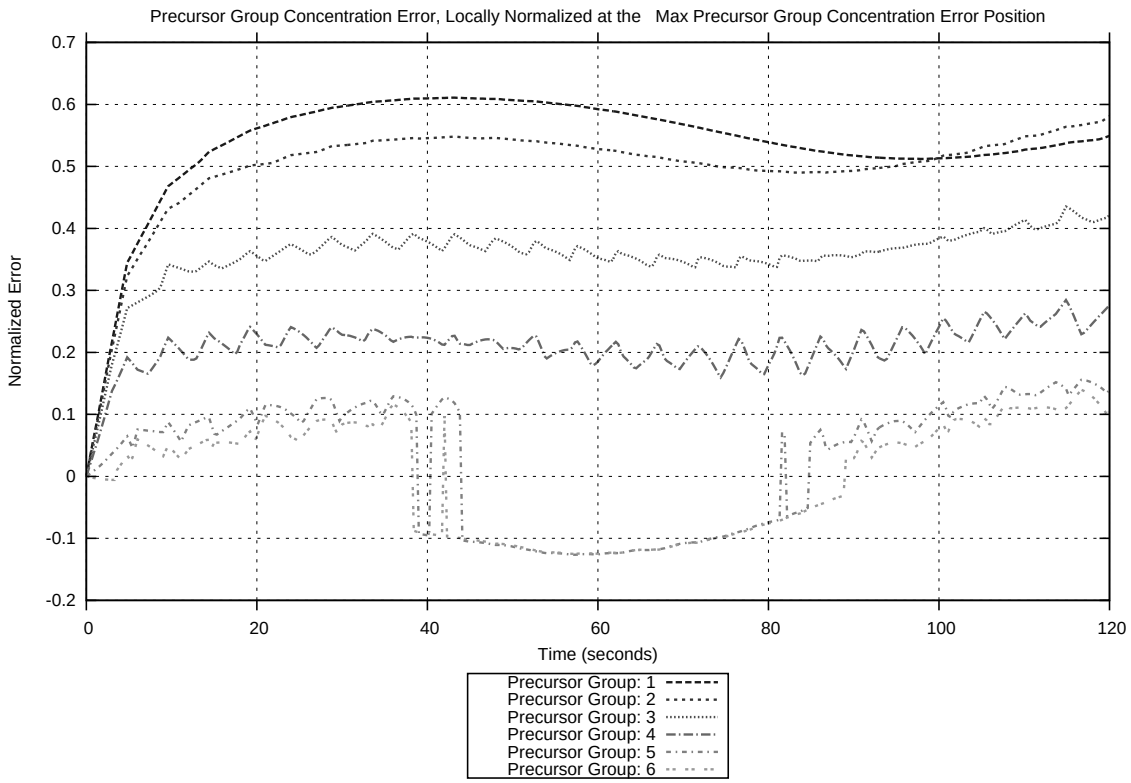

Figure 3.64: Locally Normalized Precursor Group Concentration Error at the Maximum Precursor Group Concentration Error Position (25 SS, 40 Trans)

Also, notice the small ridges present in precursor group 6 in Figure 3.56 and compare with Figure 3.64. These small variations are believed to also be the results of interpolation effects from the differing number of steady-state data points used. Again, comparing the ridges present in precursor group 6 in Figure 3.60 with Figure 3.64 it is apparent that the differing number of transient data points also has bearing on these effects. Including Figure 3.49 and comparing with Figure 3.64, it is apparent that both the number of steady-state data records and the number of transient data records affect the small ridges present in precursor group 6.

Note that both the 2 second and 120 second transients reported mixed results dependent upon the number of steady-state library and transient solution data points.

3.5 Active Model Switching Results

For the active model switching approach, three test scenarios were evaluated; one with no switching, another with only one update, and a third case with full switching capability. Each test scenario studied a fast rod insertion, duration of 2 seconds, and a slow rod insertion, duration of 120 seconds. The fidelity of the projected model was determined by comparison with the NESTLE transient solution. For the fast transient, the exact solution consist of a 2 second transient with a time-step of 0.002 seconds and a data record every 25 time-steps or 0.050 seconds, resulting in 40 data points. For the slow transient, the exact solution consist of a 120 second transient with a time-step of 0.120 seconds and a data record every 25 time-steps or 3.0 seconds, resulting in 40 data points.

Utilization of the NESTLE restart capability requires a restart input file. This file consist of various factors that are printed when NESTLE is stopped with the intention of being restarted at some later time. To facilitate the active model switching approach, a transient is executed using NESTLE and is stopped after one time-step and the restart factors are recorded. Note that some of the restart factors are time dependent. Thus, when the error is determined to be too large, at some time during the transient, the correct time dependent restart factors are unknown. To reconcile this issue, the restart factors generated after the first time-step are utilized. For the 2 second case the initial time-step was 0.0010 seconds and the rod was inserted from the ARO position, 141.250 inches, to a slightly inserted position of 141.179375 inches. For the 120 second case, the initial time-step was 0.060 seconds and the rod was inserted from the ARO position to the same 141.179375 inches position.

3.5.1 No Switching - 2 Second Transient

The shape-factors for the 2 second no switching test case were generated by NESTLE from a quick insertion transient. This consisted of an initialization of the steady-state case, at time 0 seconds, and then a rod insertion from ARO to a single rod fully inserted over a period of 0.0020 seconds, having a time-step of 0.0001 seconds, providing 20 data records. The PKE-Solver executed the 2 second transient with a time-step of 0.01 seconds. The flux error at the maximum flux error position, locally and averaged normalized, can be viewed in Figure 3.65-Figure 3.66. Also the L-2 flux error is displayed in Figure 3.67. The precursor group concentration error values are not presented because they have no bearing on this analysis due to the assumption of setting the β_i values to be negligible small (See Section 3.2).

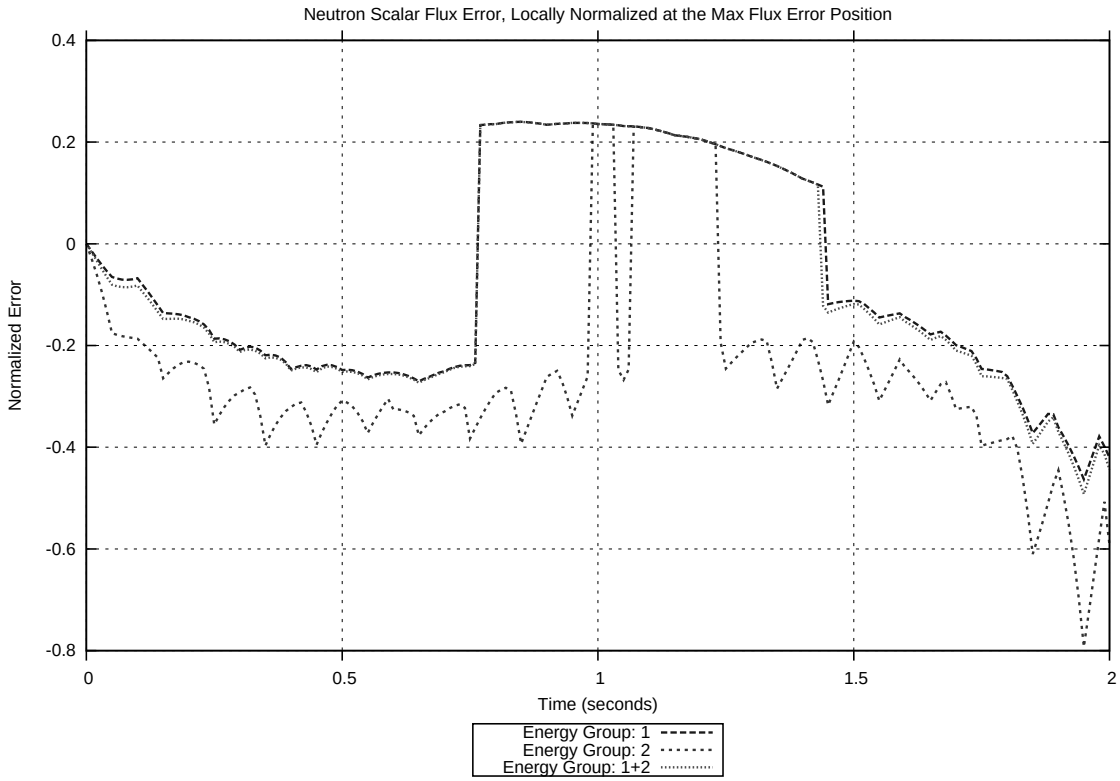

Figure 3.65: Locally Normalized Flux Error at the Maximum Flux Error Position (No switch, Trans 40)

Comparing Figure 3.23, Figure 3.32, Figure 3.38, and Figure 3.42 with Figure 3.65 it is apparent that the flux locally normalized maximum error values for the steady-state cases are roughly the same as for the no switching 2 second transient.

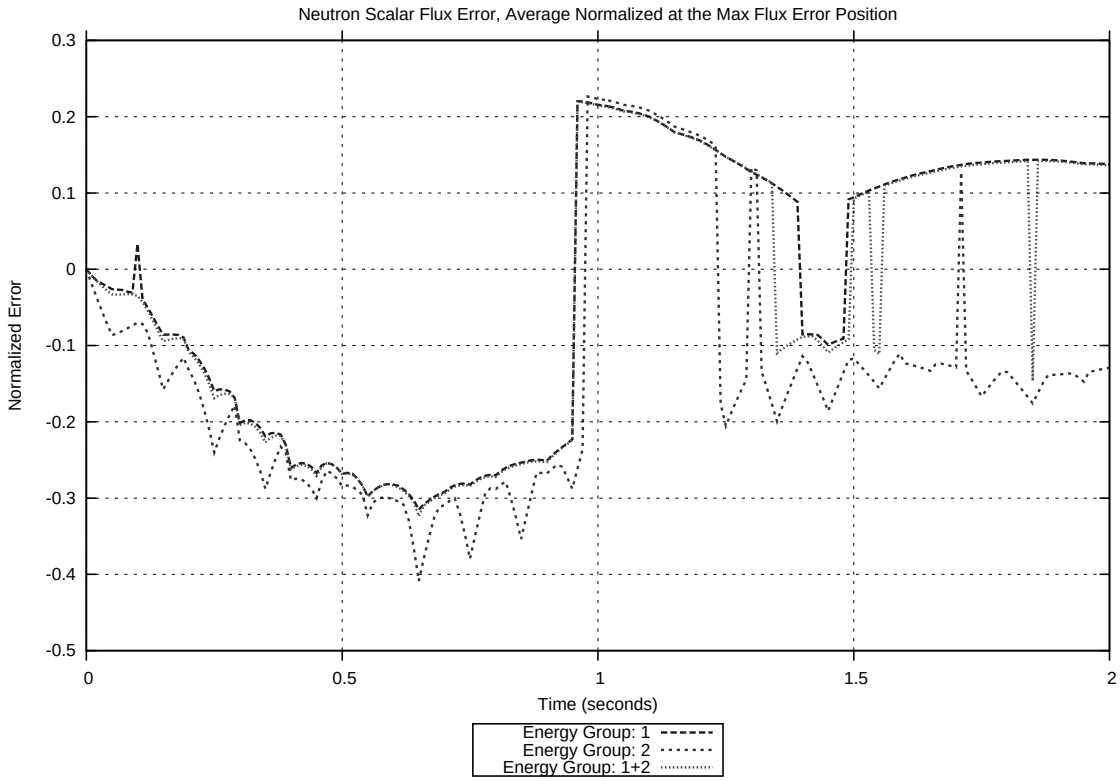

Figure 3.66: Average Normalized Flux Error at the Maximum Flux Error Position (No switch, Trans 40)

When comparing Figure 3.24, Figure B.35, Figure B.41, and Figure B.47 with Figure 3.66, the flux average normalized maximum error values are demonstrated to approximately equal those for the steady-state cases as for the no switching 2 second transient.

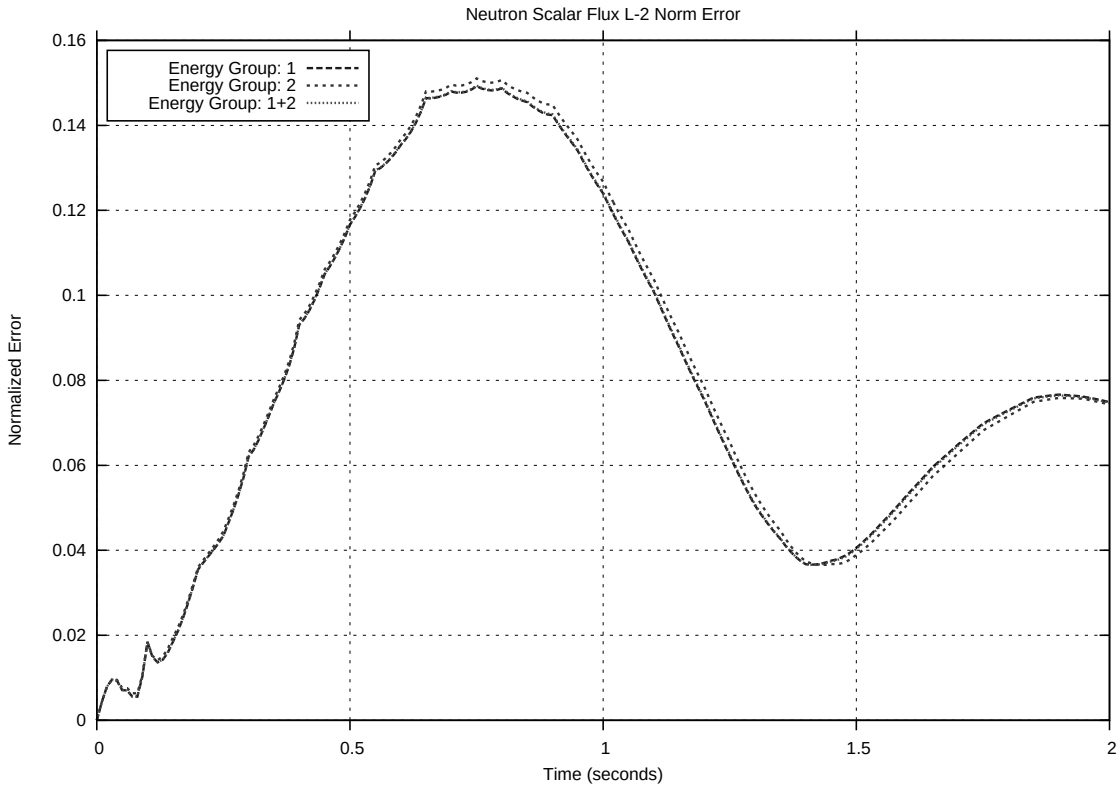

Figure 3.67: Flux L2-Error (No switch, Trans 40)

Notice that even though the maximum flux error values reach approximately 22% (Figure 3.65 and Figure 3.66) the average flux error stays marginally lower, around 15% (Figure 3.67). In addition, Appendix-C contains the flux error and error component values, locally and average normalized, (Figure C.1 - Figure C.8).

3.5.2 No Switching - 120 Second Transient

The shape-factors for the 120 second no switching test case were generated by NESTLE from a quick insertion transient. This consisted of a initialization of the steady-state case, at time 0 seconds, and then a rod insertion from ARO to a single rod fully inserted over a period of 0.0020 seconds, having a time-step of 0.0001 seconds, providing 20 data printouts. The PKE-Solver executed the 120 second transient with a time-step of 0.30 seconds. The flux error at the maximum flux error position, locally and averaged normalized can be viewed in Figure 3.68-Figure 3.69. Also the L-2 flux error is displayed in Figure 3.70.

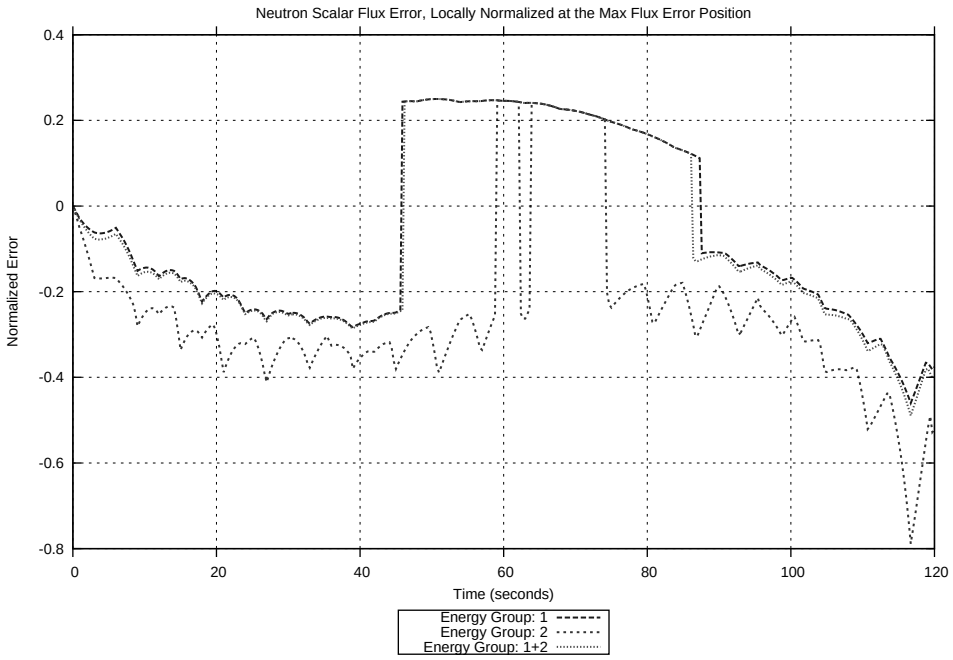

Figure 3.68: Locally Normalized Flux Error at the Maximum Flux Error Position (No switch, Trans 40)

Comparing Figure 3.46, Figure 3.54, Figure 3.58, and Figure 3.62 with Figure 3.68 it is apparent that the flux locally normalized maximum error values for the steady-state cases are roughly the same as for the no switching 120 second transients when using 10 steady-state records with 40 transient records (Figure 3.54) and 25 steady-state records with 10 transient records (Figure 3.58). The no switching 120 second transient results in Figure 3.68 appear to be worse than the 120 second transient cases utilizing 10 steady-state records with 10 transient records (Figure 3.46) and 25 steady-state records with 40 transient records (Figure 3.62).

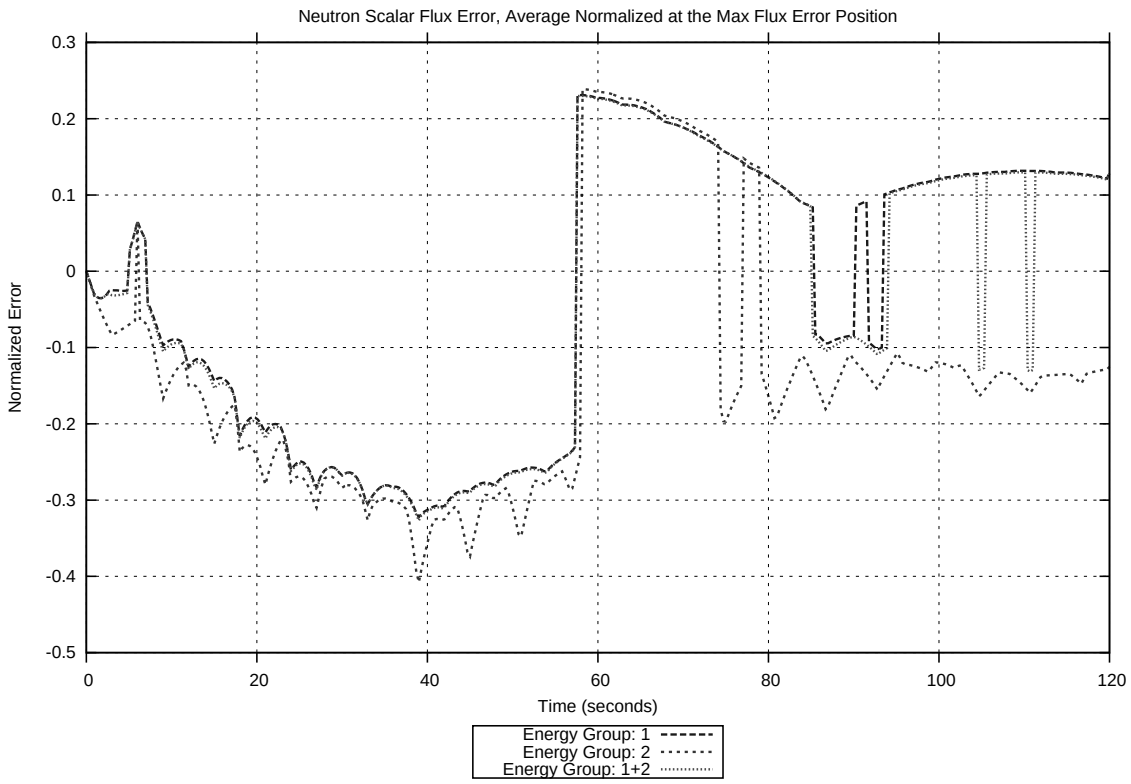

Figure 3.69: Average Normalized Flux Error at the Maximum Flux Error Position (No switch, Trans 40)

When comparing Figure B.53, Figure B.59, Figure B.65, and Figure B.71 with Figure 3.69, the flux average normalized maximum error values of the no switching 120 second transient are demonstrated to be approximately equal the transients using 10 steady-state records with 40 transient records (Figure B.59) and 25 steady-state records and 10 transient records (Figure B.65). The 120 second transient cases utilizing 10 steady-state records with 10 transient records (Figure B.53) and 25 steady-state records with 40 transient records (Figure B.71) appear to produce better values than the no switching 120 second transient (Figure 3.69).

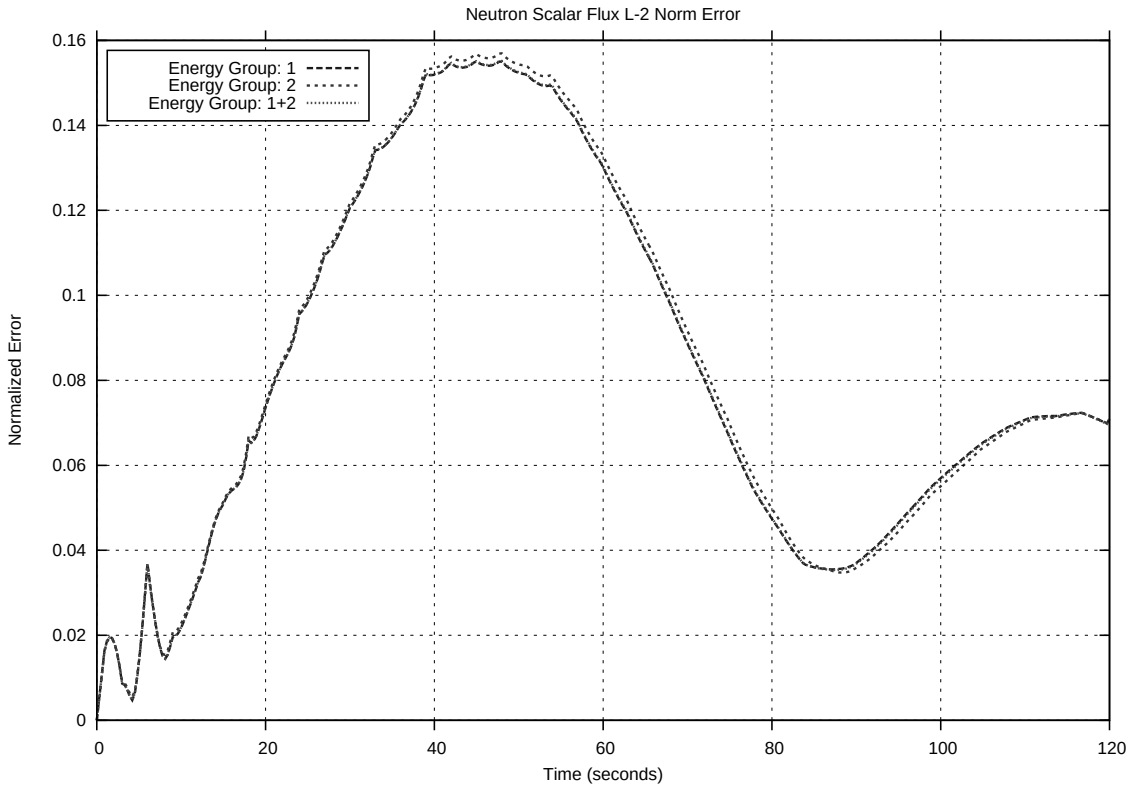

Figure 3.70: Flux L2-Error (No switch, Trans 40)

Notice that even though the maximum flux error values reach approximately 40-60% (Figure 3.68 and Figure 3.69) the average flux error stays marginally lower, around 15% (Figure 3.70). In addition, observe how similar the results from the 2 second transient (Figure 3.65 - Figure 3.67) are to the 120 second transient (Figure 3.70 - Figure 3.69). Appendix-C contains the flux error and error component values, locally and average normalized, (Figure C.9 - Figure C.16).

3.5.3 Single Update - 2 Second Transient

The initial shape-factors for the 2 second single update test case were generated by NESTLE from a quick insertion transient. This consisted of a initialization of the steady-state case, at time 0 seconds, and then a rod insertion from ARO to a single rod fully inserted over a period of 0.0020 seconds, having a time-step size of 0.0001 seconds, providing 20 data records. The PKE-Solver executed the 2 second transient with a time-step of 0.01 seconds. The single shape-factor update was performed at 1.00 second, the middle of the transient. The PKE-Solver was executed for 1.00 second. NESTLE was then restarted with the projected flux and projected precursor group concentration values from two PKE-Solver time-steps prior to the current time, at the time 0.98 seconds. NESTLE used a time-step size of 0.001 seconds until it reached the current transient time of 1.00 seconds and printed the first updated shape-factor values. Then the code was executed with a time-step size of 0.0001 seconds until the single rod was fully inserted at time 1.0010 seconds, outputting the shape-factor values at each time-step. The new shape-factor values replaced the old values and the PKE-Solver was restarted. In this case only a single update was allowed to demonstrate the abilities relative to no switching.

The flux error at the maximum flux error position, locally and averaged normalized can be viewed in Figure 3.71-Figure 3.72. Also the L-2 flux error is displayed in Figure 3.73. As with the no switching scenario, the precursor group concentration error values are not presented because they have no bearing on this analysis due to the assumption explained in Section 3.2.

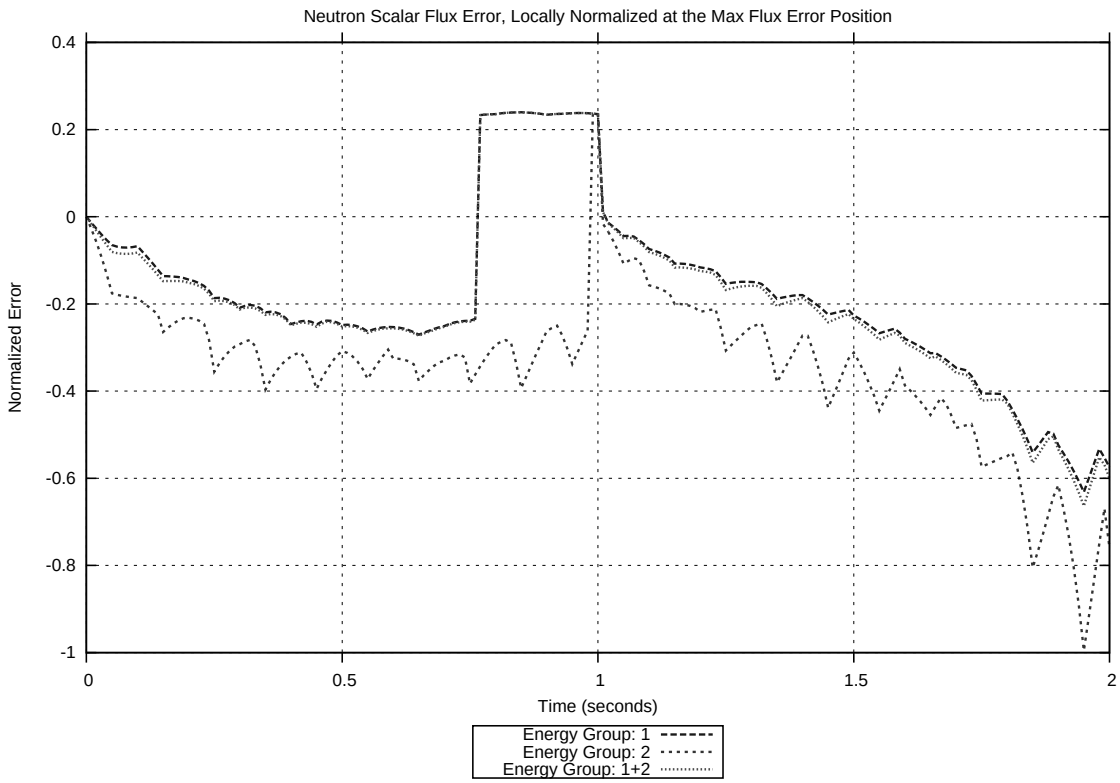

Figure 3.71: Locally Normalized Flux Error at the Maximum Flux Error Position (One update, Trans 40)

Note the drastic reduction in error for the flux locally normalized maximum error values at 1.0 seconds, Figure 3.71. Comparing Figure 3.65 with Figure 3.71, the first half of the transient cases appear identical, which they should as nothing between the two cases differs until 1.0 second. At 1.0 second the reduction in the flux locally normalized maximum error for the single update case is dramatic. After 1.0 second the flux locally normalized maximum error for the single update case rises rapidly and ends the transient with a larger value than the no switch 2 second transient case.

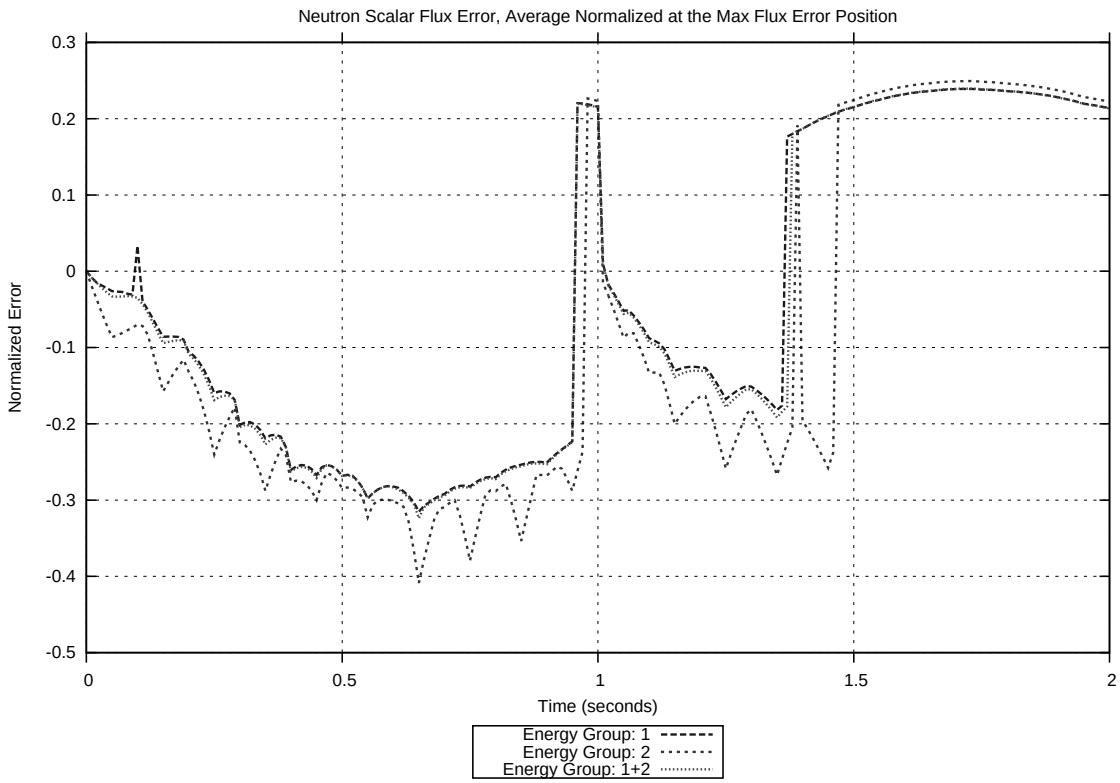

Figure 3.72: Average Normalized Flux Error at the Maximum Flux Error Position (One update, Trans 40)

Note the drastic reduction in error for the flux averaged normalized maximum error values at 1.0 seconds,Figure 3.72. Comparing Figure 3.66 with Figure 3.72, the same comments apply as made when comparing Figure 3.65 with Figure 3.71.

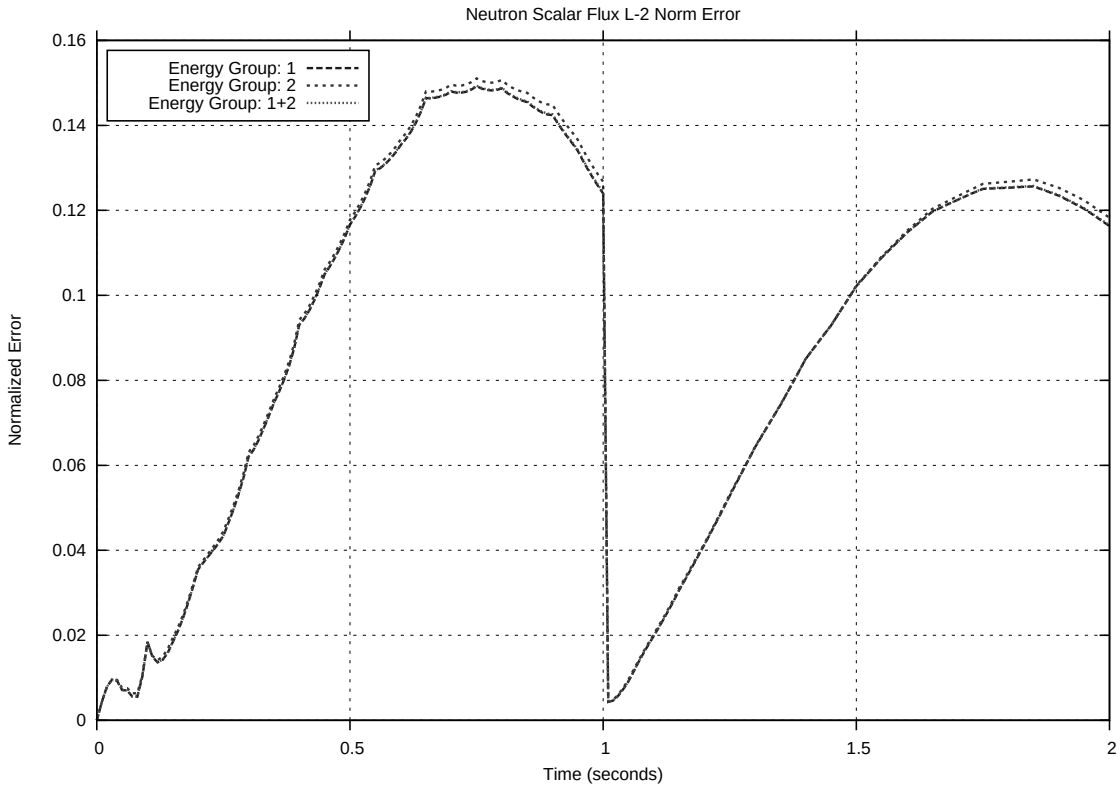

Figure 3.73: Flux L2-Error (One update, Trans 40)

Notice the drastic reduction in error for every error metric at 1.0 second (Figure 3.71 - Figure 3.73). These results agree nicely, because the flux locally normalized and average normalized maximum error values (Figure 3.71 and Figure 3.72) are roughly 2% at 1.0 second. Thus, every other error value must be smaller than this, resulting in a very small flux L2-Error ($< 1.0\%$) at 1.0 second (Figure 3.73). Comparing Figure 3.67 with Figure 3.73, the same explanation as noted for the other figures (Figure 3.65 compared with Figure 3.71 and Figure 3.66 compared with Figure 3.72) apply.

Appendix-C contains the flux error and error component values, locally and average normalized, (Figure C.17 - Figure C.24).

3.5.4 Single Update - 120 Second Transient

The initial shape-factors for the 120 second single update test case were generated by NESTLE form a quick insertion transient. This consisted of a initialization of the steady-state case, at time 0 seconds, and then a rod insertion from ARO to a single rod fully inserted over a period of 0.0020 seconds, having a time-step of 0.0001 seconds, providing 20 data printouts. The PKE-Solver executed the 120 second transient with a time-step of 0.30 seconds. The single shape-factor update was performed at 60.00 seconds, the middle of the transient. The PKE-Solver was executed for 60.00 seconds. NESTLE was then restarted with the projected flux and projected precursor group concentration values from two PKE-Solver time-steps prior to the current time, at time 59.40 seconds. NESTLE used a time-step of 0.01 seconds until it reached a transient time of 60.00 seconds and printed the first updated shape-factor values. Then the code was executed at the same time-step of 0.01 seconds until the a single rod was fully inserted at time 60.12 seconds, outputting the shape-factor values at each time-step. The new shape-factor values replaced the old values and the PKE-Solver was restarted. In this case only a single update was allowed to demonstrate the ability relative to no switching.

The flux error at the maximum flux error position, locally and averaged normalized can be viewed in Figure 3.74-Figure 3.75. Also the L-2 flux error is displayed in Figure 3.76. As with the no switching scenario, the precursor group concentration error values are not presented because they have no bearing on this analysis due to the assumption explained in Section 3.2.

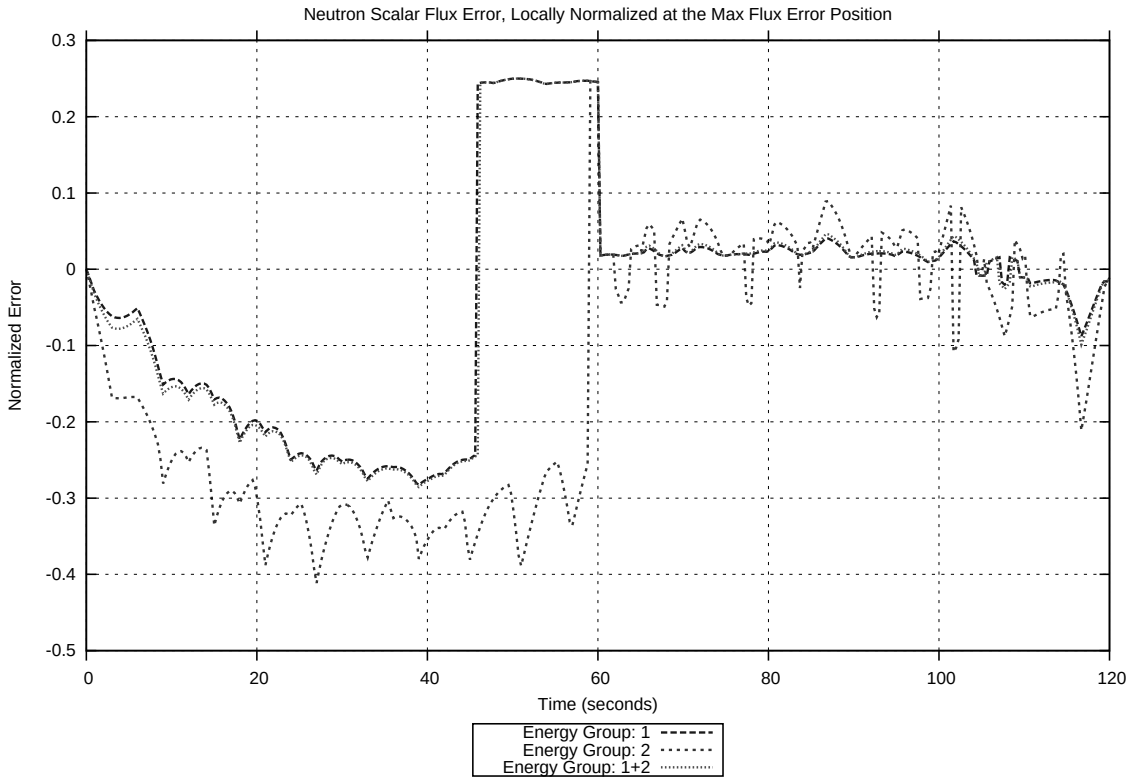

Figure 3.74: Locally Normalized Flux Error at the Maximum Flux Error Position (One update, Trans 40)

Note the drastic reduction in error for the flux locally normalized maximum error values at 60.0 seconds, Figure 3.74. Comparing Figure 3.68 with Figure 3.74, the first half of the transient cases appear identical, which they should as nothing between the two cases differ until 60.0 second. At 60.0 second the reduction in the flux locally normalized maximum error for the single update case is dramatic. After 60.0 second the flux locally normalized maximum error for the single update case maintains a relatively low value until the end of the transient, compared to the no switch 120 second transient case.

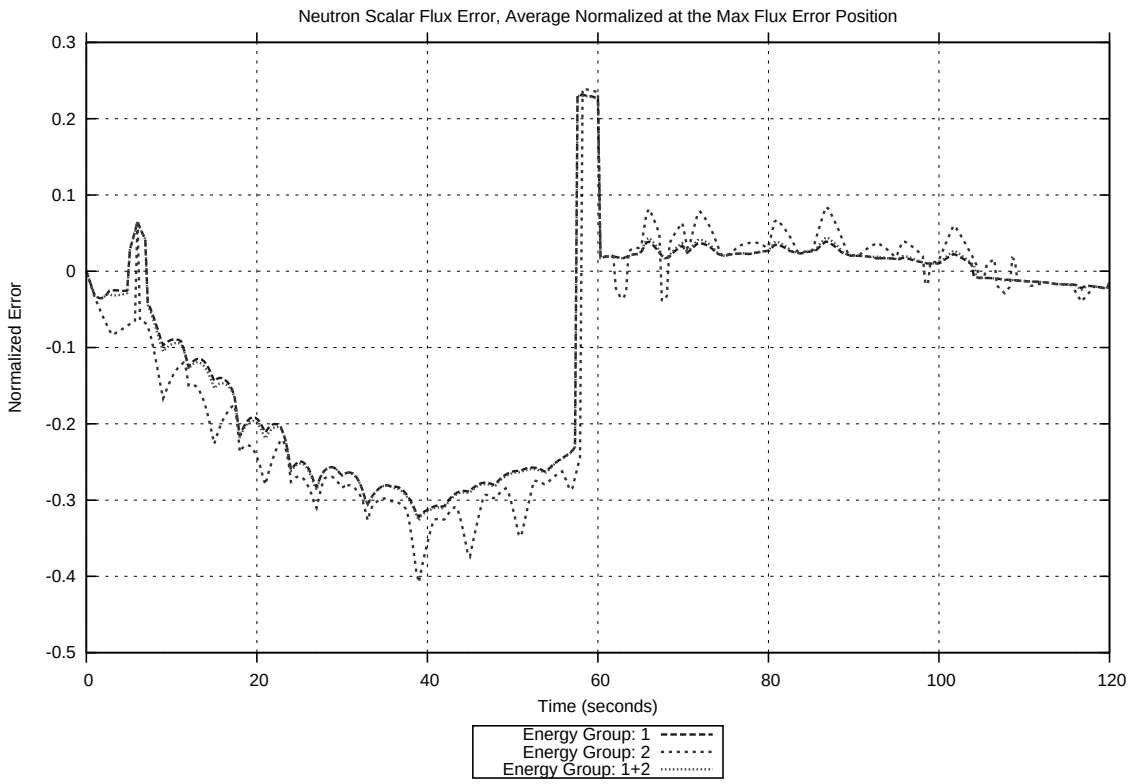

Figure 3.75: Average Normalized Flux Error at the Maximum Flux Error Position (One update, Trans 40)

Note the drastic reduction in error for the flux averaged normalized maximum error values at 60.0 seconds,Figure 3.75. Comparing Figure 3.69 with Figure 3.75, the same explanation as used when comparing Figure 3.68 with Figure 3.74 applies.

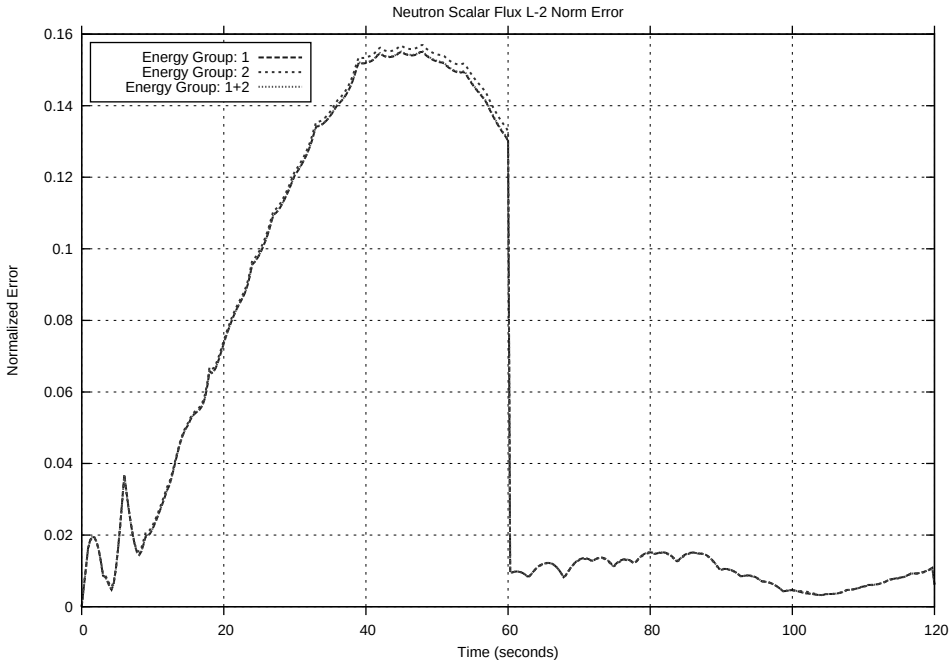

Figure 3.76: Flux L2-Error (One update, Trans 40)

Notice the drastic reduction in error for every error metric at 60.0 second (Figure 3.74 - Figure 3.76). These results agree nicely, because the locally normalized and average normalized maximum error values (Figure 3.74 and Figure 3.75) are roughly 3% at 60.0 second. Thus, every other error value must be smaller than this, resulting in a very small flux L2-Error ($< 1.5\%$) at 60.0 second (Figure 3.76). Comparing Figure 3.70 with Figure 3.76, the same explanation as noted for the other figures (Figure 3.68 compared with Figure 3.74 and Figure 3.69 compared with Figure 3.75) applies.

In addition, the behavior exhibited by the 2 second single update transient (Figure 3.71 - Figure 3.73)contrast the behavior displayed by the 120 second single update transient (Figure 3.74 - Figure 3.76). This suggest that the longer transients respond better to shape-factor updating than the shorter transients.

Appendix-C contains the flux error and error component values, locally and average normalized, (Figure C.25 - Figure C.32).

3.5.5 Active Switching - 2 Second Transient

The initial shape-factors for the 2 second active switching test case were generated by NESTLE from a quick insertion transient. This consisted of a initialization of the steady-state case, at time 0 seconds, and then a rod insertion from ARO to a single rod fully inserted over a period of 0.0020 seconds, having a time-step size of 0.0001 seconds, providing 20 data records. The PKE-Solver executed the 2 second transient with a time-step size of 0.01 seconds. The acceptable error limit was set at 25%; This value seemed to provide a nice trade-off between number of updates and precision for the 2 second transient. Eight shape-factor updates were performed for this case at times 0.15 second, 0.34 second, 0.55 second, 0.75 second, 0.95 second, 1.35 second, 1.65 second, and 1.95 second.

For the 0.15 second restart, the PKE-Solver was paused at 0.15 seconds, once the error had been determined to be in excess of the acceptable limit. NESTLE was then restarted with the projected flux and projected precursor group concentration values from two PKE-Solver time-steps prior to the current time, at the time 0.13 second. NESTLE used a time-step of 0.001 seconds until it reached the current transient time of 0.15 second. Then the code executed with a time-step of 0.0001 seconds until a single rod was fully inserted at time 0.1523 seconds, recording the shape-factor values at each time-step. The new shape-factor values replaced the old values and the PKE-Solver was restarted.

This process was then repeated at 0.34 second, 0.55 second, 0.75 second, 0.95 second, 1.35 second, 1.65 second, and 1.95 second.

The flux error at the maximum flux error position, locally and averaged normalized, can be viewed in Figure 3.77 - Figure 3.78. Also the L-2 flux error is displayed in Figure 3.79. As with the no switching scenario, the precursor group concentration error values are not presented because they have no bearing on this analysis due to the assumption explained in Section 3.2. Appendix-C contains the flux error and error component values, locally and average normalized (Figure C.33 - Figure C.40).

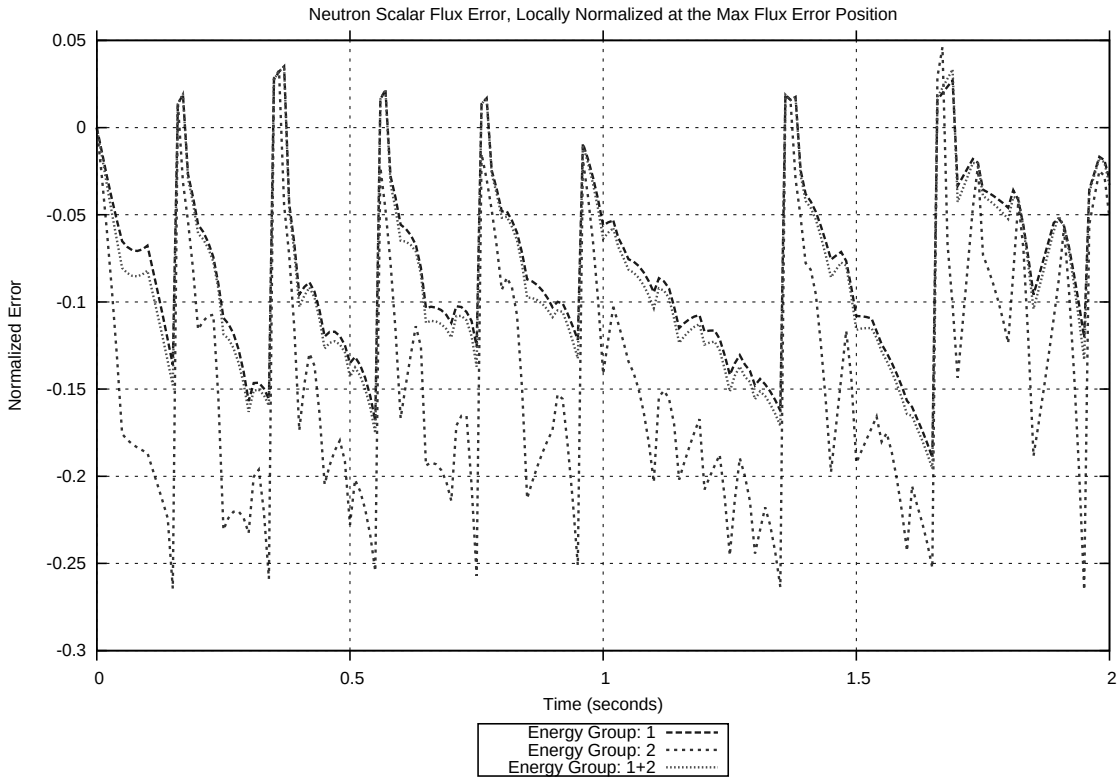

Figure 3.77: Locally Normalized Flux Error at the Maximum Flux Error Position (Active, Trans 40)

Note the drastic reduction in error for the flux locally normalized maximum error values at each shape-factor update, Figure 3.77. Comparing Figure 3.65 and Figure 3.71 with Figure 3.77, all of the cases behave identically until the first update at 0.15 second. At this point the flux locally normalized maximum error value is drastically reduced for the active switching 2 second transient. In addition, notice that the locally flux normalized maximum error value for the switching case Figure 3.77 is maintained at or below 25% error.

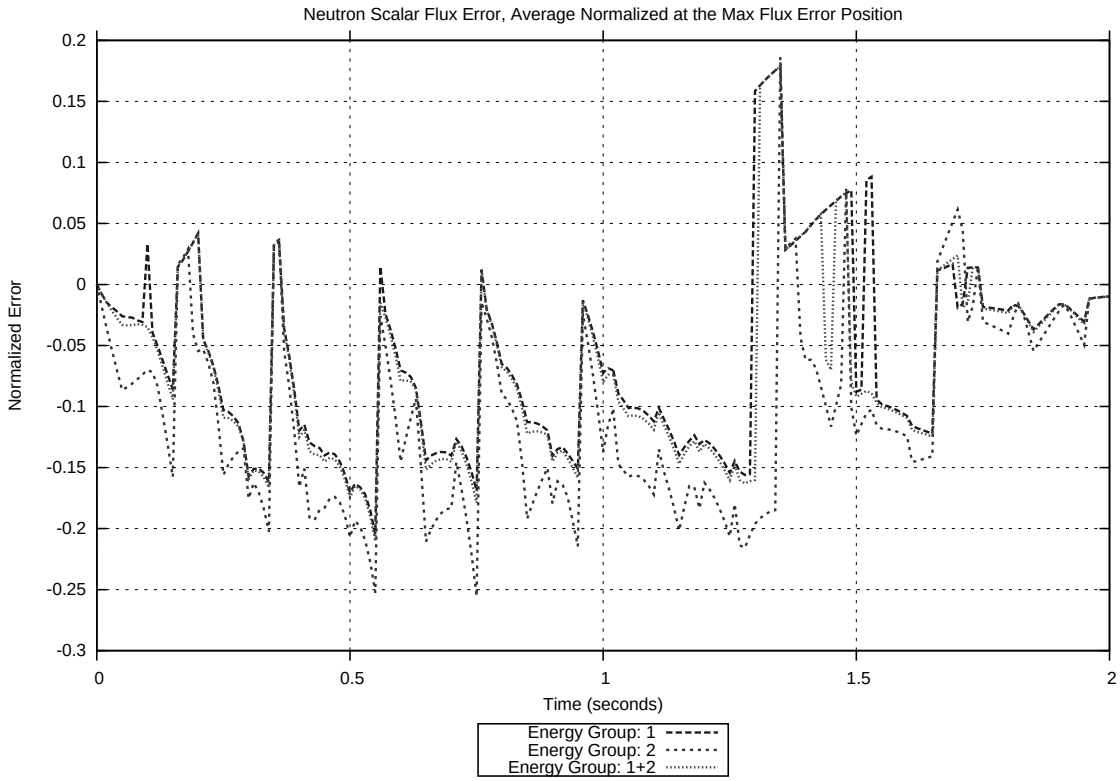

Figure 3.78: Average Normalized Flux Error at the Maximum Flux Error Position (Active, Trans 40)

Note the drastic reduction in error for the flux locally normalized maximum error values at each shape-factor update, Figure 3.78. Comparing Figure 3.66 and Figure 3.72 with Figure 3.78, the same explanation as used when comparing Figure 3.65 and Figure 3.71 with Figure 3.77 applies.

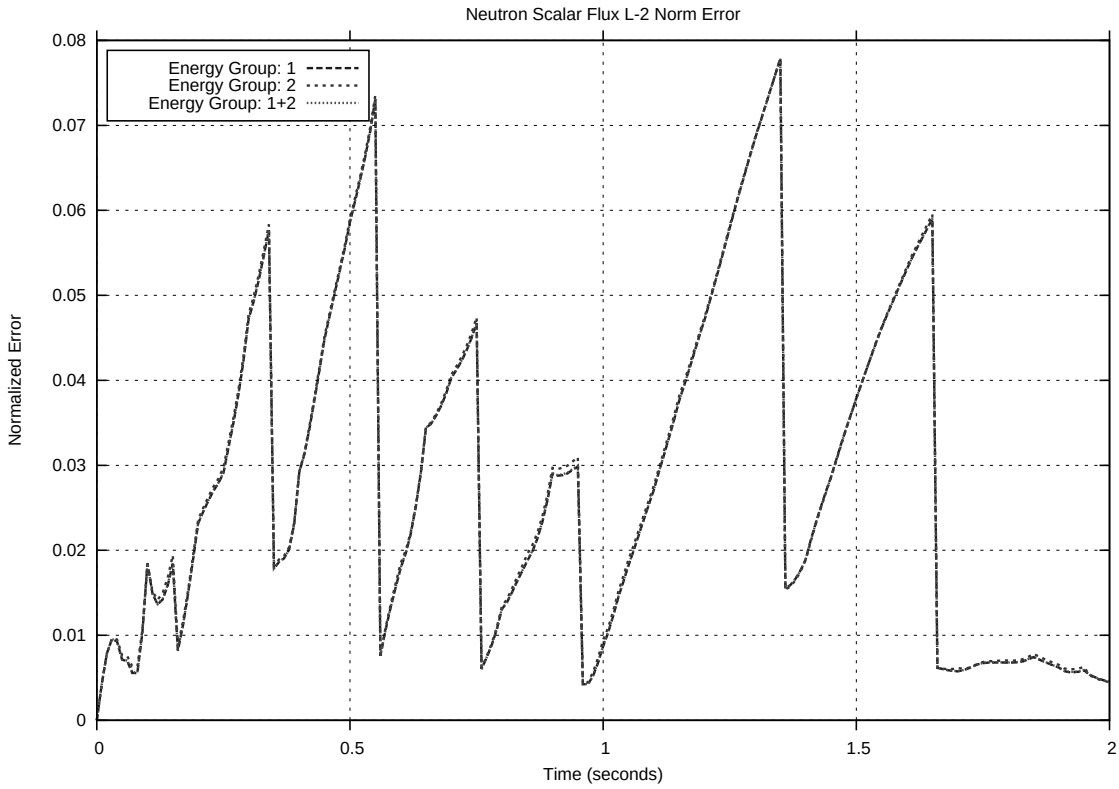

Figure 3.79: Flux L2-Error (Active, Trans 40)

Comparing Figure 3.67 and Figure 3.73 with Figure 3.79, all of the cases behave identically until the first update at 0.15 second. At this point the flux L2-Error is drastically reduced for the active switching 2 second transient. In addition, notice that the flux L2-Error for the switching case is maintained below 8.0%.

Notice the drastic reduction in error for every error metric at every shape-factor update (Figure 3.77 - Figure 3.79). These results agree nicely, because the locally normalized and average normalized maximum error values (Figure 3.77 and Figure 3.78) are maintained at or below 25% throughout the transient. Thus, every other error value must be smaller than this, resulting in a small flux L2-Error ($< 8.0\%$) (Figure 3.79). As well, observe the updating interval spacing in Figure 3.79. As the transient approaches 1.0 second, 6 updates were required to maintain the acceptable error limit; whereas, only 2 updates were required from 1.0 seconds to 2.0 seconds.

Appendix-C contains the flux error and error component values, locally and average normalized, (Figure C.33 - Figure C.40).

3.5.6 Active Switching - 120 Second Transient

The initial shape-factors for the 120 second active switching test case were generated by NESTLE from a quick insertion transient. This consisted of a initialization of the steady-state case, at time 0 seconds, and then a rod insertion from ARO to a single rod fully inserted over a period of 0.0020 seconds, having a time-step size of 0.0001 seconds, providing 20 data records. The PKE-Solver executed the 120 second transient with a time-step size of 0.30 seconds. The acceptable error limit was set at 10%; This value seemed to provide a nice trade-off between number of updates and precision for the 2 second transient. Four shape-factor updates were performed for this case at times 2.10 second, 6.00 second, 116.10 second, and 116.70 second.

For the 2.10 second restart, the PKE-Solver was paused at 2.10 seconds, once the error had been determined to be in excess of the acceptable limit. NESTLE was then restarted with the projected flux and projected precursor group concentration values from two PKE-Solver time-steps prior to the current time, at the time 1.50 second. NESTLE used a time-step size of 0.01 seconds until it reached the current transient time of 2.10 second. Then the code executed with a time-step of 0.01 seconds until a single rod was fully inserted at time 2.34 seconds, outputting the shape-factor values at each time-step. The new shape-factor values replaced the old values and the PKE-Solver was restarted.

This process was repeated at 6.00 second, 116.10 second, and 116.70 second.

The flux error at the maximum flux error position, locally and averaged normalized, can be viewed in Figure 3.80 - Figure 3.81. Also the L-2 flux error is displayed in Figure 3.82. As with the no switching scenario, the precursor group concentration error values are not presented because they have no bearing on this analysis due to the assumption explained in Section 3.2. Appendix-C contains the flux error and error component values, locally and average normalized (Figure C.41 - Figure C.48).

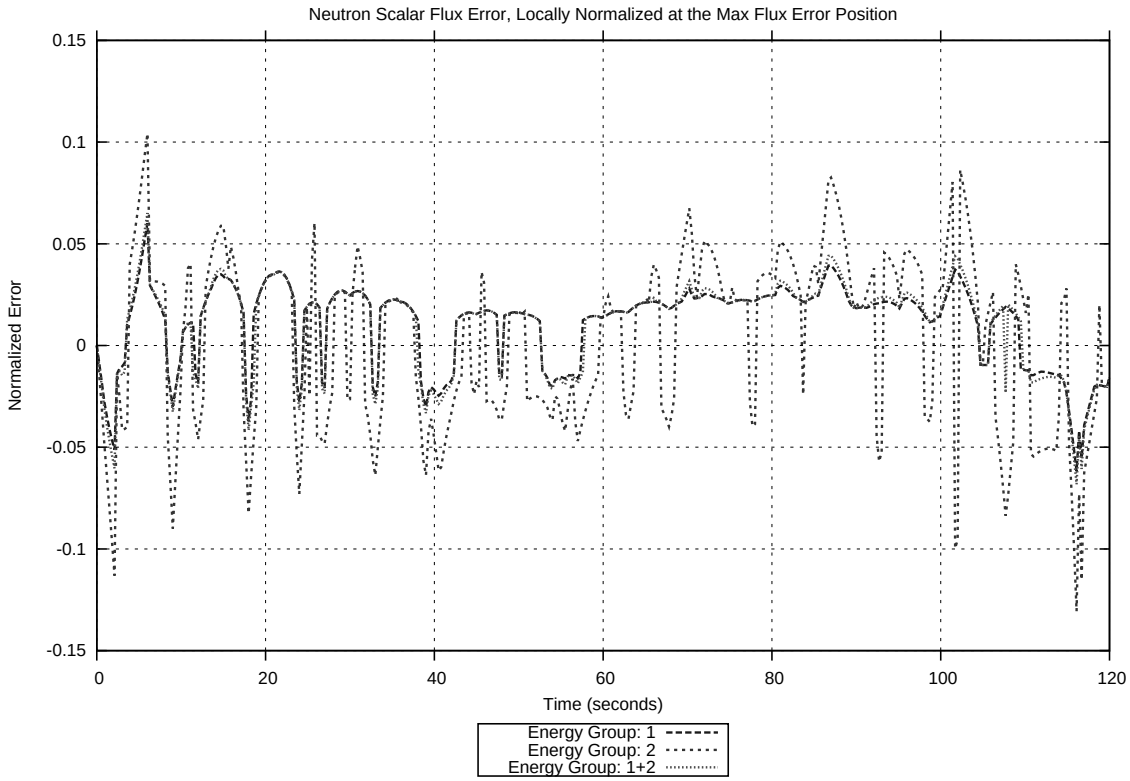

Figure 3.80: Locally Normalized Flux Error at the Maximum Flux Error Position (Active, Trans 40)

Note the reduction in error for the flux locally normalized maximum error values at each shape-factor update, Figure 3.80. Comparing Figure 3.68 and Figure 3.74 with Figure 3.80, all of the cases behave identically until the first update at 2.34 seconds. At this point the flux locally normalized maximum error value is reduced for the active switching 120 second transient. In addition, notice that the locally flux normalized maximum error value for the switching case Figure 3.80 is maintained at or below 10% error.

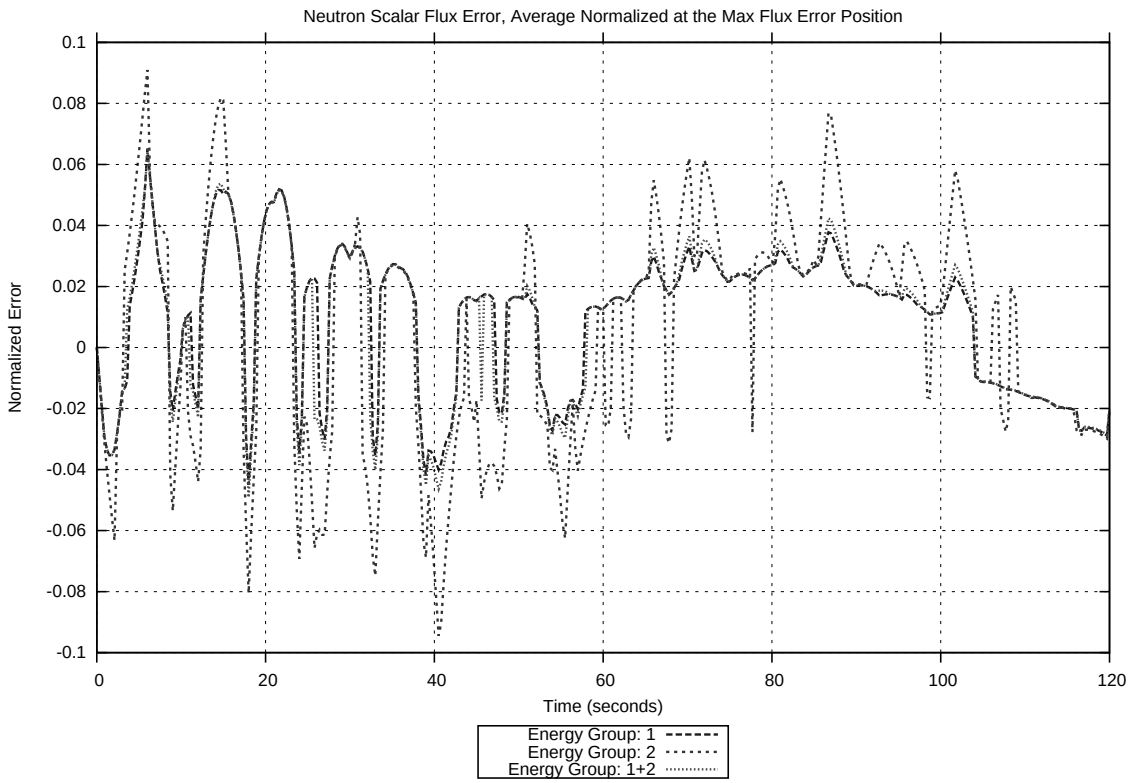

Figure 3.81: Average Normalized Flux Error at the Maximum Flux Error Position (Active, Trans 40)

Note the reduction in error for the flux locally normalized maximum error values at each shape-factor update, Figure 3.78. Comparing Figure 3.69 and Figure 3.75 with Figure 3.81, the same explanation made for comparing Figure 3.68 and Figure 3.74 with Figure 3.80 applies.

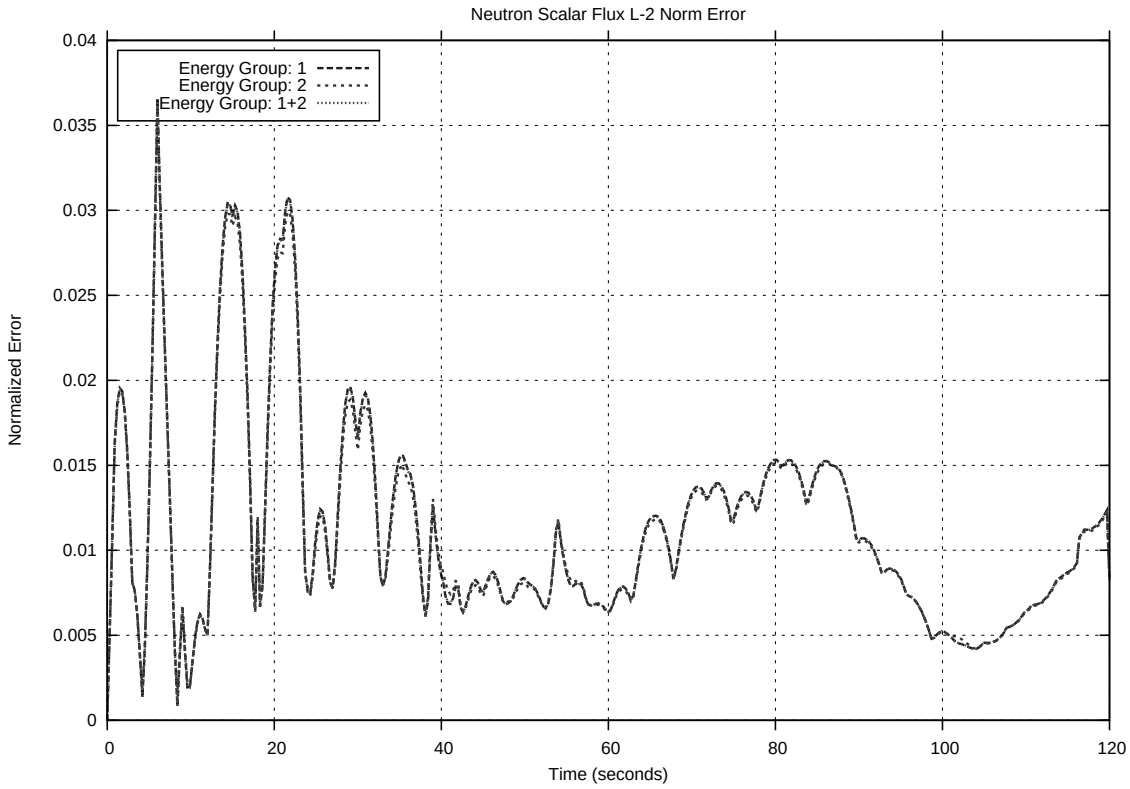

Figure 3.82: Flux L2-Error (Active, Trans 40)

Comparing Figure 3.70 and Figure 3.76 with Figure 3.82, all of the cases behave identically until the first update at 2.34 second. At this point the flux L2-Error is reduced for the active switching 120 second transient. In addition, notice that the flux L2-Error for the switching case is maintained below 4.0%.

Notice the reduction in error for every error metric at every shape-factor update (Figure 3.80 - Figure 3.82). These results agree nicely, because the locally normalized and average normalized maximum error values (Figure 3.80 and Figure 3.81) are maintained at or below 10% throughout the transient. Thus, every other error value must be smaller than this, resulting in a small flux L2-Error ($< 4.0\%$) (Figure 3.82).

In addition, the behavior exhibited by the 2 second active transient (Figure 3.77 - Figure 3.79) contrast the behavior displayed by the 120 second single update transient (Figure 3.80 - Figure 3.82). Also, recall that the 2 second transient required 8 shape-factor updates, given a PKE-Solver time-step size of 0.01 seconds, and the 120 second transient only required 4 shape-factor updates, given a PKE-Solver time-step size of 0.30 seconds. This suggest that the longer transients respond better to shape-factor updating than the shorter transients. Also, take note

that 2 updates were required within the first 6.0 seconds of the transient to maintain the acceptable error limit, after which no updates were required until 116.10 seconds. In addition, another update was needed relatively quickly at 116.70 seconds. This suggest that while the 120 second transient behaves more predictably over the majority of the transient duration, maintaining the acceptable error limit is problematic at the beginning and end of the transient.

Appendix-C contains the flux error and error component values, locally and average normalized, (Figure C.41 - Figure C.48).

Chapter 4

Conclusions and Recommendations

Designing a nuclear reactor is a complex and lengthy process made up of various technical trade-offs. Choices made during this stage result in long term economic effects, both good and bad. The constant pressure placed on designers to reduce the finical burden involved with the design process is the motivating force behind improving the reactor simulation time/accuracy ratio. The application of AMoR methods to reactor core design has the potential to help engineers increase their simulation capabilities while reducing their overhead, thus making the process more efficient. In addition, this development will help enhance researcher's abilities to explore the problem space, aiding in achieving the best possible solution. Also, investigating the capabilities of this technique may lend insight into the applicability of similar AMoR approaches to other aspects of reactor design, such as thermal-hydraulics.

Evaluating the 2 second and 120 second transients with the steady-state library AMoR approach resulted in a maximum of the locally normalized flux error values at the maximum flux position of roughly 10% and 5 - 7%, respectively, and a maximum of the locally normalized flux error values at the maximum flux error position of approximately 27 - 30% and 12 - 30%, respectively. The simulations also resulted in a maximum of the locally normalized precursor group concentration error values at the maximum precursor group concentration position of 10% for the 2 second transient and 10% for the 120 second transient, and a maximum of the locally normalized precursor group concentration error values at the maximum precursor group concentration error position around 65% for the 2 second transient and 60% for the 120 second transient.

To provide a baseline error, the active model switching AMoR approach was used with no model switching. The 2 second and 120 second transients investigated behaved similarly, yielding a maximum of the, locally normalized and average normalized, flux error at the maximum flux error position of 50 - 80% and 20 - 40%, respectively.

In addition, the 2 second and 120 second transients were evaluated with the same active

model switching approach but instead allowed a single update. This test scenario yielded a locally normalized flux error at the maximum flux error position of 60 - 100% for the 2 second transient and 30 - 40% for the 120 second transient. Also, the maximum of the average normalized flux error at the maximum flux error position was roughly 30 - 40% for both transients. Immediately following the update each transient experienced a reduction in error from roughly 25% to 5% for both the locally and averaged normalized flux error calculations. The 2 second transient experienced a reduction in the flux L2 error from roughly 13% to 0.5%, which later returned to roughly 13%, near the end of the transient. The 120 second transient experienced a reduction in the flux L2 error from approximately 13% to 1.0%, which remained below 2.0% until the end of the transient.

Evaluating the 2 second and 120 second transients with the active model switching AMoR approach using multiple updates, maintained the maximum, locally normalized and averaged normalized, flux error at the maximum flux error position below 25% and 10%, respectively. The 2 second transient flux L2 error maximum was approximately 8% and the 120 second transient flux L2 error maximum was roughly 4%.The 2 second transient required 8 updates and the 120 second transient required only 4 updates. In addition, all of the error metrics experienced significant reductions in error after each update.

In general, the application of the AMoR method proved capable of producing 3-D projected models from a combination of amplitude-shape factors. The efficacy of the active switching approach was demonstrated for prompt neutron calculations, though the ability of this approach to reduce the simulation time/accuracy ratio is still untested.

4.1 Future Work

As with most simulation techniques this early in development, there remains a wide variety of applications, methods, and variations of the AMoR technique still to be investigated. Specific to neutron transport simulations, many different variations of the approaches outlined in this research are waiting to be evaluated, three of which are on the immediate horizon; the hybrid precursor model (to be explained), the utilization of the adjoint method to perform model fidelity analysis during simulation with time, and the integration of the AMoR approaches outlined in this research with the Quasi-Static method.

Considering the active model switching AMoR approach utilized in this research, there is a definite need to extend this approach to also calculate the precursor group concentration values. It was realized during this work, that the precursor values with this approach were highly unreliable and were thus limited to not interfere with the prompt neutron calculations testing. A solution to this problem has already been conceptualized regarding a hybrid precursor model. This would involve using the 3-D precursor equations in NESTLE to calculate the time-spatial

precursor values within the PKE-Solver using the 3-D projected flux. This solution has merit because the precursor calculations are not computationally demanding.

All of the testing performed in this research used the NESTLE calculated solution to determine the projected model's fidelity. If the AMoR method is to be employed, the NESTLE calculated solution will be unknown. Instead another method for determining the model's fidelity is needed. A solution to this issue has already been conceptualized and is under development. The solution entails utilizing the adjoint method to evaluate the fidelity of the projected model. This approach would not involve the NESTLE calculated solution, only the adjoint solution.

Finally, the AMoR technique can potentially be integrated with the Quasi-Static method to yield a simulation which uses a more mathematically rigorous formulation of the amplitude and shape factor equations to solve the diffusion or transport neutron equation. This has the potential to enhance the lower and higher fidelity models' fidelity.

In addition to extending the approaches outlined in this research, there is reason to further investigate the steady-state library approach. From the steady-state library test cases evaluated for this work, it is apparent that the number of steady-state data points and the number of transient solution data points are extremely relevant to the behavior of some error values. The impact of the data library and transient solution data records, both in terms of absolute number of data points and frequency of data points relative to one another, needs to be evaluated further if this method is to be utilized heavily.

REFERENCES

[1] Electric Power Research Center. *NESTLE version 5.2.1.* NCSU, 2003.

[2] J.J. Duderstadt and L.J. Hamilton. *Nuclear reactor analysis.* Wiley, 1976.

[3] S. Dulla. *Models and methods in the neutronics of fluid fuel reactors.* PhD thesis, Politecnico di Torino, 2005.

[4] S. Dulla, E. Mund, and P. Ravetto. Accuracy of a predictor-corrector quasi-static method for space-time reactor dynamics. *Advances in Nuclear Analysis and Simulation PHYSOR*, pages 1630–1639, 2006.

[5] S. Dulla, E. Mund, and P. Ravetto. The quasi-static method revisited. *Progress in Nuclear Energy*, 50(8):908 – 920, 2008.

[6] J. Gehin. *A quasi-static polynomial nodal method for nuclear reactor analysis.* PhD thesis, Massachusetts Institute of Technology, 1992.

[7] A. Henry. Application of reactor kinetics to the analysis of experiments. *Nuclear Science and Engineering*, 3:52–70, 1958.

[8] A. Henry and N. Curlee. Verification of a method for treating neutron space-time problems. *Nuclear Science and Engineering*, 4(6):727–744, 1958.

[9] S. Kaplan, O. Marlowe, and J. Bewick. Application of synthesis thecniques to problems involving time dependence. *Nuclear Science and Engineering*, 18(2):163–176, 1964.

[10] K. Ott. Quasistatic treatment of spatial phenomena in reactor dynamics. *Nuclear Science and Engineering*, 26(4):563–565, 1966.

[11] K. Ott and D. Meneley. Accuracy of the quasistatic treatment of spatial reactor kinetics. *Nuclear Science and Engineering*, 36(3):402–411, 1969.

[12] J. Yasinsky and A. Henry. Numerical experiments concerning space-time reactor kinetics behavior. *Nuclear Science and Engineering*, 22:171–181, 1965.

APPENDICES

Appendix A

Test Cases General Behavior (Continued)

A.1 2 Second Transient

The axial and radial power distributions have been supplied for the 2 second transient case printing data over 10 rod intervals.

Table A.1: Radial Relative Power Distribution, 2 Second Transient, Rod Position: 141.25 inches - All Rods Out

Y/X	1	2	3	4	5	6	7	8
1	0.8636	1.1431	0.9905	1.2570	1.2514	1.3239	1.0740	0.7320
2	1.1442	1.1009	1.1697	1.1844	1.2782	1.2659	1.2123	0.4723
3	1.0128	1.1745	0.8908	1.1839	1.2438	1.2977	0.9951	0.3733
4	1.2586	1.1875	1.1862	1.2122	1.2969	1.2325	1.0950	0.2865
5	1.2530	1.2792	1.2446	1.2967	1.2186	1.2328	0.5955	
6	1.3239	1.2653	1.2974	1.2320	1.2327	0.5361	0.2243	
7	1.0740	1.2118	0.9945	1.0947	0.5957	0.2247		
8	0.7320	0.4723	0.3731	0.2864				

Table A.2: Radial Relative Power Distribution, 2 Second Transient, Rod Position: 127.12 inches

Y/X	1	2	3	4	5	6	7	8
1	0.8645	1.1448	0.9883	1.2453	1.2081	1.3132	1.0729	0.7335
2	1.1459	1.1018	1.1692	1.1782	1.2679	1.2610	1.2134	0.4731
3	1.0106	1.1741	0.8905	1.1850	1.2444	1.3008	0.9984	0.3745
4	1.2470	1.1813	1.1872	1.2161	1.3031	1.2392	1.1016	0.2880
5	1.2097	1.2690	1.2452	1.3030	1.2260	1.2416	0.5996	
6	1.3132	1.2604	1.3006	1.2387	1.2415	0.5398	0.2259	
7	1.0728	1.2129	0.9978	1.1013	0.5998	0.2262		
8	0.7334	0.4730	0.3743	0.2879				

Table A.3: Radial Relative Power Distribution, 2 Second Transient, Rod Position: 113.00 inches

Y/X	1	2	3	4	5	6	7	8
1	0.8656	1.1471	0.9833	1.2220	1.1349	1.2915	1.0693	0.7353
2	1.1482	1.1022	1.1671	1.1647	1.2476	1.2503	1.2142	0.4742
3	1.0056	1.1719	0.8895	1.1862	1.2450	1.3067	1.0047	0.3769
4	1.2236	1.1678	1.1885	1.2234	1.3160	1.2530	1.1154	0.2910
5	1.1366	1.2487	1.2458	1.3158	1.2417	1.2603	0.6083	
6	1.2916	1.2497	1.3064	1.2525	1.2603	0.5479	0.2293	
7	1.0692	1.2138	1.0041	1.1151	0.6085	0.2297		
8	0.7353	0.4741	0.3767	0.2909				

Table A.4: Radial Relative Power Distribution, 2 Second Transient, Rod Position: 98.88 inches

Y/X	1	2	3	4	5	6	7	8
1	0.8673	1.1494	0.9783	1.1958	1.0550	1.2667	1.0648	0.7367
2	1.1505	1.1028	1.1643	1.1501	1.2247	1.2384	1.2143	0.4753
3	1.0005	1.1692	0.8887	1.1873	1.2459	1.3128	1.0117	0.3796
4	1.1974	1.1532	1.1896	1.2318	1.3303	1.2685	1.1307	0.2946
5	1.0566	1.2258	1.2467	1.3302	1.2596	1.2815	0.6182	
6	1.2668	1.2377	1.3125	1.2680	1.2814	0.5573	0.2333	
7	1.0648	1.2138	1.0110	1.1303	0.6184	0.2337		
8	0.7367	0.4753	0.3794	0.2945				

Table A.5: Radial Relative Power Distribution, 2 Second Transient, Rod Position: 84.75 inches

Y/X	1	2	3	4	5	6	7	8
1	0.8703	1.1522	0.9737	1.1665	0.9654	1.2385	1.0600	0.7378
2	1.1533	1.1041	1.1614	1.1349	1.1989	1.2254	1.2138	0.4768
3	0.9958	1.1663	0.8889	1.1886	1.2473	1.3190	1.0193	0.3829
4	1.1680	1.1379	1.1909	1.2415	1.3459	1.2855	1.1470	0.2986
5	0.9669	1.1999	1.2480	1.3457	1.2795	1.3044	0.6292	
6	1.2385	1.2247	1.3187	1.2850	1.3043	0.5680	0.2378	
7	1.0599	1.2133	1.0186	1.1466	0.6293	0.2382		
8	0.7378	0.4768	0.3827	0.2985				

Table A.6: Radial Relative Power Distribution, 2 Second Transient, Rod Position: 70.63 inches

Y/X	1	2	3	4	5	6	7	8
1	0.8742	1.1550	0.9700	1.1384	0.8799	1.2110	1.0555	0.7386
2	1.1561	1.1060	1.1588	1.1211	1.1739	1.2133	1.2129	0.4784
3	0.9920	1.1637	0.8896	1.1898	1.2489	1.3245	1.0265	0.3862
4	1.1400	1.1241	1.1921	1.2510	1.3603	1.3016	1.1621	0.3026
5	0.8813	1.1749	1.2497	1.3601	1.2985	1.3257	0.6396	
6	1.2110	1.2126	1.3242	1.3010	1.3256	0.5783	0.2422	
7	1.0554	1.2124	1.0258	1.1617	0.6398	0.2426		
8	0.7386	0.4783	0.3859	0.3025				

Table A.7: Radial Relative Power Distribution, 2 Second Transient, Rod Position: 56.50 inches

Y/X	1	2	3	4	5	6	7	8
1	0.8783	1.1577	0.9668	1.1121	0.8000	1.1851	1.0516	0.7393
2	1.1588	1.1082	1.1564	1.1087	1.1504	1.2022	1.2119	0.4799
3	0.9887	1.1613	0.8907	1.1907	1.2507	1.3294	1.0332	0.3893
4	1.1137	1.1117	1.1930	1.2600	1.3734	1.3164	1.1759	0.3063
5	0.8012	1.1514	1.2515	1.3732	1.3164	1.3453	0.6493	
6	1.1851	1.2016	1.3290	1.3159	1.3452	0.5880	0.2463	
7	1.0515	1.2114	1.0325	1.1755	0.6495	0.2467		
8	0.7393	0.4799	0.3890	0.3062				

Table A.8: Radial Relative Power Distribution, 2 Second Transient, Rod Position: 42.38 inches

Y/X	1	2	3	4	5	6	7	8
1	0.8820	1.1600	0.9639	1.0887	0.7292	1.1619	1.0482	0.7401
2	1.1611	1.1103	1.1541	1.0980	1.1293	1.1926	1.2111	0.4814
3	0.9857	1.1590	0.8916	1.1914	1.2525	1.3335	1.0392	0.3921
4	1.0902	1.1010	1.1937	1.2681	1.3849	1.3296	1.1881	0.3097
5	0.7302	1.1303	1.2532	1.3846	1.3323	1.3626	0.6580	
6	1.1619	1.1919	1.3331	1.3290	1.3626	0.5966	0.2500	
7	1.0481	1.2106	1.0385	1.1877	0.6582	0.2504		
8	0.7400	0.4813	0.3919	0.3096				

Table A.9: Radial Relative Power Distribution, 2 Second Transient, Rod Position: 28.25 inches

Y/X	1	2	3	4	5	6	7	8
1	0.8847	1.1615	0.9615	1.0707	0.6757	1.1443	1.0459	0.7408
2	1.1626	1.1118	1.1522	1.0899	1.1132	1.1854	1.2106	0.4825
3	0.9833	1.1570	0.8922	1.1917	1.2538	1.3365	1.0439	0.3943
4	1.0722	1.0929	1.1940	1.2743	1.3934	1.3396	1.1975	0.3123
5	0.6767	1.1141	1.2546	1.3932	1.3444	1.3759	0.6647	
6	1.1443	1.1847	1.3361	1.3390	1.3758	0.6032	0.2528	
7	1.0458	1.2101	1.0432	1.1971	0.6649	0.2533		
8	0.7408	0.4825	0.3940	0.3122				

Table A.10: Radial Relative Power Distribution, 2 Second Transient, Rod Position: 14.13 inches

Y/X	1	2	3	4	5	6	7	8
1	0.8863	1.1624	0.9595	1.0576	0.6375	1.1317	1.0445	0.7416
2	1.1635	1.1127	1.1506	1.0841	1.1014	1.1804	1.2106	0.4834
3	0.9812	1.1555	0.8924	1.1918	1.2548	1.3387	1.0473	0.3959
4	1.0591	1.0871	1.1941	1.2786	1.3995	1.3468	1.2044	0.3141
5	0.6383	1.1023	1.2555	1.3992	1.3531	1.3854	0.6695	
6	1.1317	1.1797	1.3383	1.3463	1.3854	0.6079	0.2548	
7	1.0444	1.2101	1.0466	1.2040	0.6697	0.2553		
8	0.7416	0.4834	0.3956	0.3140				

Table A.11: Radial Relative Power Distribution, 2 Second Transient, Rod Position: 0.00 inches

Y/X	1	2	3	4	5	6	7	8
1	0.8869	1.1626	0.9585	1.0516	0.6194	1.1260	1.0441	0.7422
2	1.1637	1.1131	1.1499	1.0815	1.0959	1.1783	1.2108	0.4839
3	0.9802	1.1548	0.8924	1.1918	1.2553	1.3398	1.0490	0.3966
4	1.0531	1.0846	1.1941	1.2805	1.4022	1.3501	1.2076	0.3149
5	0.6202	1.0968	1.2560	1.4019	1.3570	1.3897	0.6717	
6	1.1260	1.1776	1.3394	1.3495	1.3896	0.6099	0.2557	
7	1.0440	1.2103	1.0483	1.2072	0.6718	0.2562		
8	0.7422	0.4839	0.3964	0.3148				

Table A.12: Axial Relative Power Distribution, 2 Second Transient, Rod Position: 141.25 inches - All Rods Out

Z(in.)	Value	Z(in.)	Value	Z(in.)	Value	Z(in.)	Value	Z(in.)	Value
3.00	0.1365	8.76	0.3126	11.76	0.3624	15.00	0.4079	21.00	0.4944
27.00	0.5787	33.00	0.6653	39.00	0.7559	45.00	0.8511	51.00	0.9501
57.00	1.0512	63.00	1.1523	69.00	1.2506	75.00	1.3428	81.00	1.4250
87.00	1.4930	93.00	1.5421	99.00	1.5676	105.00	1.5634	111.00	1.5227
117.00	1.4370	123.00	1.2952	129.00	1.0795	134.76	0.7902	137.76	0.6559
141.00	0.3424								

Table A.13: Axial Relative Power Distribution, 2 Second Transient, Rod Position: 127.12 inches

Z(in.)	Value	Z(in.)	Value	Z(in.)	Value	Z(in.)	Value	Z(in.)	Value
3.00	0.1402	8.76	0.3211	11.76	0.3722	15.00	0.4187	21.00	0.5073
27.00	0.5935	33.00	0.6818	39.00	0.7741	45.00	0.8706	51.00	0.9707
57.00	1.0725	63.00	1.1736	69.00	1.2712	75.00	1.3619	81.00	1.4414
87.00	1.5053	93.00	1.5491	99.00	1.5674	105.00	1.5544	111.00	1.5033
117.00	1.4056	123.00	1.2509	129.00	1.0230	134.76	0.7346	137.76	0.6049
141.00	0.3147								

Table A.14: Axial Relative Power Distribution, 2 Second Transient, Rod Position: 113.00 inches

Z(in.)	Value	Z(in.)	Value	Z(in.)	Value	Z(in.)	Value	Z(in.)	Value
3.00	0.1499	8.76	0.3432	11.76	0.3977	15.00	0.4471	21.00	0.5410
27.00	0.6317	33.00	0.7240	39.00	0.8196	45.00	0.9187	51.00	1.0204
57.00	1.1225	63.00	1.2222	69.00	1.3161	75.00	1.4005	81.00	1.4707
87.00	1.5218	93.00	1.5488	99.00	1.5464	105.00	1.5084	111.00	1.4284
117.00	1.2998	123.00	1.1371	129.00	0.9284	134.76	0.6707	137.76	0.5532
141.00	0.2882								

Table A.15: Axial Relative Power Distribution, 2 Second Transient, Rod Position: 98.88 inches

Z(in.)	Value	Z(in.)	Value	Z(in.)	Value	Z(in.)	Value	Z(in.)	Value
3.00	0.1613	8.76	0.3691	11.76	0.4276	15.00	0.4804	21.00	0.5801
27.00	0.6756	33.00	0.7718	39.00	0.8704	45.00	0.9712	51.00	1.0730
57.00	1.1730	63.00	1.2681	69.00	1.3543	75.00	1.4272	81.00	1.4816
87.00	1.5122	93.00	1.5137	99.00	1.4803	105.00	1.4099	111.00	1.3264
117.00	1.2196	123.00	1.0784	129.00	0.8868	134.76	0.6434	137.76	0.5316
141.00	0.2771								

Table A.16: Axial Relative Power Distribution, 2 Second Transient, Rod Position: 84.75 inches

Z(in.)	Value	Z(in.)	Value	Z(in.)	Value	Z(in.)	Value	Z(in.)	Value
3.00	0.1723	8.76	0.3939	11.76	0.4560	15.00	0.5117	21.00	0.6163
27.00	0.7154	33.00	0.8137	39.00	0.9128	45.00	1.0123	51.00	1.1102
57.00	1.2035	63.00	1.2881	69.00	1.3597	75.00	1.4132	81.00	1.4429
87.00	1.4437	93.00	1.4267	99.00	1.4019	105.00	1.3620	111.00	1.3002
117.00	1.2084	123.00	1.0770	129.00	0.8905	134.76	0.6483	137.76	0.5363
141.00	0.2797								

Table A.17: Axial Relative Power Distribution, 2 Second Transient, Rod Position: 70.63 inches

Z(in.)	Value	Z(in.)	Value	Z(in.)	Value	Z(in.)	Value	Z(in.)	Value
3.00	0.1793	8.76	0.4095	11.76	0.4737	15.00	0.5310	21.00	0.6377
27.00	0.7373	33.00	0.8344	39.00	0.9303	45.00	1.0241	51.00	1.1135
57.00	1.1947	63.00	1.2635	69.00	1.3145	75.00	1.3436	81.00	1.3692
87.00	1.3908	93.00	1.4025	99.00	1.3992	105.00	1.3752	111.00	1.3243
117.00	1.2390	123.00	1.1094	129.00	0.9203	134.76	0.6714	137.76	0.5559
141.00	0.2900								

Table A.18: Axial Relative Power Distribution, 2 Second Transient, Rod Position: 56.50 inches

Z(in.)	Value	Z(in.)	Value	Z(in.)	Value	Z(in.)	Value	Z(in.)	Value
3.00	0.1811	8.76	0.4133	11.76	0.4776	15.00	0.5346	21.00	0.6398
27.00	0.7361	33.00	0.8280	39.00	0.9162	45.00	0.9994	51.00	1.0749
57.00	1.1384	63.00	1.1899	69.00	1.2465	75.00	1.3029	81.00	1.3542
87.00	1.3960	93.00	1.4237	99.00	1.4325	105.00	1.4171	111.00	1.3714
117.00	1.2876	123.00	1.1560	129.00	0.9607	134.76	0.7017	137.76	0.5811
141.00	0.3033								

Table A.19: Axial Relative Power Distribution, 2 Second Transient, Rod Position: 42.38 inches

Z(in.)	Value	Z(in.)	Value	Z(in.)	Value	Z(in.)	Value	Z(in.)	Value
3.00	0.1766	8.76	0.4024	11.76	0.4647	15.00	0.5191	21.00	0.6185
27.00	0.7073	33.00	0.7895	39.00	0.8651	45.00	0.9330	51.00	1.0016
57.00	1.0769	63.00	1.1552	69.00	1.2330	75.00	1.3067	81.00	1.3723
87.00	1.4257	93.00	1.4625	99.00	1.4781	105.00	1.4671	111.00	1.4233
117.00	1.3389	123.00	1.2036	129.00	1.0012	134.76	0.7317	137.76	0.6061
141.00	0.3164								

Table A.20: Axial Relative Power Distribution, 2 Second Transient, Rod Position: 28.25 inches

Z(in.)	Value	Z(in.)	Value	Z(in.)	Value	Z(in.)	Value	Z(in.)	Value
3.00	0.1667	8.76	0.3794	11.76	0.4376	15.00	0.4879	21.00	0.5785
27.00	0.6569	33.00	0.7270	39.00	0.8024	45.00	0.8845	51.00	0.9717
57.00	1.0619	63.00	1.1527	69.00	1.2410	75.00	1.3236	81.00	1.3967
87.00	1.4562	93.00	1.4978	99.00	1.5169	105.00	1.5078	111.00	1.4646
117.00	1.3788	123.00	1.2403	129.00	1.0322	134.76	0.7545	137.76	0.6251
141.00	0.3263								

Table A.21: Axial Relative Power Distribution, 2 Second Transient, Rod Position: 14.13 inches

Z(in.)	Value	Z(in.)	Value	Z(in.)	Value	Z(in.)	Value	Z(in.)	Value
3.00	0.1525	8.76	0.3465	11.76	0.3993	15.00	0.4441	21.00	0.5265
27.00	0.6072	33.00	0.6905	39.00	0.7779	45.00	0.8697	51.00	0.9651
57.00	1.0622	63.00	1.1589	69.00	1.2523	75.00	1.3394	81.00	1.4162
87.00	1.4788	93.00	1.5228	99.00	1.5436	105.00	1.5355	111.00	1.4922
117.00	1.4054	123.00	1.2646	129.00	1.0526	134.76	0.7695	137.76	0.6376
141.00	0.3328								

Table A.22: Axial Relative Power Distribution, 2 Second Transient, Rod Position: 0.00 inches

Z(in.)	Value	Z(in.)	Value	Z(in.)	Value	Z(in.)	Value	Z(in.)	Value
3.00	0.1403	8.76	0.3209	11.76	0.3721	15.00	0.4188	21.00	0.5073
27.00	0.5930	33.00	0.6804	39.00	0.7712	45.00	0.8660	51.00	0.9639
57.00	1.0633	63.00	1.1621	69.00	1.2574	75.00	1.3461	81.00	1.4244
87.00	1.4883	93.00	1.5333	99.00	1.5549	105.00	1.5472	111.00	1.5039
117.00	1.4167	123.00	1.2749	129.00	1.0613	134.76	0.7760	137.76	0.6429
141.00	0.3356								

A.2 120 Second Transient

The axial and radial power distributions have been supplied for the 120 second transient case printing data over 10 rod intervals.

Table A.23: Radial Relative Power Distribution, 120 Second Transient, Rod Position: 141.25 inches - All Rods Out

Y/X	1	2	3	4	5	6	7	8
1	0.8636	1.1431	0.9905	1.2570	1.2514	1.3239	1.0740	0.7320
2	1.1442	1.1009	1.1697	1.1844	1.2782	1.2659	1.2123	0.4723
3	1.0128	1.1745	0.8908	1.1839	1.2438	1.2977	0.9951	0.3733
4	1.2586	1.1875	1.1862	1.2122	1.2969	1.2325	1.0950	0.2865
5	1.2530	1.2792	1.2446	1.2967	1.2186	1.2328	0.5955	
6	1.3239	1.2653	1.2974	1.2320	1.2327	0.5361	0.2243	
7	1.0740	1.2118	0.9945	1.0947	0.5957	0.2247		
8	0.7320	0.4723	0.3731	0.2864				

Table A.24: Radial Relative Power Distribution, 120 Second Transient, Rod Position: 127.12 inches

Y/X	1	2	3	4	5	6	7	8
1	0.8642	1.1445	0.9880	1.2451	1.2079	1.3131	1.0728	0.7335
2	1.1456	1.1014	1.1690	1.1778	1.2678	1.2608	1.2134	0.4730
3	1.0103	1.1739	0.8903	1.1849	1.2444	1.3010	0.9985	0.3745
4	1.2467	1.1809	1.1872	1.2161	1.3034	1.2394	1.1020	0.2880
5	1.2096	1.2688	1.2451	1.3032	1.2263	1.2420	0.5998	
6	1.3131	1.2602	1.3007	1.2390	1.2420	0.5400	0.2259	
7	1.0727	1.2130	0.9979	1.1016	0.5999	0.2263		
8	0.7335	0.4730	0.3743	0.2879				

Table A.25: Radial Relative Power Distribution, 120 Second Transient, Rod Position: 113.00 inches

Y/X	1	2	3	4	5	6	7	8
1	0.8640	1.1460	0.9820	1.2215	1.1366	1.2917	1.0689	0.7353
2	1.1471	1.1008	1.1662	1.1636	1.2476	1.2499	1.2143	0.4739
3	1.0043	1.1710	0.8884	1.1860	1.2447	1.3072	1.0049	0.3768
4	1.2231	1.1667	1.1883	1.2233	1.3168	1.2537	1.1164	0.2911
5	1.1383	1.2487	1.2455	1.3166	1.2423	1.2616	0.6087	
6	1.2917	1.2493	1.3069	1.2532	1.2616	0.5482	0.2294	
7	1.0688	1.2139	1.0043	1.1160	0.6089	0.2298		
8	0.7353	0.4739	0.3766	0.2910				

Table A.26: Radial Relative Power Distribution, 120 Second Transient, Rod Position: 98.87 inches

Y/X	1	2	3	4	5	6	7	8
1	0.8640	1.1470	0.9759	1.1958	1.0613	1.2680	1.0641	0.7365
2	1.1481	1.0997	1.1625	1.1485	1.2257	1.2380	1.2144	0.4748
3	0.9980	1.1674	0.8867	1.1869	1.2452	1.3136	1.0117	0.3793
4	1.1974	1.1515	1.1892	1.2311	1.3314	1.2694	1.1320	0.2945
5	1.0629	1.2268	1.2460	1.3313	1.2602	1.2833	0.6187	
6	1.2680	1.2374	1.3133	1.2689	1.2833	0.5576	0.2333	
7	1.0640	1.2139	1.0111	1.1317	0.6188	0.2337		
8	0.7365	0.4748	0.3791	0.2944				

Table A.27: Radial Relative Power Distribution, 120 Second Transient, Rod Position: 84.75 inches

Y/X	1	2	3	4	5	6	7	8
1	0.8655	1.1484	0.9702	1.1670	0.9767	1.2407	1.0588	0.7373
2	1.1495	1.0994	1.1587	1.1326	1.2008	1.2251	1.2137	0.4761
3	0.9923	1.1636	0.8860	1.1878	1.2462	1.3201	1.0192	0.3824
4	1.1686	1.1357	1.1901	1.2404	1.3473	1.2866	1.1488	0.2985
5	0.9783	1.2018	1.2470	1.3471	1.2802	1.3069	0.6298	
6	1.2408	1.2244	1.3198	1.2861	1.3068	0.5683	0.2379	
7	1.0587	1.2132	1.0186	1.1483	0.6299	0.2383		
8	0.7373	0.4760	0.3822	0.2984				

Table A.28: Radial Relative Power Distribution, 120 Second Transient, Rod Position: 70.63 inches

Y/X	1	2	3	4	5	6	7	8
1	0.8682	1.1500	0.9654	1.1383	0.8929	1.2131	1.0538	0.7378
2	1.1511	1.1000	1.1550	1.1179	1.1757	1.2126	1.2125	0.4774
3	0.9874	1.1599	0.8860	1.1887	1.2477	1.3260	1.0266	0.3857
4	1.1399	1.1210	1.1910	1.2499	1.3625	1.3035	1.1647	0.3026
5	0.8944	1.1767	1.2485	1.3623	1.3002	1.3295	0.6408	
6	1.2131	1.2119	1.3256	1.3029	1.3295	0.5792	0.2425	
7	1.0537	1.2120	1.0259	1.1642	0.6409	0.2429		
8	0.7378	0.4774	0.3854	0.3025				

Table A.29: Radial Relative Power Distribution, 120 Second Transient, Rod Position: 56.50 inches

Y/X	1	2	3	4	5	6	7	8
1	0.8716	1.1516	0.9611	1.1098	0.8101	1.1853	1.0490	0.7382
2	1.1527	1.1012	1.1514	1.1041	1.1505	1.2006	1.2111	0.4789
3	0.9830	1.1562	0.8866	1.1893	1.2495	1.3312	1.0339	0.3891
4	1.1114	1.1071	1.1916	1.2596	1.3769	1.3200	1.1800	0.3068
5	0.8114	1.1514	1.2503	1.3767	1.3200	1.3515	0.6517	
6	1.1852	1.1999	1.3308	1.3194	1.3514	0.5901	0.2472	
7	1.0490	1.2106	1.0332	1.1795	0.6518	0.2476		
8	0.7382	0.4789	0.3888	0.3067				

Table A.30: Radial Relative Power Distribution, 120 Second Transient, Rod Position: 42.37 inches

Y/X	1	2	3	4	5	6	7	8
1	0.8751	1.1529	0.9572	1.0831	0.7332	1.1591	1.0449	0.7387
2	1.1540	1.1025	1.1478	1.0917	1.1267	1.1896	1.2097	0.4805
3	0.9789	1.1526	0.8872	1.1896	1.2514	1.3357	1.0407	0.3924
4	1.0846	1.0947	1.1919	1.2687	1.3900	1.3353	1.1941	0.3107
5	0.7343	1.1277	1.2522	1.3898	1.3387	1.3718	0.6619	
6	1.1591	1.1889	1.3353	1.3347	1.3717	0.6004	0.2516	
7	1.0448	1.2092	1.0400	1.1937	0.6621	0.2520		
8	0.7386	0.4804	0.3921	0.3106				

Table A.31: Radial Relative Power Distribution, 120 Second Transient, Rod Position: 28.25 inches

Y/X	1	2	3	4	5	6	7	8
1	0.8776	1.1536	0.9537	1.0619	0.6735	1.1387	1.0420	0.7393
2	1.1547	1.1034	1.1447	1.0820	1.1079	1.1812	1.2088	0.4818
3	0.9753	1.1495	0.8875	1.1895	1.2530	1.3391	1.0462	0.3950
4	1.0635	1.0850	1.1918	1.2759	1.4000	1.3473	1.2054	0.3138
5	0.6745	1.1089	1.2537	1.3998	1.3534	1.3878	0.6701	
6	1.1386	1.1805	1.3387	1.3467	1.3877	0.6084	0.2550	
7	1.0419	1.2083	1.0455	1.2049	0.6703	0.2555		
8	0.7393	0.4817	0.3947	0.3137				

Table A.32: Radial Relative Power Distribution, 120 Second Transient, Rod Position: 14.12 inches

Y/X	1	2	3	4	5	6	7	8
1	0.8790	1.1538	0.9509	1.0466	0.6310	1.1241	1.0403	0.7401
2	1.1549	1.1039	1.1422	1.0751	1.0943	1.1754	1.2086	0.4828
3	0.9724	1.1470	0.8874	1.1892	1.2541	1.3416	1.0503	0.3969
4	1.0481	1.0781	1.1915	1.2809	1.4070	1.3559	1.2136	0.3161
5	0.6319	1.0952	1.2548	1.4068	1.3639	1.3993	0.6759	
6	1.1240	1.1747	1.3412	1.3554	1.3992	0.6141	0.2575	
7	1.0402	1.2081	1.0495	1.2131	0.6761	0.2579		
8	0.7401	0.4827	0.3966	0.3159				

Table A.33: Radial Relative Power Distribution, 120 Second Transient, Rod Position: 0.00 inches

Y/X	1	2	3	4	5	6	7	8
1	0.8794	1.1536	0.9495	1.0396	0.6115	1.1177	1.0398	0.7407
2	1.1547	1.1040	1.1410	1.0721	1.0881	1.1730	1.2088	0.4833
3	0.9710	1.1458	0.8873	1.1890	1.2546	1.3427	1.0522	0.3977
4	1.0411	1.0751	1.1913	1.2831	1.4101	1.3598	1.2173	0.3171
5	0.6123	1.0890	1.2553	1.4099	1.3686	1.4044	0.6785	
6	1.1176	1.1723	1.3423	1.3592	1.4043	0.6167	0.2586	
7	1.0397	1.2083	1.0515	1.2168	0.6787	0.2590		
8	0.7406	0.4833	0.3975	0.3170				

Table A.34: Axial Relative Power Distribution, 120 Second Transient, Rod Position: 141.25 inches - All Rods Out

Z(in.)	Value	Z(in.)	Value	Z(in.)	Value	Z(in.)	Value	Z(in.)	Value
3.00	0.1365	8.76	0.3126	11.76	0.3624	15.00	0.4079	21.00	0.4944
27.00	0.5787	33.00	06653	39.00	0.7559	45.00	0.8511	51.00	0.9501
57.00	1.0512	63.00	1.1523	69.00	1.2506	75.00	1.3428	81.00	1.4250
87.00	1.4930	93.00	1.5421	99.00	1.5676	105.00	1.5634	111.00	1.5227
117.00	1.4370	123.00	1.2952	129.00	1.0795	134.76	0.7902	137.76	0.6559
141.00	0.3424								

Table A.35: Axial Relative Power Distribution, 120 Second Transient, Rod Position: 127.12 inches

Z(in.)	Value	Z(in.)	Value	Z(in.)	Value	Z(in.)	Value	Z(in.)	Value
3.00	0.1412	8.76	0.3235	11.76	0.3750	15.00	0.4218	21.00	0.5109
27.00	0.5975	33.00	0.6861	39.00	0.7785	45.00	0.8751	51.00	0.9751
57.00	1.0766	63.00	1.1773	69.00	1.2743	75.00	1.3640	81.00	1.4424
87.00	1.5050	93.00	1.5473	99.00	1.5641	105.00	1.5496	111.00	1.4971
117.00	1.3985	123.00	1.2433	129.00	1.0160	134.76	0.7290	137.76	0.6001
141.00	0.3122								

Table A.36: Axial Relative Power Distribution, 120 Second Transient, Rod Position: 113.00 inches

Z(in.)	Value	Z(in.)	Value	Z(in.)	Value	Z(in.)	Value	Z(in.)	Value
3.00	0.1551	8.76	0.3550	11.76	0.4113	15.00	0.4622	21.00	0.5584
27.00	0.6508	33.00	0.7443	39.00	0.8405	45.00	0.9395	5100	1.0404
57.00	1.1407	63.00	1.2378	69.00	1.3281	75.00	1.4079	81.00	1.4726
87.00	1.5176	93.00	1.5380	99.00	1.5290	105.00	1.4850	111.00	1.4002
117.00	1.2689	123.00	1.1059	129.00	0.9001	134.76	0.6488	137.76	0.5347
141.00	0.2784								

Table A.37: Axial Relative Power Distribution, 120 Second Transient, Rod Position: 98.88 inches

Z(in.)	Value	Z(in.)	Value	Z(in.)	Value	Z(in.)	Value	Z(in.)	Value
3.00	0.1726	8.76	0.3946	11.76	0.4567	15.00	0.5125	21.00	0.6171
27.00	0.7161	33.00	0.8144	39.00	0.9136	45.00	1.0137	51.00	1.1130
57.00	1.2086	63.00	1.2974	69.00	1.3753	75.00	1.4381	81.00	1.4808
87.00	1.4988	93.00	1.4875	99.00	1.4421	105.00	1.3617	111.00	1.2706
117.00	1.1597	123.00	1.0192	129.00	0.8342	134.76	0.6033	137.76	0.4977
141.00	0.2593								

Table A.38: Axial Relative Power Distribution, 120 Second Transient, Rod Position: 84.75 inches

Z(in.)	Value	Z(in.)	Value	Z(in.)	Value	Z(in.)	Value	Z(in.)	Value
3.00	0.1898	8.76	0.4333	11.76	0.5011	15.00	0.5613	21.00	0.6732
27.00	0.7772	33.00	0.8781	39.00	0.9775	45.00	1.0747	51.00	1.1677
57.00	1.2532	63.00	1.3271	69.00	1.3852	75.00	1.4230	81.00	1.4352
87.00	1.4182	93.00	1.3840	99.00	1.3436	105.00	1.2909	111.00	1.2202
117.00	1.1247	123.00	0.9957	129.00	0.8192	134.76	0.5945	137.76	0.4910
141.00	0.2560								

Table A.39: Axial Relative Power Distribution, 120 Second Transient, Rod Position: 70.63 inches

Z(in.)	Value	Z(in.)	Value	Z(in.)	Value	Z(in.)	Value	Z(in.)	Value
3.00	0.2013	8.76	0.4592	11.76	0.5305	15.00	0.5932	21.00	0.7086
27.00	0.8136	33.00	0.9130	39.00	1.0080	45.00	1.0976	51.00	1.1793
57.00	1.2493	63.00	1.3035	69.00	1.3372	75.00	1.3469	81.00	1.3525
87.00	1.3544	93.00	1.3478	99.00	1.3286	105.00	1.2921	111.00	1.2332
117.00	1.1453	123.00	1.0196	129.00	0.8422	134.76	0.6127	137.76	0.5066
141.00	0.2642								

Table A.40: Axial Relative Power Distribution, 120 Second Transient, Rod Position: 56.50 inches

Z(in.)	Value	Z(in.)	Value	Z(in.)	Value	Z(in.)	Value	Z(in.)	Value
3.00	0.2047	8.76	0.4663	11.76	0.5381	15.00	0.6007	21.00	0.7144
27.00	0.8155	33.00	0.9084	39.00	0.9940	45.00	1.0709	51.00	1.1364
57.00	1.1864	63.00	1.2217	69.00	1.2608	75.00	1.2990	81.00	1.3320
87.00	1.3562	93.00	1.3678	99.00	1.3629	105.00	1.3369	111.00	1.2845
117.00	1.1991	123.00	1.0717	129.00	0.8876	134.76	0.6468	137.76	0.5352
141.00	0.2792								

Table A.41: Axial Relative Power Distribution, 120 Second Transient, Rod Position: 42.38 inches

Z(in.)	Value	Z(in.)	Value	Z(in.)	Value	Z(in.)	Value	Z(in.)	Value
3.00	0.1982	876	0.4509	11.76	0.5197	15.00	0.5790	21.00	0.6854
27.00	0.7772	33.00	0.8587	39.00	0.9301	45.00	0.9904	51.00	1.0490
57.00	1.1126	63.00	1.1779	69.00	1.2417	75.00	1.3010	81.00	1.3520
87.00	1.3914	93.00	1.4153	99.00	1.4199	105.00	1.4003	111.00	1.3512
117.00	1.2654	123.00	1.1336	129.00	0.9406	134.76	0.6861	137.76	0.5679
141.00	0.2963								

Table A.42: Axial Relative Power Distribution, 120 Second Transient, Rod Position: 28.25 inches

Z(in.)	Value	Z(in.)	Value	Z(in.)	Value	Z(in.)	Value	Z(in.)	Value
3.00	0.1836	8.76	0.4172	11.76	0.4804	15.00	0.5343	21.00	0.6295
27.00	0.7093	33.00	0.7776	39.00	0.8493	45.00	0.9262	51.00	1.0068
57.00	1.0890	63.00	1.1706	69.00	1.2488	75.00	1.3208	81.00	1.3829
87.00	1.4316	93.00	1.4632	99.00	1.4735	105.00	1.4575	111.00	1.4097
117.00	1.3226	123.00	1.1864	129.00	0.9853	134.76	0.7192	137.76	0.5954
141.00	0.3107								

Table A.43: Axial Relative Power Distribution, 120 Second Transient, Rod Position: 14.13 inches

Z(in.)	Value	Z(in.)	Value	Z(in.)	Value	Z(in.)	Value	Z(in.)	Value
3.00	0.1641	8.76	0.3722	11.76	0.4284	15.00	0.4755	21.00	0.5610
27.00	0.6430	33.00	0.7262	39.00	0.8122	45.00	0.9012	51.00	0.9926
57.00	1.0845	63.00	1.1749	69.00	1.2611	75.00	1.3402	81.00	1.4087
87.00	1.4628	93.00	1.4988	99.00	1.5123	105.00	1.4984	111.00	1.4510
117.00	1.3627	123.00	1.2233	129.00	1.0165	134.76	0.7422	137.76	0.6146
141.00	0.3207								

Table A.44: Axial Relative Power Distribution, 120 Second Transient, Rod Position: 0.00 inches

Z(in.)	Value	Z(in.)	Value	Z(in.)	Value	Z(in.)	Value	Z(in.)	Value
3.00	0.1485	8.76	0.3388	11.76	0.3926	15.00	0.4413	21.00	0.5329
27.00	0.6204	33.00	0.7084	39.00	0.7989	45.00	0.8921	51.00	0.9874
57.00	1.0830	63.00	1.1770	69.00	1.2665	75.00	1.3488	81.00	1.4202
87.00	1.4769	93.00	1.5150	99.00	1.5302	105.00	1.5173	111.00	1.4704
117.00	1.3817	123.00	1.2409	129.00	1.0314	134.76	0.7532	137.76	0.6237
141.00	0.3255								

A.3 2 Second Transient, $\beta_i = 0.0001$

The axial and radial power distributions have been supplied for the 2 second transient case printing data over 40 rod intervals (Though only the same 10 intervals printed for Sections A.1 and A.2 will be shown here to save space), utilizing the precursor assumption, $\beta_i = 0.0001$.

Table A.45: Radial Relative Power Distribution, 2 Second Transient, Rod Position: 141.25 inches - All Rods Out

Y/X	1	2	3	4	5	6	7	8
1	0.8636	1.1431	0.9905	1.2570	1.2514	1.3239	1.0740	0.7320
2	1.1442	1.1009	1.1697	1.1844	1.2782	1.2659	1.2123	0.4723
3	1.0128	1.1745	0.8908	1.1839	1.2438	1.2977	0.9951	0.3733
4	1.2586	1.1875	1.1862	1.2122	1.2969	1.2325	1.0950	0.2865
5	1.2530	1.2792	1.2446	1.2967	1.2186	1.2328	0.5955	
6	1.3239	1.2653	1.2974	1.2320	1.2327	0.5361	0.2243	
7	1.0740	1.2118	0.9945	1.0947	0.5957	0.2247		
8	0.7320	0.4723	0.3731	0.2864				

Table A.46: Radial Relative Power Distribution, 2 Second Transient, Rod Position: 127.12 inches

Y/X	1	2	3	4	5	6	7	8
1	0.8639	1.1443	0.9877	1.2448	1.2079	1.3130	1.0727	0.7335
2	1.1454	1.1012	1.1688	1.1775	1.2676	1.2607	1.2134	0.4730
3	1.0100	1.1737	0.8901	1.1849	1.2443	1.3011	0.9986	0.3746
4	1.2465	1.1806	1.1871	1.2161	1.3036	1.2396	1.1022	0.2880
5	1.2096	1.2687	1.2451	1.3034	1.2265	1.2423	0.5999	
6	1.3130	1.2601	1.3008	1.2392	1.2423	0.5401	0.2260	
7	1.0726	1.2130	0.9980	1.1019	0.6001	0.2263		
8	0.7335	0.4730	0.3743	0.2879				

Table A.47: Radial Relative Power Distribution, 2 Second Transient, Rod Position: 113.00 inches

Y/X	1	2	3	4	5	6	7	8
1	0.8636	1.1457	0.9817	1.2216	1.1376	1.2918	1.0687	0.7352
2	1.1468	1.1004	1.1660	1.1634	1.2478	1.2498	1.2142	0.4739
3	1.0040	1.1709	0.8882	1.1859	1.2446	1.3072	1.0049	0.3768
4	1.2232	1.1665	1.1882	1.2232	1.3169	1.2538	1.1165	0.2911
5	1.1393	1.2489	1.2454	1.3168	1.2424	1.2618	0.6088	
6	1.2918	1.2492	1.3069	1.2533	1.2618	0.5483	0.2294	
7	1.0686	1.2138	1.0043	1.1162	0.6090	0.2298		
8	0.7352	0.4738	0.3766	0.2910				

Table A.48: Radial Relative Power Distribution, 2 Second Transient, Rod Position: 98.88 inches

Y/X	1	2	3	4	5	6	7	8
1	0.8641	1.1471	0.9760	1.1961	1.0626	1.2680	1.0638	0.7362
2	1.1482	1.0998	1.1627	1.1486	1.2259	1.2380	1.2141	0.4748
3	0.9982	1.1675	0.8869	1.1869	1.2451	1.3134	1.0116	0.3794
4	1.1977	1.1517	1.1892	1.2312	1.3313	1.2692	1.1318	0.2945
5	1.0642	1.2269	1.2459	1.3311	1.2601	1.2831	0.6187	
6	1.2680	1.2373	1.3131	1.2687	1.2831	0.5576	0.2334	
7	1.0638	1.2136	1.0110	1.1314	0.6188	0.2338		
8	0.7362	0.4748	0.3792	0.2944				

Table A.49: Radial Relative Power Distribution, 2 Second Transient, Rod Position: 84.75 inches

Y/X	1	2	3	4	5	6	7	8
1	0.8665	1.1490	0.9710	1.1669	0.9760	1.2399	1.0585	0.7369
2	1.1502	1.1004	1.1591	1.1331	1.2003	1.2248	1.2131	0.4761
3	0.9930	1.1640	0.8867	1.1880	1.2464	1.3196	1.0192	0.3827
4	1.1685	1.1362	1.1903	1.2408	1.3471	1.2865	1.1483	0.2987
5	0.9776	1.2014	1.2472	1.3469	1.2804	1.3065	0.6299	
6	1.2399	1.2242	1.3192	1.2860	1.3065	0.5686	0.2382	
7	1.0584	1.2126	1.0185	1.1479	0.6301	0.2386		
8	0.7369	0.4761	0.3825	0.2986				

Table A.50: Radial Relative Power Distribution, 2 Second Transient, Rod Position: 70.63 inches

Y/X	1	2	3	4	5	6	7	8
1	0.8704	1.1514	0.9668	1.1376	0.8891	1.2111	1.0535	0.7373
2	1.1525	1.1020	1.1559	1.1186	1.1743	1.2121	1.2116	0.4777
3	0.9888	1.1607	0.8874	1.1889	1.2482	1.3251	1.0266	0.3862
4	1.1391	1.1217	1.1912	1.2508	1.3622	1.3035	1.1640	0.3030
5	0.8906	1.1753	1.2489	1.3620	1.3007	1.3291	0.6411	
6	1.2111	1.2114	1.3247	1.3029	1.3290	0.5798	0.2430	
7	1.0534	1.2111	1.0260	1.1636	0.6412	0.2434		
8	0.7373	0.4777	0.3860	0.3028				

Table A.51: Radial Relative Power Distribution, 2 Second Transient, Rod Position: 56.50 inches

Y/X	1	2	3	4	5	6	7	8
1	0.8748	1.1537	0.9633	1.1089	0.8045	1.1827	1.0489	0.7377
2	1.1548	1.1041	1.1527	1.1053	1.1486	1.2000	1.2100	0.4794
3	0.9851	1.1576	0.8886	1.1897	1.2502	1.3299	1.0339	0.3898
4	1.1104	1.1084	1.1920	1.2608	1.3763	1.3198	1.1789	0.3072
5	0.8057	1.1496	1.2510	1.3761	1.3206	1.3506	0.6520	
6	1.1827	1.1993	1.3295	1.3192	1.3505	0.5908	0.2477	
7	1.0488	1.2095	1.0332	1.1785	0.6521	0.2481		
8	0.7376	0.4793	0.3895	0.3071				

Table A.52: Radial Relative Power Distribution, 2 Second Transient, Rod Position: 42.38 inches

Y/X	1	2	3	4	5	6	7	8
1	0.8791	1.1557	0.9600	1.0828	0.7280	1.1568	1.0451	0.7382
2	1.1568	1.1063	1.1497	1.0937	1.1252	1.1894	1.2086	0.4810
3	0.9817	1.1546	0.8897	1.1901	1.2523	1.3340	1.0406	0.3931
4	1.0844	1.0967	1.1923	1.2699	1.3887	1.3344	1.1923	0.3110
5	0.7291	1.1262	1.2530	1.3885	1.3386	1.3699	0.6619	
6	1.1568	1.1887	1.3337	1.3339	1.3698	0.6008	0.2520	
7	1.0450	1.2081	1.0399	1.1919	0.6620	0.2525		
8	0.7381	0.4810	0.3928	0.3109				

Table A.53: Radial Relative Power Distribution, 2 Second Transient, Rod Position: 28.25 inches

Y/X	1	2	3	4	5	6	7	8
1	0.8820	1.1569	0.9573	1.0632	0.6712	1.1376	1.0426	0.7388
2	1.1580	1.1079	1.1473	1.0851	1.1076	1.1816	1.2078	0.4823
3	0.9790	1.1521	0.8904	1.1901	1.2538	1.3370	1.0456	0.3956
4	1.0648	1.0881	1.1924	1.2767	1.3978	1.3454	1.2025	0.3139
5	0.6722	1.1085	1.2546	1.3976	1.3521	1.3843	0.6693	
6	1.1376	1.1809	1.3366	1.3448	1.3843	0.6082	0.2552	
7	1.0425	1.2073	1.0449	1.2021	0.6695	0.2557		
8	0.7388	0.4823	0.3953	0.3138				

Table A.54: Radial Relative Power Distribution, 2 Second Transient, Rod Position: 14.13 inches

Y/X	1	2	3	4	5	6	7	8
1	0.8837	1.1577	0.9552	1.0496	0.6321	1.1245	1.0412	0.7397
2	1.1587	1.1089	1.1455	1.0792	1.0953	1.1765	1.2077	0.4833
3	0.9768	1.1503	0.8906	1.1900	1.2549	1.3391	1.0492	0.3973
4	1.0511	1.0822	1.1923	1.2812	1.4039	1.3529	1.2096	0.3159
5	0.6329	1.0962	1.2556	1.4037	1.3612	1.3942	0.6744	
6	1.1244	1.1758	1.3388	1.3523	1.3942	0.6131	0.2574	
7	1.0411	1.2072	1.0485	1.2092	0.6746	0.2578		
8	0.7397	0.4832	0.3970	0.3158				

Table A.55: Radial Relative Power Distribution, 2 Second Transient, Rod Position: 0.00 inches

Y/X	1	2	3	4	5	6	7	8
1	0.8844	1.1580	0.9543	1.0438	0.6144	1.1190	1.0409	0.7403
2	1.1591	1.1094	1.1449	1.0768	1.0900	1.1745	1.2080	0.4838
3	0.9759	1.1497	0.8906	1.1900	1.2554	1.3401	1.0508	0.3980
4	1.0453	1.0798	1.1923	1.2831	1.4064	1.3559	1.2126	0.3167
5	0.6152	1.0909	1.2561	1.4062	1.3649	1.3982	0.6764	
6	1.1189	1.1738	1.3397	1.3554	1.3982	0.6151	0.2582	
7	1.0408	1.2075	1.0501	1.2122	0.6766	0.2586		
8	0.7403	0.4837	0.3977	0.3166				

Table A.56: Axial Relative Power Distribution, 2 Second Transient, Rod Position: 141.25 inches - All Rods Out

Z(in.)	Value	Z(in.)	Value	Z(in.)	Value	Z(in.)	Value	Z(in.)	Value
3.00	0.1365	8.76	0.3126	11.76	0.3624	15.00	0.4079	21.00	0.4944
27.00	0.5787	33.00	0.6653	39.00	0.7559	45.00	0.8511	51.00	0.9501
57.00	1.0512	63.00	1.1523	69.00	1.2506	75.00	1.3428	81.00	1.4250
87.00	1.4930	93.00	1.5421	99.00	1.5676	105.00	1.5634	111.00	1.5227
117.00	1.4370	123.00	1.2952	129.00	1.0795	134.76	0.7902	137.76	0.6559
141.00	0.3424								

Table A.57: Axial Relative Power Distribution, 2 Second Transient, Rod Position: 127.12 inches

Z(in.)	Value	Z(in.)	Value	Z(in.)	Value	Z(in.)	Value	Z(in.)	Value
3.00	0.1427	8.76	0.3268	11.76	0.3788	15.00	0.4261	21.00	0.5158
27.00	0.6029	33.00	0.6918	39.00	0.7844	45.00	0.8809	51.00	0.9806
57.00	1.0817	63.00	1.1816	69.00	1.2776	75.00	1.3661	81.00	1.4429
87.00	1.5039	93.00	1.5444	99.00	1.5595	105.00	1.5432	111.00	1.4894
117.00	1.3898	123.00	1.2344	129.00	1.0078	134.76	0.7228	137.76	0.5948
141.00	0.3094								

Table A.58: Axial Relative Power Distribution, 2 Second Transient, Rod Position: 113.00 inches

Z(in.)	Value	Z(in.)	Value	Z(in.)	Value	Z(in.)	Value	Z(in.)	Value
3.00	0.1582	8.76	0.3619	11.76	0.4192	15.00	0.4709	21.00	0.5684
27.00	0.6618	33.00	0.7558	39.00	0.8522	45.00	0.9510	51.00	1.0511
57.00	1.1502	63.00	1.2455	69.00	1.3336	75.00	1.4107	81.00	1.4723
87.00	1.5139	93.00	1.5309	99.00	1.5186	105.00	1.4717	111.00	1.3849
117.00	1.2528	123.00	1.0902	129.00	0.8864	134.76	0.6384	137.76	0.5260
141.00	0.2738								

Table A.59: Axial Relative Power Distribution, 2 Second Transient, Rod Position: 98.88 inches

Z(in.)	Value	Z(in.)	Value	Z(in.)	Value	Z(in.)	Value	Z(in.)	Value
3.00	0.1750	8.76	0.4000	11.76	0.4629	15.00	0.5193	21.00	0.6248
27.00	0.7245	33.00	0.8230	39.00	0.9223	45.00	1.0219	51.00	1.1203
57.00	1.2148	63.00	1.3019	69.00	1.3779	75.00	1.4384	81.00	1.4787
87.00	1.4943	93.00	1.4807	99.00	1.4335	105.00	1.3519	111.00	1.2604
117.00	1.1497	123.00	1.0100	129.00	0.8264	134.76	0.5976	137.76	0.4930
141.00	0.2569								

Table A.60: Axial Relative Power Distribution, 2 Second Transient, Rod Position: 84.75 inches

Z(in.)	Value	Z(in.)	Value	Z(in.)	Value	Z(in.)	Value	Z(in.)	Value
3.00	0.1896	8.76	0.4329	11.76	0.5005	15.00	0.5607	21.00	0.6724
27.00	0.7761	33.00	0.8767	39.00	0.9756	45.00	1.0724	51.00	1.1648
57.00	1.2497	63.00	1.3233	69.00	1.3811	75.00	1.4189	81.00	1.4316
87.00	1.4155	93.00	1.3828	99.00	1.3443	105.00	1.2936	111.00	1.2249
117.00	1.1308	123.00	1.0025	129.00	0.8256	134.76	0.5995	137.76	0.4953
141.00	0.2583								

Table A.61: Axial Relative Power Distribution, 2 Second Transient, Rod Position: 70.63 inches

Z(in.)	Value	Z(in.)	Value	Z(in.)	Value	Z(in.)	Value	Z(in.)	Value
3.00	0.1968	8.76	0.4490	11.76	0.5188	15.00	0.5803	21.00	0.6937
27.00	0.7972	33.00	0.8955	39.00	0.9900	45.00	1.0796	51.00	1.1619
57.00	1.2332	63.00	1.2896	69.00	1.3265	75.00	1.3404	81.00	1.3512
87.00	1.3588	93.00	1.3581	99.00	1.3446	105.00	1.3131	111.00	1.2580
117.00	1.1720	123.00	1.0460	129.00	0.8657	134.76	0.6305	137.76	0.5215
141.00	0.2721								

Table A.62: Axial Relative Power Distribution, 2 Second Transient, Rod Position: 56.50 inches

Z(in.)	Value	Z(in.)	Value	Z(in.)	Value	Z(in.)	Value	Z(in.)	Value
3.00	0.1956	8.76	0.4458	11.76	0.5147	15.00	0.5750	21.00	0.6850
27.00	0.7835	33.00	0.8751	39.00	0.9604	45.00	1.0384	51.00	1.1065
57.00	1.1606	63.00	1.2017	69.00	1.2478	75.00	1.2941	81.00	1.3359
87.00	1.3692	93.00	1.3898	99.00	1.3930	105.00	1.3737	111.00	1.3261
117.00	1.2426	123.00	1.1139	129.00	0.9246	134.76	0.6747	137.76	0.5585
141.00	0.2914								

Table A.63: Axial Relative Power Distribution, 2 Second Transient, Rod Position: 42.38 inches

Z(in.)	Value	Z(in.)	Value	Z(in.)	Value	Z(in.)	Value	Z(in.)	Value
3.00	0.1853	8.76	0.4218	11.76	0.4866	15.00	0.5428	21.00	0.6443
27.00	0.7333	33.00	0.8138	39.00	0.8863	45.00	0.9496	51.00	1.0132
57.00	1.0832	63.00	1.1564	69.00	1.2294	75.00	1.2989	81.00	1.3607
87.00	1.4110	93.00	1.4453	99.00	1.4592	105.00	1.4471	111.00	1.4030
117.00	1.3191	123.00	1.1852	129.00	0.9854	134.76	0.7198	137.76	0.5961
141.00	0.3112								

Table A.64: Axial Relative Power Distribution, 2 Second Transient, Rod Position: 28.25 inches

Z(in.)	Value	Z(in.)	Value	Z(in.)	Value	Z(in.)	Value	Z(in.)	Value
3.00	0.1695	8.76	0.3854	11.76	0.4443	15.00	0.4950	21.00	0.5856
27.00	0.6632	33.00	0.7318	39.00	0.8055	45.00	0.8858	51.00	0.9714
57.00	1.0602	63.00	1.1499	69.00	1.2374	75.00	1.3197	81.00	1.3926
87.00	1.4523	93.00	1.4942	99.00	1.5138	105.00	1.5053	111.00	1.4624
117.00	1.3770	123.00	1.2387	129.00	1.0307	134.76	0.7533	137.76	0.6239
141.00	0.3257								

Table A.65: Axial Relative Power Distribution, 2 Second Transient, Rod Position: 14.13 inches

Z(in.)	Value	Z(in.)	Value	Z(in.)	Value	Z(in.)	Value	Z(in.)	Value
3.00	0.1509	8.76	0.3429	11.76	0.3952	15.00	0.4397	21.00	0.5214
27.00	0.6016	33.00	0.6845	39.00	0.7718	45.00	0.8638	51.00	0.9596
57.00	1.0575	63.00	1.1552	69.00	1.2500	75.00	1.3387	81.00	1.4172
87.00	1.4815	93.00	1.5272	99.00	1.5494	105.00	1.5424	111.00	1.4998
117.00	1.4131	123.00	1.2718	129.00	1.0586	134.76	0.7738	137.76	0.6410
141.00	0.3346								

Table A.66: Axial Relative Power Distribution, 2 Second Transient, Rod Position: 0.00 inches

Z(in.)	Value	Z(in.)	Value	Z(in.)	Value	Z(in.)	Value	Z(in.)	Value
3.00	0.1373	8.76	0.3143	11.76	0.3647	15.00	0.4110	21.00	0.4986
27.00	0.5840	33.00	0.6714	39.00	0.7627	45.00	0.8582	51.00	0.9572
57.00	1.0580	63.00	1.1584	69.00	1.2556	75.00	1.3464	81.00	1.4269
87.00	1.4929	93.00	1.5399	99.00	1.5631	105.00	1.5567	111.00	1.5141
117.00	1.4270	123.00	1.2845	129.00	1.0694	134.76	0.7817	137.76	0.6476
141.00	0.3381								

A.4 120 Second Transient, $\beta_i = 0.0001$

The axial and radial power distributions have been supplied for the 120 second transient case printing data over 10 rod intervals (Though only the same 10 intervals printed for Sections A.1 and A.2 will be shown here to save space), utilizing the precursor assumption, $\beta_i = 0.0001$.

Table A.67: Radial Relative Power Distribution, 120 Second Transient, Rod Position: 141.25 inches - All Rods Out

Y/X	1	2	3	4	5	6	7	8
1	0.8636	1.1431	0.9905	1.2570	1.2514	1.3239	1.0740	0.7320
2	1.1442	1.1009	1.1697	1.1844	1.2782	1.2659	1.2123	0.4723
3	1.0128	1.1745	0.8908	1.1839	1.2438	1.2977	0.9951	0.3733
4	1.2586	1.1875	1.1862	1.2122	1.2969	1.2325	1.0950	0.2865
5	1.2530	1.2792	1.2446	1.2967	1.2186	1.2328	0.5955	
6	1.3239	1.2653	1.2974	1.2320	1.2327	0.5361	0.2243	
7	1.0740	1.2118	0.9945	1.0947	0.5957	0.2247		
8	0.7320	0.4723	0.3731	0.2864				

Table A.68: Radial Relative Power Distribution, 120 Second Transient, Rod Position: 127.12 inches

Y/X	1	2	3	4	5	6	7	8
1	0.8638	1.1443	0.9876	1.2448	1.2079	1.3130	1.0727	0.7335
2	1.1454	1.1011	1.1688	1.1775	1.2677	1.2607	1.2134	0.4730
3	1.0100	1.1737	0.8901	1.1849	1.2443	1.3012	0.9986	0.3745
4	1.2465	1.1806	1.1872	1.2161	1.3037	1.2396	1.1022	0.2880
5	1.2096	1.2688	1.2451	1.3035	1.2265	1.2424	0.5999	
6	1.3130	1.2601	1.3009	1.2392	1.2423	0.5401	0.2260	
7	1.0726	1.2130	0.9980	1.1019	0.6001	0.2263		
8	0.7334	0.4729	0.3743	0.2879				

Table A.69: Radial Relative Power Distribution, 120 Second Transient, Rod Position: 113.00 inches

Y/X	1	2	3	4	5	6	7	8
1	0.8634	1.1456	0.9816	1.2216	1.1379	1.2919	1.0686	0.7352
2	1.1467	1.1003	1.1659	1.1633	1.2479	1.2498	1.2142	0.4738
3	1.0039	1.1708	0.8881	1.1859	1.2445	1.3073	1.0049	0.3768
4	1.2232	1.1664	1.1882	1.2232	1.3170	1.2538	1.1166	0.2911
5	1.1396	1.2490	1.2453	1.3169	1.2424	1.2619	0.6088	
6	1.2919	1.2491	1.3070	1.2533	1.2619	0.5482	0.2294	
7	1.0685	1.2138	1.0043	1.1162	0.6089	0.2298		
8	0.7352	0.4738	0.3765	0.2909				

Table A.70: Radial Relative Power Distribution, 120 Second Transient, Rod Position: 98.87 inches

Y/X	1	2	3	4	5	6	7	8
1	0.8637	1.1469	0.9758	1.1963	1.0635	1.2683	1.0638	0.7362
2	1.1480	1.0995	1.1625	1.1485	1.2261	1.2380	1.2141	0.4747
3	0.9980	1.1674	0.8867	1.1869	1.2451	1.3135	1.0116	0.3794
4	1.1979	1.1516	1.1892	1.2311	1.3314	1.2693	1.1319	0.2945
5	1.0651	1.2272	1.2458	1.3312	1.2600	1.2832	0.6187	
6	1.2683	1.2373	1.3132	1.2687	1.2832	0.5576	0.2334	
7	1.0637	1.2136	1.0109	1.1315	0.6188	0.2338		
8	0.7362	0.4747	0.3791	0.2944				

Table A.71: Radial Relative Power Distribution, 120 Second Transient, Rod Position: 84.75 inches

Y/X	1	2	3	4	5	6	7	8
1	0.8660	1.1487	0.9707	1.1671	0.9774	1.2403	1.0584	0.7368
2	1.1498	1.0999	1.1589	1.1329	1.2007	1.2249	1.2131	0.4761
3	0.9927	1.1638	0.8864	1.1879	1.2463	1.3197	1.0191	0.3827
4	1.1687	1.1360	1.1903	1.2407	1.3472	1.2865	1.1483	0.2986
5	0.9790	1.2017	1.2471	1.3470	1.2803	1.3066	0.6299	
6	1.2403	1.2242	1.3193	1.2860	1.3066	0.5686	0.2381	
7	1.0583	1.2126	1.0184	1.1479	0.6300	0.2385		
8	0.7368	0.4760	0.3824	0.2985				

Table A.72: Radial Relative Power Distribution, 120 Second Transient, Rod Position: 70.63 inches

Y/X	1	2	3	4	5	6	7	8
1	0.8698	1.1510	0.9665	1.1377	0.8906	1.2114	1.0534	0.7372
2	1.1521	1.1014	1.1556	1.1184	1.1746	1.2121	1.2116	0.4776
3	0.9884	1.1605	0.8871	1.1889	1.2480	1.3252	1.0266	0.3862
4	1.1393	1.1215	1.1912	1.2507	1.3623	1.3036	1.1641	0.3029
5	0.8921	1.1756	1.2488	1.3621	1.3007	1.3293	0.6411	
6	1.2114	1.2114	1.3248	1.3030	1.3292	0.5798	0.2430	
7	1.0533	1.2111	1.0259	1.1637	0.6413	0.2434		
8	0.7372	0.4776	0.3859	0.3028				

Table A.73: Radial Relative Power Distribution, 120 Second Transient, Rod Position: 56.50 inches

Y/X	1	2	3	4	5	6	7	8
1	0.8743	1.1532	0.9628	1.1088	0.8055	1.1827	1.0487	0.7376
2	1.1543	1.1035	1.1523	1.1049	1.1487	1.1999	1.2099	0.4793
3	0.9846	1.1572	0.8883	1.1896	1.2501	1.3301	1.0340	0.3898
4	1.1103	1.1080	1.1919	1.2608	1.3766	1.3200	1.1792	0.3072
5	0.8067	1.1497	1.2509	1.3764	1.3209	1.3511	0.6522	
6	1.1827	1.1992	1.3297	1.3195	1.3510	0.5910	0.2478	
7	1.0486	1.2094	1.0333	1.1788	0.6523	0.2482		
8	0.7375	0.4792	0.3895	0.3071				

Table A.74: Radial Relative Power Distribution, 120 Second Transient, Rod Position: 42.37 inches

Y/X	1	2	3	4	5	6	7	8
1	0.8785	1.1551	0.9594	1.0824	0.7284	1.1566	1.0448	0.7380
2	1.1562	1.1056	1.1492	1.0931	1.1250	1.1891	1.2085	0.4809
3	0.9812	1.1540	0.8894	1.1899	1.2522	1.3342	1.0407	0.3931
4	1.0839	1.0962	1.1922	1.2700	1.3892	1.3349	1.1928	0.3111
5	0.7295	1.1260	1.2529	1.3889	1.3391	1.3706	0.6622	
6	1.1566	1.1884	1.3338	1.3343	1.3706	0.6011	0.2522	
7	1.0447	1.2080	1.0400	1.1924	0.6624	0.2526		
8	0.7380	0.4809	0.3928	0.3110				

Table A.75: Radial Relative Power Distribution, 120 Second Transient, Rod Position: 28.25 inches

Y/X	1	2	3	4	5	6	7	8
1	0.8814	1.1563	0.9567	1.0625	0.6711	1.1371	1.0422	0.7387
2	1.1574	1.1071	1.1467	1.0844	1.1071	1.1813	1.2077	0.4822
3	0.9783	1.1515	0.8900	1.1900	1.2538	1.3372	1.0458	0.3956
4	1.0640	1.0874	1.1922	1.2768	1.3984	1.3460	1.2032	0.3141
5	0.6720	1.1080	1.2545	1.3981	1.3529	1.3853	0.6698	
6	1.1371	1.1806	1.3369	1.3455	1.3853	0.6086	0.2554	
7	1.0421	1.2072	1.0451	1.2028	0.6700	0.2559		
8	0.7387	0.4822	0.3954	0.3139				

Table A.76: Radial Relative Power Distribution, 120 Second Transient, Rod Position: 14.12 inches

Y/X	1	2	3	4	5	6	7	8
1	0.8831	1.1569	0.9544	1.0487	0.6315	1.1238	1.0408	0.7396
2	1.1580	1.1081	1.1448	1.0784	1.0947	1.1760	1.2075	0.4832
3	0.9760	1.1496	0.8901	1.1898	1.2548	1.3394	1.0495	0.3974
4	1.0502	1.0814	1.1921	1.2814	1.4046	1.3537	1.2104	0.3161
5	0.6324	1.0956	1.2555	1.4043	1.3622	1.3954	0.6749	
6	1.1238	1.1753	1.3390	1.3531	1.3954	0.6137	0.2576	
7	1.0407	1.2070	1.0488	1.2100	0.6751	0.2580		
8	0.7395	0.4832	0.3971	0.3159				

Table A.77: Radial Relative Power Distribution, 120 Second Transient, Rod Position: 0.00 inches

Y/X	1	2	3	4	5	6	7	8
1	0.8838	1.1573	0.9535	1.0427	0.6137	1.1182	1.0405	0.7402
2	1.1584	1.1086	1.1441	1.0759	1.0893	1.1740	1.2078	0.4837
3	0.9751	1.1489	0.8902	1.1898	1.2553	1.3404	1.0511	0.3981
4	1.0443	1.0789	1.1921	1.2833	1.4071	1.3568	1.2134	0.3169
5	0.6145	1.0902	1.2560	1.4069	1.3659	1.3995	0.6770	
6	1.1182	1.1733	1.3400	1.3562	1.3995	0.6157	0.2585	
7	1.0404	1.2073	1.0504	1.2130	0.6772	0.2589		
8	0.7401	0.4837	0.3978	0.3168				

Table A.78: Axial Relative Power Distribution, 120 Second Transient, Rod Position: 141.25 inches - All Rods Out

Z(in.)	Value	Z(in.)	Value	Z(in.)	Value	Z(in.)	Value	Z(in.)	Value
3.00	0.1365	8.76	0.3126	11.76	0.3624	15.00	0.4079	21.00	0.4944
27.00	0.5787	33.00	0.6653	39.00	0.7559	45.00	0.8511	51.00	0.9501
57.00	1.0512	63.00	1.1523	69.00	1.2506	75.00	1.3428	81.00	1.4250
87.00	1.4930	93.00	1.5421	99.00	1.5676	105.00	1.5634	111.00	1.5227
117.00	1.4370	123.00	1.2952	129.00	1.0795	134.76	0.7902	137.76	0.6559
141.00	0.3424								

Table A.79: Axial Relative Power Distribution, 120 Second Transient, Rod Position: 127.12 inches

Z(in.)	Value	Z(in.)	Value	Z(in.)	Value	Z(in.)	Value	Z(in.)	Value
3.00	0.1430	8.76	0.3275	11.76	0.3796	15.00	0.4269	21.00	0.5168
27.00	0.6040	33.00	0.6930	39.00	0.7856	45.00	0.8821	51.00	0.9818
57.00	1.0827	63.00	1.1825	69.00	1.2782	75.00	1.3665	81.00	1.4430
87.00	1.5037	93.00	1.5438	99.00	1.5585	105.00	1.5419	111.00	1.4878
117.00	1.3881	123.00	1.2327	129.00	1.0062	134.76	0.7215	137.76	0.5938
141.00	0.3089								

Table A.80: Axial Relative Power Distribution, 120 Second Transient, Rod Position: 113.00 inches

Z(in.)	Value	Z(in.)	Value	Z(in.)	Value	Z(in.)	Value	Z(in.)	Value
3.00	0.1591	8.76	0.3640	11.76	0.4215	15.00	0.4735	21.00	0.5714
27.00	0.6651	33.00	0.7592	39.00	0.8556	45.00	0.9543	51.00	1.0542
57.00	1.1530	63.00	1.2478	69.00	1.3352	75.00	1.4115	81.00	1.4722
87.00	1.5128	93.00	1.5288	99.00	1.5155	105.00	1.4679	111.00	1.3804
117.00	1.2480	123.00	1.0855	129.00	0.8822	134.76	0.6352	137.76	0.5233
141.00	0.2724								

Table A.81: Axial Relative Power Distribution, 120 Second Transient, Rod Position: 98.88 inches

Z(in.)	Value	Z(in.)	Value	Z(in.)	Value	Z(in.)	Value	Z(in.)	Value
3.00	0.1766	8.76	0.4037	11.76	0.4671	15.00	0.5239	21.00	0.6302
27.00	0.7303	33.00	0.8291	39.00	0.9283	45.00	1.0277	51.00	1.1257
57.00	1.2194	63.00	1.3056	69.00	1.3802	75.00	1.4393	81.00	1.4780
87.00	1.4919	93.00	1.4766	99.00	1.4280	105.00	1.3453	111.00	1.2529
117.00	1.1419	123.00	1.0023	129.00	0.8197	134.76	0.5925	137.76	0.4887
141.00	0.2546								

Table A.82: Axial Relative Power Distribution, 120 Second Transient, Rod Position: 84.75 inches

Z(in.)	Value	Z(in.)	Value	Z(in.)	Value	Z(in.)	Value	Z(in.)	Value
3.00	0.1917	8.76	0.4377	11.76	0.5060	15.00	0.5667	21.00	0.6793
27.00	0.7835	33.00	0.8843	39.00	0.9832	45.00	1.0796	51.00	1.1714
57.00	1.2553	63.00	1.3275	69.00	1.3837	75.00	1.4196	81.00	1.4303
87.00	1.4122	93.00	1.3776	99.00	1.3375	105.00	1.2854	111.00	1.2157
117.00	1.1213	123.00	0.9933	129.00	0.8176	134.76	0.5934	137.76	0.4902
141.00	0.2556								

Table A.83: Axial Relative Power Distribution, 120 Second Transient, Rod Position: 70.63 inches

Z(in.)	Value	Z(in.)	Value	Z(in.)	Value	Z(in.)	Value	Z(in.)	Value
3.00	0.1992	8.76	0.4544	11.76	0.5250	15.00	0.5872	21.00	0.7015
27.00	0.8055	33.00	0.9041	39.00	0.9984	45.00	1.0875	51.00	1.1689
57.00	1.2390	63.00	1.2938	69.00	1.3288	75.00	1.3407	81.00	1.3493
87.00	1.3548	93.00	1.3523	99.00	1.3371	105.00	1.3043	111.00	1.2482
117.00	1.1619	123.00	1.0363	129.00	0.8572	134.76	0.6241	137.76	0.5161
141.00	0.2692								

Table A.84: Axial Relative Power Distribution, 120 Second Transient, Rod Position: 56.50 inches

Z(in.)	Value	Z(in.)	Value	Z(in.)	Value	Z(in.)	Value	Z(in.)	Value
3.00	0.1979	8.76	0.4510	11.76	0.5206	15.00	0.5814	21.00	0.6923
27.00	0.7913	33.00	0.8829	39.00	0.9680	45.00	1.0454	51.00	1.1124
57.00	1.1653	63.00	1.2049	69.00	1.2493	75.00	1.2939	81.00	1.3340
87.00	1.3656	93.00	1.3846	99.00	1.3864	105.00	1.3660	111.00	1.3176
117.00	1.2338	123.00	1.1053	129.00	0.9171	134.76	0.6690	137.76	0.5537
141.00	0.2889								

Table A.85: Axial Relative Power Distribution, 120 Second Transient, Rod Position: 42.38 inches

Z(in.)	Value	Z(in.)	Value	Z(in.)	Value	Z(in.)	Value	Z(in.)	Value
3.00	0.1873	8.76	0.4264	11.76	0.4918	15.00	0.5485	21.00	0.6507
27.00	0.7400	33.00	0.8205	39.00	0.8926	45.00	0.9553	51.00	1.0180
57.00	1.0870	63.00	1.1590	69.00	1.2308	75.00	1.2989	81.00	1.3593
87.00	1.4081	93.00	1.4411	99.00	1.4537	105.00	1.4406	111.00	1.3957
117.00	1.3114	123.00	1.1778	129.00	0.9789	134.76	0.7149	137.76	0.5919
141.00	0.3089								

Table A.86: Axial Relative Power Distribution, 120 Second Transient, Rod Position: 28.25 inches

Z(in.)	Value	Z(in.)	Value	Z(in.)	Value	Z(in.)	Value	Z(in.)	Value
3.00	0.1711	8.76	0.3890	11.76	0.4484	15.00	0.4994	21.00	0.5905
27.00	0.6683	33.00	0.7369	39.00	0.8103	45.00	0.8902	51.00	0.9754
57.00	1.0635	63.00	1.1523	69.00	1.2389	75.00	1.3201	81.00	1.3919
87.00	1.4503	93.00	1.4911	99.00	1.5095	105.00	1.5000	111.00	1.4564
117.00	1.3706	123.00	1.2324	129.00	1.0251	134.76	0.7490	137.76	0.6203
141.00	0.3238								

Table A.87: Axial Relative Power Distribution, 120 Second Transient, Rod Position: 14.13 inches

Z(in.)	Value	Z(in.)	Value	Z(in.)	Value	Z(in.)	Value	Z(in.)	Value
3.00	0.1519	8.76	0.3452	11.76	0.3977	15.00	0.4427	21.00	0.5246
27.00	0.6049	33.00	0.6880	39.00	0.7753	45.00	0.8671	51.00	0.9627
57.00	1.0602	63.00	1.1575	69.00	1.2516	75.00	1.3395	81.00	1.4171
87.00	1.4805	93.00	1.5251	99.00	1.5464	105.00	1.5386	111.00	1.4953
117.00	1.4082	123.00	1.2669	129.00	1.0542	134.76	0.7704	137.76	0.6381
141.00	0.3331								

Table A.88: Axial Relative Power Distribution, 120 Second Transient, Rod Position: 0.00 inches

Z(in.)	Value	Z(in.)	Value	Z(in.)	Value	Z(in.)	Value	Z(in.)	Value
3.00	0.1386	8.76	0.3168	11.76	0.3676	15.00	0.4141	21.00	0.5023
27.00	0.5880	33.00	0.6756	39.00	0.7669	45.00	0.8623	51.00	0.9610
57.00	1.0613	63.00	1.1611	69.00	1.2575	75.00	1.3474	81.00	1.4267
87.00	1.4916	93.00	1.5374	99.00	1.5595	105.00	1.5521	111.00	1.5088
117.00	1.4212	123.00	1.2788	129.00	1.0642	134.76	0.7778	137.76	0.6442
141.00	0.3363								

Appendix B

Steady-State Library Results (Continued)

B.1 2 Second Insertion Transient Using the 10 Entry Steady-State Library and the 10 Output Exact Solution

For the 2 second transient utilizing the 10 record steady-state library and the 10 record transient solution, the following results were obtained regarding the flux error and precursor error equations developed in Chapter 2 (See section 2.1.6). The flux error and error components at the maximum flux position and maximum flux error position, locally and averaged normalized results can be viewed in Figure B.1-Figure B.8. The precursor group concentration error and error components at the maximum precursor group concentration position and the maximum precursor group concentration error position, locally and averaged normalized, results can be viewed in Figure B.9 - Figure B.32.

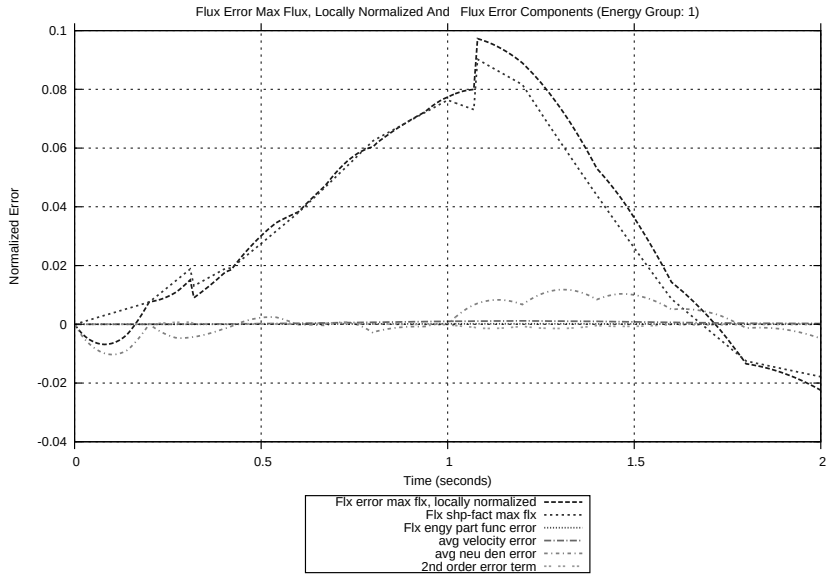

Figure B.1: Flux Error and Error Components at the Maximum Flux Position Locally Normalized (Group: 1, 10 SS, 10 Trans)

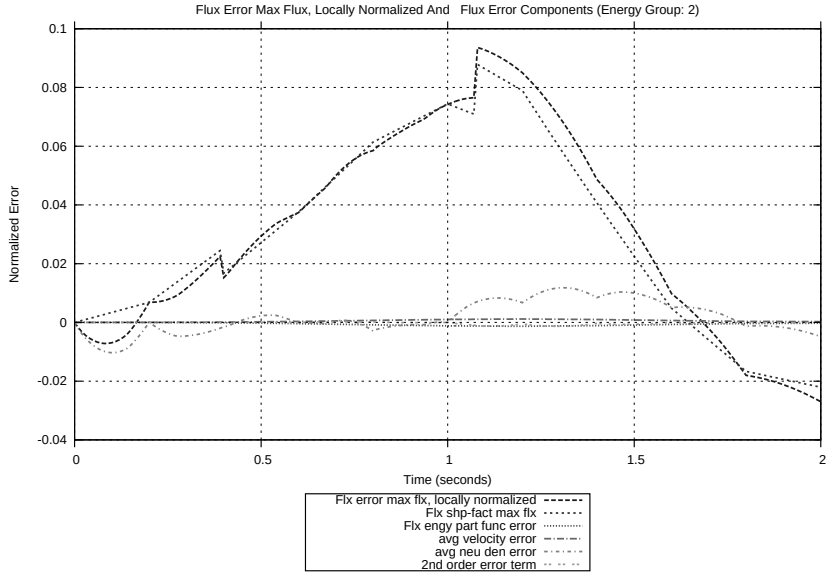

Figure B.2: Flux Error and Error Components at the Maximum Flux Position Locally Normalized (Group: 2, 10 SS, 10 Trans)

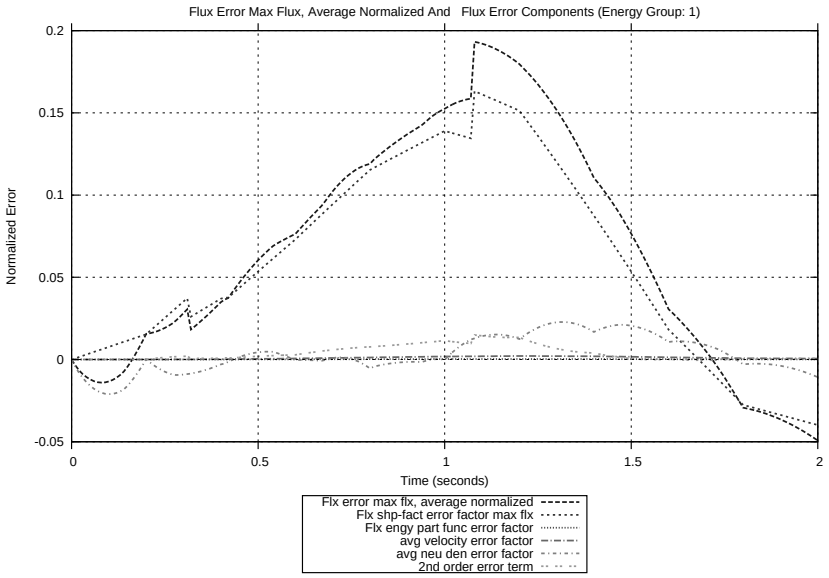

Figure B.3: Flux Error and Error Components at the Maximum Flux Position Average Normalized (Group: 1, 10 SS, 10 Trans)

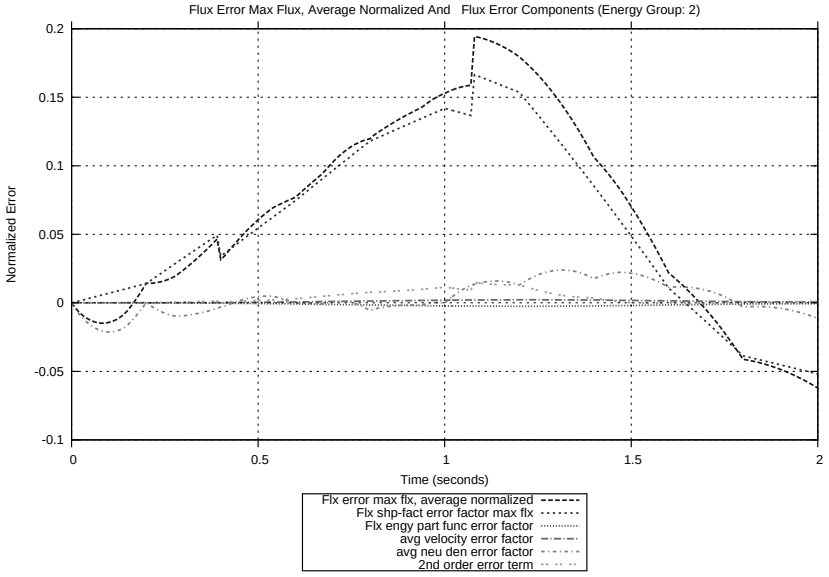

Figure B.4: Flux Error and Error Components at the Maximum Flux Position Average Normalized (Group: 2, 10 SS, 10 Trans)

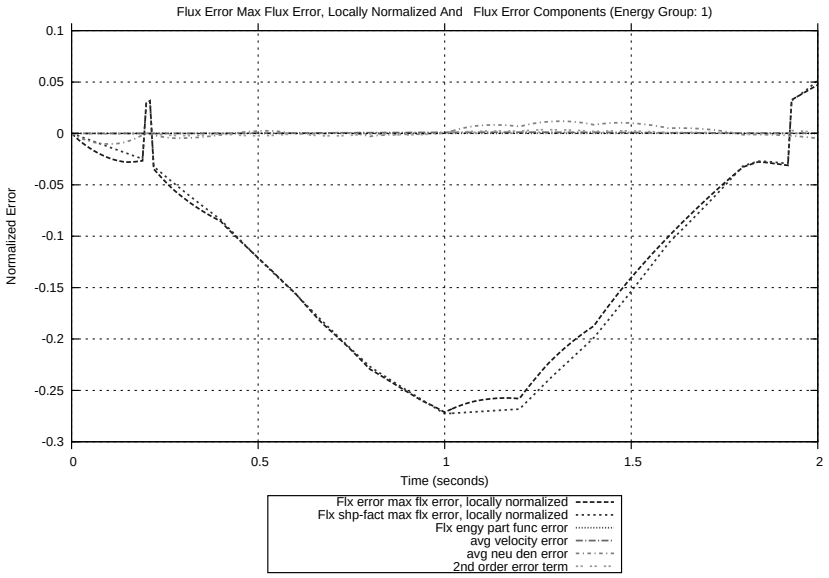

Figure B.5: Flux Error and Error Components at the Maximum Flux Error Position Locally Normalized (Group: 1, 10 SS, 10 Trans)

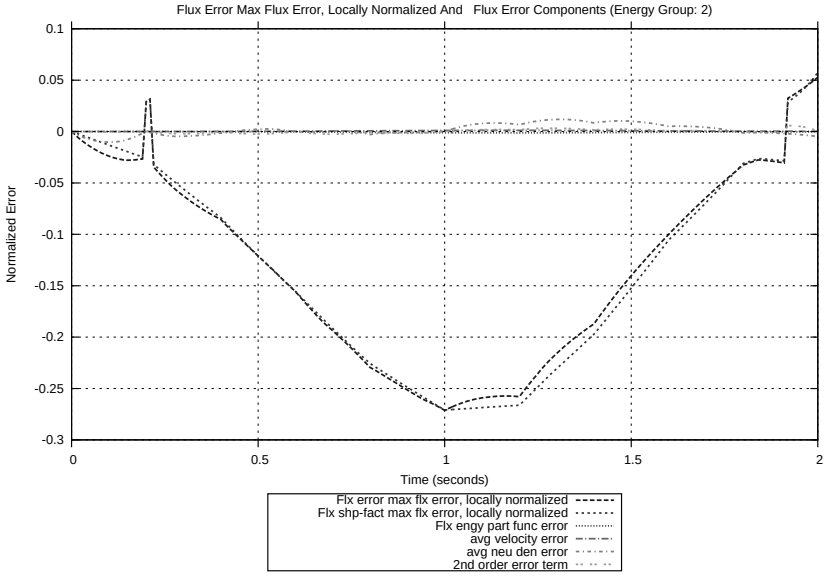

Figure B.6: Flux Error and Error Components at the Maximum Flux Position Locally Normalized (Group: 2, 10 SS, 10 Trans)

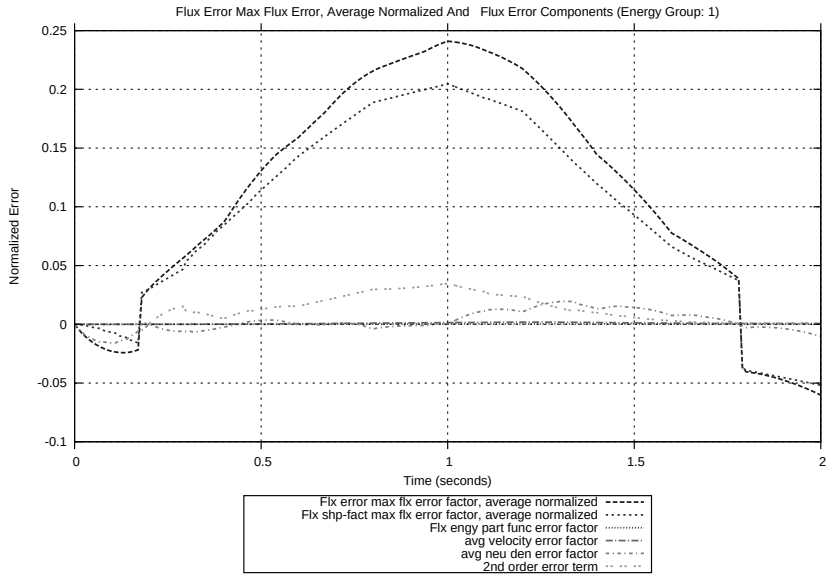

Figure B.7: Flux Error and Error Components at the Maximum Flux Error Position Average Normalized (Group: 1, 10 SS, 10 Trans)

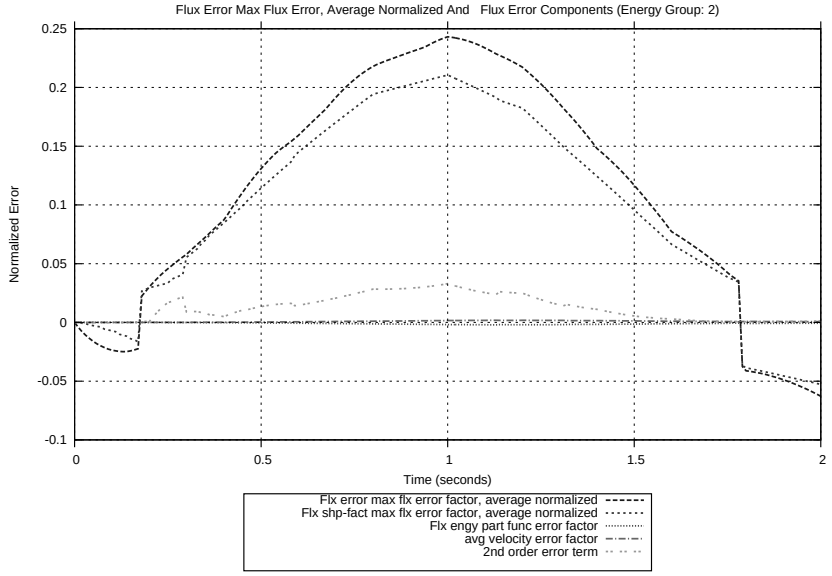

Figure B.8: Flux Error and Error Components at the Maximum Flux Position Average Normalized (Group: 2, 10 SS, 10 Trans)

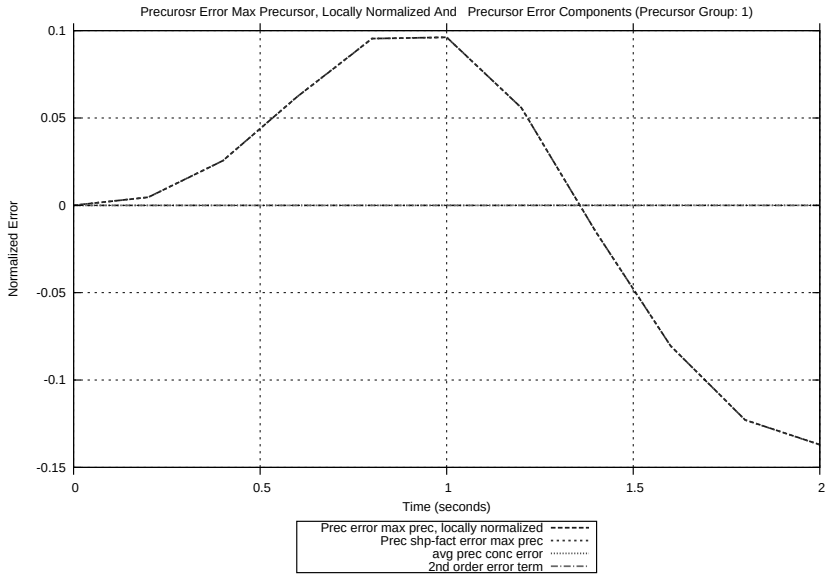

Figure B.9: Precursor Concentration Error and Error Components at the Maximum Precursor Concentration Position Locally Normalized (Group: 1, 10 SS, 10 Trans)

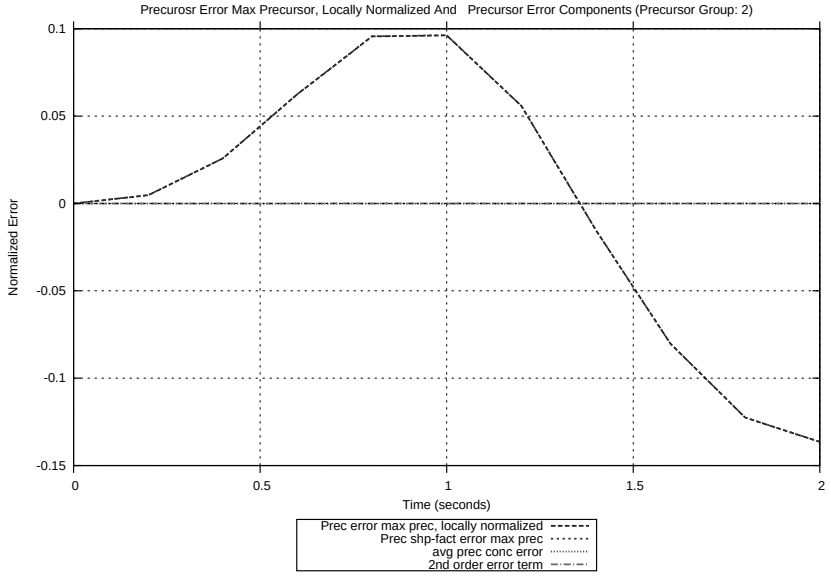

Figure B.10: Precursor Concentration Error and Error Components at the Maximum Precursor Concentration Position Locally Normalized (Group: 2, 10 SS, 10 Trans)

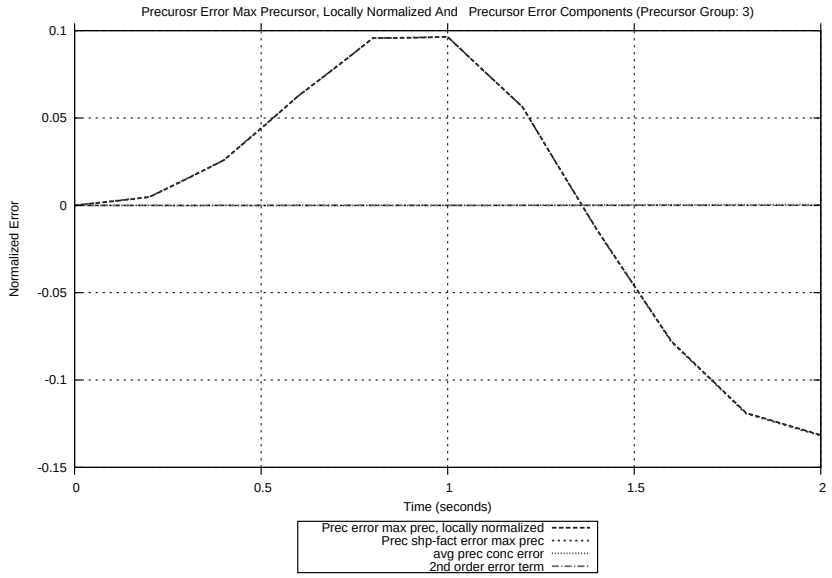

Figure B.11: Precursor Concentration Error and Error Components at the Maximum Precursor Concentration Position Locally Normalized (Group: 3, 10 SS, 10 Trans)

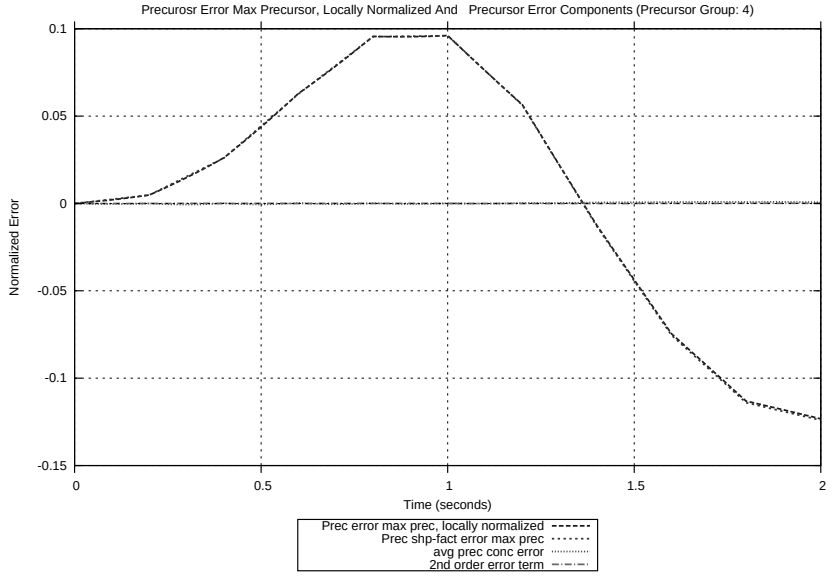

Figure B.12: Precursor Concentration Error and Error Components at the Maximum Precursor Concentration Position Locally Normalized (Group: 4, 10 SS, 10 Trans)

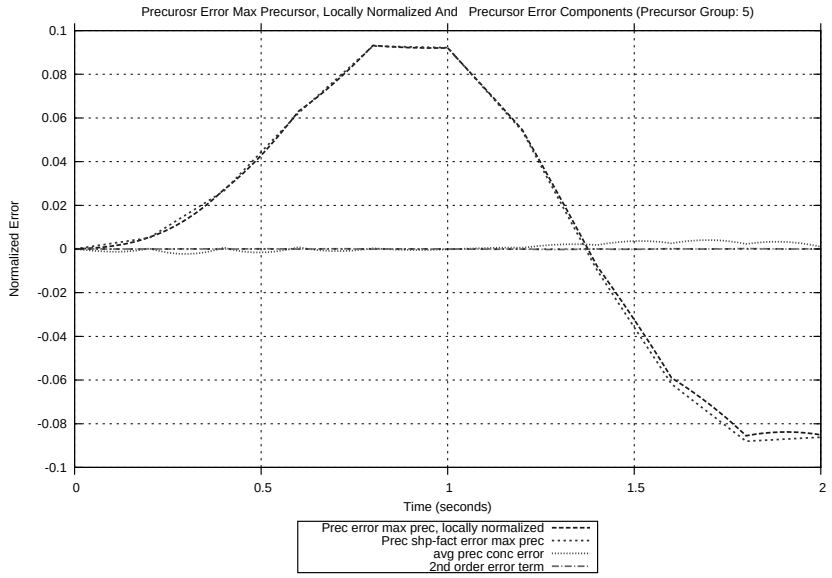

Figure B.13: Precursor Concentration Error and Error Components at the Maximum Precursor Concentration Position Locally Normalized (Group: 5, 10 SS, 10 Trans)

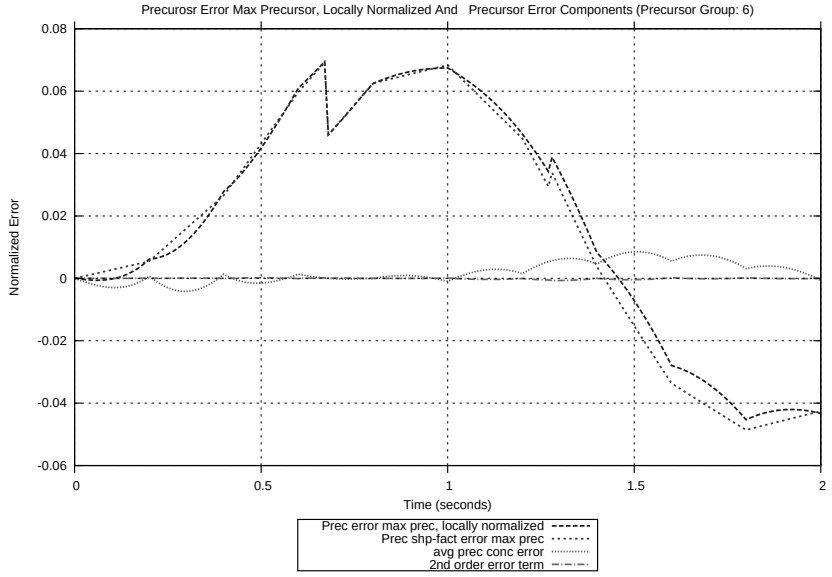

Figure B.14: Precursor Concentration Error and Error Components at the Maximum Precursor Concentration Position Locally Normalized (Group: 6, 10 SS, 10 Trans)

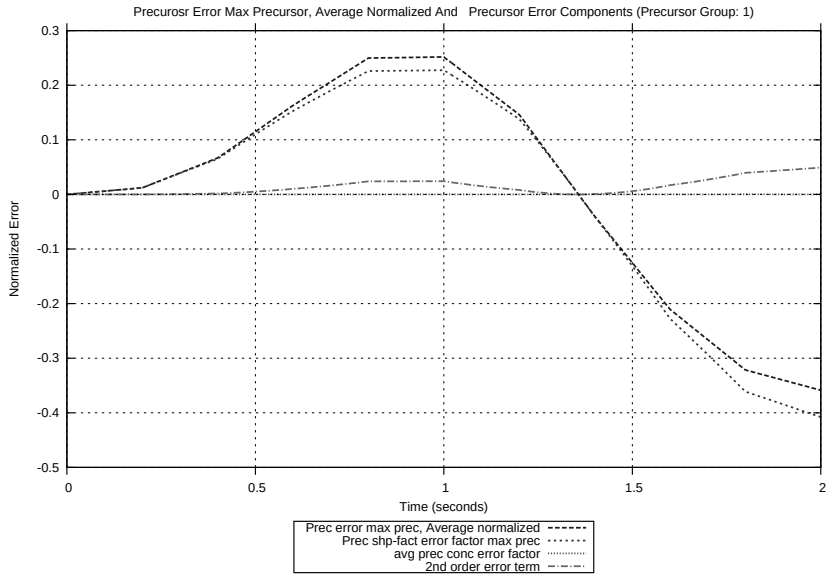

Figure B.15: Precursor Concentration Error and Error Components at the Maximum Precursor Concentration Position Average Normalized (Group: 1, 10 SS, 10 Trans)

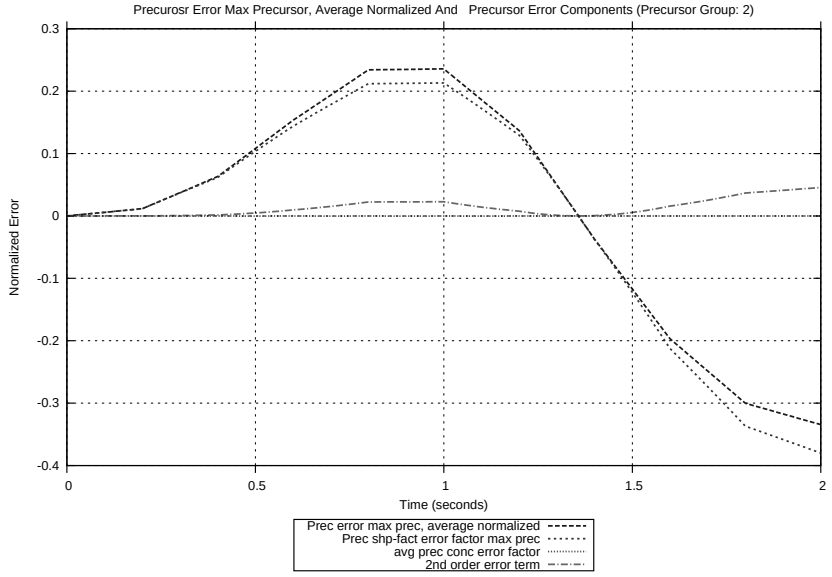

Figure B.16: Precursor Concentration Error and Error Components at the Maximum Precursor Concentration Position Average Normalized (Group: 2, 10 SS, 10 Trans)

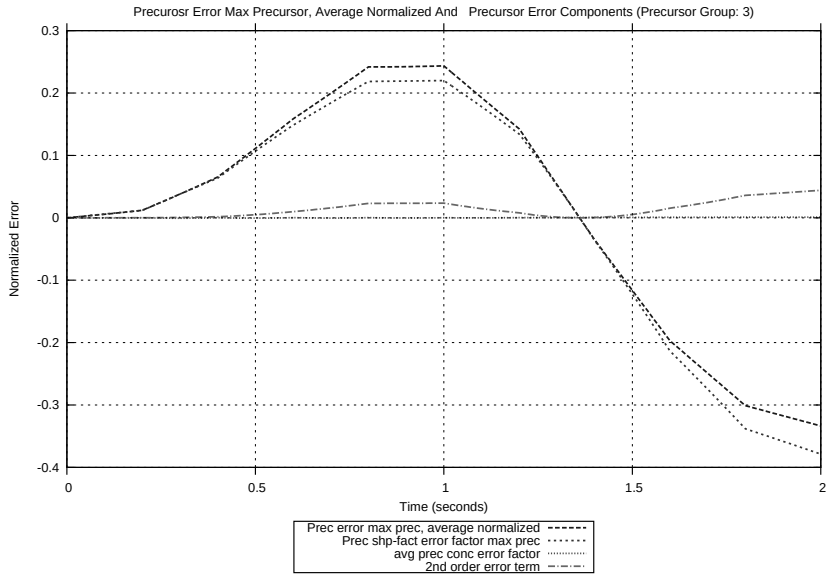

Figure B.17: Precursor Concentration Error and Error Components at the Maximum Precursor Concentration Position Average Normalized (Group: 3, 10 SS, 10 Trans)

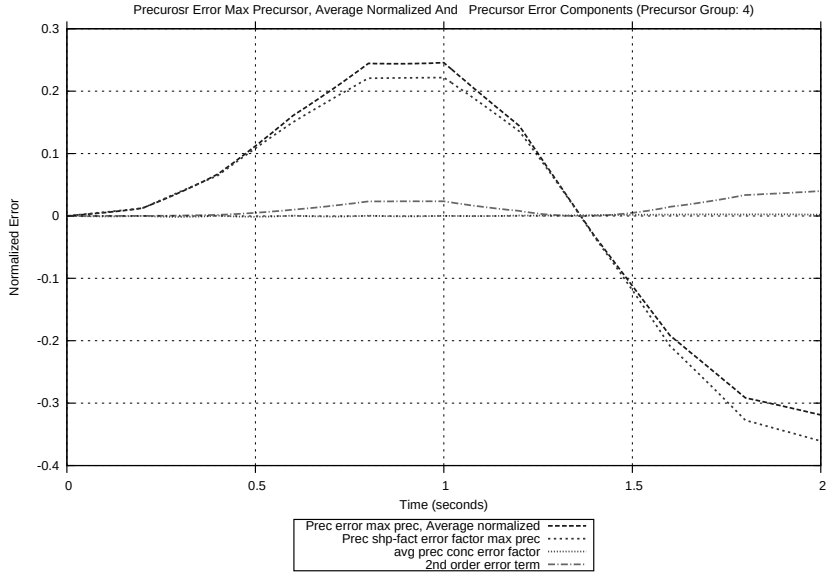

Figure B.18: Precursor Concentration Error and Error Components at the Maximum Precursor Concentration Position Average Normalized (Group: 4, 10 SS, 10 Trans)

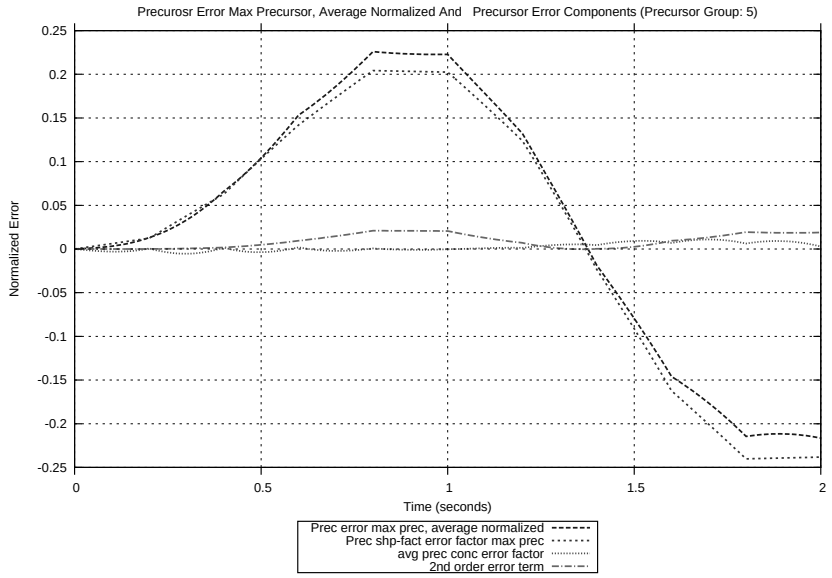

Figure B.19: Precursor Concentration Error and Error Components at the Maximum Precursor Concentration Position Average Normalized (Group: 5, 10 SS, 10 Trans)

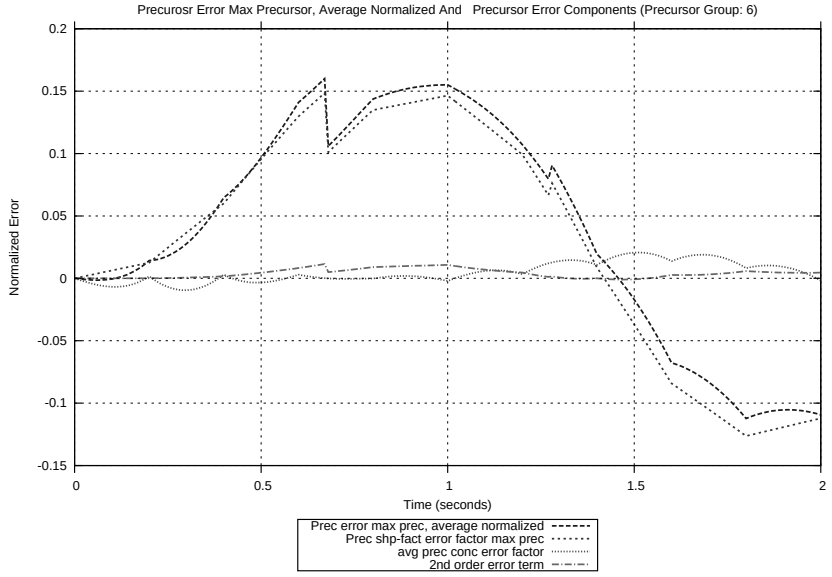

Figure B.20: Precursor Concentration Error and Error Components at the Maximum Precursor Concentration Position Average Normalized (Group: 6, 10 SS, 10 Trans)

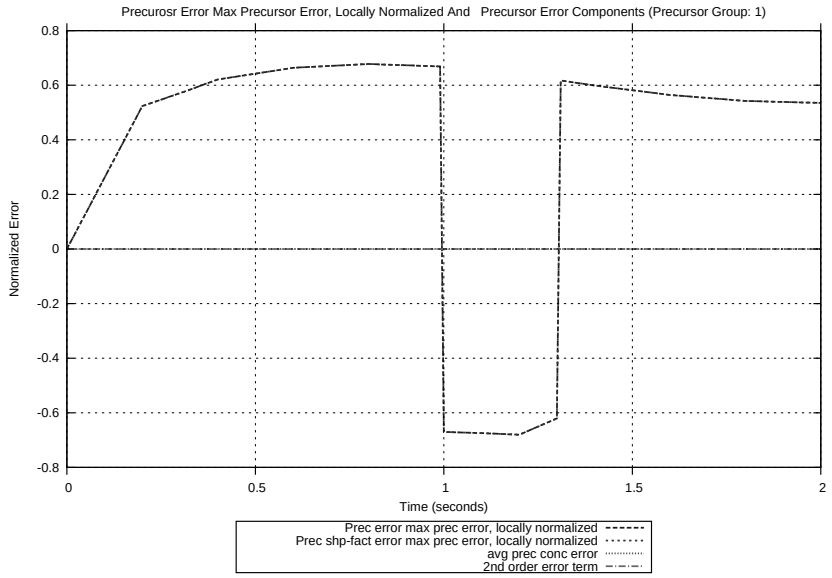

Figure B.21: Precursor Concentration Error and Error Components at the Maximum Precursor Concentration Error Position Locally Normalized (Group: 1, 10 SS, 10 Trans)

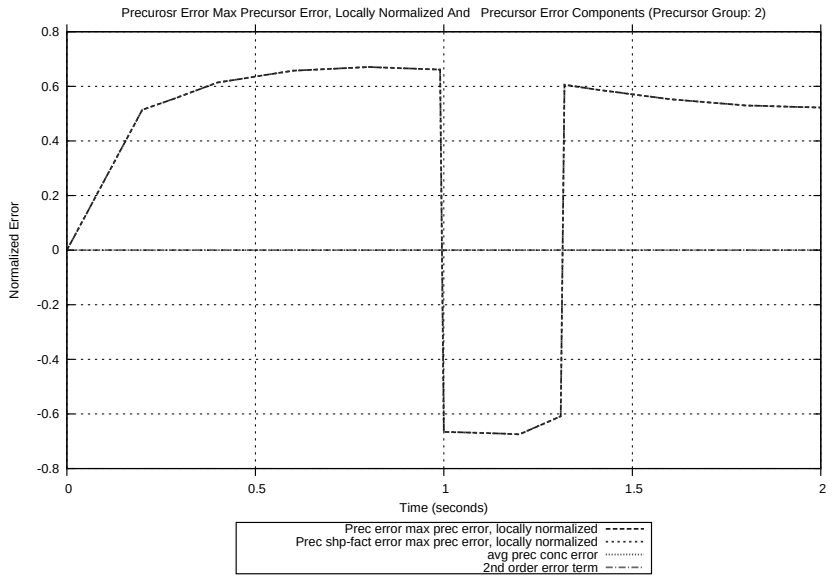

Figure B.22: Precursor Concentration Error and Error Components at the Maximum Precursor Concentration Error Position Locally Normalized (Group: 2, 10 SS, 10 Trans)

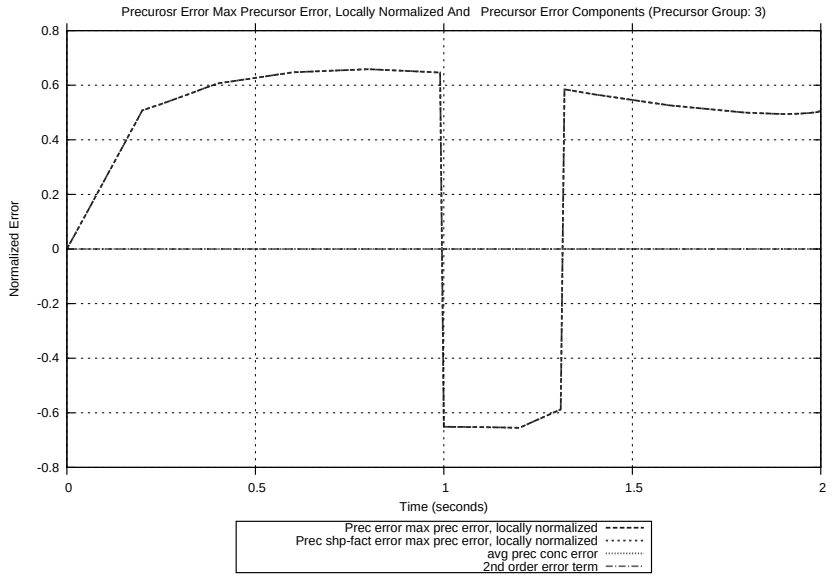

Figure B.23: Precursor Concentration Error and Error Components at the Maximum Precursor Concentration Error Position Locally Normalized (Group: 3, 10 SS, 10 Trans)

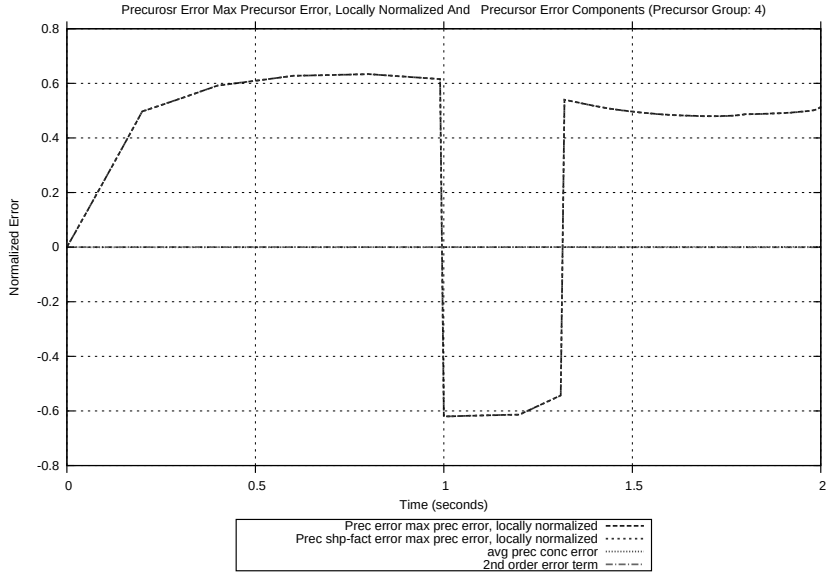

Figure B.24: Precursor Concentration Error and Error Components at the Maximum Precursor Concentration Error Position Locally Normalized (Group: 4, 10 SS, 10 Trans)

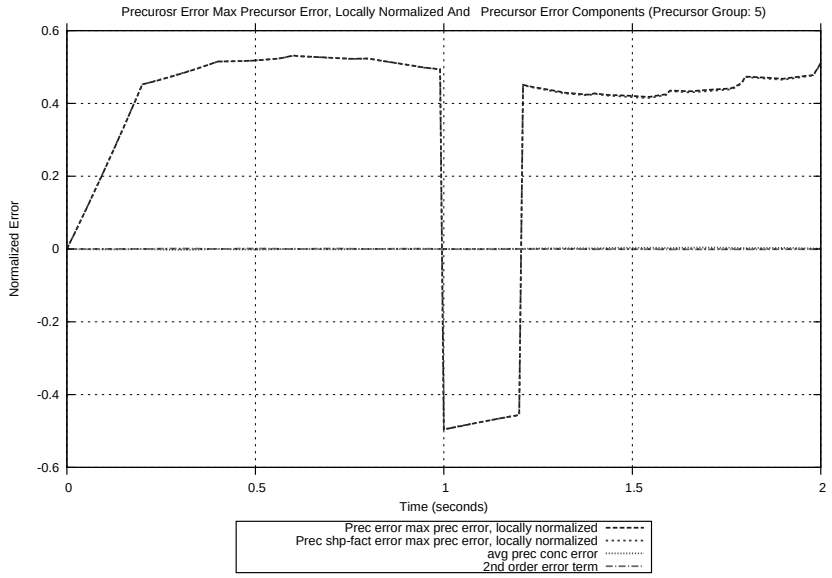

Figure B.25: Precursor Concentration Error and Error Components at the Maximum Precursor Concentration Error Position Locally Normalized (Group: 5, 10 SS, 10 Trans)

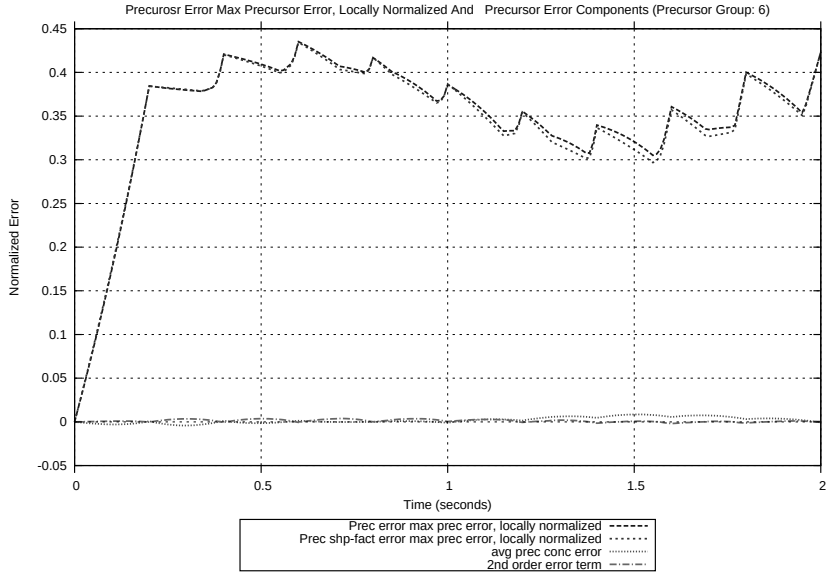

Figure B.26: Precursor Concentration Error and Error Components at the Maximum Precursor Concentration Error Position Locally Normalized (Group: 6, 10 SS, 10 Trans)

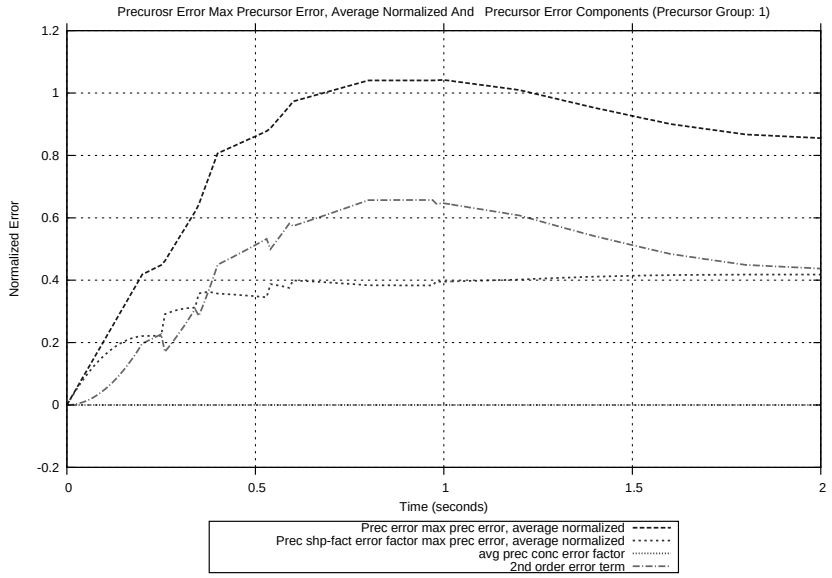

Figure B.27: Precursor Concentration Error and Error Components at the Maximum Precursor Concentration Error Position Average Normalized (Group: 1, 10 SS, 10 Trans)

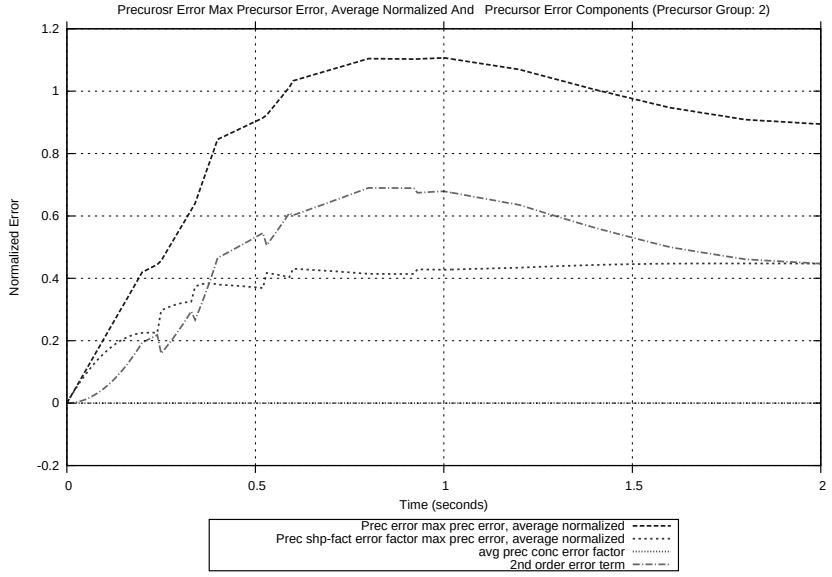

Figure B.28: Precursor Concentration Error and Error Components at the Maximum Precursor Concentration Error Position Average Normalized (Group: 2, 10 SS, 10 Trans)

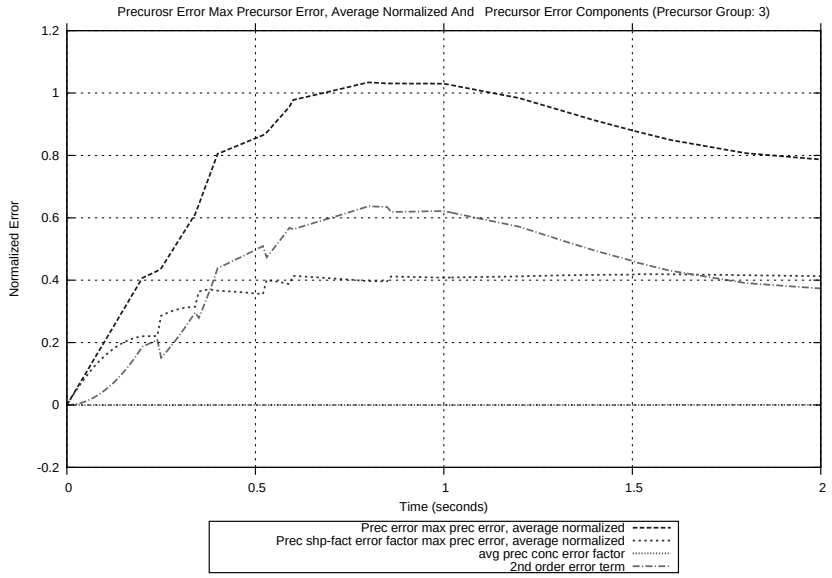

Figure B.29: Precursor Concentration Error and Error Components at the Maximum Precursor Concentration Error Position Average Normalized (Group: 3, 10 SS, 10 Trans)

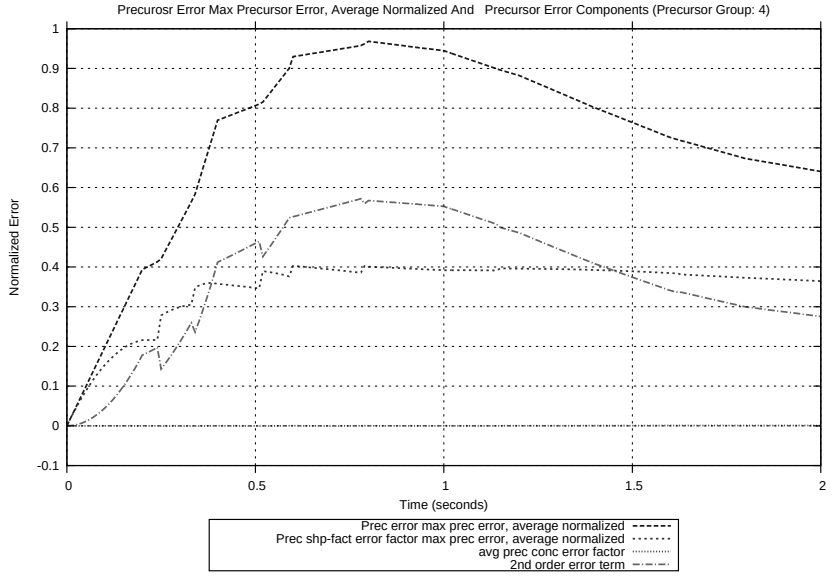

Figure B.30: Precursor Concentration Error and Error Components at the Maximum Precursor Concentration Error Position Average Normalized (Group: 4, 10 SS, 10 Trans)

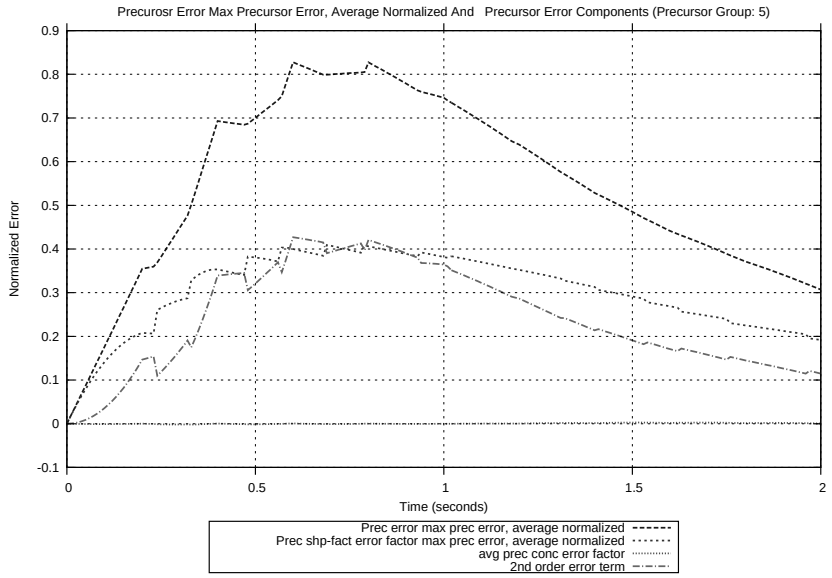

Figure B.31: Precursor Concentration Error and Error Components at the Maximum Precursor Concentration Error Position Average Normalized (Group: 5, 10 SS, 10 Trans)

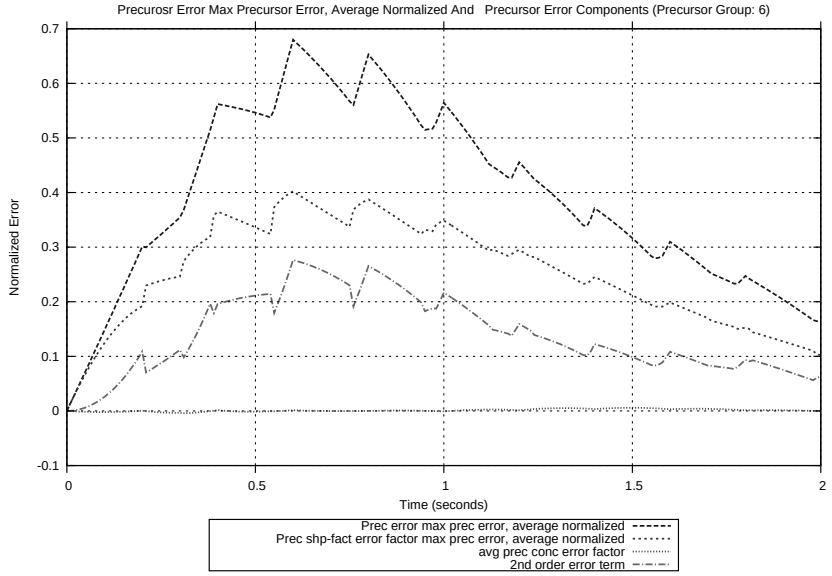

Figure B.32: Precursor Concentration Error and Error Components at the Maximum Precursor Concentration Error Position Average Normalized (Group: 6, 10 SS, 10 Trans)

B.2 2 Second Insertion Transient Using the 10 Entry Steady-State Library and the 40 Output Exact Solution

For the 2 second transient utilizing the 10 record steady-state library and the 40 record transient solution, the following results were obtained regarding the flux error and precursor error equations. The average normalized flux and precursor group concentration error values at the maximum and maximum error positions are viewable in Figure B.34 - Figure B.35 and Figure B.36 - Figure B.37, respectively. Also, the L2 error flux and precursor group concentration values can be observed in Figure B.33 and Figure B.38, respectively.

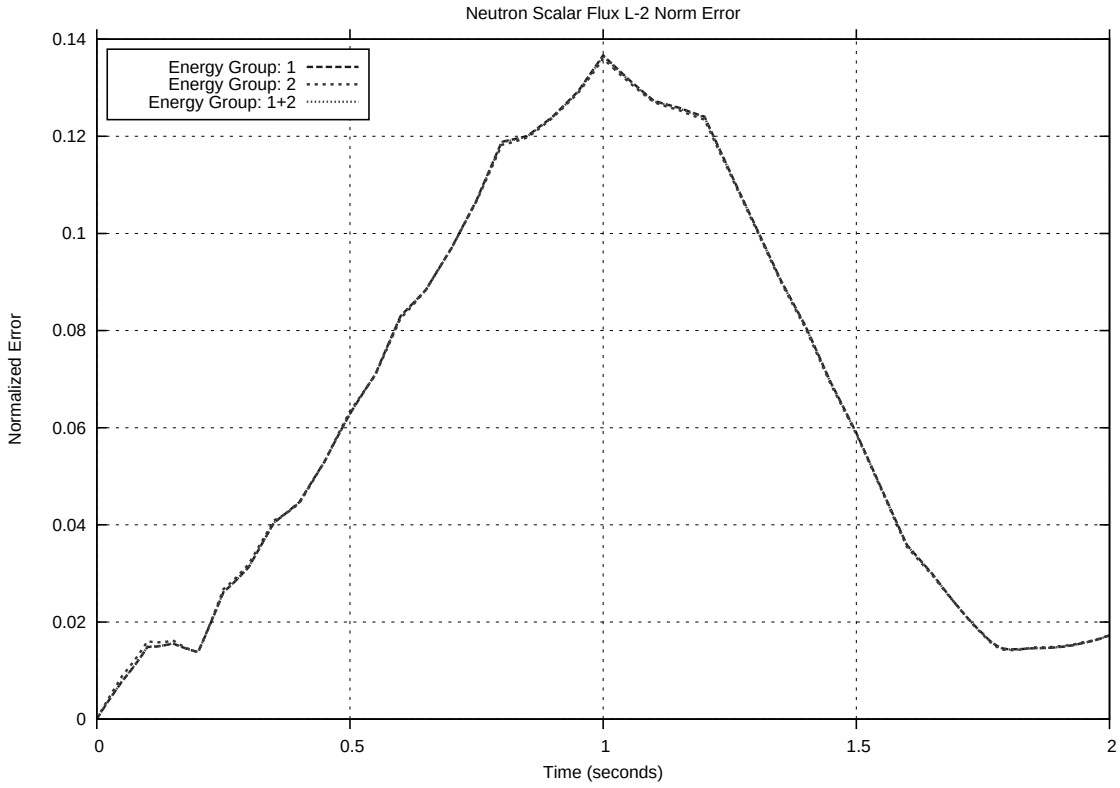

Figure B.33: Flux L2-Error (10 SS, 40 Trans)

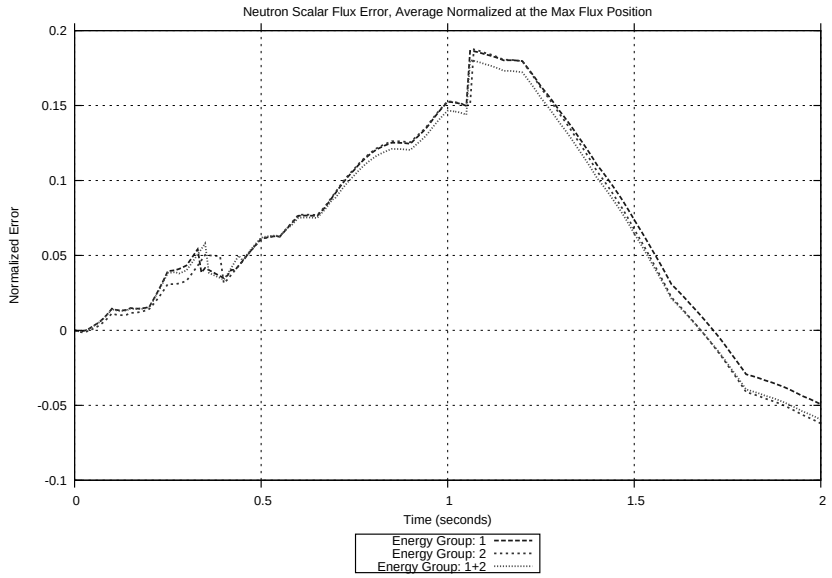

Figure B.34: Average Normalized Flux Error at the Maximum Flux Position (10 SS, 40 Trans)

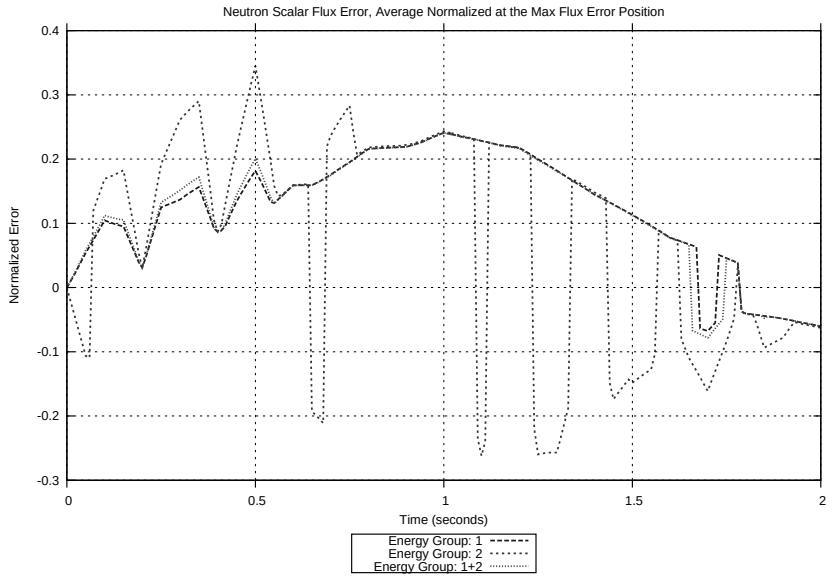

Figure B.35: Average Normalized Flux Error at the Maximum Flux Error Position (10 SS, 40 Trans)

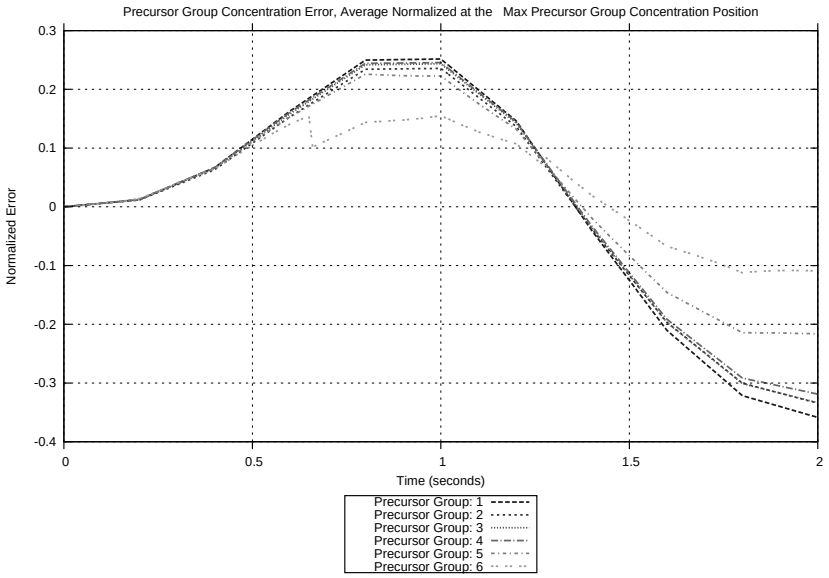

Figure B.36: Average Normalized Precursor Group Concentration Error at the Maximum Precursor Group Concentration Position (10 SS, 40 Trans)

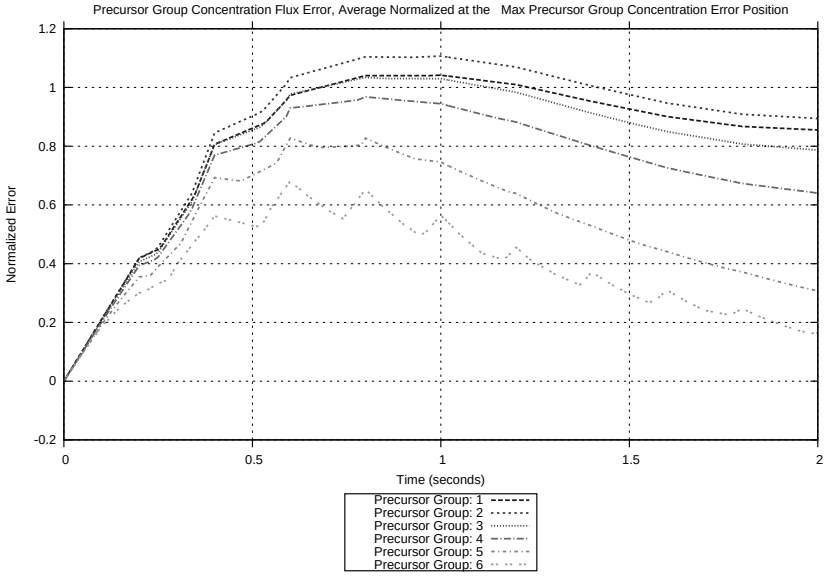

Figure B.37: Average Normalized Precursor Group Concentration Error at the Maximum Precursor Group Concentration Error Position (10 SS, 40 Trans)

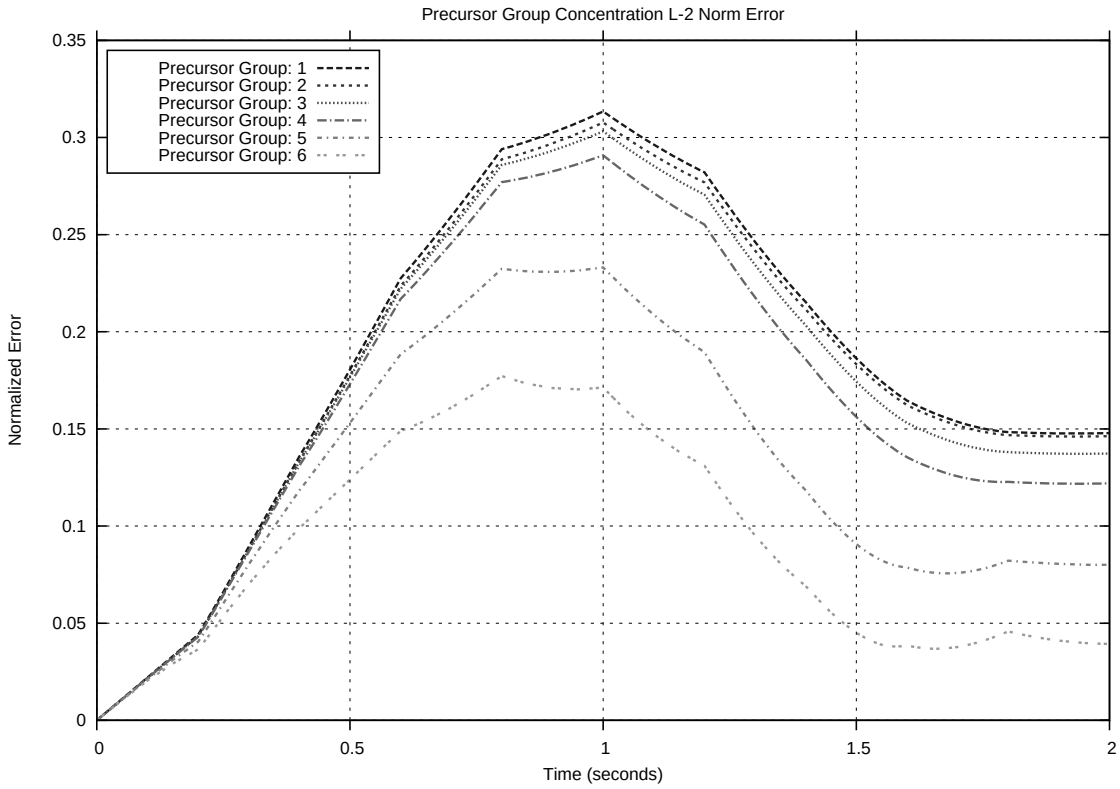

Figure B.38: Precursor Group Concentration L2-Error (10 SS, 40 Trans)

B.3 2 Second Insertion Transient Using the 25 Entry Steady-State Library and the 10 Output Exact Solution

For the 2 second transient utilizing the 25 record steady-state library and the 10 record transient solution, the following results were obtained regarding the flux error and precursor error equations. The average normalized flux and precursor group concentration error values at the maximum and maximum error positions are viewable in Figure B.40 - Figure B.41 and Figure B.42 - Figure B.43, respectively. Also, the L2 error flux and precursor group concentration values can be observed in Figure B.39 and Figure B.44, respectively.

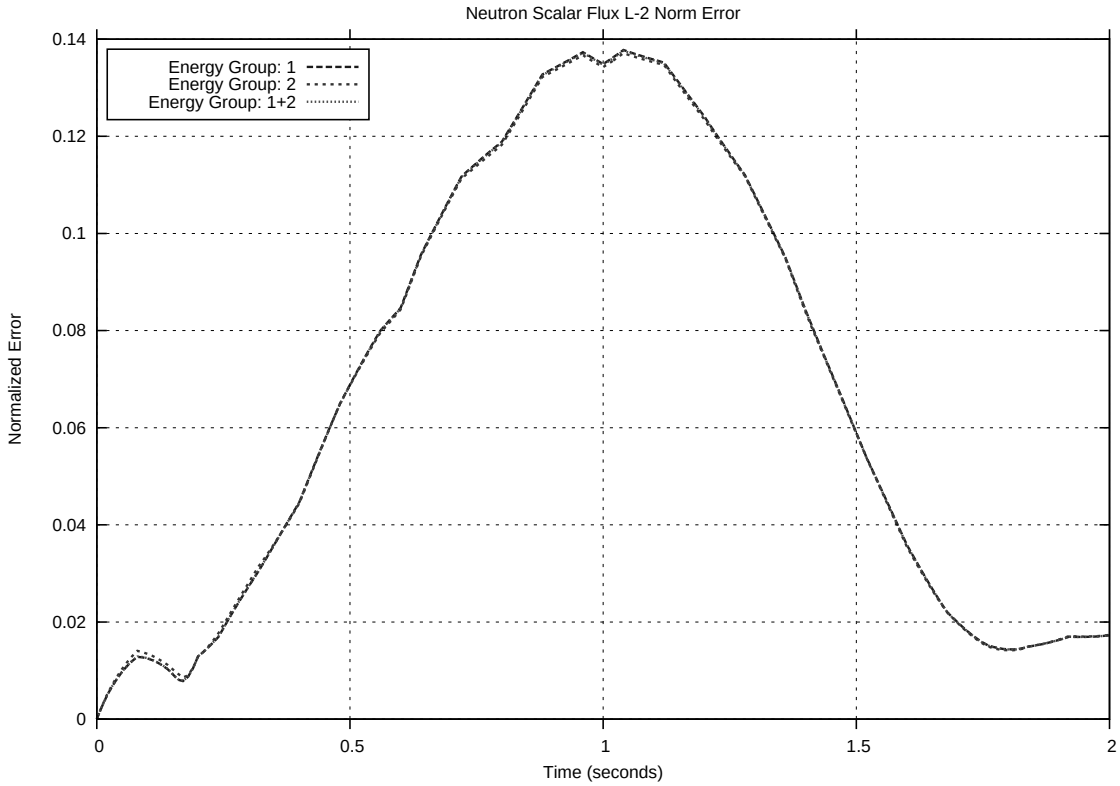

Figure B.39: Flux L2-Error (25 SS, 10 Trans)

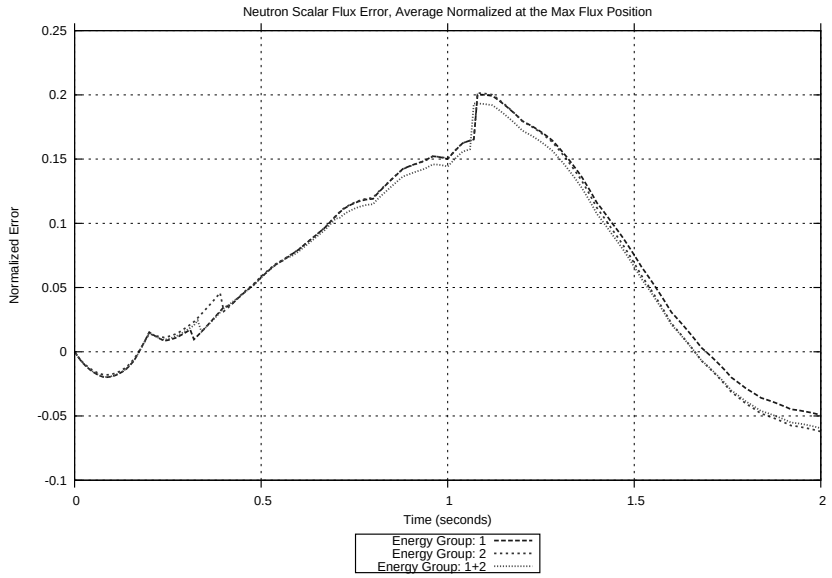

Figure B.40: Average Normalized Flux Error at the Maximum Flux Position (25 SS, 10 Trans)

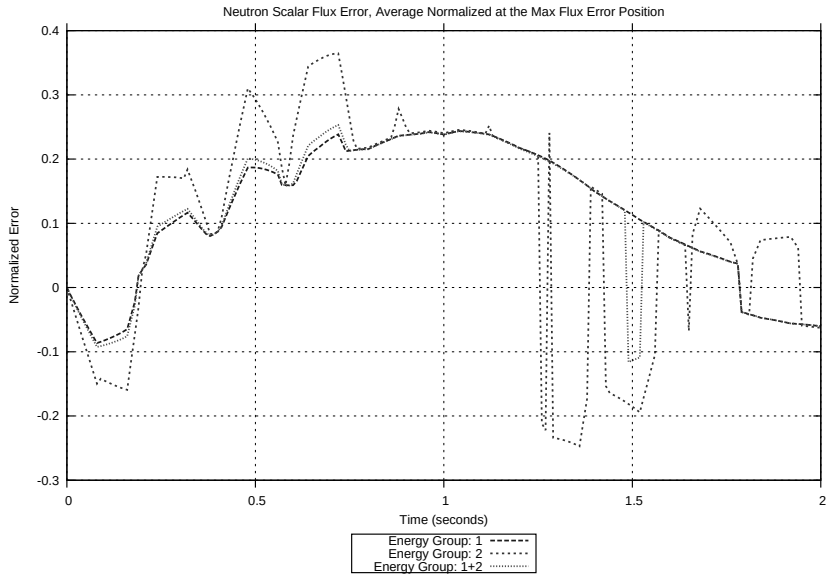

Figure B.41: Average Normalized Flux Error at the Maximum Flux Error Position (25 SS, 10 Trans)

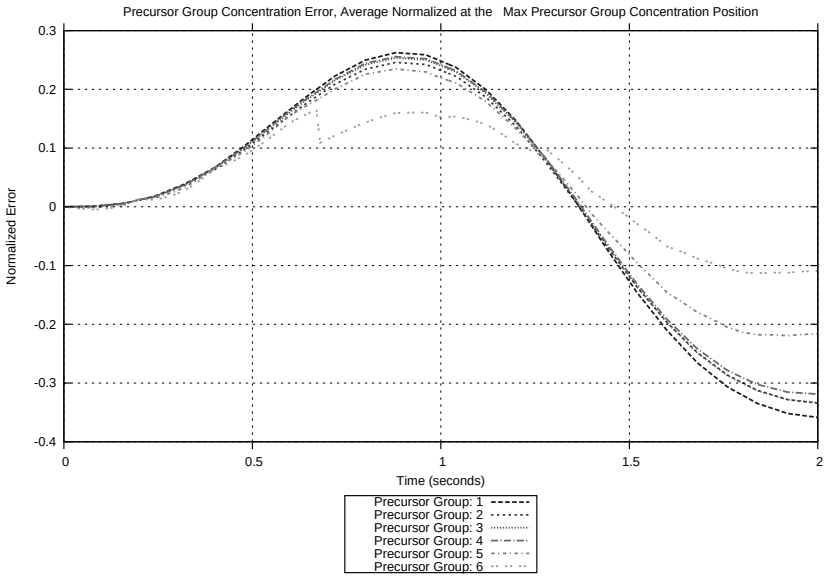

Figure B.42: Average Normalized Precursor Group Concentration Error at the Maximum Precursor Group Concentration Position (25 SS, 10 Trans)

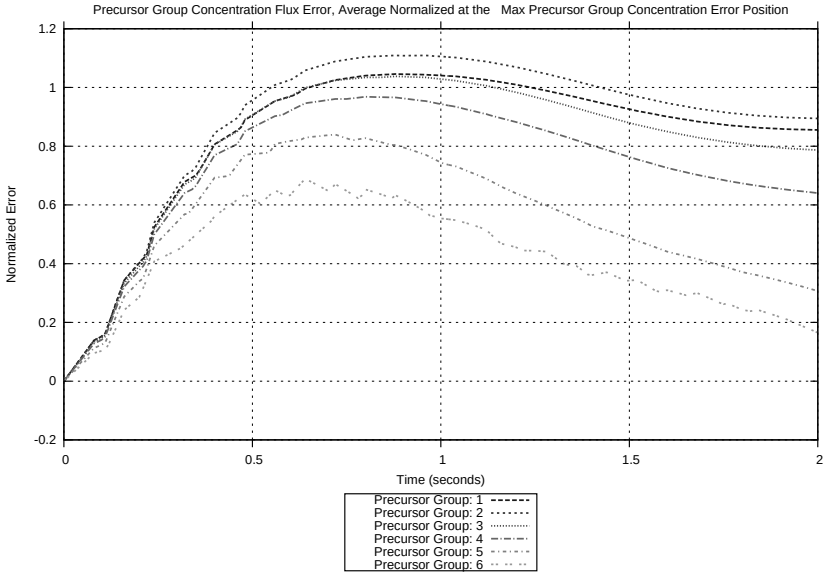

Figure B.43: Average Normalized Precursor Group Concentration Error at the Maximum Precursor Group Concentration Error Position (25 SS, 10 Trans)

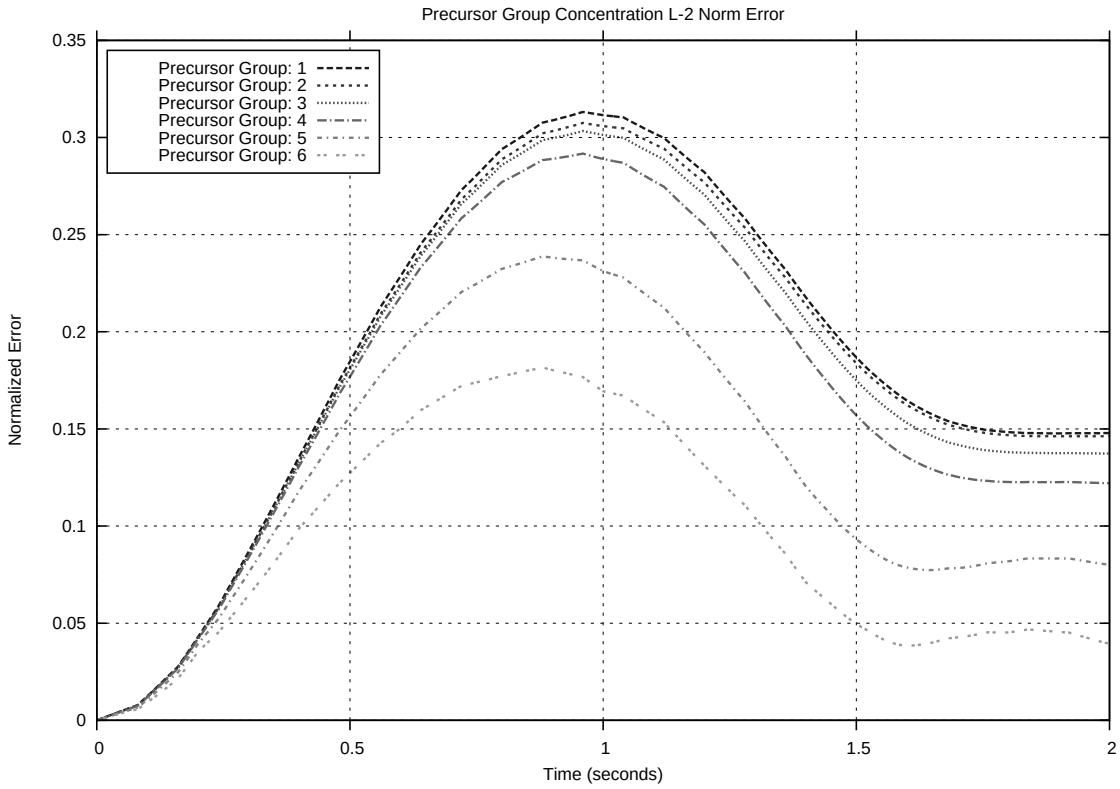

Figure B.44: Precursor Group Concentration L2-Error (25 SS, 10 Trans)

B.4 2 Second Insertion Transient Using the 25 Entry Steady-State Library and the 40 Output Exact Solution

For the 2 second transient utilizing the 25 record steady-state library and the 40 record transient solution, the following results were obtained regarding the flux error and precursor error equations. The average normalized flux and precursor group concentration error values at the maximum and maximum error positions are viewable in Figure B.46 - Figure B.47 and Figure B.48 - Figure B.49, respectively. Also, the L2 error flux and precursor group concentration values can be observed in Figure B.45 and Figure B.50, respectively.

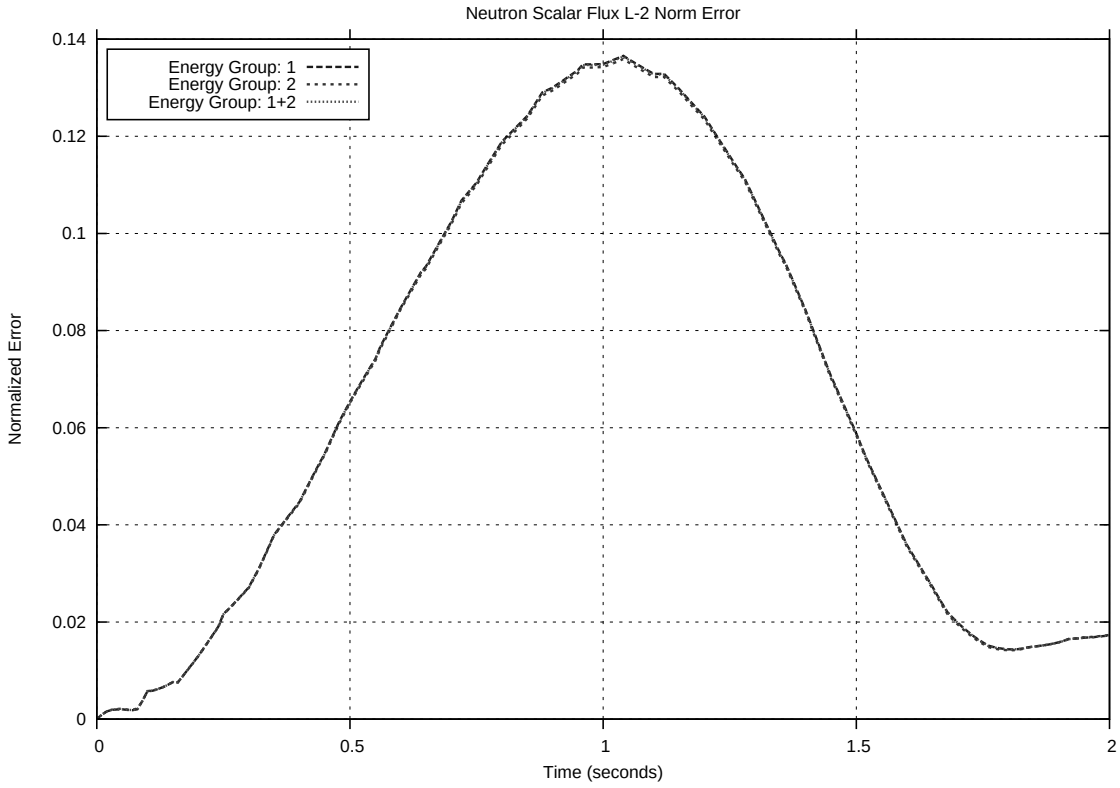

Figure B.45: Flux L2-Error (25 SS, 40 Trans)

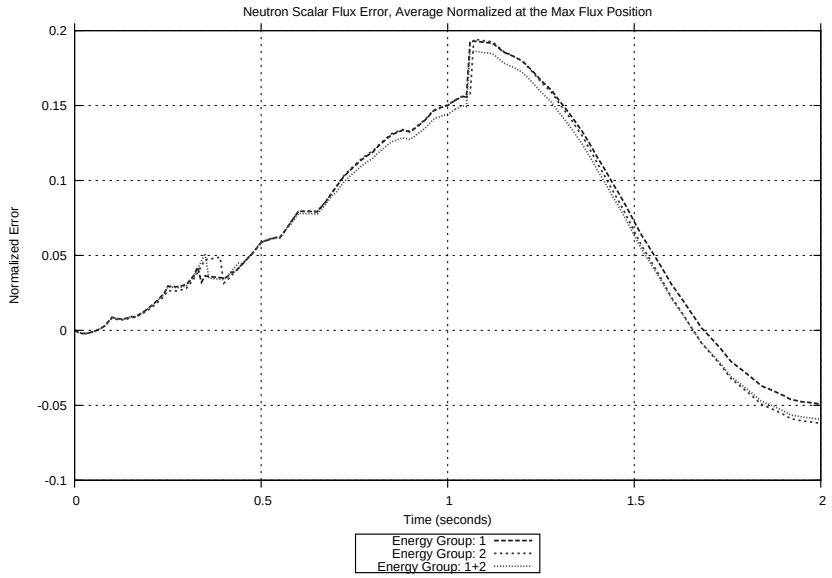

Figure B.46: Average Normalized Flux Error at the Maximum Flux Position (25 SS, 40 Trans)

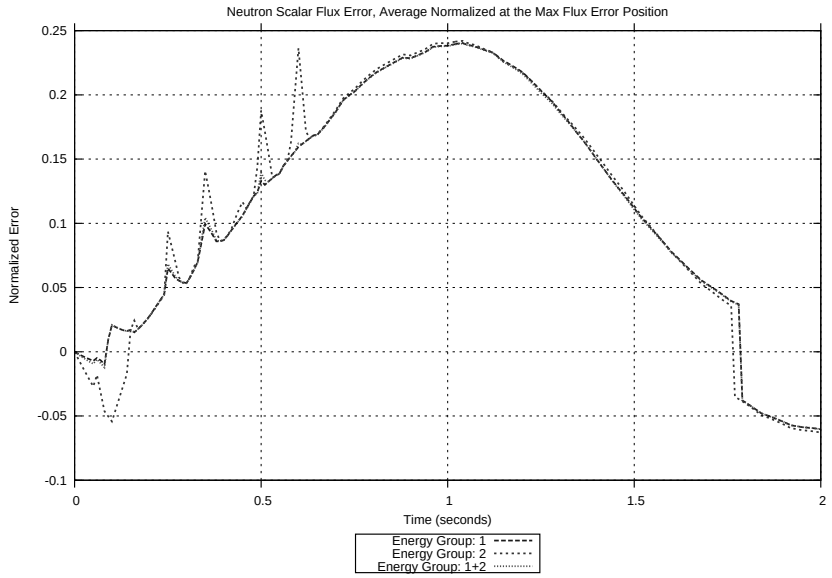

Figure B.47: Average Normalized Flux Error at the Maximum Flux Error Position (25 SS, 40 Trans)

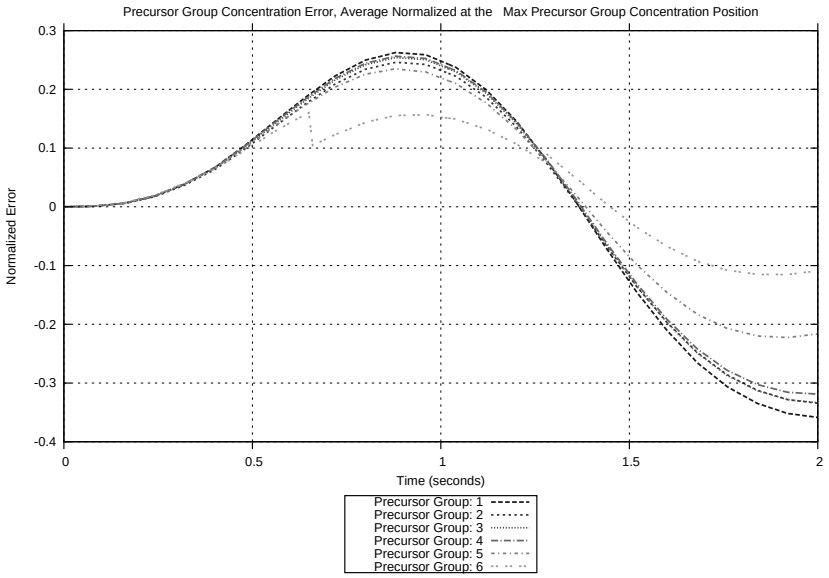

Figure B.48: Average Normalized Precursor Group Concentration Error at the Maximum Precursor Group Concentration Position (25 SS, 40 Trans)

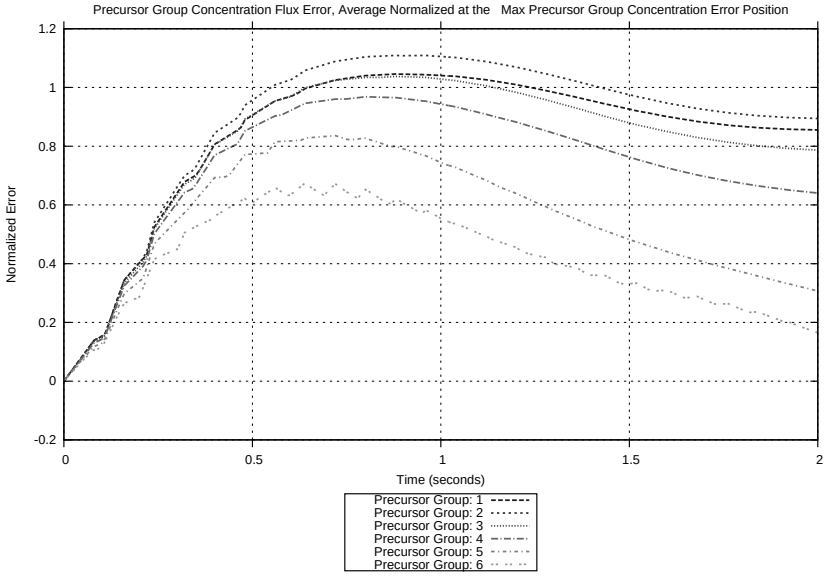

Figure B.49: Average Normalized Precursor Group Concentration Error at the Maximum Precursor Group Concentration Error Position (25 SS, 40 Trans)

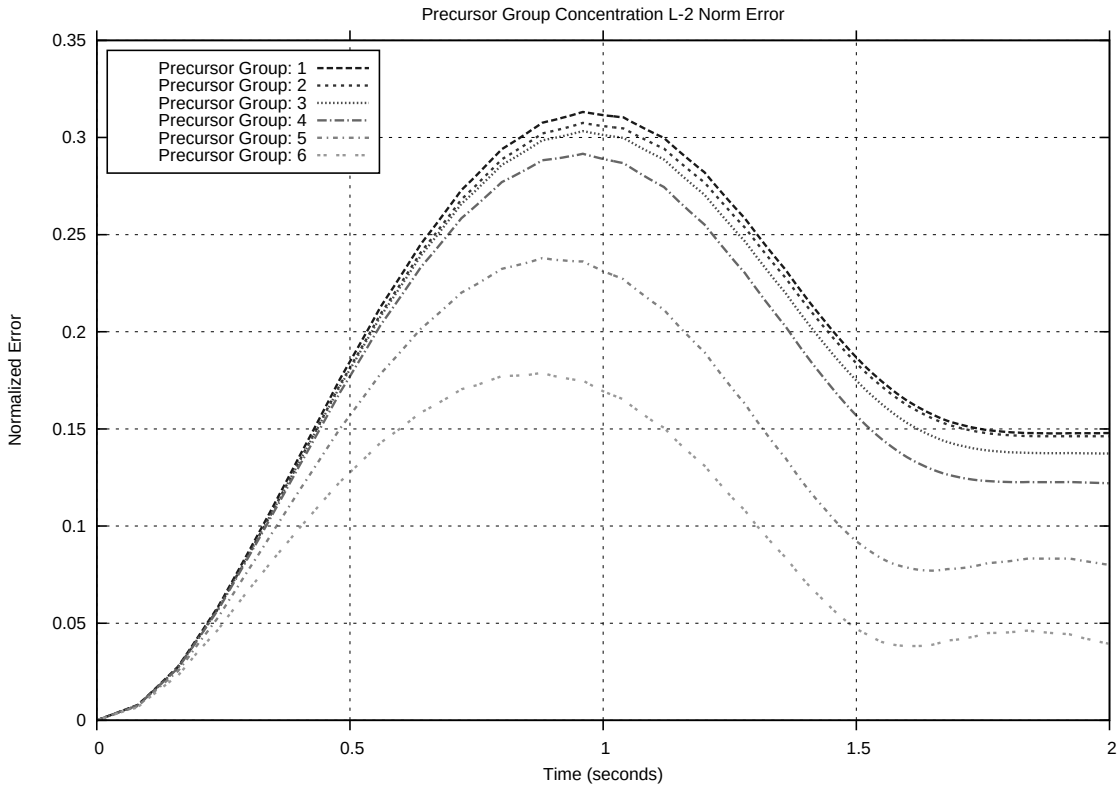

Figure B.50: Precursor Group Concentration L2-Error (25 SS, 40 Trans)

B.5 120 Second Insertion Transient Using the 10 Entry Steady-State Library and the 10 Output Exact Solution

For the 120 second transient utilizing the 10 record steady-state library and the 10 record transient solution, the following results were obtained regarding the flux error and precursor error equations. The average normalized flux and precursor group concentration error values at the maximum and maximum error positions are viewable in Figure B.52 - Figure B.53 and Figure B.54 - Figure B.55, respectively. Also, the L2 error flux and precursor group concentration values can be observed in Figure B.51 and Figure B.56, respectively.

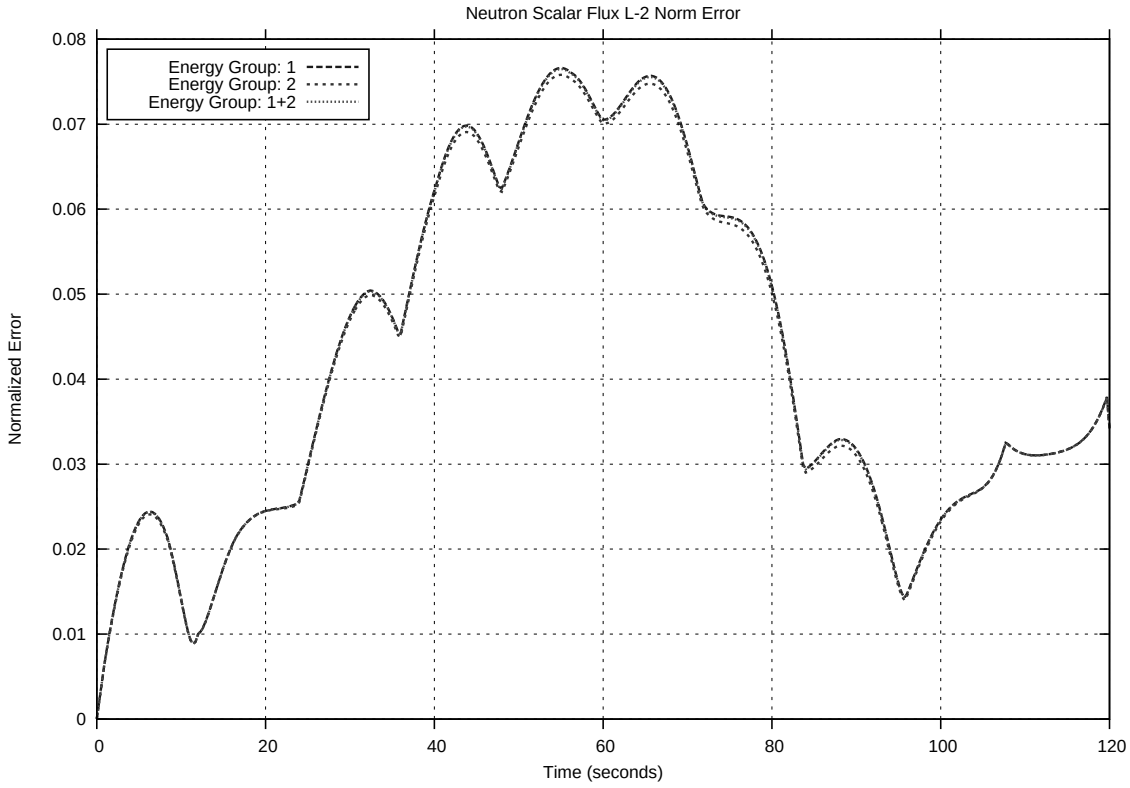

Figure B.51: Flux L2-Error (10 SS, 10 Trans)

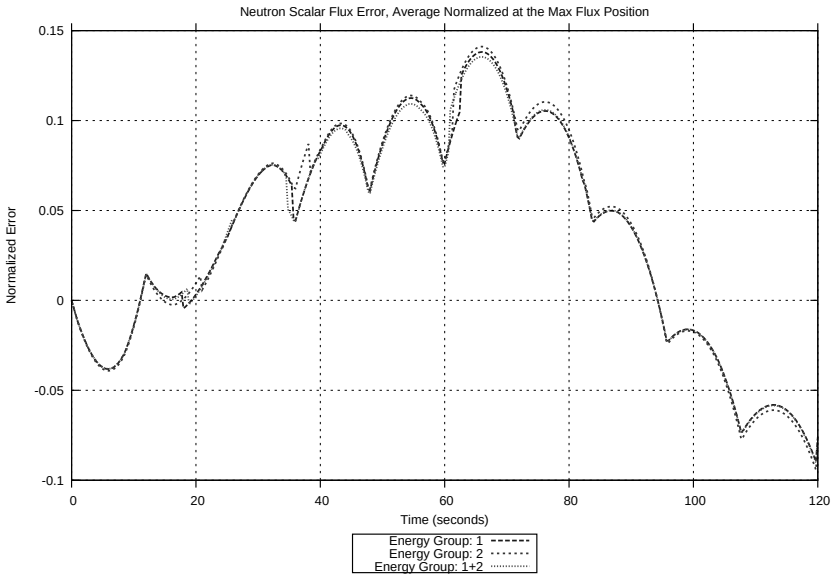

Figure B.52: Average Normalized Flux Error at the Maximum Flux Position (10 SS, 10 Trans)

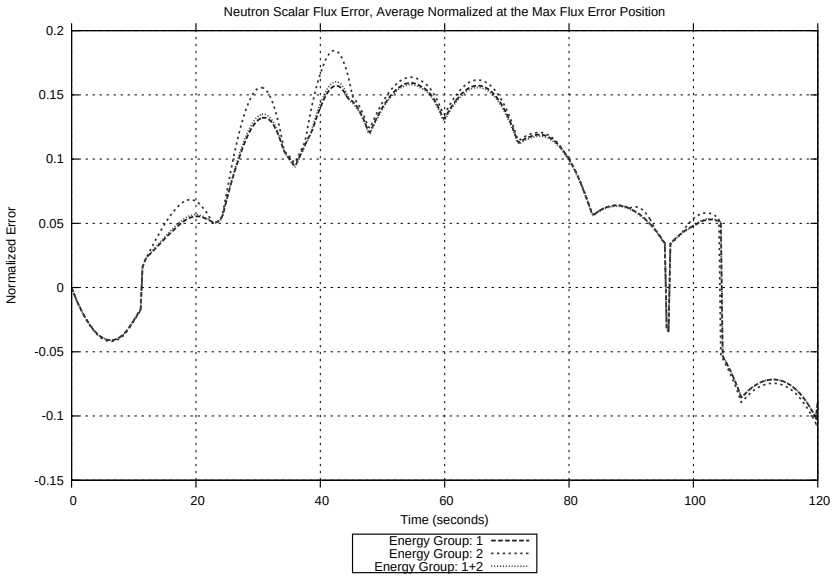

Figure B.53: Average Normalized Flux Error at the Maximum Flux Error Position (10 SS, 10 Trans)

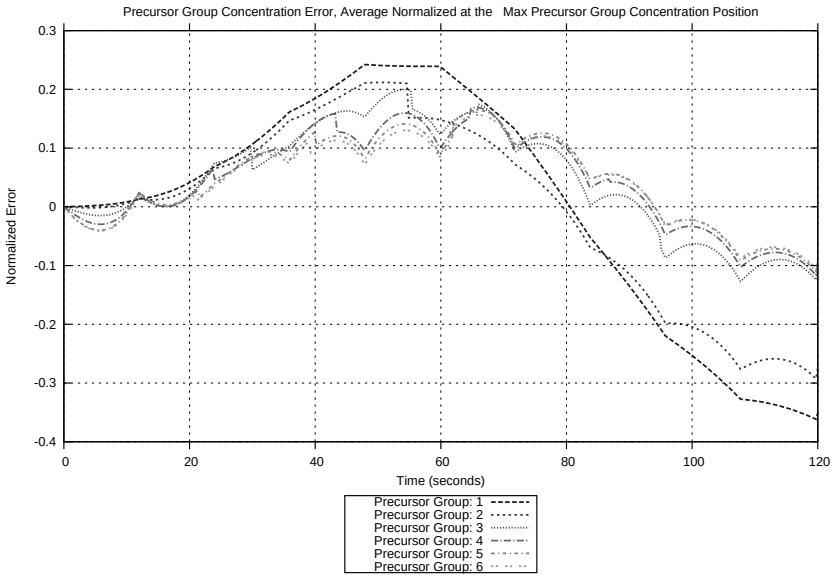

Figure B.54: Average Normalized Precursor Group Concentration Error at the Maximum Precursor Group Concentration Position (10 SS, 10 Trans)

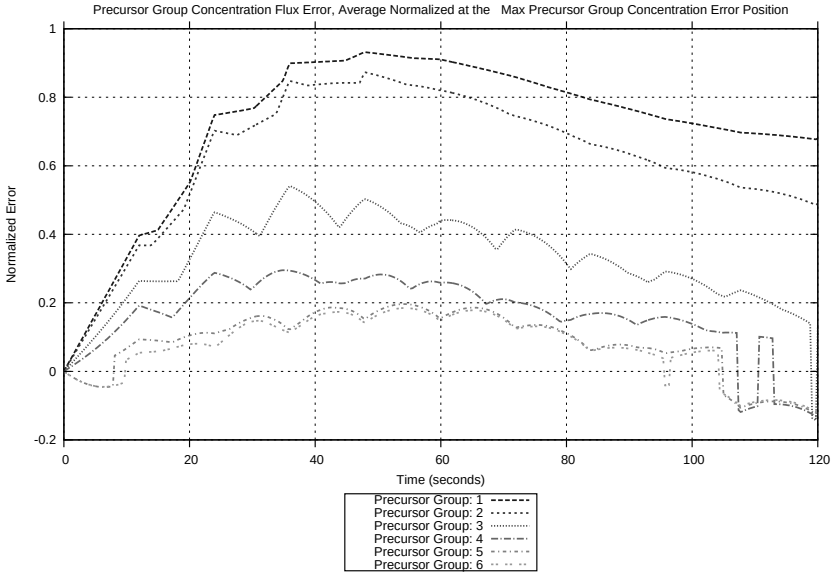

Figure B.55: Average Normalized Precursor Group Concentration Error at the Maximum Precursor Group Concentration Error Position (10 SS, 10 Trans)

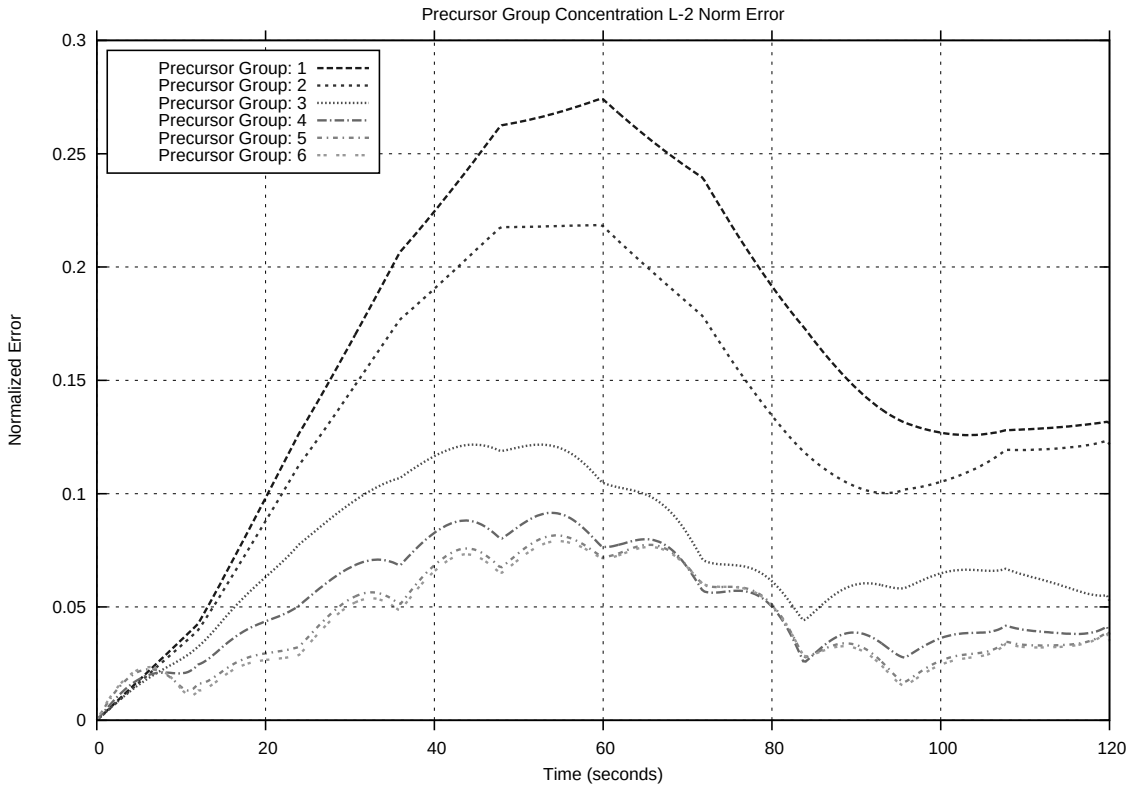

Figure B.56: Precursor Group Concentration L2-Error (10 SS, 10 Trans)

B.6 120 Second Insertion Transient Using the 10 Entry Steady-State Library and the 40 Output Exact Solution

For the 120 second transient utilizing the 10 record steady-state library and the 40 record transient solution, the following results were obtained regarding the flux error and precursor error equations. The average normalized flux and precursor group concentration error values at the maximum and maximum error positions are viewable in Figure B.58 - Figure B.59 and Figure B.60 - Figure B.61, respectively. Also, the L2 error flux and precursor group concentration values can be observed in Figure B.57 and Figure B.62, respectively.

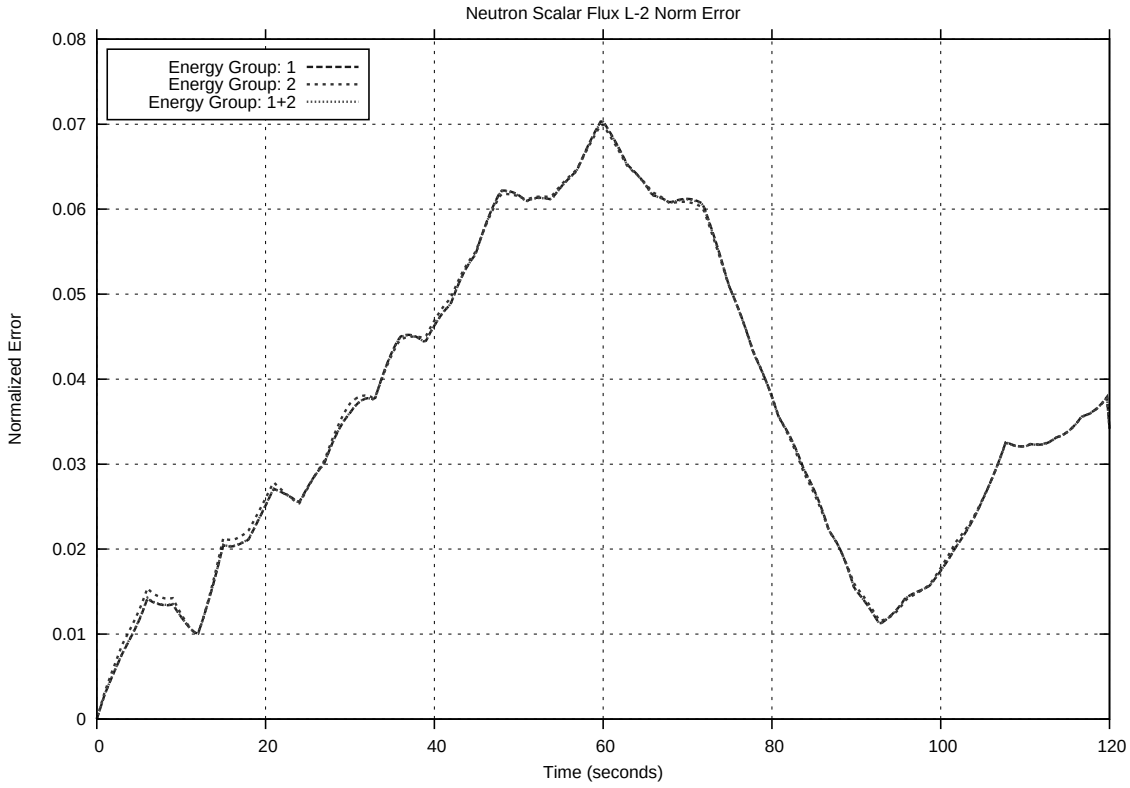

Figure B.57: Flux L2-Error (10 SS, 40 Trans)

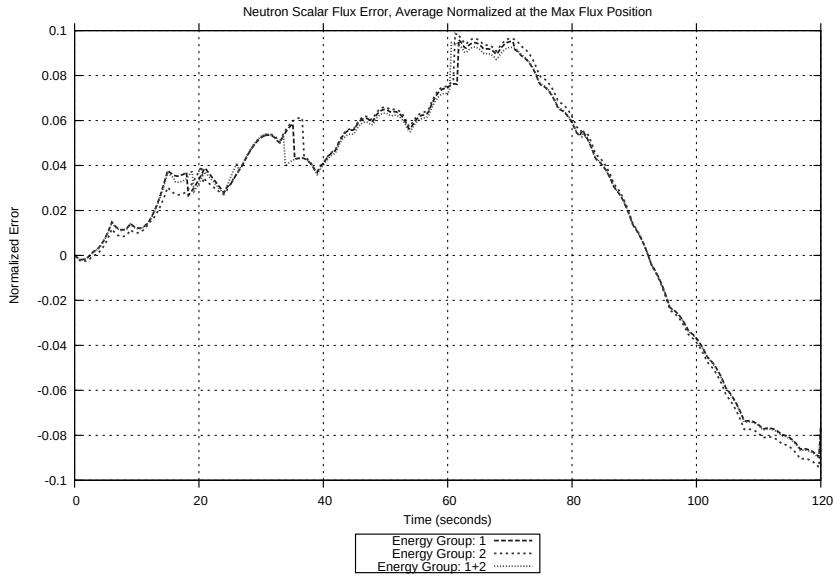

Figure B.58: Average Normalized Flux Error at the Maximum Flux Position (10 SS, 40 Trans)

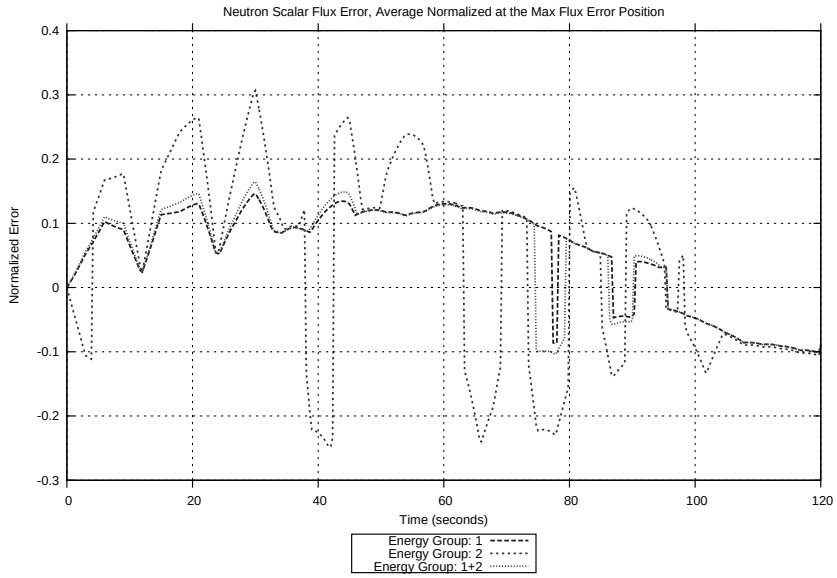

Figure B.59: Average Normalized Flux Error at the Maximum Flux Error Position (10 SS, 40 Trans)

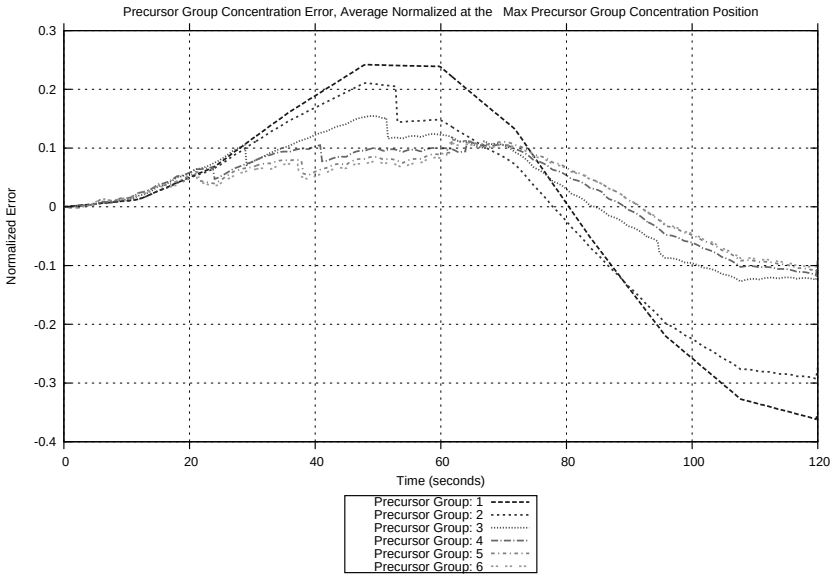

Figure B.60: Average Normalized Precursor Group Concentration Error at the Maximum Precursor Group Concentration Position (10 SS, 40 Trans)

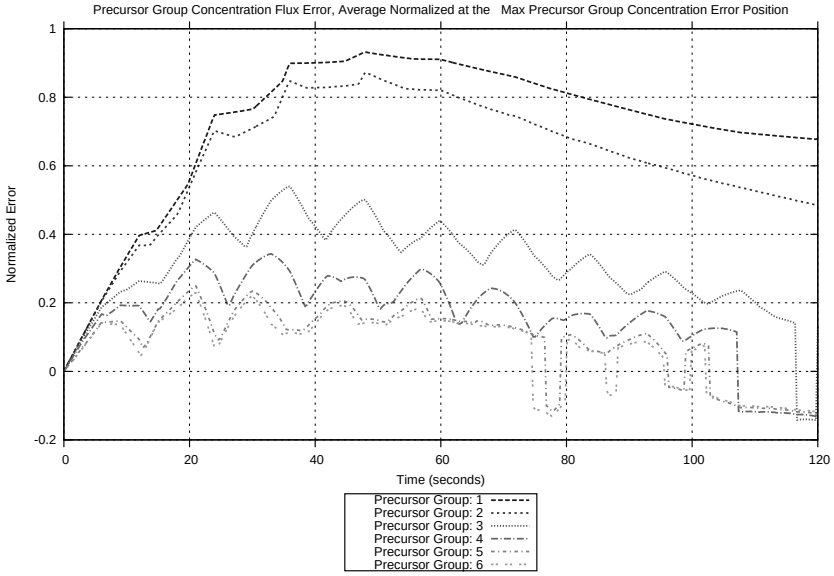

Figure B.61: Average Normalized Precursor Group Concentration Error at the Maximum Precursor Group Concentration Error Position (10 SS, 40 Trans)

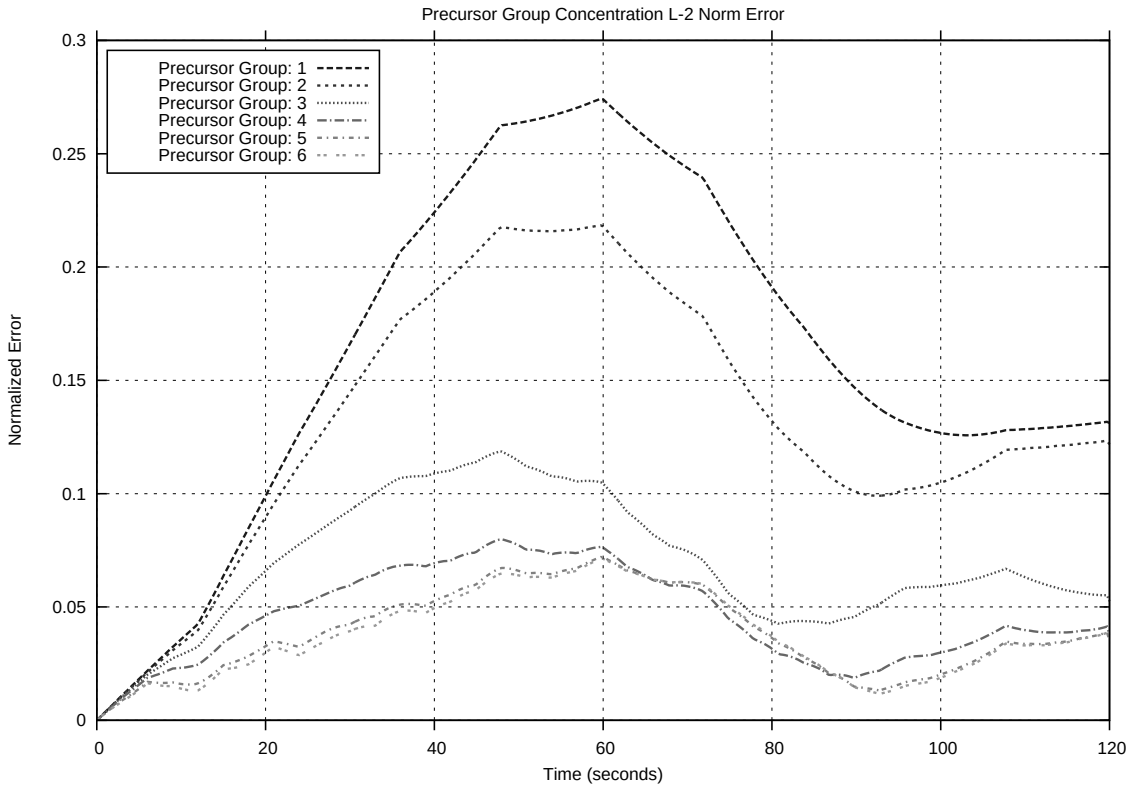

Figure B.62: Precursor Group Concentration L2-Error (10 SS, 40 Trans)

B.7 120 Second Insertion Transient Using the 25 Entry Steady-State Library and the 10 Output Exact Solution

For the 120 second transient utilizing the 25 record steady-state library and the 10 record transient solution, the following results were obtained regarding the flux error and precursor error equations. The average normalized flux and precursor group concentration error values at the maximum and maximum error positions are viewable in Figure B.64 - Figure B.65 and Figure B.66 - Figure B.67, respectively. Also, the L2 error flux and precursor group concentration values can be observed in Figure B.63 and Figure B.68, respectively.

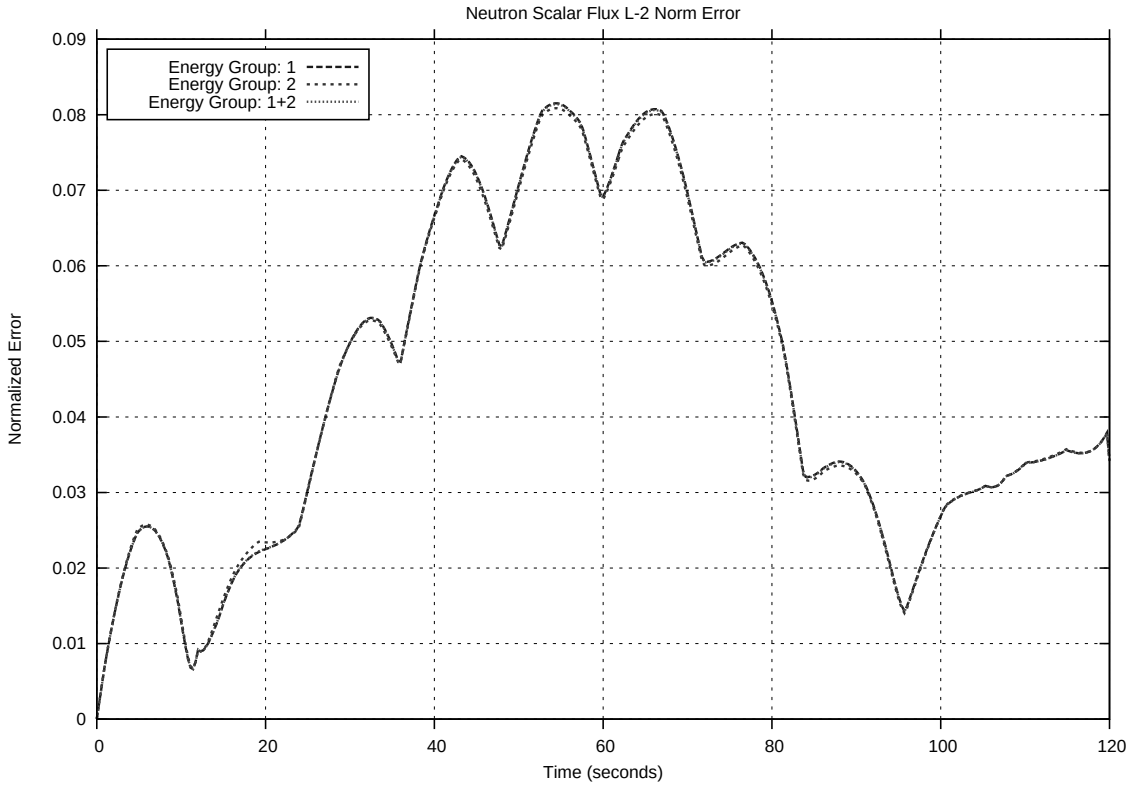

Figure B.63: Flux L2-Error (25 SS, 10 Trans)

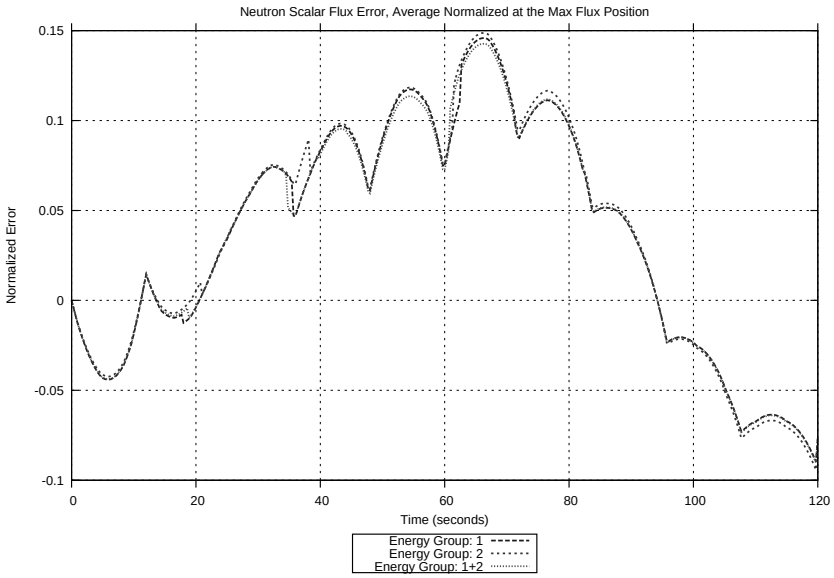

Figure B.64: Average Normalized Flux Error at the Maximum Flux Position (25 SS, 10 Trans)

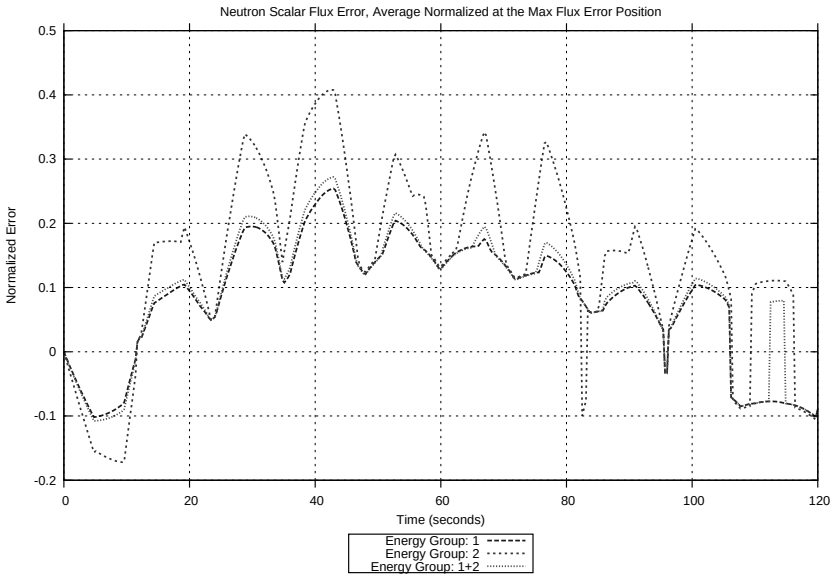

Figure B.65: Average Normalized Flux Error at the Maximum Flux Error Position (25 SS, 10 Trans)

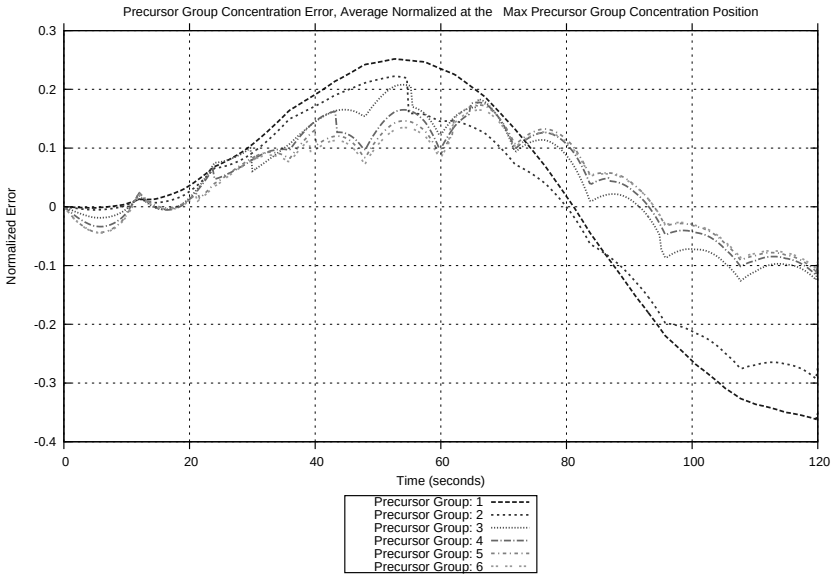

Figure B.66: Average Normalized Precursor Group Concentration Error at the Maximum Precursor Group Concentration Position (25 SS, 10 Trans)

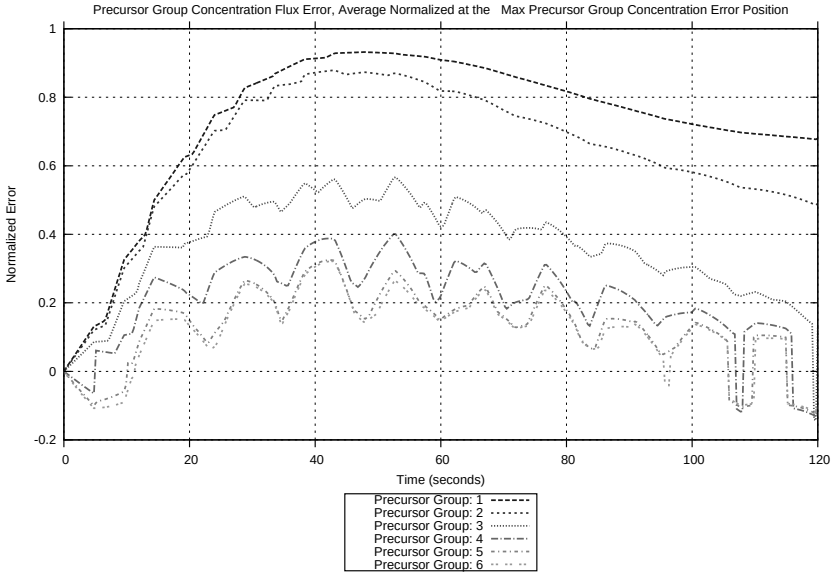

Figure B.67: Average Normalized Precursor Group Concentration Error at the Maximum Precursor Group Concentration Error Position (25 SS, 10 Trans)

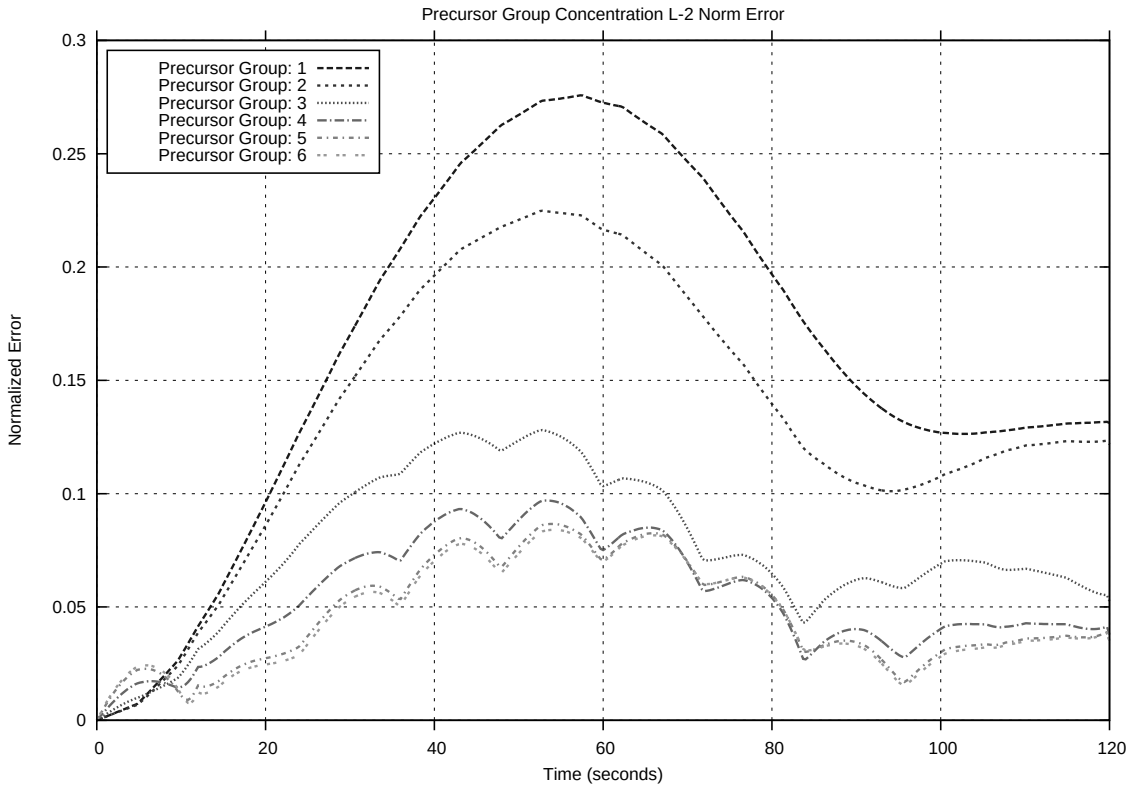

Figure B.68: Precursor Group Concentration L2-Error (25 SS, 10 Trans)

B.8 120 Second Insertion Transient Using the 25 Entry Steady-State Library and the 40 Output Exact Solution

For the 120 second transient utilizing the 25 record steady-state library and the 40 record transient solution, the following results were obtained regarding the flux error and precursor error equations. The average normalized flux and precursor group concentration error values at the maximum and maximum error positions are viewable in Figure B.70 - Figure B.71 and Figure B.72 - Figure B.73, respectively. Also, the L2 error flux and precursor group concentration values can be observed in Figure B.69 and Figure B.74, respectively.

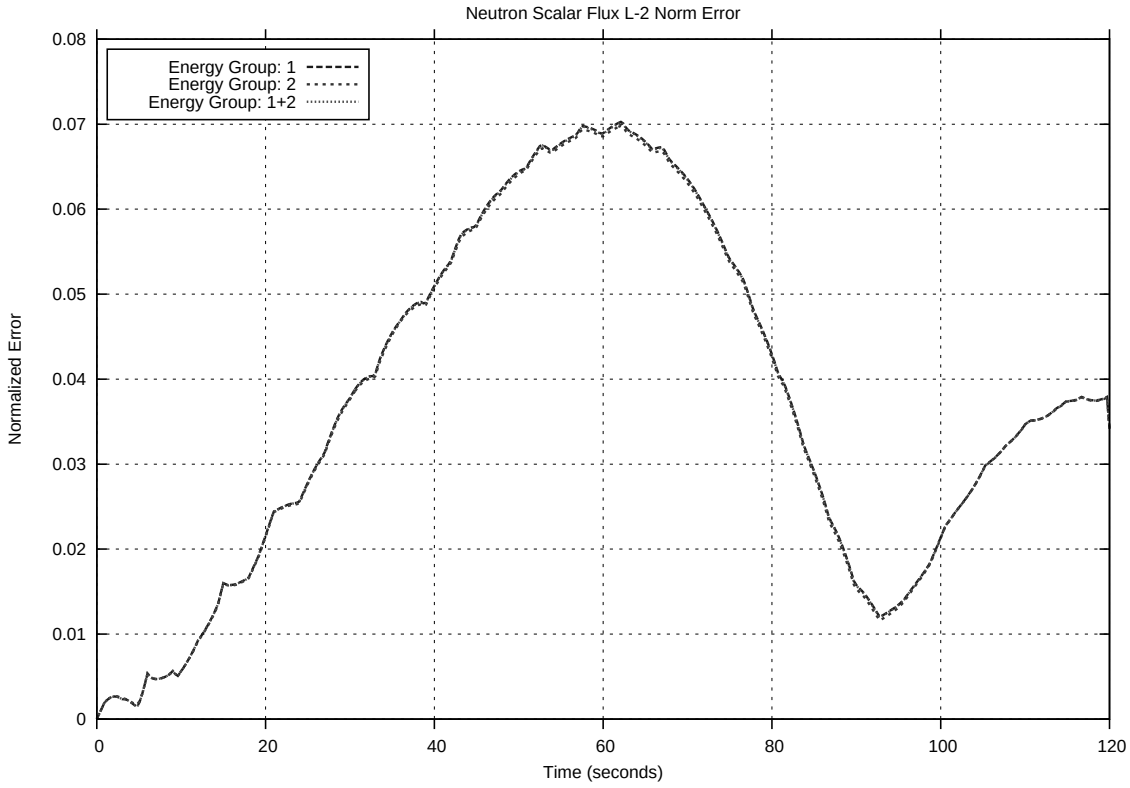

Figure B.69: Flux L2-Error (25 SS, 40 Trans)

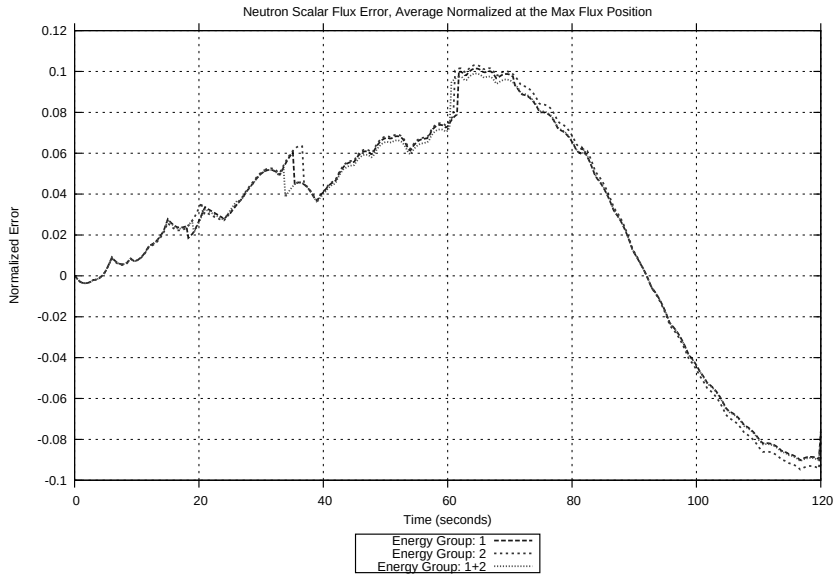

Figure B.70: Average Normalized Flux Error at the Maximum Flux Position (25 SS, 40 Trans)

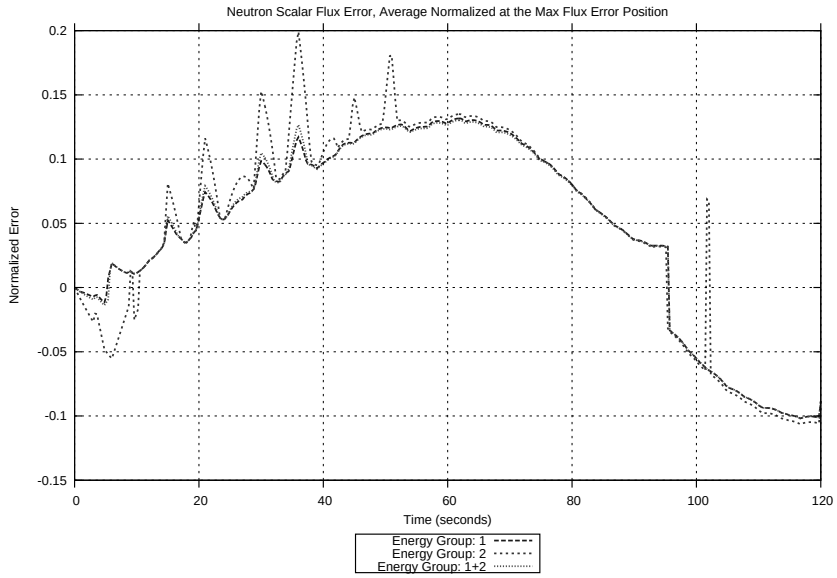

Figure B.71: Average Normalized Flux Error at the Maximum Flux Error Position (25 SS, 40 Trans)

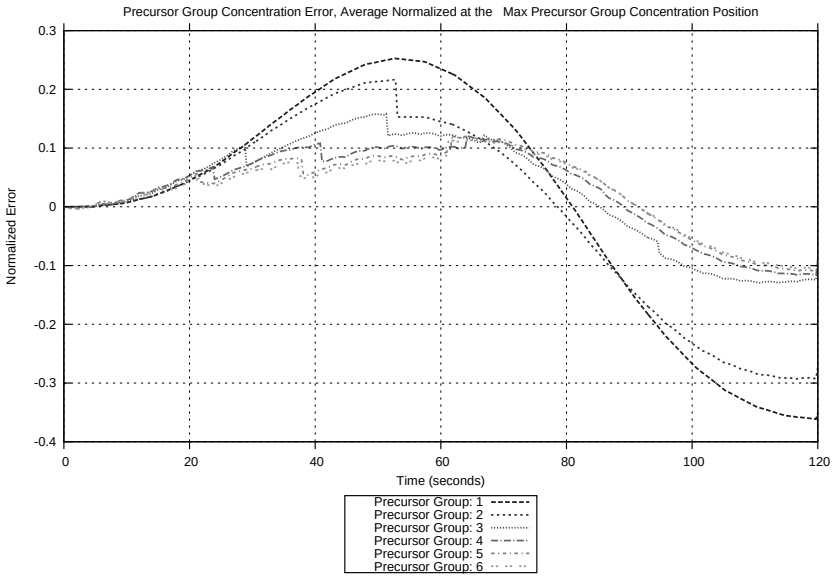

Figure B.72: Average Normalized Precursor Group Concentration Error at the Maximum Precursor Group Concentration Position (25 SS, 40 Trans)

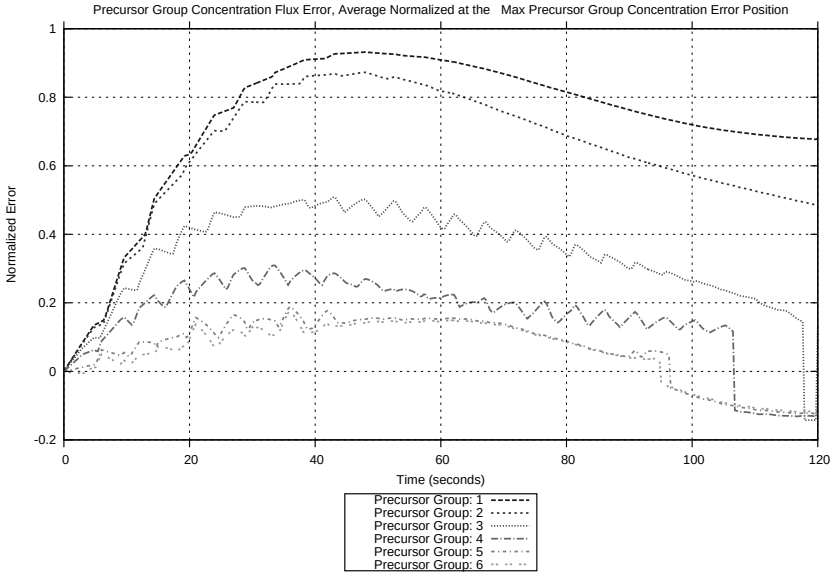

Figure B.73: Average Normalized Precursor Group Concentration Error at the Maximum Precursor Group Concentration Error Position (25 SS, 40 Trans)

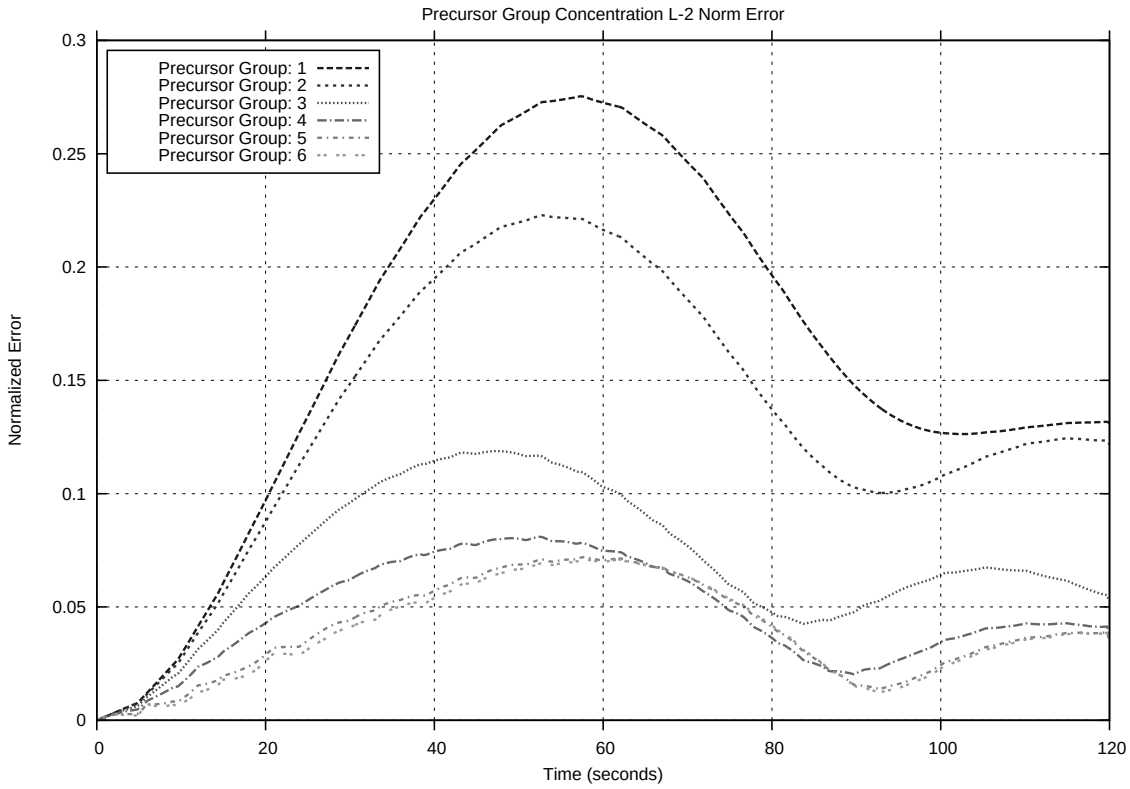

Figure B.74: Precursor Group Concentration L2-Error (25 SS, 40 Trans)

Appendix C

Active Model Switching (Continued)

C.1 No Switching - 2 Second Transient

For the no switching 2 second transient, the following results were obtained regarding the flux error equations developed in Chapter 2 (See Section 2.1.6). The flux error and error components at the maximum flux position and maximum flux error position, locally and averaged normalized results can be viewed in Figure C.1-Figure C.8.

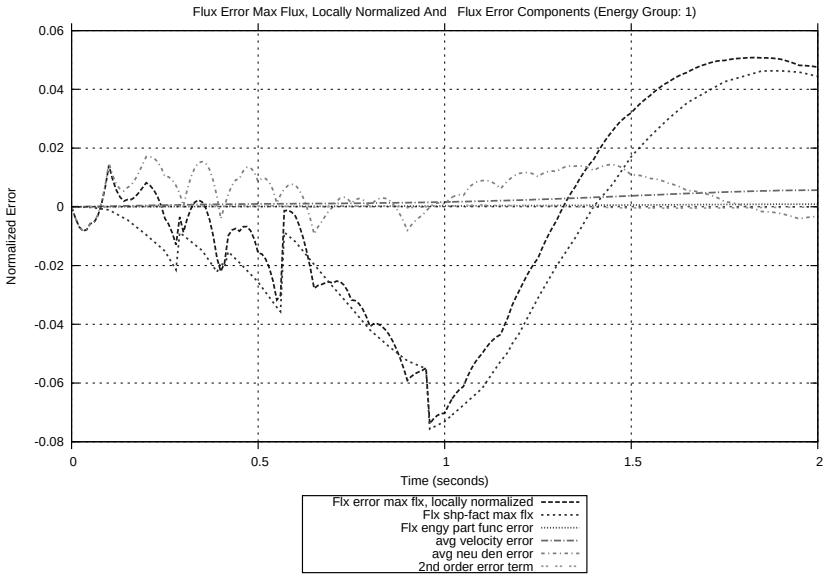

Figure C.1: Flux Error and Error Components at the Maximum Flux Position Locally Normalized (No switch, Trans 40, Group: 1)

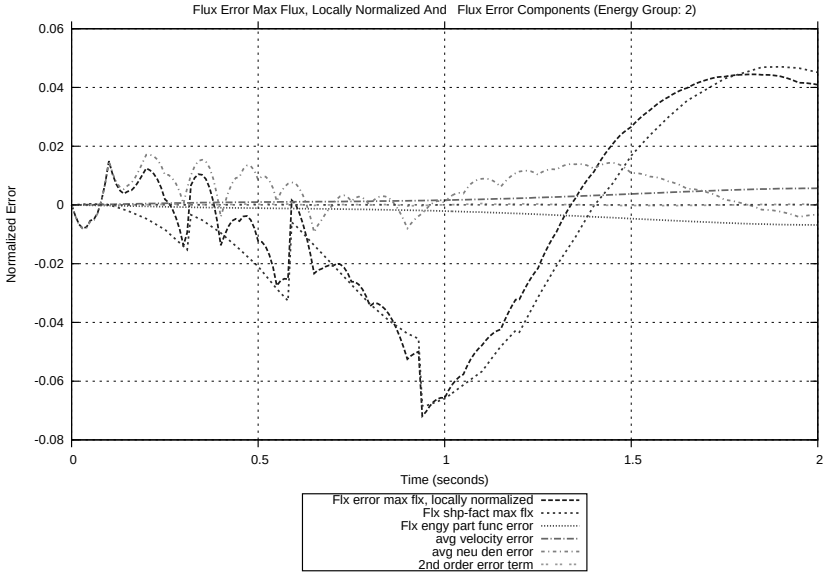

Figure C.2: Flux Error and Error Components at the Maximum Flux Position Locally Normalized (No switch, Trans 40, Group: 2)

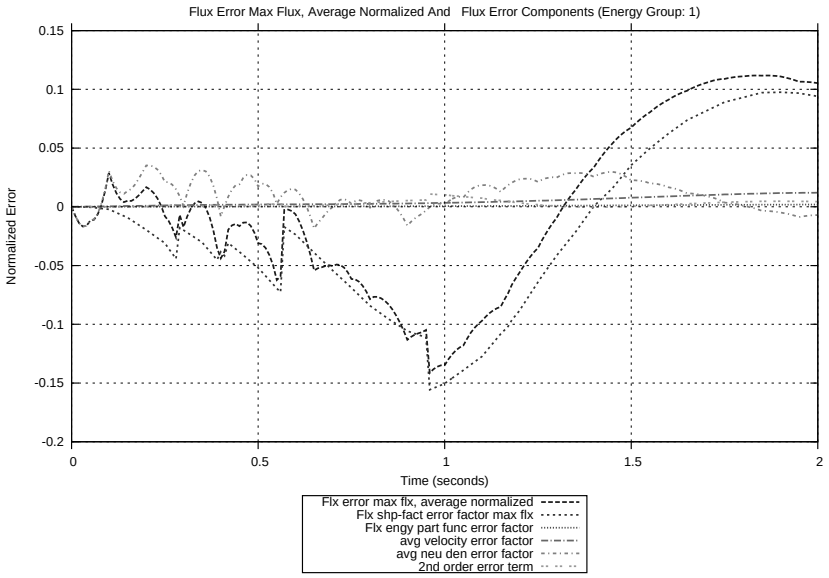

Figure C.3: Flux Error and Error Components at the Maximum Flux Position Average Normalized (No switch, Trans 40, Group: 1)

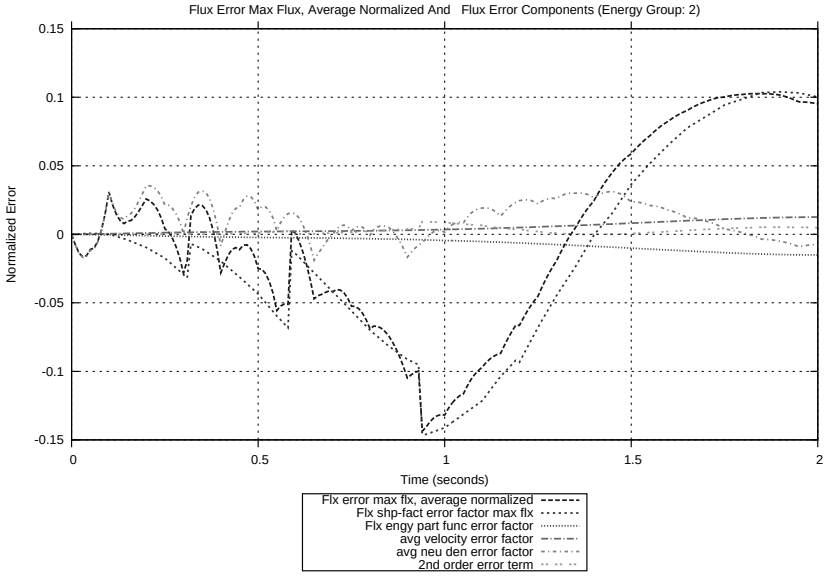

Figure C.4: Flux Error and Error Components at the Maximum Flux Position Average Normalized (No switch, Trans 40, Group: 2)

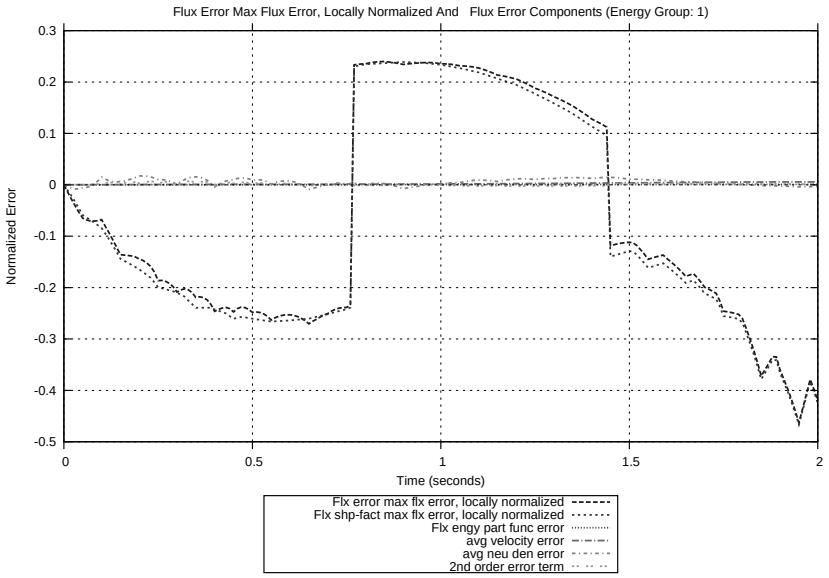

Figure C.5: Flux Error and Error Components at the Maximum Flux Error Position Locally Normalized (No switch, Trans 40, Group: 1)

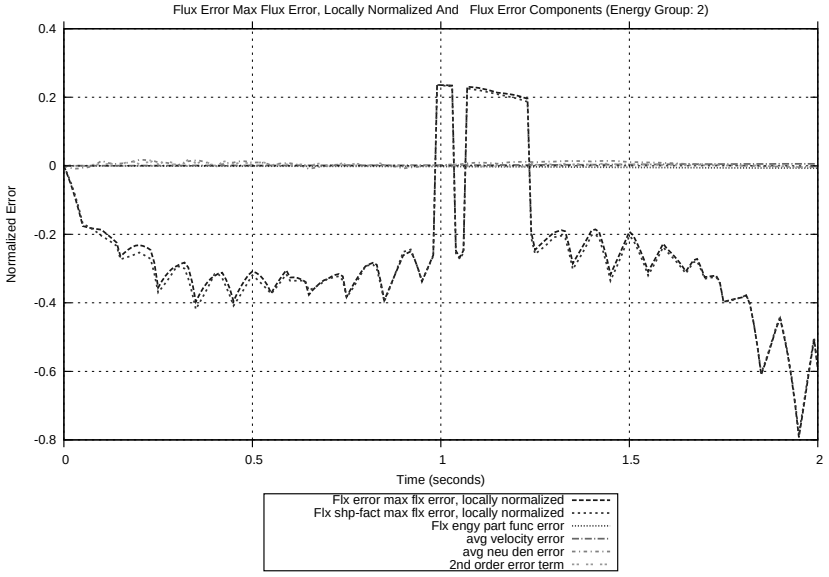

Figure C.6: Flux Error and Error Components at the Maximum Flux Error Position Locally Normalized (No switch, Trans 40, Group: 2)

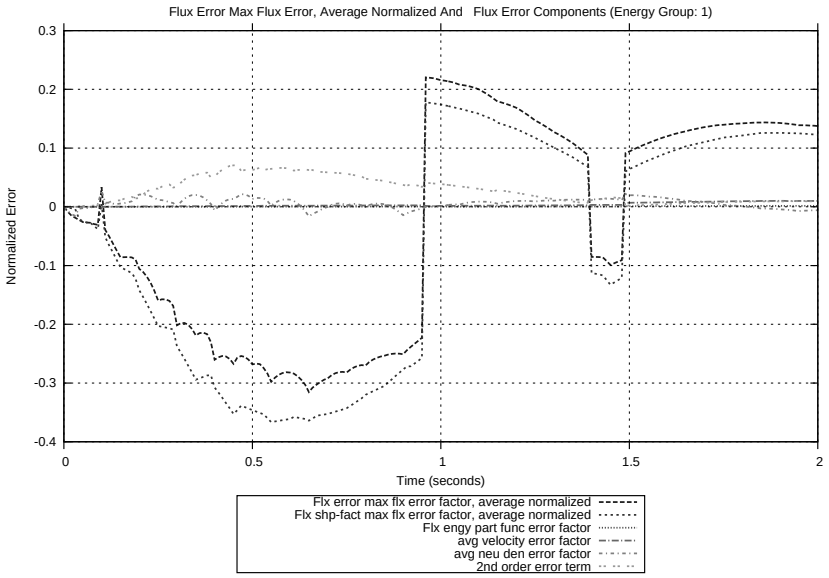

Figure C.7: Flux Error and Error Components at the Maximum Flux Error Position Average Normalized (No switch, Trans 40, Group: 1)

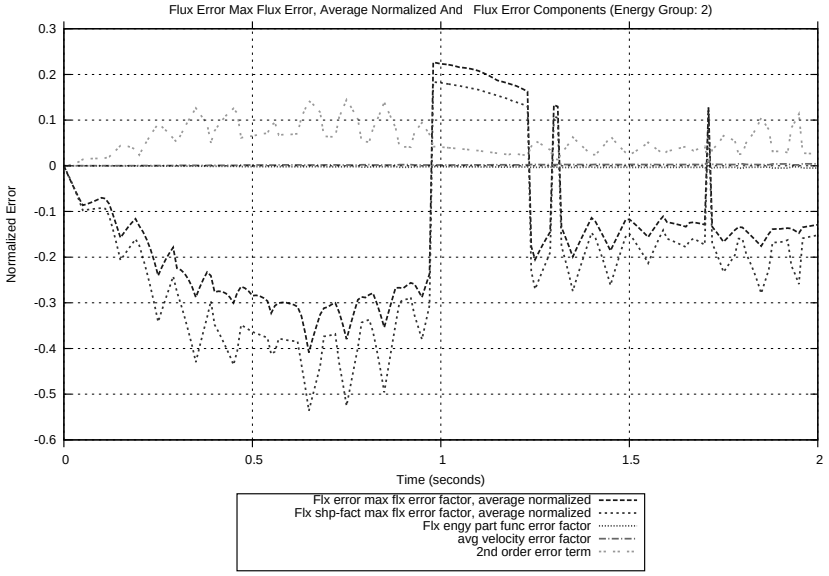

Figure C.8: Flux Error and Error Components at the Maximum Flux Error Position Average Normalized (No switch, Trans 40, Group: 2)

C.2 No Switching - 120 Second Transient

For the no switching 120 second transient, the following results were obtained regarding the flux error equations. The flux error and error components at the maximum flux position and maximum flux error position, locally and averaged normalized results can be viewed in Figure C.9-Figure C.16.

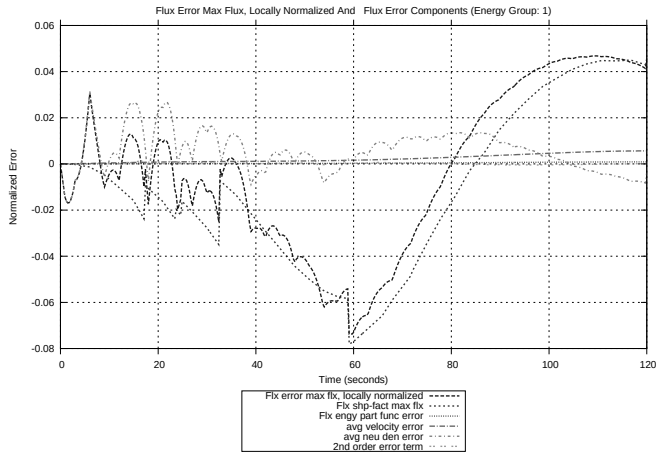

Figure C.9: Flux Error and Error Components at the Maximum Flux Position Locally Normalized (No switch, Trans 40, Group: 1)

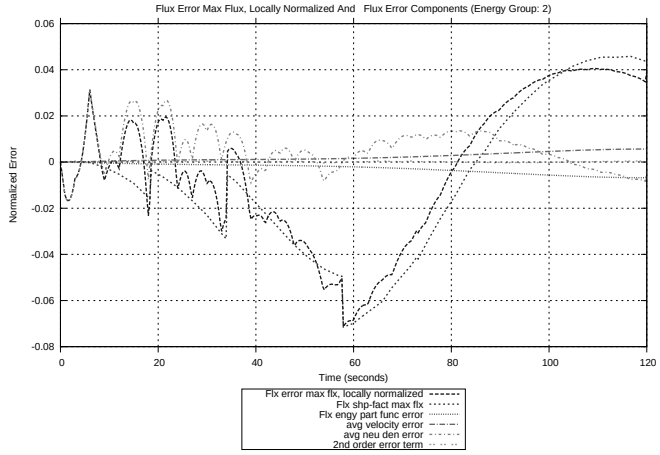

Figure C.10: Flux Error and Error Components at the Maximum Flux Position Locally Normalized (No switch, Trans 40, Group: 2)

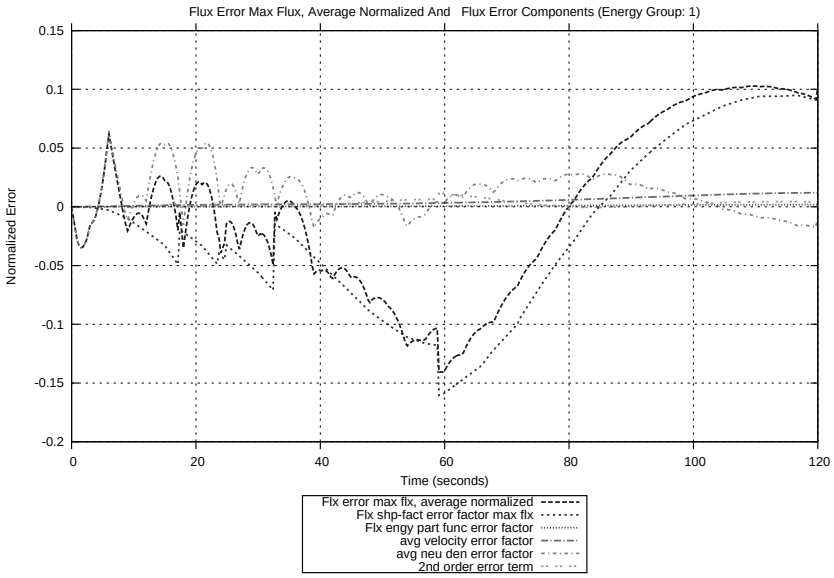

Figure C.11: Flux Error and Error Components at the Maximum Flux Position Average Normalized (No switch, Trans 40, Group: 1)

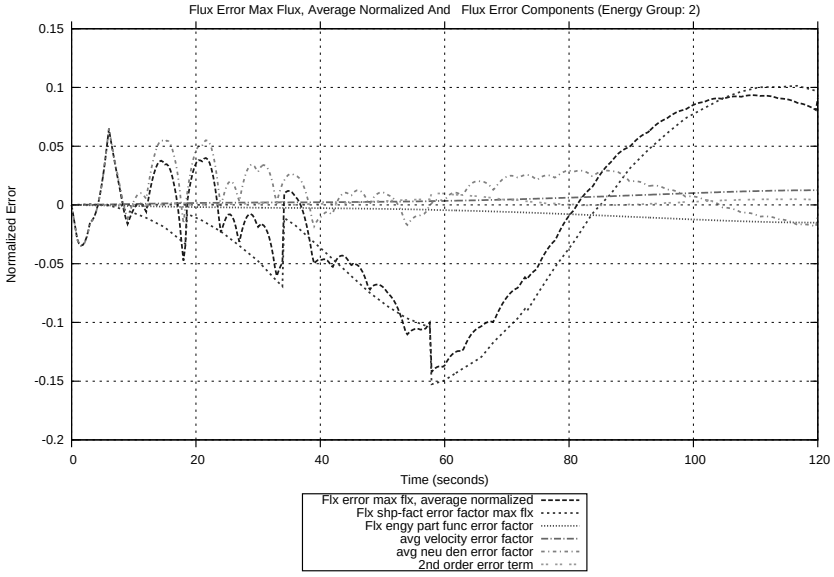

Figure C.12: Flux Error and Error Components at the Maximum Flux Position Average Normalized (No switch, Trans 40, Group: 2)

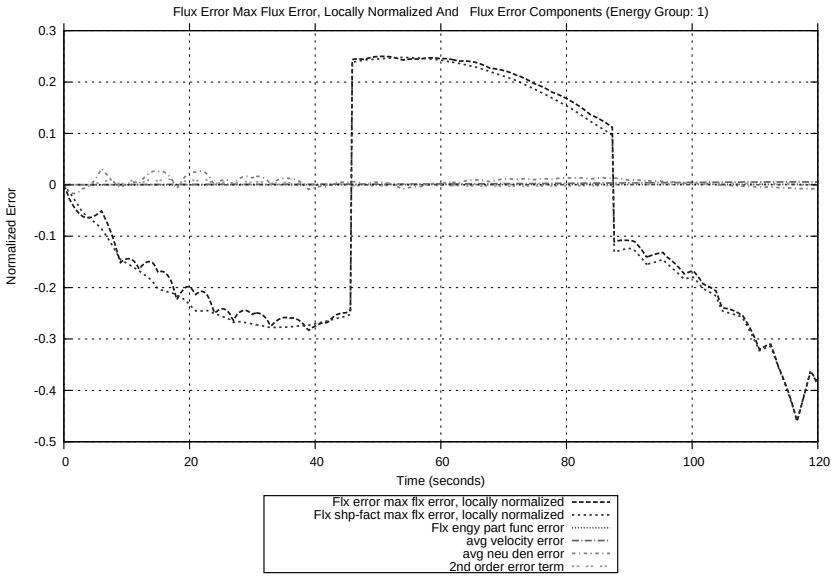

Figure C.13: Flux Error and Error Components at the Maximum Flux Error Position Locally Normalized (No switch, Trans 40, Group: 1)

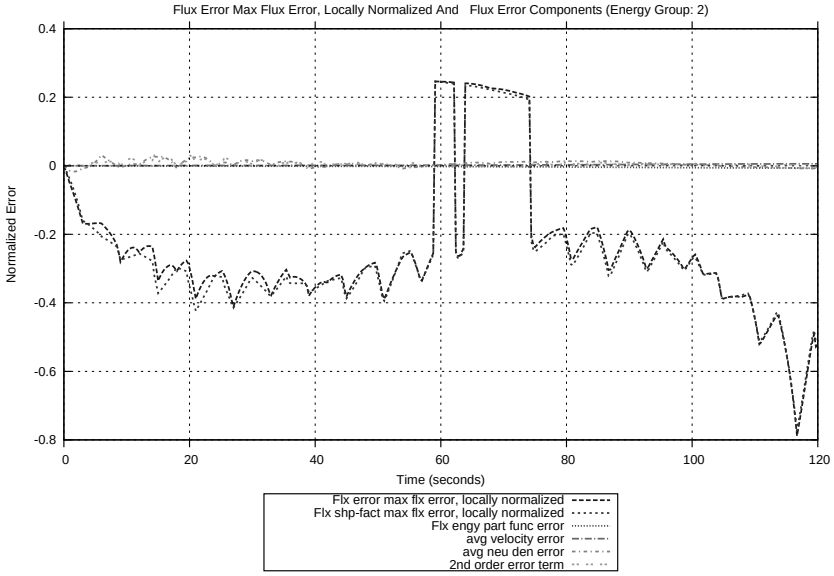

Figure C.14: Flux Error and Error Components at the Maximum Flux Error Position Locally Normalized (No switch, Trans 40, Group: 2)

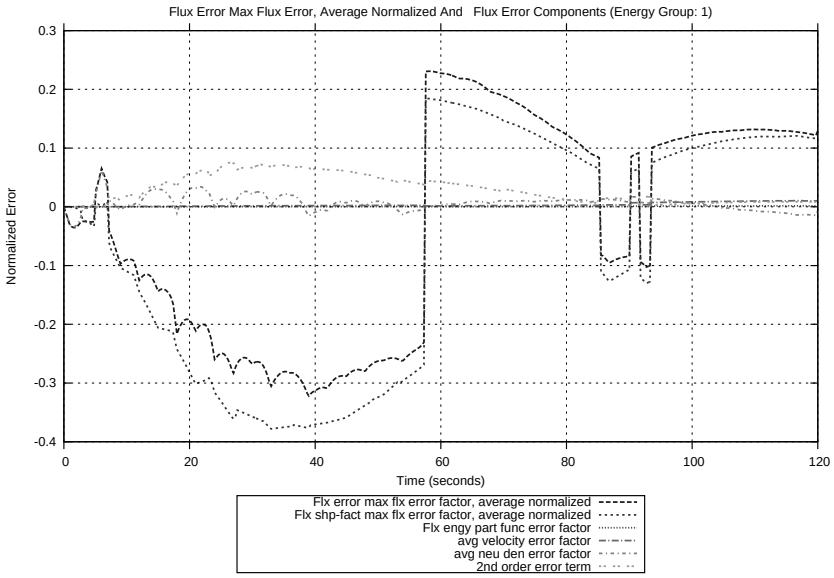

Figure C.15: Flux Error and Error Components at the Maximum Flux Error Position Average Normalized (No switch, Trans 40, Group: 1)

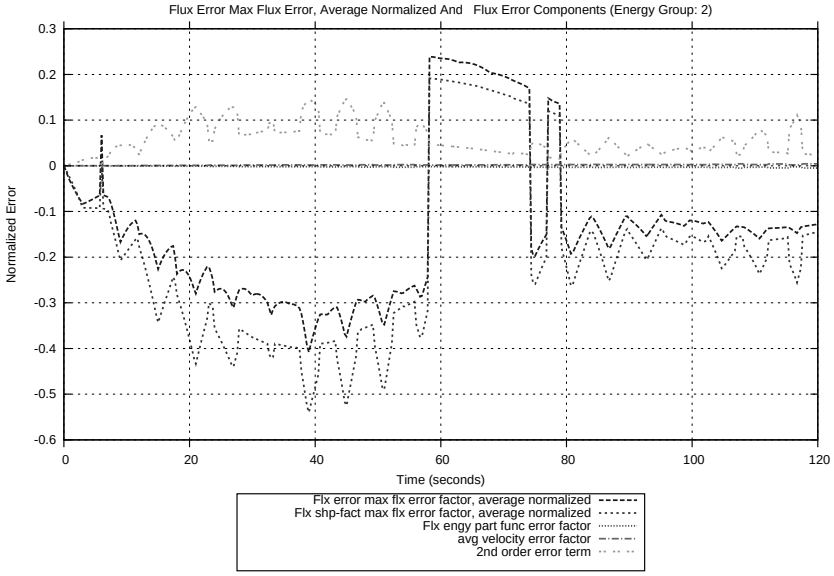

Figure C.16: Flux Error and Error Components at the Maximum Flux Error Position Average Normalized (No switch, Trans 40, Group: 2)

C.3 Single Update - 2 Second Transient

For the single update 2 second transient, the following results were obtained regarding the flux error equations. The flux error and error components at the maximum flux position and maximum flux error position, locally and averaged normalized results can be viewed in Figure C.17-Figure C.24.

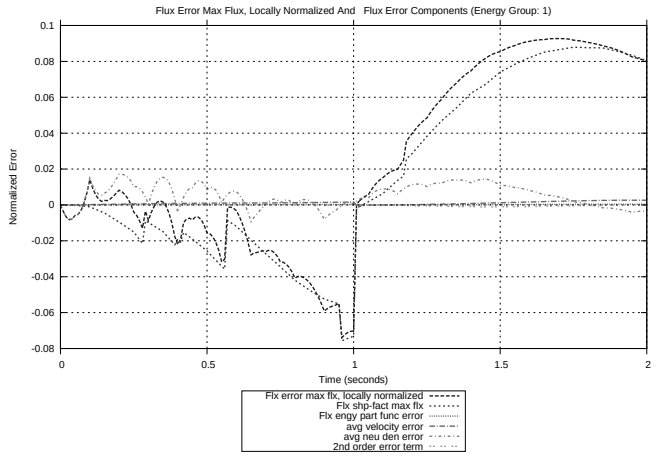

Figure C.17: Flux Error and Error Components at the Maximum Flux Position Locally Normalized (One update, Trans 40, Group: 1)

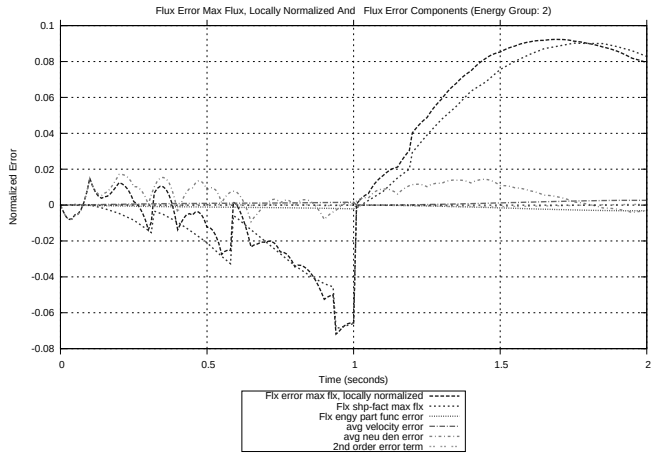

Figure C.18: Flux Error and Error Components at the Maximum Flux Position Locally Normalized (One update, Trans 40, Group: 2)

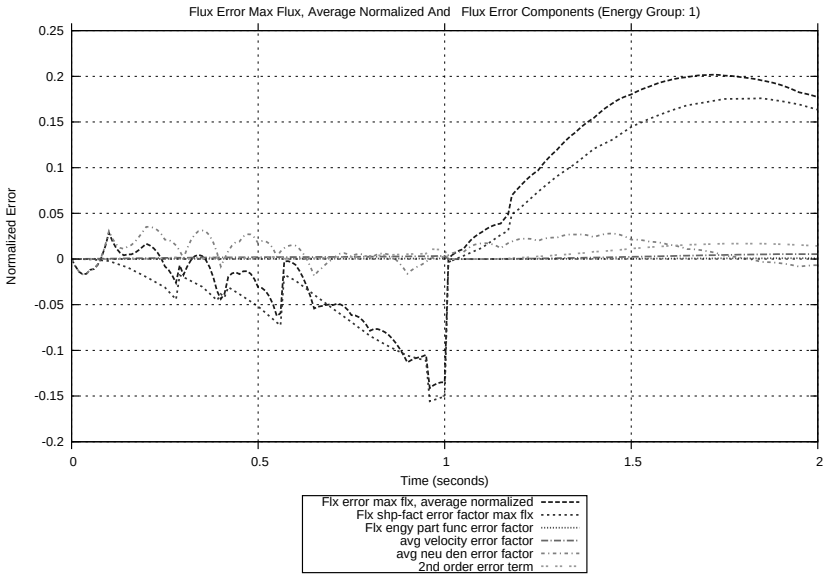

Figure C.19: Flux Error and Error Components at the Maximum Flux Position Average Normalized (One update, Trans 40, Group: 1)

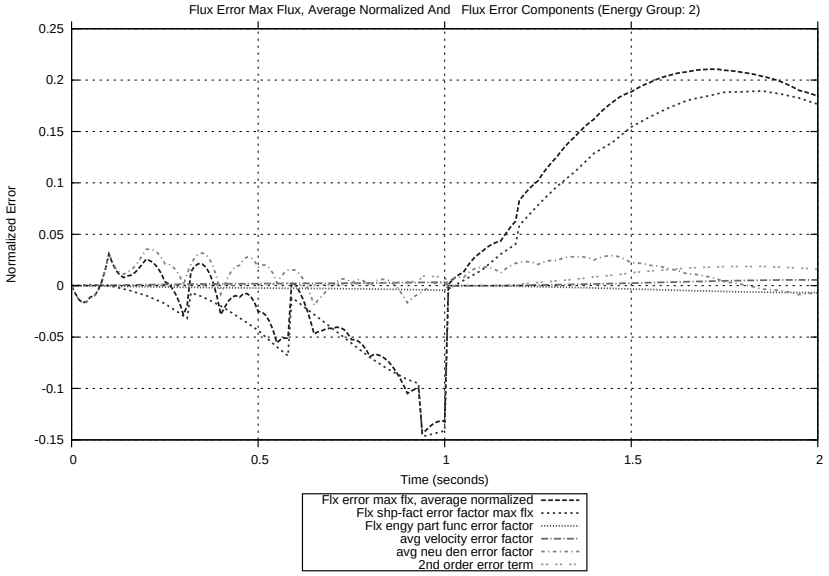

Figure C.20: Flux Error and Error Components at the Maximum Flux Position Average Normalized (One update, Trans 40, Group: 2)

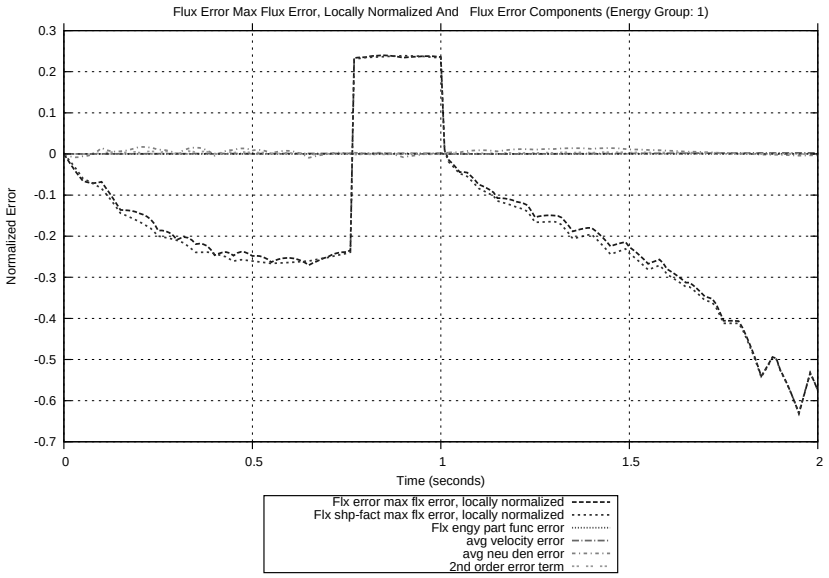

Figure C.21: Flux Error and Error Components at the Maximum Flux Error Position Locally Normalized (One update, Trans 40, Group: 1)

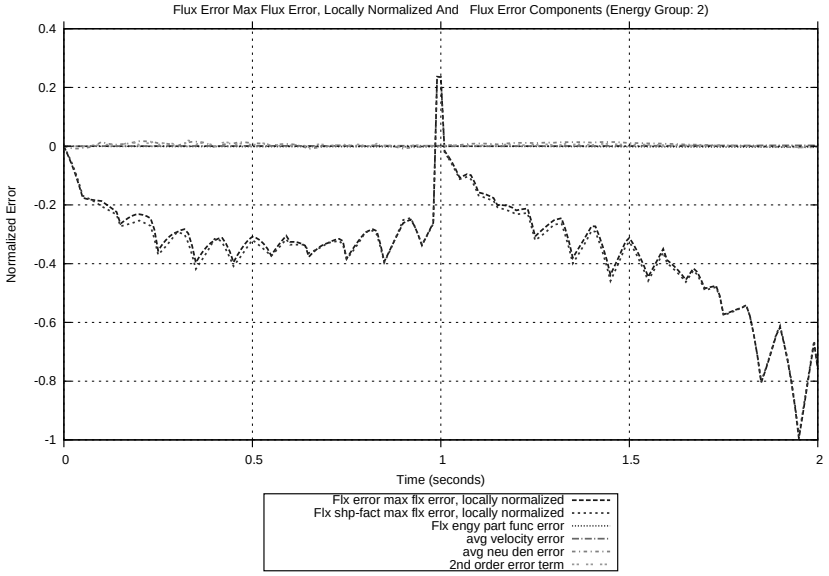

Figure C.22: Flux Error and Error Components at the Maximum Flux Error Position Locally Normalized (One update, Trans 40, Group: 2)

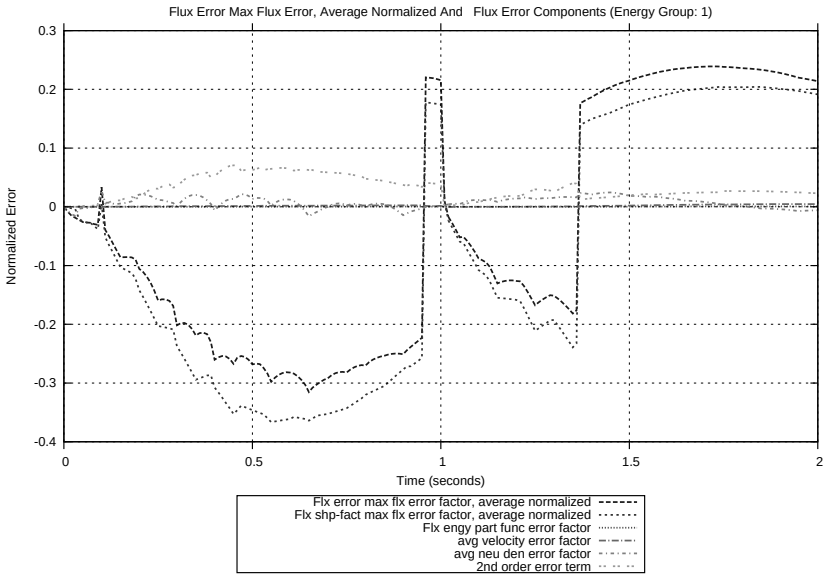

Figure C.23: Flux Error and Error Components at the Maximum Flux Error Position Average Normalized (One update, Trans 40, Group: 1)

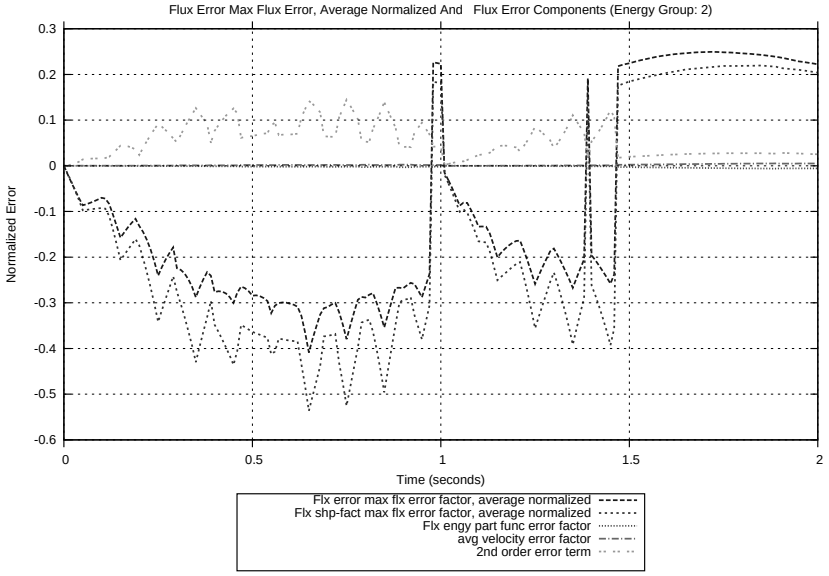

Figure C.24: Flux Error and Error Components at the Maximum Flux Error Position Average Normalized (One update, Trans 40, Group: 2)

C.4 Single Update - 120 Second Transient

For the single update 120 second transient, the following results were obtained regarding the flux error equations. The flux error and error components at the maximum flux position and maximum flux error position, locally and averaged normalized results can be viewed in Figure C.25-Figure C.32.

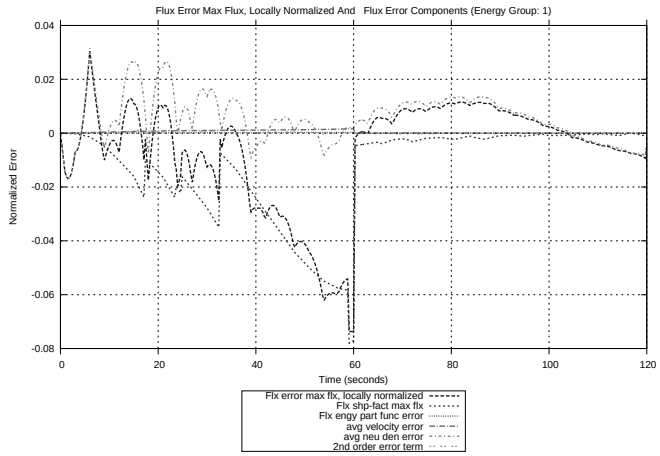

Figure C.25: Flux Error and Error Components at the Maximum Flux Position Locally Normalized (One update, Trans 40, Group: 1)

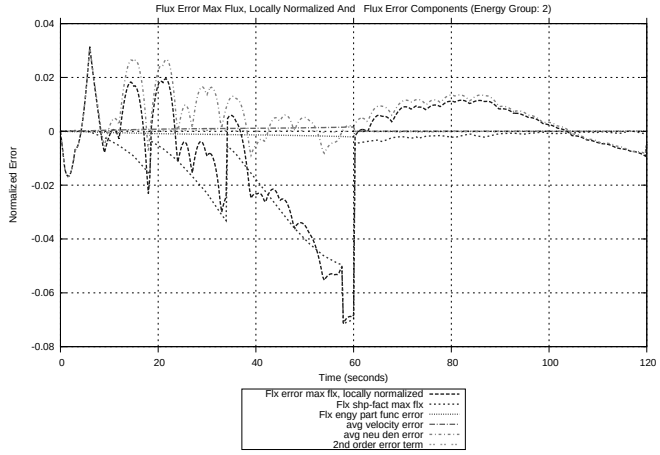

Figure C.26: Flux Error and Error Components at the Maximum Flux Position Locally Normalized (One update, Trans 40, Group: 2)

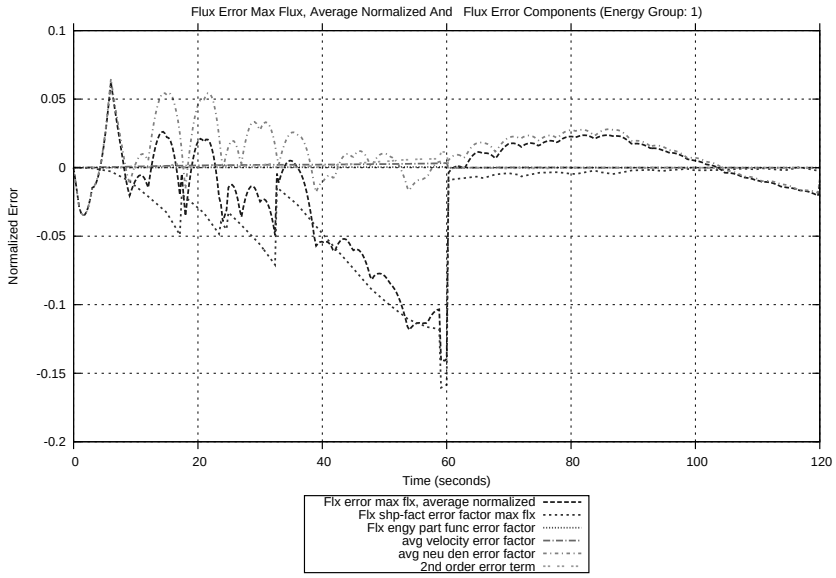

Figure C.27: Flux Error and Error Components at the Maximum Flux Position Average Normalized (One update, Trans 40, Group: 1)

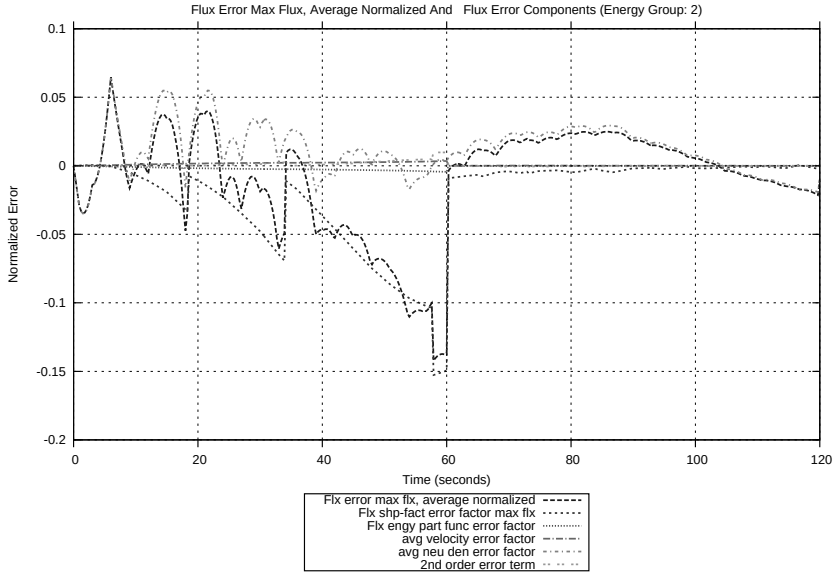

Figure C.28: Flux Error and Error Components at the Maximum Flux Position Average Normalized (One update, Trans 40, Group: 2)

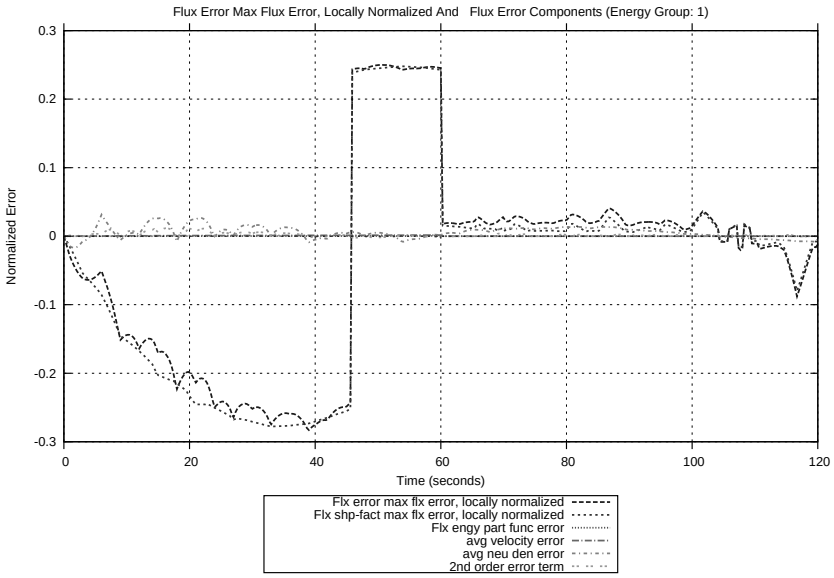

Figure C.29: Flux Error and Error Components at the Maximum Flux Error Position Locally Normalized (One update, Trans 40, Group: 1)

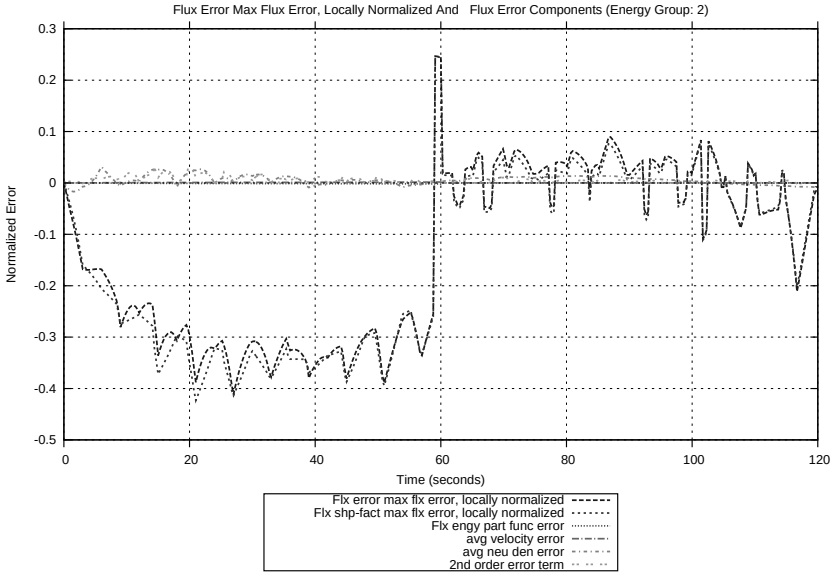

Figure C.30: Flux Error and Error Components at the Maximum Flux Error Position Locally Normalized (One update, Trans 40, Group: 2)

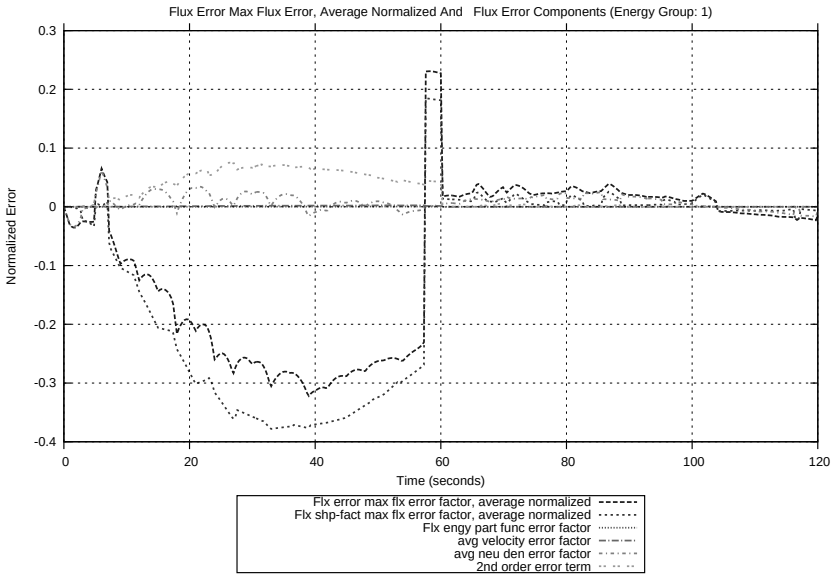

Figure C.31: Flux Error and Error Components at the Maximum Flux Error Position Average Normalized (One update, Trans 40, Group: 1)

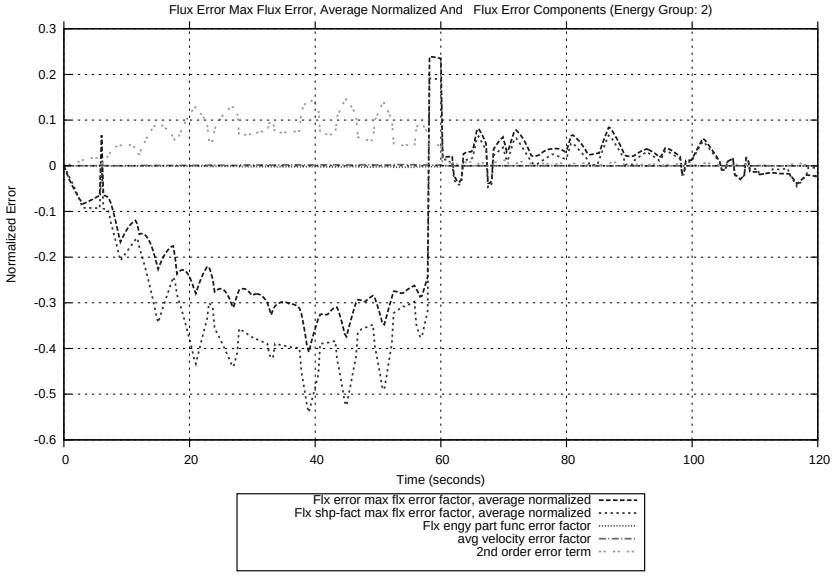

Figure C.32: Flux Error and Error Components at the Maximum Flux Error Position Average Normalized (One update, Trans 40, Group: 2)

C.5 Active Switching - 2 Second Transient

For the single update 2 second transient, the following results were obtained regarding the flux error equations. The flux error and error components at the maximum flux position and maximum flux error position, locally and averaged normalized results can be viewed in Figure C.33-Figure C.40.

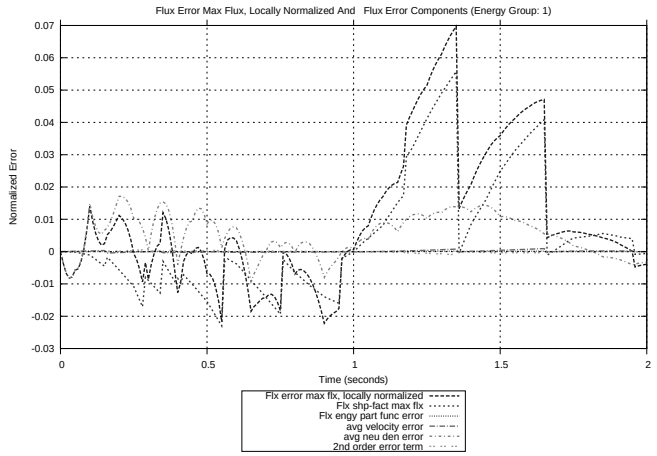

Figure C.33: Flux Error and Error Components at the Maximum Flux Position Locally Normalized (Active, Trans 40, Group: 1)

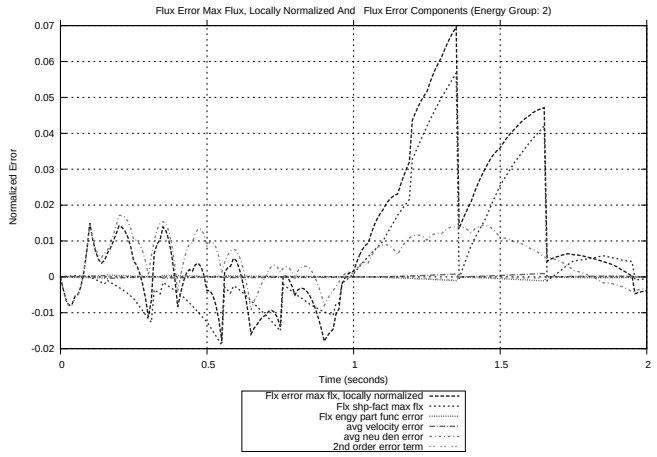

Figure C.34: Flux Error and Error Components at the Maximum Flux Position Locally Normalized (Active, Trans 40, Group: 2)

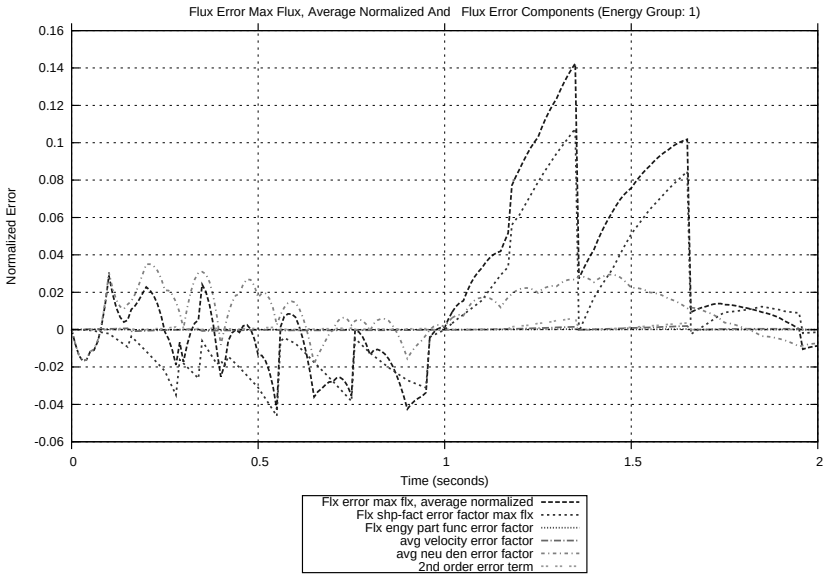

Figure C.35: Flux Error and Error Components at the Maximum Flux Position Average Normalized (Active, Trans 40, Group: 1)

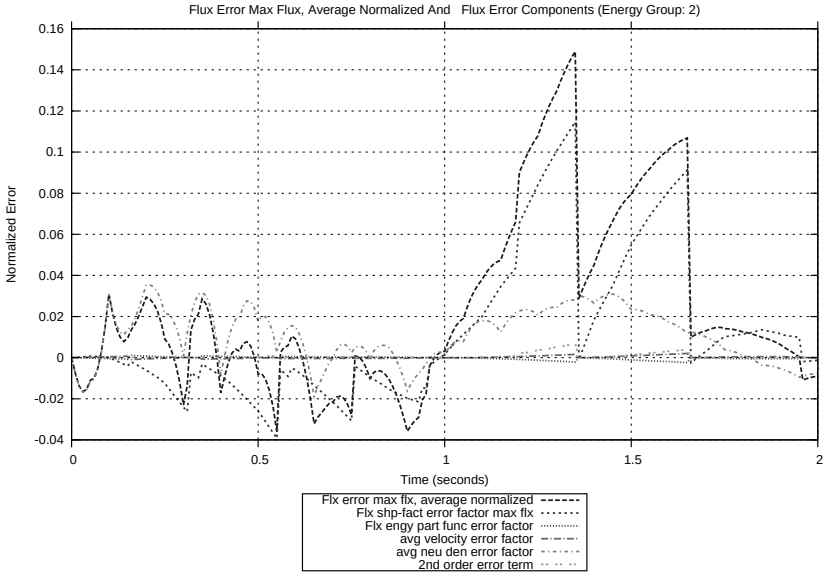

Figure C.36: Flux Error and Error Components at the Maximum Flux Position Average Normalized (Active, Trans 40, Group: 2)

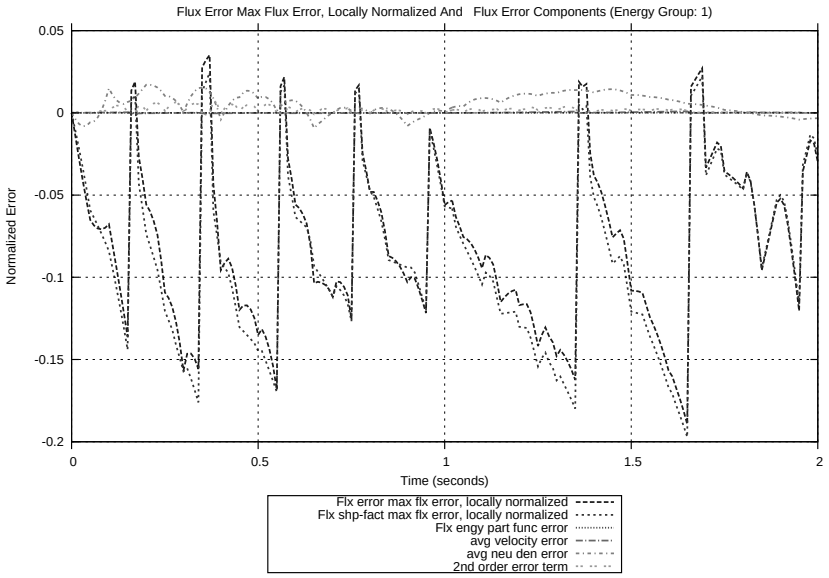

Figure C.37: Flux Error and Error Components at the Maximum Flux Error Position Locally Normalized (Active, Trans 40, Group: 1)

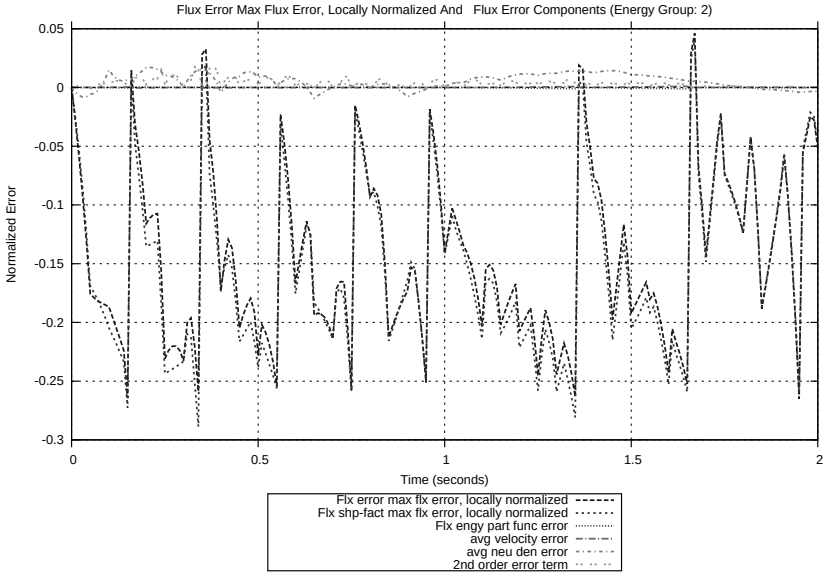

Figure C.38: Flux Error and Error Components at the Maximum Flux Error Position Locally Normalized (Active, Trans 40, Group: 2)

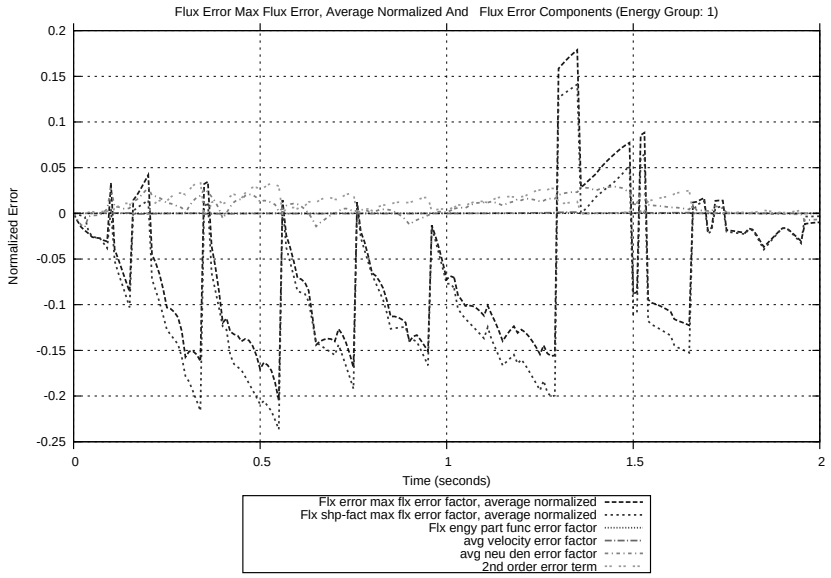

Figure C.39: Flux Error and Error Components at the Maximum Flux Error Position Average Normalized (Active, Trans 40, Group: 1)

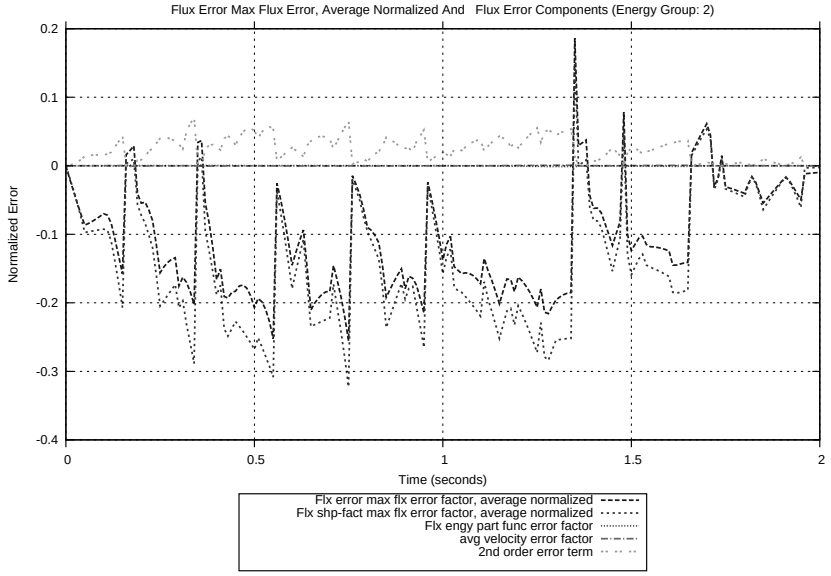

Figure C.40: Flux Error and Error Components at the Maximum Flux Error Position Average Normalized (Active, Trans 40, Group: 2)

C.6 Active Switching - 120 Second Transient

For the single update 120 second transient, the following results were obtained regarding the flux error equations. The flux error and error components at the maximum flux position and maximum flux error position, locally and averaged normalized results can be viewed in Figure C.41-Figure C.48.

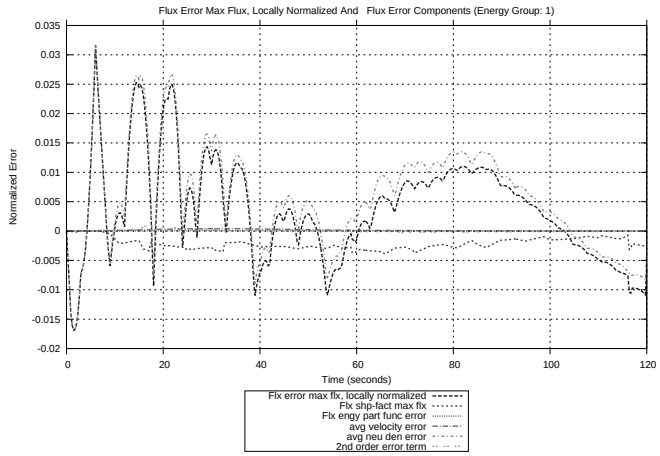

Figure C.41: Flux Error and Error Components at the Maximum Flux Position Locally Normalized (Active, Trans 40, Group: 1)

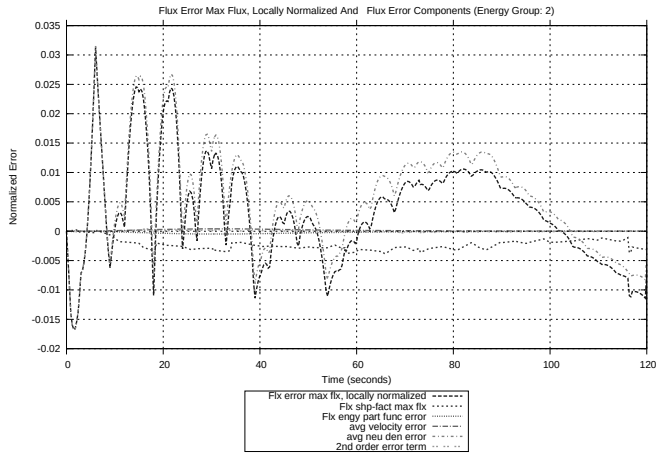

Figure C.42: Flux Error and Error Components at the Maximum Flux Position Locally Normalized (Active, Trans 40, Group: 2)

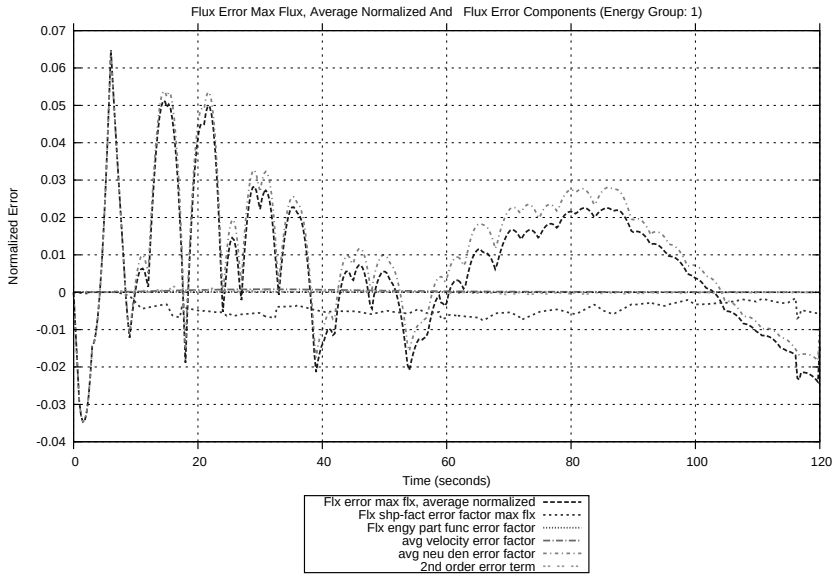

Figure C.43: Flux Error and Error Components at the Maximum Flux Position Average Normalized (Active, Trans 40, Group: 1)

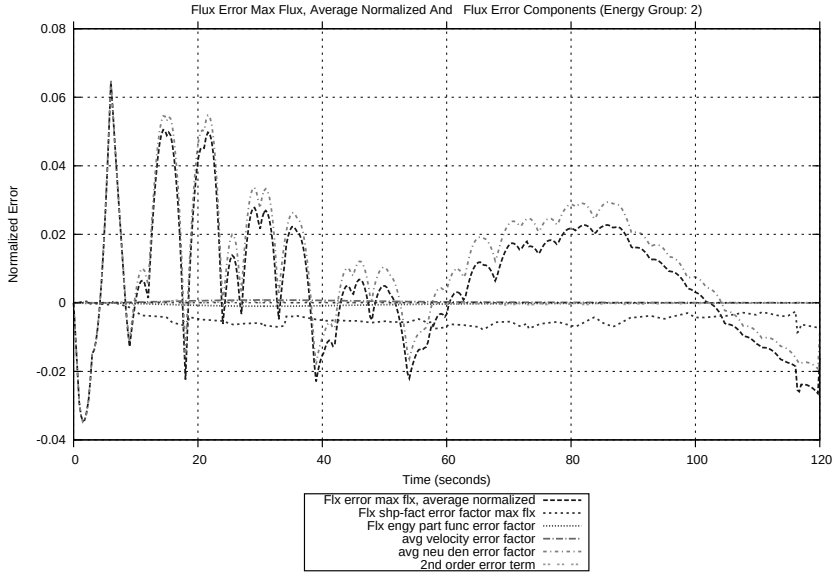

Figure C.44: Flux Error and Error Components at the Maximum Flux Position Average Normalized (Active, Trans 40, Group: 2)

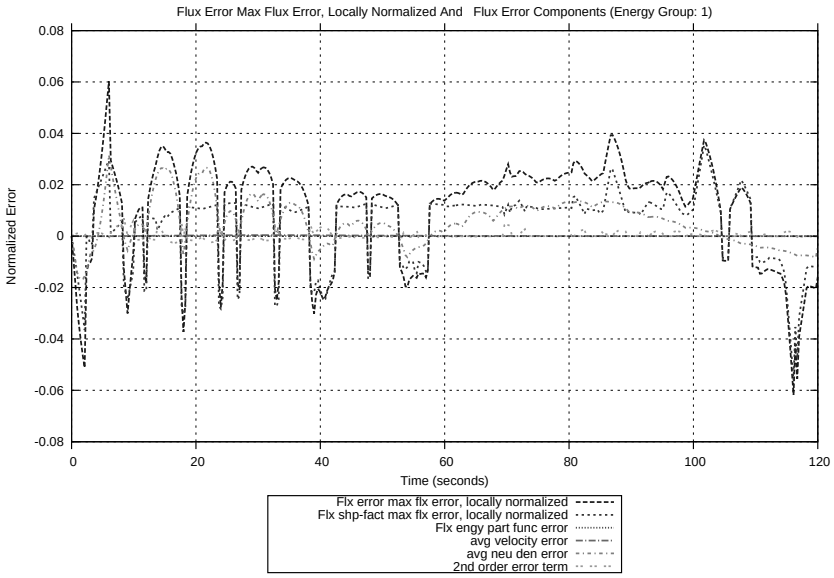

Figure C.45: Flux Error and Error Components at the Maximum Flux Error Position Locally Normalized (Active, Trans 40, Group: 1)

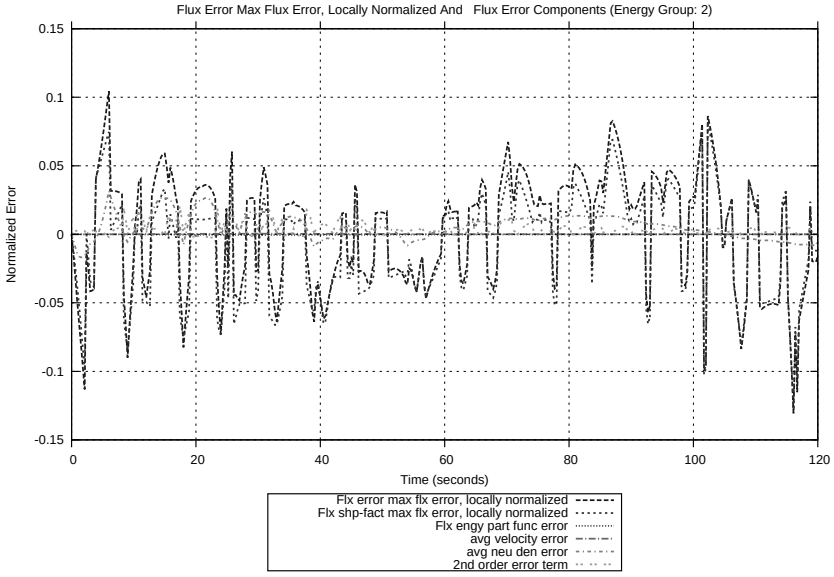

Figure C.46: Flux Error and Error Components at the Maximum Flux Error Position Locally Normalized (Active, Trans 40, Group: 2)

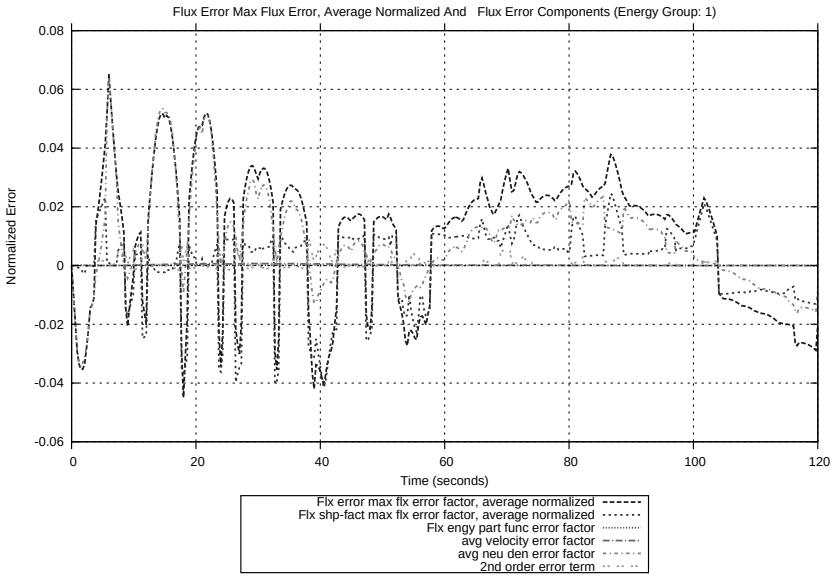

Figure C.47: Flux Error and Error Components at the Maximum Flux Error Position Average Normalized (Active, Trans 40, Group: 1)

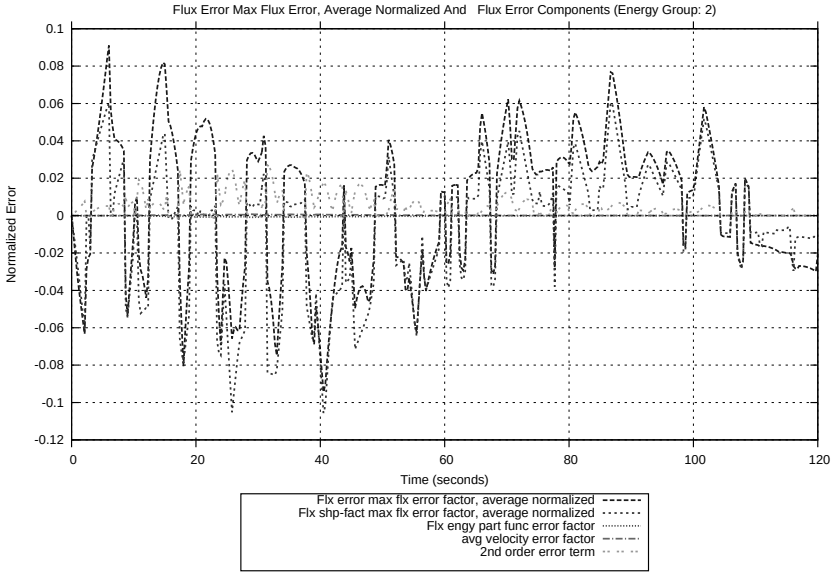

Figure C.48: Flux Error and Error Components at the Maximum Flux Error Position Average Normalized (Active, Trans 40, Group: 2)

Section B

Thermal-hydraulics Results

ABSTRACT

DACUS, ROBERT WARREN. Development of an Adaptive Thermal Conductivity Modeling Capability. (Under the direction of Paul Turinsky.)

This thesis presents a study of a generalized perturbation theory approach to determining the difference in the values of a Quantity of Interest (QoI) as predicted by two physics models. This is accomplished by forming an inner product of a generalized adjoint solution for one model with its respective residual formed from that model's operators acting upon the other model's determined solution. This study supports the development of an adaptive model refinement capability where the value of the QoI is used to decide among models of various fidelity levels satisfying accuracy requirements.

The specific application for this thesis is the modeling of the temperature profile of a single nuclear reactor core fuel pin of ceramic uranium oxide. The fuel pin has a radius of 0.3325 inches and height of 150 inches. It is assumed to deposit heat by conduction into a closed flow channel of water surrounding the fuel. The low fidelity model chosen utilizes a finite difference model with coarse spatial meshing whereas the high fidelity model employs finer spatial meshing. Lumped parameters are used for the low fidelity model's heat transfer coefficients. Several alternative adjoint methods were developed to estimate the difference in high and low fidelity fuel temperatures. These adjoint methods include mathematical, physical, and analytical types as derived from their respective equations. The associated high fidelity adjoint solutions were found to accurately predict fuel pin temperature differences for cases where the low fidelity solution was assumed constant due to equivalent forward problem high fidelity residual values. The physical and analytical adjoint solutions were unable to predict temperature differences for cases where spatial derivatives of the low fidelity temperatures were not equal to zero. In all cases, usage of the low fidelity adjoint solution in place of the high fidelity adjoint solution resulted in inaccurate predictions of temperature differences, while the high fidelity mathematical adjoint was able to predict differences exactly at every axial and radial location.

Development of an Adaptive Thermal Conductivity Modeling Capability

by
Robert Warren Dacus

A thesis submitted to the Graduate Faculty of
North Carolina State University
in partial fulfillment of the
requirements for the Degree of
Master of Science

Nuclear Engineering

Raleigh, North Carolina

2014

APPROVED BY:

Michael Doster	Sharon Lubkin
Troy Becker	Paul Turinsky Chair of Advisory Committee

DEDICATION

To my family and dear friends.

BIOGRAPHY

The author was born in Nashville, TN to Linda and Tad Dacus, later moving to Chattanooga, TN. He completed his undergraduate degree at the University of Tennessee at Chattanooga in chemical engineering. He moved to Raleigh, NC in order to pursue his Ph.D. in nuclear engineering from North Carolina State University under the direction of Paul Turinsky.

ACKNOWLEDGEMENTS

I would like to thank my advisor, Paul Turinsky, for his patience and help with this difficult and elusary project. I would also like to thank the Rickover Fellowship staff and coworkers at both Knolls Atmoic Power Lab (KAPL) and the nuclear engineering department at NC State for their willingness to listen and offer advice in technical and non-technical areas alike. Finally, my family and friends were instrumental in supplying the much needed moral support necessary to complete this degree.

TABLE OF CONTENTS

LIST OF TABLES

LIST OF FIGURES

Chapter 1

Introduction

In computational engineering, there is always a tension between being able to predict a physical phenomenon with the highest accuracy while maintaining a reasonable computational resource requirement. Oftentimes, the interests of accuracy and CPU resource demand are directly opposed, and designers find themselves sacrificing one advantage for another. In some cases, higher fidelity models are only necessary for problems with complex geometry or rapid transients, while at other times low fidelity models offer acceptable resolution for predicting spatial or temporal behavior.

Thermal hydraulic predictions of flow regimes within nuclear reactor cores require significant computational resources and accuracy to ensure that the core design does not violate the thermal limits of involved materials. These predictions often sacrifice accuracy for efficiency or vice versa. Fluid models like direct numerical simulation (DNS) resolve flow field phenomena at the smallest physical and temporal length scales. These simulations are able to deterministically calculate velocity and pressure fields of turbulent flow but at an extreme computational cost. Other models such as Reynolds Average Navier Stokes (RANS), using turbulence models, are able to approximate system wide pressures and velocities but are unable to determine local eddy configurations on the scale of DNS. In many cases, these turbulence approximations and averaging techniques are all that is needed for simple problems such as channel flow. However, for complex geometry, it is oftentimes desired to resolve smaller length scales in order to understand and simulate appropriate thermal hydraulic behavior at, for example, downstream locations from assembly grid spacers with mixing vanes.

Even for less sophisticated methods like drift-flux or homogeneous equilibrium mixture modeling, there can still be a significant trade off between computational demand and accuracy. Ideally, a model would exist that could actively switch between higher and lower fidelity

problems such that it would employ levels of fidelity where appropriate in order to save computational resources and improve accuracy at respective locations of interest. This approach is referred to as Adaptive Model Refinement (AMoR) and has the potential of capitalizing on the accuracy and CPU resource advantages of high and low fidelity models during a single simulation. In order to employ AMoR techniques, there must be a way to estimate the differences between predicted values for the high and low fidelity models such that the computational resource requirement for the prediction still remains less than the requirement for the high fidelity model. If the adaptation algorithm exceeds the high fidelity model CPU requirement, then the advantage of using the CPU efficient low fidelity model is lost. In a related field, AMoR techniques have been shown by Jackson, Cacuci, and Finnemann to produce accurate results using three fidelity levels for nuclear reactor safety transients that require only 30% to 70% of the CPU time needed using the highest fidelity level. [1], [2].

This masters thesis project examines an adaptive model refinement approach using adjoint methods for predicting differences between high and low fidelity models and its potential application to thermal hydraulic simulations. The focus of the work is on the generalized adjoint equations formulation. What follows is a rigorous derivation of all mathematics pertaining to the investigated adaptive model refinement method as well as an investigation of the numerical results from using this method with application to a heat conduction and convection model for a single fuel pin within a fuel assembly.

1.1 Thermal Hydraulic Design and Simulation

For safe and efficient operation of a thermal nuclear power core, a fluid must effectively cool the reactor core to appropriate temperatures in order to maintain the functional integrity of materials without compromising the configuration necessary to sustain a self-propagating chain reaction of the nuclear fuel. It is necessary for designers to understand the behavior of system wide pressures and velocities and how they affect overall plant performance as well as local fluid behavior that can influence things like corrosion and neutron flux. A wide variety of numerical tools is necessary in order to properly design and simulate a nuclear reactor and its plant and safety components. Each tool essentially presents a solution or approximation of the three dimensional mass, momentum, and energy balance equations for single or multiphase fluid flow. The level of simplification and estimation of these equations coincides with the demand for accuracy that a designer requires to predict a specific quantity of interest.

One dimensional or three dimensional techniques for solving the two phase mixture equa-

tions are typical for basic system wide simulation. Design codes such as RELAP and TRAC implement these methods for best-estimate thermal hydraulic design [19], [20]. Correlations are chosen in order to close the six-equation two phase system describing the mass, momentum, and internal energy of a flow field. For simulation and analysis focused on core internal thermal hydraulic behavior, either closed-channel methods or sub-channel methods as incorporated by COBRA and VIPRE codes are employed [21], [22]. The two-phase drift flux model, which considers only mixture momentum instead of separate phasic momentum equations and uses a correlation for determining the relative velocity of phases, may be employed for similar simulation conditions. Alternatively, the homogeneous equilibrium mixture (HEM) model assumes that both phases are at saturation and moving at the same velocity; therefore one only needs to solve for mixture momentum, mass, and energy. Although these methods are fast, they typically are unable to resolve flow mechanics close to the wall of the system, where oftentimes safety criteria such as critical heat flux (CHF) are a concern.

For simulating the wall resolved effects of turbulent flow, various computational multiphase fluid dynamics (CMFD) methods can be used to investigate flow phenomena that cannot be resolved by using simplified equations. In most cases momentum, mass, and energy are solved explicitly for each phase. Equations for turbulent kinetic energy and turbulent dispersion are also necessary in order to describe the effect of turbulence on the flow regime. Models such as k-ϵ or k-ω are typical for RANS equations and use correlations to describe the velocity distribution near the wall. As a consequence, the averaging technique used by RANS loses information regarding small eddy formation and dissipation within the flow field. Large eddy simulation (LES) can be used in its stead in order to retain the turbulence induced time dependent perturbation in the flow field. However, this is often computationally limiting due to the need for finer spatial meshing and time dependent ensemble average solutions. Codes such as STAR-CCM+ and HYDRA-TH enable RANS and LES methods to be used, employing a multiphase, N-field model [23], [24].

DNS methods mentioned previously have the capability of resolving all micro scales of fluid flow. These methods employ a variety of techniques for tracking the interface between liquid and vapor. Examples are front tracking and level set methods which both have the capability of simulating individual bubble or droplet interaction within a fluid. In this case, no wall models or correlations are necessary due to the fact that the length scale of individual bubbles has been resolved. The computational resources needed to implement these methods for a single reactor core channel containing thousands of bubbles are vast and DNS techniques are not typically used for large scale design. The computational codes PHASTA and FTC3D employ these DNS methods [25], [26]. They have proven useful for gaining insights and developing closure rela-

tionships for LES and RANS models, e.g. bubble lift and drag forces.

Each of the aforementioned fluid simulation techniques have advantages and disadvantages in terms of accuracy and computational resource requirement. Depending on the level of resolution required at the wall of a channel or whether full system response phenomena is of interest, designers will choose a model which exhibits a level of accuracy analogous with their design requirements.

All of these fidelity levels are used in concert with one other to ensure proper design of a nuclear reactor core and its supporting thermal hydraulic systems. Within each method, various closure models or equation parameters can help improve the physical accuracy of the problem at the cost of additional computational resources. In some cases though, the fidelity required at one point in the problem's geometry may not be necessary at other parts of the problem and the resulting computational requirement of using the higher fidelity model for the entire geometry may prove burdensome.

1.2 Adjoint Methods

Adjoint problems are mathematical constructs that mirror behavior found in physical or forward problems and help describe the importance of functionals with respect to a specific quantity of interest. Adjoint methods have found widespread use in the field of radiation transport due to its usefulness in perturbation analysis [1] - [3]. For small changes in specific parameters, adjoint solutions can describe the influence that these changes have within the detection region of interest. In neutronics, these changes can include material properties, source distributions, and cross sections. In thermal hydraulics, these changes include material properties as well as heat conduction estimations for inverse problems [4] - [8].

In computational fluid dynamics (CFD - single phase fluids as opposed to CMFD), adjoint methods are often used for adaptive grid refinement. These methods provide error controlled localized grid refinement as an attempt to reduce the numerical error present in CFD methods. Refining the grid needlessly does not explicitly reduce the numerical error, and there is a need to understand where and when grid refinement improves accuracy in order to maximize the efficiency of the refinement. Adjoint solution shapes can be thought of as importance weighting functions, and they can be used to quantify the importance of functionals like lift or drag within specific geometric locations of the spatial grid. Analysts can then use this information to determine where and to what degree a grid can be improved in order to reduce the numerical

error of the functional [9].

1.2.1 Detector Example

In adjoint problems, one has the freedom to describe boundary conditions and source terms such that the evaluation of a function yields the desired quantity of interest. A simple example is the detector response problem which is applicable to both thermal hydraulics and neutronics problems. In this problem, the response of a detector is desired as a function of source location. Typically, moving the source anywhere within the geometry of the problem necessitates a new temperature or flux field solution in order to evaluate detector response. Adjoint methods present an alternative approach.

Starting with the following forward and adjoint linear equations

$$A\left[\phi\right] = Q, \qquad A^*\left[\phi^*\right] = Q^* \tag{1.1}$$

the adjoint operator A^* is defined such that the following inner product equality holds for all ϕ and $\phi*$ within the solution space

$$\left\langle A\left[\phi\right], \phi^*\right\rangle = \left\langle A^*\left[\,\phi^*\,\right], \phi\right\rangle \tag{1.2}$$

Ensuring equality of (1.2) imposes restrictions on the boundary conditions of the adjoint problem. If the response function desired is defined as $R = \langle \Sigma, \phi \rangle$ then one can provide an exact evaluation of the response when the adjoint source term is given by $Q^* = \Sigma$

$$\langle \Sigma, \phi \rangle = \langle Q^*, \phi \rangle = \langle A^*[\phi^*], \phi \rangle = \left\langle A\left[\phi\right], \phi^*\right\rangle = \langle Q, \phi^* \rangle \tag{1.3}$$

Using (1.3), one is able to determine the response of a detector for various Q locations without having to solve for ϕ each time Q is moved. Instead, ϕ^* is determined once and then can provide the response for any value of Q in the solution space. This method of functional response prediction with respect to adjoint solutions can provide a means for performing adaptive model refinement with application to simple fuel conduction and convection problems investigated by this thesis.

1.2.2 Physical and Mathematical Adjoint Operators

There are two distinct methods for deriving the adjoint A^* operator. A physical adjoint is defined as an adjoint operator that is derived from the continuous set of forward equations. One constrains the adjoint operator in order to satisfy equation (1.2) and, using integration by parts,

comes to an appropriate adjoint operator. The application of appropriate boundary conditions (generally homogeneous) ensures that the equality in (1.2) holds.

Each forward operator present in a set of equations will have a corresponding adjoint operator. These operators are said to be self adjoint if $A^* = A$. Second derivatives and constant multipliers are examples of self adjoint operators while first order derivatives are not self adjoint [1]. Adjoints of matrix operators can be derived as well by taking the conjugate transpose of the original matrix.

Discrete adjoint solutions can be found by solving for the discretized set of adjoint equations as derived from the forward equations. This adjoint problem is referred to in this work as a physical adjoint.

Another method of arriving at a set of discretized adjoint equations is to derive them from the discretized forward equations. Since the adjoint of a matrix operator is the conjugate transpose of the matrix, then for a discretized forward matrix $\bar{\bar{\mathbf{A}}}$ operating on the forward solution vector $\bar{\phi}$, we have the following forward and adjoint problem

$$\bar{\bar{\mathbf{A}}}\left[\bar{\phi}\right] = \bar{\mathbf{Q}}, \qquad \bar{\bar{\mathbf{A}}}^{\mathbf{T}}\left[\bar{\phi}^*\right] = \bar{\mathbf{Q}}^* \tag{1.4}$$

This method requires no integration by parts, and the appropriate boundary and initial conditions for the adjoint problem are embedded in the transposed matrix $\bar{\bar{\mathbf{A}}}^T$. In this work, the previously defined adjoint problem is referred to as the mathematical adjoint. As the time and spatial discretization steps approach zero, the discrete mathematical adjoint equations are expected to approach the physical adjoint equations. For discrete problems, there is no guarantee that the discretized physical adjoint solution will be the same as the mathematical adjoint solution. However, if the problems are defined correctly, the functional as predicted by the adjoint solutions should be the same for both the physical and mathematical problems.

1.3 Problem Definition

1.3.1 Forward Problem

This forward problem models one dimensional heat conduction through a cylindrical fuel pin of uranium oxide. This fuel pin has a radius of 0.3325 inches and a height of 150 inches. It is assumed to deposit heat directly into a channel of water surrounding the fuel. The heat generation can either vary sinusoidally in the axial direction and is constant in the radial direction or is constant in all directions. The coolant model assumes that the steam and liquid are both

have the same pressure and velocity, and have temperatures that vary in the axial direction. The equation set, initial conditions, and boundary conditions below model the fuel conduction and convection of a cylindrical fuel pin.

$$c_p^f \rho_f \frac{\partial}{\partial t} T_f - k_f \nabla_r^2 \, T_f = q''' \tag{1.5}$$

$$c_p^c \rho_c A_x \frac{\partial}{\partial t} T_c + c_p^c \dot{m}_c \frac{\partial}{\partial z} T_c + S_f k_f \nabla_r \, T_f|_{r=R} = 0 \tag{1.6}$$

$$h_c \left(T_f|_{r=R} - T_c \right) = -k_f \nabla_r \, T_f|_{r=R} \tag{1.7}$$

$$T_c|_{t=0} = T_c^{(o)} \qquad T_f|_{t=0} = T_f^{(o)} \tag{1.8}$$

$$T_c|_{z=0} = T_c^{In} \qquad \nabla_r \, T_f|_{r=o} = 0 \tag{1.9}$$

where T_f is the fuel temperature as a function of time t, axial location z, and radial location r; T_c is the coolant temperature as a function of time t and axial location z. Heat energy generated, denoted by the z dependent variable q''', conducts radially through the pin. Axial heat conduction is ignored, however T_f is still z dependent. This dependency arises from the axial coupling present in equation (1.7) which describes heat convection along the outside surface of the pin. All heat generated in the pin by the q''' term is conducted to the outside surface and passes into the coolant and out the exit boundary condition at the top of the channel. Fluid flow properties are represented by a single mass flow rate term $\dot{m}_c$ where closed flow channel, single phase, and constant density are assumed to make the flow rate constant with z.

Figure 1.1 contains a visual representation of the cylindrical UO_2 fuel pin and its respective radial and axial discretization. There are 4 radial cells or rings and 4 axial meshes shown in the figure. Each fuel and coolant temperature location, denoted by $T_{f-i,j}$ and T_{c-j} respectively with $i \in [1, 2, ..., N_r]$ and $j \in [1, 2, ..., N_z]$, is shown along with its node number, denoted by ϕ_l with $l \in [1, 2, ..., N_l]$ where N_l represents the total number of discretized cells. Again, $\bar{\boldsymbol{\phi}}$ is the solution vector containing all fuel and coolant temperatures. The cell numbering starts at the center radial cell of the first axial mesh and then increases as it moves in the positive r direction. Upon reaching the outer most radial cell, the numbering drops below to the next axial mesh, center radial ring and increases in node number as r increases. The coolant temperature nodes are at the end of the $\bar{\phi}$ vector, starting at the top axial mesh and moving downward.

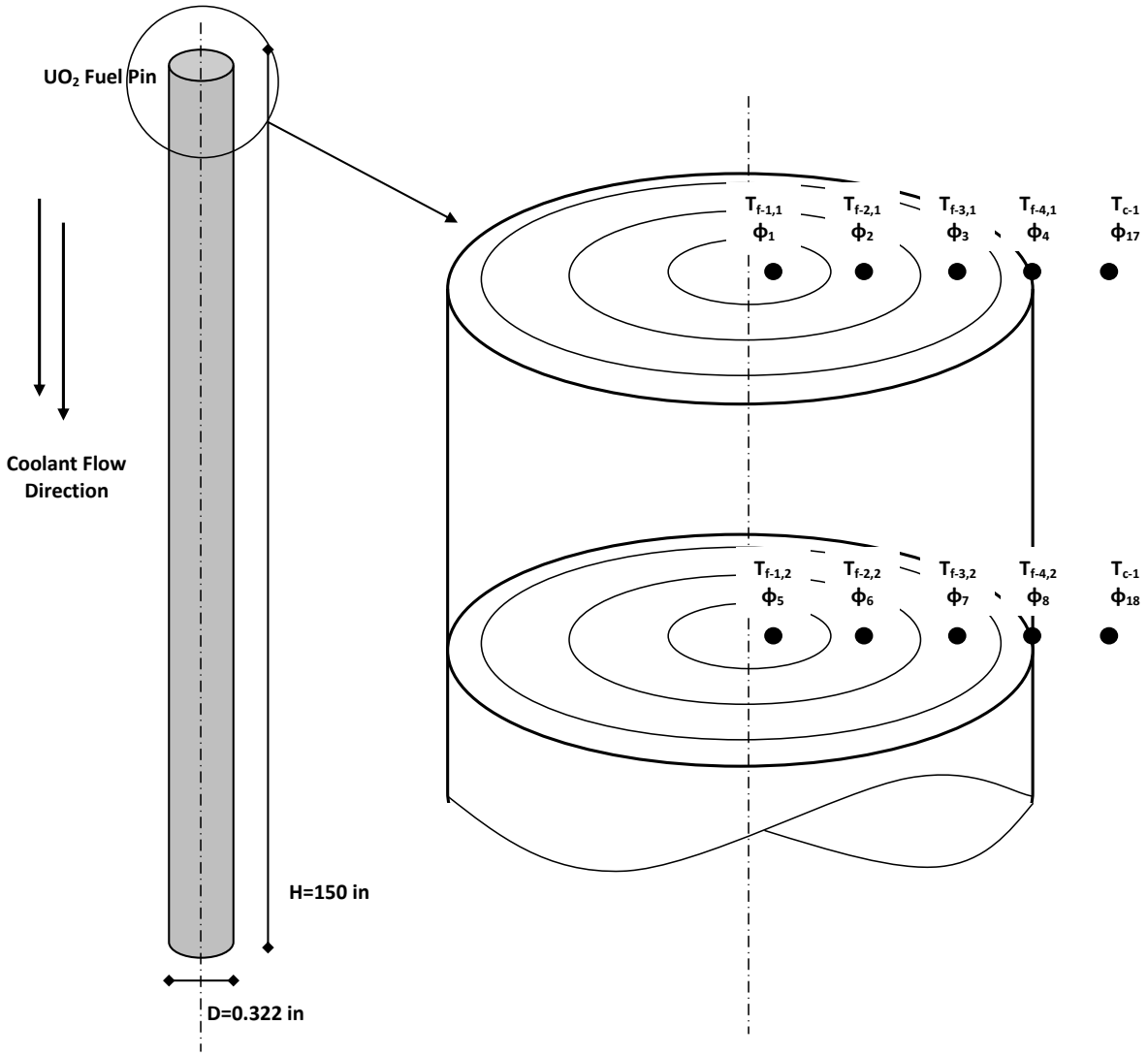

$$\overline{\phi} = \left[\phi_1 \;\; \phi_2 \;\; \phi_3 \;\; \phi_4 \cdots \phi_{17} \;\; \phi_{18} \;\; \phi_{19} \;\; \phi_{20}\right]^{\mathrm{T}}$$

Figure 1.1: **Physical geometry of simplified forward problem and example discretization and node numbering**

The gradient and Laplacian operators, ∇_r and ∇_r^2 respectively, denote the use of cylindrical coordinates. Table 1.1 contains a list of constants and their values used for the high fidelity forward problem. These values are assumed to remain constant regardless of material temperature for the high fidelity case. In the low fidelity case, k_f and h_c are adjusted in order to conserve the heat flux between collapsed discretized radial mesh cells, simply refered to as rings throughout this thesis.

Table 1.1: **Physical properties for fuel pin equations**

Property	**Symbol**	**Value**
Fuel Specific Heat	c_p^f	0.0762 BTU/lbm-F
Coolant Specific Heat	c_p^c	1.394 BTU/lbm-F
Fuel Thermal Conductivity	k_f	2.00 BTU/hr-ft-F
Fuel Density	ρ_f	685 lbm/ft^3
Coolant Mass Flow Rate	$\dot{m}_c$	3124 lbm/hr
Coolant Convection Coefficient	h_c	8,500 BTU/hr-ft$^2 - F$
Coolant Flow Area	A_x	0.174 in^2
Fuel Pin Radius	R	0.161 in
Fuel Pin Circumference	S_f	1.013 in

Equations (1.5) and (1.6) are solved using two separate levels of discretization. The high fidelity model employs a finite difference model for approximating both radial and axial derivatives. The low fidelity problem uses lumped parameters in order to determine material conductivities of the fuel and coolant. It also uses finite difference to approximate derivatives with fewer radial rings as compared to the high fidelity model. The number of axial nodes remains constant and equal for both the high fidelity and low fidelity simulations.

Additionally, for q'''constant, there is a simple analytical solution to the forward continuous equation set. This can be used to verify the discrete numerical solution for the high fidelity forward problem. Additionally, this analytic solution can be used in conjunction with the adjoint analytical solution to verify the continuous adjoint's evaluation of a functional. The analytic solution provides insight into the ability of low fidelity adjoints for use in the approximation of functional values. The discrete high and low fidelity models and continuous forward model are investigated rigorously in the derivation section of this thesis.

1.3.2 Adjoint Problem

Three adjoint problems are considered with application for adaptive model refinement. These are referred to as the mathematical, physical, and analytic adjoint models respectively. The adjoint equation set, final conditions, and boundary conditions presented below are derived from the forward continuous equations (1.5) - (1.9)

$$-\rho_f \frac{\partial}{\partial t} T_f^* - k_f \nabla_r^2 T_f^* = Q^* \tag{1.10}$$

$$c_p^c \rho_c A_c \frac{\partial}{\partial t} T_c^* + c_p^c \dot{m}_c \frac{\partial}{\partial z} T_c^* = S_f k_f \nabla_r \, T_f^* \big|_{r=R} \tag{1.11}$$

$$-k_f \nabla_r T_f^* \big|_{r=R} = h_c \left(T_f^* \big|_{r=R} - T_c^* \right) = q''^* \big|_{r=R} \tag{1.12}$$

$$T_c^* \big|_{t=t_F} = \quad T_f^* \big|_{t=t_F} = 0 \tag{1.13}$$

$$T_c^\dagger \Big|_{z=H} = 0, \quad \nabla_r \, T_f^\dagger \Big|_{r=0} = 0 \tag{1.14}$$

with t_f denoting the final time. This equation set is referred to as the analytic adjoint and is derived rigorously in the following section. Q^* varies according to the problem definition and the quantity of interest to be evaluated by the response. For certain Q^*, this equation set admits an analytic solution.

Similar to the analytic forward solution, the analytic adjoint solution presents a continuous solution to the simplified adjoint problem for use in verifying the physical and mathematical adjoint results. The physical adjoint refers to the discretized version the above equation set using finite difference in the same manner as the high fidelity forward problem.

Another method for arriving at a discretized adjoint is to take the conjugate transpose of the forward matrix operator. The time dependent forward problem can be described by the following matrix equation

$$\bar{\bar{\mathbf{C}}}_{\mathbf{n+1}} \bar{\boldsymbol{\phi}}_{\mathbf{n+1}} = \bar{\bar{\mathbf{B}}}_{\mathbf{n+1}} \bar{\boldsymbol{\phi}}_{\mathbf{n}} + \bar{\mathbf{Q}}_{\mathbf{n+1}} \tag{1.15}$$

where $n+1$ is the current timestep, n is the previous timestep, and the $\bar{\bar{\mathbf{C}}}$ and $\bar{\bar{\mathbf{B}}}$ are matrix operators acting on the appropriate time dependent solution vector $\bar{\boldsymbol{\phi}}$. Equation (1.15) can be written in block matrix form as

$$\begin{bmatrix} \bar{\bar{\mathbf{C}}}_{\mathbf{1}} & & & & \\ \bar{\bar{\mathbf{B}}}_{\mathbf{2}} & \bar{\bar{\mathbf{C}}}_{\mathbf{2}} & & & \\ & \bar{\bar{\mathbf{B}}}_{\mathbf{3}} & \bar{\bar{\mathbf{C}}}_{\mathbf{3}} & & \\ & & \ddots & \ddots & \end{bmatrix} \begin{bmatrix} \bar{\phi}_1 \\ \bar{\phi}_2 \\ \bar{\phi}_3 \\ \vdots \end{bmatrix} = \begin{bmatrix} \bar{\mathbf{Q}}_1 \\ \bar{\mathbf{Q}}_2 \\ \bar{\mathbf{Q}}_3 \\ \vdots \end{bmatrix}$$

which can be explicitly solved for a given set of initial conditions. The time dependent mathematical adjoint is then simply the conjugate transpose of this block matrix structure and each individual matrix operator. Similar to the analytic forward solution, the analytic adjoint solution admits a continuous solution to the simplified adjoint problem for use in verifying the physical and mathematical adjoint results. Therefore, one has for the mathematical adjoint problem

$$\begin{bmatrix} \bar{\bar{\mathbf{C}}}^*_{\mathbf{1}} & \bar{\bar{\mathbf{B}}}^*_{\mathbf{2}} & & & \\ & \bar{\bar{\mathbf{C}}}^*_{\mathbf{2}} & \bar{\bar{\mathbf{B}}}^*_{\mathbf{3}} & & \\ & & \bar{\bar{\mathbf{C}}}^*_{\mathbf{3}} & \ddots & \\ & & & \ddots & \end{bmatrix} \begin{bmatrix} \bar{\phi}^*_1 \\ \bar{\phi}^*_2 \\ \bar{\phi}^*_3 \\ \vdots \end{bmatrix} = \begin{bmatrix} \bar{\mathbf{Q}}^*_1 \\ \bar{\mathbf{Q}}^*_2 \\ \bar{\mathbf{Q}}^*_3 \\ \vdots \end{bmatrix}$$

which can also be explicitly solved for a given a set of final conditions. The definition of adjoint matrix operators results in

$$\bar{\bar{\mathbf{C}}}^* = \bar{\bar{\mathbf{C}}}^{\mathbf{T}}, \qquad \bar{\bar{\mathbf{B}}}^* = \bar{\bar{\mathbf{B}}}^{\mathbf{T}}$$

Chapter 2

Derivation of Forward and Adjoint Problems

The following section describes the derivation of the forward and adjoint methods used by the adaptive model refinement method for heat conduction and convection. The first section outlines the continuous and discrete high fidelity forward problem. The next section shows the derivation of adjoint equations by two separate means - formulating both the physical adjoint and a mathematical adjoint. The physical adjoint equation derives discrete adjoint equations from the continuous adjoint equations. Conversely, mathematical adjoint equations derives operators from discrete forward equations by taking the conjugate transpose of the forward linear operator. Ideally, a physical and mathematical adjoint derivation should arrive at the same set of continuous adjoint equations in the limit where time and spatial step sizes approach zero.

Due to the simplicity of the forward heat conduction and single node convection problem, it was possible under certain conditions to formulate an analytical solution for both the steady state forward and adjoint problem. One can then show explicitly that the response function of interest with regards to the adjoint solution can represent the exact quantity of interest. The final section of this chapter describes the low fidelity problem.

2.1 Forward Problem

The following section describes the forward fuel conduction and convection problem discretization for both the low and high fidelity models. Also included is a derivation of the analytic solution to the steady state problem with constant heat generation.

2.1.1 High Fidelity Discretization

In order to discretize the forward problem using finite difference methods, the steady state problem is first considered. Setting time derivatives to zero we have the following forward problem

$$k_f \nabla_r^2 T_f = q''', \qquad -c_{p_c} \dot{m}_c \frac{\partial T_c}{\partial z} + q''\big|_{r=R} = 0$$

$$-k_f \nabla_r \, T_f|_{r=R} = h_c \left(T_f|_{r=R} - T_c \right)$$

$$\nabla_r \, T_f|_{r=0} = 0, \quad T_c|_{z=0} = T_{c,in}$$

$$q''\big|_{r=R} = h_c S_f \left(T_f|_{r=R} - T_c \right)$$

Integrating the fuel equation over $\int_{r_i}^{r_{i+1}} \cdot 2\pi r \mathrm{d}r$ results in

$$k_f \int_{r_i}^{r_{i+1}} \nabla^2 T_f 2\pi r \mathrm{d}r = k_f \int_{r_i}^{r_{i+1}} 2\pi r \left(\frac{1}{r} \frac{\partial}{\partial r} \left(r \frac{\partial T_f}{\partial r} \right) \right) \mathrm{d}r$$

$$= 2\pi k_f \int_{r_i}^{r_{i+1}} \left(\frac{\partial}{\partial r} \left(r \frac{\partial T_f}{\partial r} \right) \right) \mathrm{d}r = 2\pi k_f r \left. \frac{\partial T_f}{\partial r} \right|_{r_i}^{r_{i+1}}$$

Taking the finite difference of $\dfrac{\partial T_f}{\partial r}$, assuming Δr is constant, and setting $z = z_j$ we have

$$2\pi k_f r \left. \frac{\partial T_f}{\partial r} \right|_{r_i}^{r_{i+1}} \approx 2\pi k_f \left[r_h \frac{T_{f_{h,j}} - T_{f_{h-1,j}}}{\Delta r} \right|_{h=r_i}^{h=r_i+1}$$

$$= 2\pi k_f \left[r_i \frac{T_{f_{i+1,j}} - T_{f_{i,j}}}{\Delta r} - r_{i-1} \frac{T_{f_{i,j}} - T_{f_{i-1,j}}}{\Delta r} \right]$$

$$= 2\pi k_f \left[\frac{r_i}{\Delta r} T_{f_{i+1,j}} - \left(\frac{r_i}{\Delta r} + \frac{r_{i-1}}{\Delta r} \right) T_{f_{i,j}} + \frac{r_{i-1}}{\Delta r} T_{f_{i-1,j}} \right]$$

where $r_i^+ \equiv r_i + \Delta r/2$ and $T_{f_{i,j}} \equiv T_f \left(r_i^+, z_j + \Delta z/2 \right)$.

Define the following constants for $i = (1, N_r - 1)$:

$$\mathrm{a}_i \equiv 2\pi k_f \frac{r_i}{\Delta r}$$

$$\mathrm{b}_i \equiv -\left(a_{i-1} + a_i \right)$$

Using these constants, the previous expression becomes

$$= a_i T_{f_{i+1,j}} + b_i T_{f_{i,j}} + a_{i-1} T_{f_{i-1,j}}$$

In order to evaluate the expression $2\pi k_f r \left.\dfrac{\partial T_f}{\partial r}\right|_{r_i}^{r_{i+1}}$ at the first node, the boundary condition for $\nabla_r T_f|_{r=0}$ is directly substituted resulting in:

$$2\pi k_f r \left.\frac{\partial T_f}{\partial r}\right|_{r_1}^{r_2} = 2\pi k_f r \left.\frac{\partial T_f}{\partial r}\right|_{r_2} - 2\pi k_f r \left.\frac{\partial T_f}{\partial r}\right|_{r_1}$$

$$= 2\pi k_f r_2 \left(\frac{T_{f_{2,j}} - T_{f_{1,j}}}{\Delta r}\right) = 2\pi k_f \left[\frac{r_2}{\Delta r} T_{f_{2,j}} - \frac{r_2}{\Delta r} T_{f_{1,j}}\right]$$

$$= a_2 T_{f_{2,j}} - a_2 T_{f_{1,j}}$$

At the fuel pin surface, there is a special definition for $T_{f^*_{N_r}}$ such that $T_{f^*_{N_r}} \equiv T_f\left(R, z_j + \Delta z/2\right)$. The pin edge fuel temperature, $T_f|_R$, is assumed to equal the average fuel temperature for the outermost ring. Applying this relationship to the final radial node of the fuel pin results in the following

$$2\pi k_f r \left.\frac{\partial T_f}{\partial r}\right|_{r_{N_r-1}}^{r_{N_r}} = 2\pi k_f r \left.\frac{\partial T_f}{\partial r}\right|_{r_{N_r}} - 2\pi k_f r \left.\frac{\partial T_f}{\partial r}\right|_{r_{N_r-1}}$$

$$= 2\pi R k_f \left[-\frac{h_c}{k_f}\left(T_{f^*_{N_r,j}} - T_{c_j}\right)\right] - 2\pi k_f r_{N_r-1} \left(\frac{T_{f^*_{N_r,j}} - T_{f_{N_r-1,j}}}{\Delta r}\right)$$

$$= 2\pi R h_c T_{c_j} - \left(2\pi R h_c + \frac{2\pi k_f r_{N_r-1}}{\Delta r}\right) T^*_{f_{N_r,j}} + \left(\frac{2\pi k_f r_{N_r-1}}{\Delta r}\right) T_{f_{N_r-1,j}}$$

Noting that $2\pi R = S_f$ the following constants are defined

$$f = S_f h_c$$

$$e = -\left(\mathrm{f} + \mathrm{a}_{N_r-1}\right)$$

Using these constants, the previous expression is then

$$= f T_{c_j} + e T_{f^*_{N_r,j}} + a_{N_{r-1}} T_{f_{N_r-1,j}}$$

For the coolant, we assume that Δz is uniform axially along the pin, and we define $T_{c_j} \equiv T_c\left(z_j\right)$ at the axial node position for $z_j \in [0, H]$. At $j = 0$, we have $T_{c_o} = T_c(0) = T_{c,in}$.

For the surface boundary condition of the pin we have the following expression

$$q''|_{r=R} = h_c S_f \left(T_f|_{r=R} - T_c\right) = h_c S_f \left(T_{f^*_{N_r}} - T_{c_{j+1/2}}\right) = h_c S_f \left(T_{f^*_{N_r}} - T_{c_j}\right)$$

Substituting the upwinded finite difference for $\frac{\partial T_c}{\partial z}$ at cell $j + 1/2$ results in the following

$$-c_{p_c}\dot{m}_c \frac{\partial T_c}{\partial z} + q''|_{r=R} \approx -c_{p_c}\dot{m}_c \left(\frac{T_{c_{j+1}} - T_{c_j}}{\Delta z}\right) + h_c S_f \left(T_{f^*_{N_r,j}} - T_{c_j}\right)$$

$$= \left(\frac{c_{p_c}\dot{m}_c}{\Delta z} - h_c S_f\right) T_{c_j} - \left(\frac{c_{p_c}\dot{m}_c}{\Delta z}\right) T_{c_{j+1}} + h_c S_f T_{f^*_{N_r,j}}$$

Define the following constants

$$k = -\frac{c_{p_c}\dot{m}_c}{\Delta z}$$

$$m = -\left(\mathrm{k} + \mathrm{f}\right)$$

Using these constants, the previous expression becomes

$$= mT_{c_j} + kT_{c_{j+1}} + fT_{f^*_{N_r,j}}$$

The steady state discretized problem is then

$$\bar{\bar{\mathbf{A}}}\bar{\boldsymbol{\phi}} + \bar{\mathbf{d}} = 0 \tag{2.1}$$

with $\bar{\boldsymbol{\phi}} = \left[\bar{T_f}\ \bar{T_c}\right]^T$ and, the steady state temperature operator $\bar{\bar{\mathbf{A}}}$ defined as

$$\bar{\bar{\mathbf{A}}} = \begin{bmatrix} \bar{\bar{\mathbf{D}}}_f & \bar{\bar{\mathbf{O}}}_f \\ \bar{\bar{\mathbf{O}}}_c & \bar{\bar{\mathbf{D}}}_c \end{bmatrix}$$

with

$$\bar{\bar{\mathbf{D}}}_f = \begin{bmatrix} -a_2 & a_2 & & & & & \\ a_2 & b_3 & a_3 & & & & \\ & a_3 & b_4 & a_4 & & & \\ & & & \ddots & & & \\ & & & a_{N_r-2} & b_{N_r-1} & a_{Nr-1} & \\ & & & & a_{N_r-1} & e & \\ & & & & & \ddots & \end{bmatrix}, \quad \bar{\bar{\mathbf{O}}}_f = \begin{bmatrix} \vdots & & & & \\ f & & & & \\ & \ddots & & & \\ & & f & & \\ & & & \ddots & \\ & & & & f \end{bmatrix},$$

$$\bar{\bar{\mathbf{D}}}_c = \begin{bmatrix} m & & & \\ k & m & & \\ & & \ddots & \\ & & & k \quad m \end{bmatrix}, \quad \bar{\bar{\mathbf{O}}}_c = \begin{bmatrix} \cdots & f & & \\ & & \ddots & \\ & & & f \end{bmatrix}$$

In order to solve the time dependent system, we consider the following spatially discretized system

$$\bar{\boldsymbol{\gamma}} \frac{\partial \bar{\boldsymbol{\phi}}}{\partial t} = \bar{\bar{\mathbf{A}}} \bar{\boldsymbol{\phi}} + \bar{\mathbf{d}} \tag{2.2}$$

with $\bar{\boldsymbol{\gamma}} = [c_p^f \rho_f \; c_p^f \rho_f \ldots c_p^f \rho_f]^T$. Integrate equation (2.1) over the interval $\int_{t_n}^{t_{n+1}} \cdot dt$

$$\int_{t_n}^{t_{n+1}} \left[\bar{\boldsymbol{\gamma}} \frac{\partial \bar{\boldsymbol{\phi}}}{\partial t} = \bar{\bar{\mathbf{A}}} \bar{\boldsymbol{\phi}} + \bar{\mathbf{d}} \right] dt$$

$$\bar{\boldsymbol{\gamma}} \bar{\boldsymbol{\phi}}_{n+1} - \bar{\boldsymbol{\gamma}} \bar{\boldsymbol{\phi}}_n = \int_{t_n}^{t_{n+1}} \left(\bar{\bar{\mathbf{A}}} \bar{\boldsymbol{\phi}} + \bar{\mathbf{d}} \right) dt$$

We approximate the time integration by using the following equation

$$\bar{\boldsymbol{\gamma}} \bar{\boldsymbol{\phi}}_{n+1} - \bar{\boldsymbol{\gamma}} \bar{\boldsymbol{\phi}}_n \approx \left\{ \alpha \left[\bar{\bar{\mathbf{A}}} \bar{\boldsymbol{\phi}} + \bar{\mathbf{d}} \right]_{t_{n+1}} + (1-\alpha) \left[\bar{\bar{\mathbf{A}}} \bar{\boldsymbol{\phi}} + \bar{\mathbf{d}} \right]_{t_n} \right\} \Delta t_n$$

which is an explicit or implicit time discretization with $\alpha = (0, 1)$. Reordering the previous equation results in

$$\bar{\boldsymbol{\gamma}}\bar{\boldsymbol{\phi}}_{n+1} - \alpha\Delta t_n \bar{\bar{\mathbf{A}}}_{n+1}\bar{\boldsymbol{\phi}}_{n+1} = \bar{\boldsymbol{\gamma}}\bar{\boldsymbol{\phi}}_n + (1-\alpha)\Delta t_n \bar{\bar{\mathbf{A}}}_n\bar{\boldsymbol{\phi}}_n + \alpha\Delta t_n \bar{\mathbf{d}}_{n+1}$$

This expression can be written generally as

$$\bar{\bar{\mathbf{C}}}_{n+1}\bar{\boldsymbol{\phi}}_{n+1} = -\bar{\bar{\mathbf{B}}}_{n+1}\bar{\boldsymbol{\phi}}_n + \bar{\mathbf{Q}}_{n+1} \tag{2.3}$$

with

$$\begin{aligned}
\bar{\bar{\mathbf{C}}}_{n+1} &\equiv \bar{\boldsymbol{\gamma}}\bar{\bar{\mathbf{I}}} - \Delta t_n \bar{\bar{\mathbf{A}}}_{n+1} \\
\bar{\bar{\mathbf{B}}}_{n+1} &\equiv \bar{\boldsymbol{\gamma}}\bar{\bar{\mathbf{I}}} - \Delta t_n \bar{\bar{\mathbf{A}}}_{n} \\
\bar{\mathbf{Q}}_{n+1} &\equiv \alpha\Delta t_n \bar{\mathbf{d}}_{n+1} + (1-\alpha)\Delta t_n \bar{\mathbf{d}}_n
\end{aligned}$$

This time discretization structure results in a block matrix similar to the one presented in the previous mathematical adjoint example.

$$\begin{bmatrix}
\bar{\bar{\mathbf{C}}}_{\mathbf{1}} & & & \\
\bar{\bar{\mathbf{B}}}_{\mathbf{2}} & \bar{\bar{\mathbf{C}}}_{\mathbf{2}} & & \\
 & \bar{\bar{\mathbf{B}}}_{\mathbf{3}} & \bar{\bar{\mathbf{C}}}_{\mathbf{3}} & \\
 & & \ddots & \ddots
\end{bmatrix}
\begin{bmatrix} \bar{\boldsymbol{\phi}}_1 \\ \bar{\boldsymbol{\phi}}_2 \\ \bar{\boldsymbol{\phi}}_3 \\ \vdots \end{bmatrix}
=
\begin{bmatrix} \bar{\mathbf{Q}}_1 \\ \bar{\mathbf{Q}}_2 \\ \bar{\mathbf{Q}}_3 \\ \vdots \end{bmatrix}$$

The above system of equations can be solved given an appropriate set of initial conditions.

2.1.2 Low Fidelity Problem

The low fidelity problem is roughly the same as the high fidelity problem but with fewer radial rings. Adjusted values for thermal conductivities are used in the low fidelity problem such that the volume averaged temperatures for the high fidelity solution are equivalent to the low fidelity solution. This resulting low fidelity solution must then be mapped onto the high fidelity mesh in order to evaluate the high fidelity residual used with the adjoint to evaluate the difference metric. The current mapping method is simple linear interpolation between low fidelity node solutions. Figure 2.1 below shows a representative grid of a high and low fidelity problem containing 8 and 4 nodes respectively. The Δr_l values are selected such that the high and low temperature locations for the quantity of interest match.

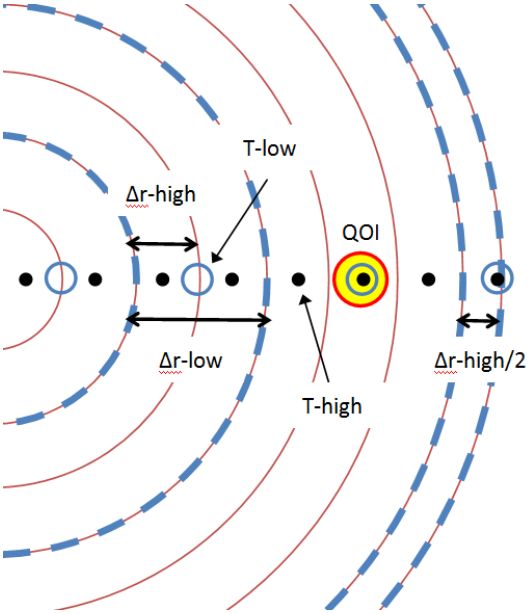

Figure 2.1: **Low and high fidelity representative mesh such that the quantity of interest locations match for four and eight ring models**

The adjusted parameters used in the low fidelity problem are defined as follows. For the fuel region, we have

$$k_{eff} = k_f \left[\frac{T_{f_{i+1,j}} - T_{f_{i,j}}}{\bar{T}_{f_{l+1,j}} - \bar{T}_{f_{l,j}}} \right] \frac{\Delta r_l}{\Delta r_i} \tag{2.4}$$

where the subscript l denotes the low fidelity node number and $\bar{T}_{f_{l,j}}$ denotes the high fidelity temperature solution mapped to the low fidelity mesh. Using k_{eff} values instead of k values ensures that the heat flux between radial rings is equal for both models.

Similarly, for the low fidelity coolant equations, the following adjusted convection coefficient is used

$$h_{eff} = h_c \left[\frac{T_{f_{N_r^*,j}} - T_{c_j}}{\bar{T}_{f_{N_{rl},j}} - \bar{T}_{c_{jl}}} \right] \tag{2.5}$$

where $\bar{T}_{f_{N_{rl},j}}$ and $\bar{T}_{c_{jl}}$ denote the low fidelity final ring temperature and coolant temperature respectively for node j. Similarly to the previous expression, this ensures that the heat flux at the pin boundary is the same for both the high and low fidelity. Using these adjusted parameters with the finite differenced coolant equations represented in the previous section will result in

an equality between high and low fidelity volume averaged temperatures. Because the adjusted parameters are calculated using steady state values, the average high fidelity fuel temperatures will not match the low fidelity fuel temperatures during transients.

Similarly to the high fidelity forward problem, the low fidelity steady state discretized problem is

$$\widetilde{\bar{\mathbf{A}}}\widetilde{\boldsymbol{\phi}} + \widetilde{\mathbf{d}} = 0 \tag{2.6}$$

with $\widetilde{\boldsymbol{\phi}} = \left[\widetilde{T_f}\ \widetilde{T_c}\right]^T$. The low fidelity steady state temperature operator $\widetilde{\bar{\mathbf{A}}}$ is a coarse version of $\bar{\bar{\mathbf{A}}}$ using the k_{eff} and h_{eff} constants for the fluid and fuel equations. The matrix structure of $\widetilde{\bar{\mathbf{A}}}$ will have the same structure as $\bar{\bar{\mathbf{A}}}$ but with fewer rows dedicated to radial temperatures.

The time dependent low fidelity solution will have the following structure

$$\widetilde{\bar{\mathbf{C}}}_{n+1}\widetilde{\boldsymbol{\phi}}_{n+1} = -\widetilde{\bar{\mathbf{B}}}_{n+1}\widetilde{\boldsymbol{\phi}}_n + \widetilde{\mathbf{Q}}_{n+1} \tag{2.7}$$

with

$$\begin{aligned}
\widetilde{\bar{\mathbf{C}}}_{n+1} &\equiv \left[\widetilde{\gamma}\bar{\bar{\mathbf{I}}} - \Delta t_n \widetilde{\bar{\mathbf{A}}}_{n+1}\right] \\
\widetilde{\bar{\mathbf{B}}}_{n+1} &\equiv \left[\widetilde{\gamma}\bar{\bar{\mathbf{I}}} - \Delta t_n \widetilde{\bar{\mathbf{A}}}_{n}\right] \\
\widetilde{\mathbf{Q}}_{n+1} &\equiv \alpha\Delta t_n \widetilde{\mathbf{d}}_{n+1} + (1-\alpha)\Delta t_n \widetilde{\mathbf{d}}_n
\end{aligned}$$

Linear interpolation between low fidelity temperatures for mapping onto the high fidelity mesh will also cause a discrepancy between fidelity temperatures for both steady state and time dependent problems. It is important to note that although the low fidelity problem is using a finite difference scheme on a coarser mesh, refinement is not the only difference between high fidelity and low fidelity problems. If this were the case, the adjoint methods presented in this thesis would simply be an extension to adaptive meshing applied to a heat conduction problem. Since the low fidelity problem uses adjusted convection and conduction coefficients in addition to linear interpolation, it can be thought of as a separate mathematical model for predicting fuel temperatures on a radial mesh comparable to the high fidelity finite difference scheme.

2.1.3 Forward Analytic Solution

An analytic solution to the steady state forward equations was determined for verification purposes. For this thesis, much of the verification work was done with the steady state problem

since time dependent adjoint behavior was found to be a trivial extension. A constant heat generation was assumed to help simplify analytic derivations. What follows is the determination of an analytic solution to the steady state forward problem with constant heat generation.

Start with the steady state forward problem definition

$$-\frac{k_f}{r}\frac{\partial}{\partial r}\left(r\frac{\partial T_f}{\partial r}\right) = q''' = \text{constant} \tag{2.8}$$

$$c_p^c \dot{m}_c \frac{dT_c}{dz} - 2\pi R q'' = 0 \tag{2.9}$$

$$T_c|_{z=0} = T_{c_{in}}, \quad \left.\frac{\partial T_f}{\partial r}\right|_{r=0} = 0$$

$$\left.-k_f \frac{\partial T_f}{\partial r}\right|_{r=R} = h_c\left(T_f|_{r=R} - T_c\right) = \left. q''\right|_{r=R}$$

Solving for the heat flux q'' at the pin surface:

$$q'''\left(\pi R^2 H\right) = q''\left(2\pi R H\right)$$

$$\left. q''\right|_{r=R} = q''' \frac{\pi R^2 H}{2\pi R H} = q''' \frac{R}{2}$$

The coolant equation becomes

$$\frac{\partial T_c}{\partial z} = q''' \frac{R}{2c_p^c \dot{m}_c} 2\pi R = \frac{q''' \pi R^2}{c_p^c \dot{m}_c}$$

Integrating from 0 to z

$$\int_0^z \left(\frac{\partial T_c}{\partial z'} = \frac{q''' \pi R^2}{c_p^c \dot{m}_c}\right) dz'$$

$$T_c(z) - T_c(0) = \frac{q''' \pi R^2}{c_p^c \dot{m}_c} z$$

$$T_c(z) = \frac{q''' \pi R^2}{c_p^c \dot{m}_c} z + T_c(0)$$

which is defined for a given incoming coolant temperature.

To solve for $T_f(r)$, the fuel equation is first integrated from 0 to r:

$$\int_0^r \left(-\frac{k_f}{r'}\frac{\partial}{\partial r'}\left(r'\frac{\partial T_f}{\partial r'}\right) = q'''\right) r' dr'$$

$$-k_f\, r' \frac{\partial T_f}{\partial r'}\bigg|_0^r = \frac{q'''}{2} r^2$$

Applying the boundary condition $\left.\frac{\partial T_f}{\partial r}\right|_{r=0} = 0$ results in

$$\frac{\partial T_f}{\partial r} = -\frac{q'''}{2k_f} r$$

Integrating from r to R

$$\int_r^R \left(\frac{\partial T_f}{\partial r'} = -\frac{q'''}{2k_f} r' \right) dr'$$

$$\left[T_f\left(r', z\right) = -\frac{q'''}{4k_f} r'^2 \right]_r^R$$

$$T_f(r,z) = T_f(R,z) + \frac{q'''}{4k_f}\left(R^2 - r^2\right)$$

Examining the boundary condition for $T_f(R)$:

$$q''\big|_{r=R} = q''' \frac{R}{2} = h_c \left(T_f(R,z) - T_c(z)\right)$$

$$T_f(R,z) = q''' \frac{R}{2h_c} + T_c(z)$$

and substituting this expression for $T_f(R,z)$ into the previous solution for $T_f(r,z)$ results in the following expression:

$$T_f(r,z) = q''' \frac{R}{2h_c} + T_c(z) + \frac{q'''}{4k_f}\left(R^2 - r^2\right)$$

This analytic forward solution is used for verification with the discrete forward problem as well as with the analytical adjoint.

2.2 Adjoint Problem

Adjoint techniques are employed in order to evaluate the difference between a high fidelity and low fidelity fuel temperature at specific locations of interest. In order to derive the functional, the following Quantity of Interest associated with the difference between the high and low fidelity solution is examined. This response is written as

$$\Re \equiv \left\langle \bar{f}_R, \bar{T} - \widetilde{T} \right\rangle_{t,z,r}$$

where subscripts t, z, and r define the dimensions of the inner product, $\bar{f}_R$ defines the response

function for the Quantity of Interest, $\bar{T}$ denotes the high-fidelity solution vector, and $\widetilde{T}$ denotes the low fidelity solution vector. The vector dependence captures the coolant and fuel temperatures, $\bar{T} = (T_f \; T_c)^T$. Set $\bar{Q^\dagger} \equiv \bar{f_R}$ and $\bar{\bar{A}}^\dagger \left[\bar{T}^\dagger\right] = \bar{Q}^\dagger$, where the matrix operators still denote continuous versus discretized operators, produces

$$\Re \equiv \left\langle \bar{f_R}, \bar{T} - \widetilde{T} \right\rangle_{t,z,r} = \left\langle \bar{\bar{A}}^\dagger [\bar{T}^\dagger], \bar{T} - \widetilde{T} \right\rangle_{t,z,r}$$
$$= \left\langle \bar{T}^\dagger, \bar{\bar{A}}[\bar{T} - \widetilde{T}] \right\rangle_{t,z,r} + BC + IC + FC = \left\langle \bar{T}^\dagger, \bar{\bar{A}}[\bar{T}] - \bar{\bar{A}}[\widetilde{T}] \right\rangle_{t,z,r} + BC + IC + FC$$

where BC, IC, and FC represent the boundary conditions, initial condition, and final condition that are the byproducts of the formulation of $\bar{\bar{A}}$ from $\bar{\bar{A}}^\dagger$. Note that the expression $\bar{\bar{A}}[\bar{T}] = \bar{Q}$ is exact. Therefore we have

$$\Re = \left\langle \bar{T}^\dagger, \bar{Q} - \bar{\bar{A}}[\widetilde{T}] \right\rangle + BC + IC + FC$$

After defining the residual, $\bar{r} = \bar{Q} - \bar{\bar{A}}[\widetilde{T}]$, the response is written as

$$\Re = \left\langle \bar{T}^\dagger, \bar{r} \right\rangle_{t,z,r} + BC + IC + FC$$

Properly defining the adjoint problem will ensure that

$$BC + IC + FC = 0$$

so that the only remaining term is the inner product. Therefore, given a residual from the low fidelity solution $\widetilde{T}$ operated on by the high fidelity operator, an inner product with the appropriate adjoint will yield the difference between the high and low fidelity temperatures at the appropriate location of interest.

This project investigated the possibility to estimate the response by using a low fidelity adjoint solution in place of the high fidelity adjoint. This approach would evaluate the response using

$$\widetilde{\Re} = \left\langle \widetilde{T}^\dagger, \bar{r} \right\rangle_{t,z,r}$$

where $\widetilde{T}^\dagger$ is the elongated low fidelity adjoint solution found by evaluating

$$\widetilde{\bar{\bar{A}}}^\dagger \left[\widehat{T}^\dagger\right] = \widetilde{Q}^\dagger$$

and

$$\widetilde{T}^{\dagger} = \widetilde{\bar{E}}_T^{\dagger} \hat{T}^{\dagger}$$

We define $\widetilde{\bar{E}}_t^{\dagger}$ is an elongation operator that projects the coarsened low fidelity adjoint solution onto the high fidelity mesh. This implies that if

$$\bar{\bar{A}}^{\dagger} \widetilde{\bar{E}}_T^{\dagger} \widetilde{\bar{A}}^{\dagger -1} = \widetilde{Q}^{\dagger} = \bar{Q}^{\dagger}$$

then exact values of the response are obtained. By inspection, it can be seen that if

$$\widetilde{\bar{E}}_T^{\dagger} \widetilde{\bar{A}}^{\dagger -1} = \bar{\bar{A}}^{\dagger -1}$$

holds, one would think that there may also be definitions for $\widetilde{Q}^{\dagger}$ that could enforce this equality. However, since $\widetilde{\bar{E}}_T^{\dagger}$ is a non-square matrix leading to an ill posed problem, the best one can do is a least squares approximation.

If the response found using the low fidelity adjoint solution results in temperature differences that are within an appropriate tolerance, then the low fidelity solution could be used to effectively estimate the difference between the high and low fidelity solutions without ever needing to explicitly solve the high fidelity problem. This method is the primary means for which a low fidelity problem can determine at which times and locations it is necessary to use a higher level of fidelity without unduly compromising its greater level of computational efficiency as compared to the high fidelity problem.

In order to accomplish this, an appropriate method for determining a low fidelity adjoint operator and elongation operator that will map the low fidelity problem onto the high fidelity spatial and temporal mesh must be developed. What follows in this section is a detailed account of various adjoint problem definitions and their resulting system of expressions used to determine either the high or the low fidelity adjoint solutions. Understanding their similarities and differences is integral to evaluating the behavior of adjoint methods used for adaptive model refinement.

2.2.1 Mathematical Adjoint

The mathematical adjoint is derived from the forward time dependent discretized problem much in the same way as described in section 1.3.2. Starting with the block matrix system from the discretized forward problem represented by equation (2.3)

$$\begin{bmatrix} \bar{\bar{\mathbf{C}}}_1 & & & \\ \bar{\bar{\mathbf{B}}}_2 & \bar{\bar{\mathbf{C}}}_2 & & \\ & \bar{\bar{\mathbf{B}}}_3 & \bar{\bar{\mathbf{C}}}_3 & \\ & & \ddots & \ddots \end{bmatrix} \begin{bmatrix} \bar{\phi}_1 \\ \bar{\phi}_2 \\ \bar{\phi}_3 \\ \vdots \end{bmatrix} = \begin{bmatrix} \bar{\mathbf{Q}}_1 \\ \bar{\mathbf{Q}}_2 \\ \bar{\mathbf{Q}}_3 \\ \vdots \end{bmatrix}$$

we derive the adjoint problem by taking the transpose of the above system.

$$\begin{bmatrix} \bar{\bar{\mathbf{C}}}_1^* & \bar{\bar{\mathbf{B}}}_2^* & & \\ & \bar{\bar{\mathbf{C}}}_2^* & \bar{\bar{\mathbf{B}}}_3^* & \\ & & \bar{\bar{\mathbf{C}}}_3^* & \ddots \\ & & & \ddots \end{bmatrix} \begin{bmatrix} \bar{\phi}_1^* \\ \bar{\phi}_2^* \\ \bar{\phi}_3^* \\ \vdots \end{bmatrix} = \begin{bmatrix} \bar{\mathbf{Q}}_1^* \\ \bar{\mathbf{Q}}_2^* \\ \bar{\mathbf{Q}}_3^* \\ \vdots \end{bmatrix}$$

with the adjoint matrix operators

$$\bar{\bar{\mathbf{C}}}^* = \bar{\bar{\mathbf{C}}}^{\mathbf{T}}, \qquad \bar{\bar{\mathbf{B}}}^* = \bar{\bar{\mathbf{B}}}^{\mathbf{T}}$$

and

$$\begin{aligned} \bar{\bar{\mathbf{C}}}_{n+1}^* &\equiv \left[\bar{\gamma}\bar{\bar{\mathbf{I}}} - \Delta t_n \bar{\bar{\mathbf{A}}}_{n+1}^*\right] \\ \bar{\bar{\mathbf{B}}}_{n+1}^* &\equiv \left[\bar{\gamma}\bar{\bar{\mathbf{I}}} - \Delta t_n \bar{\bar{\mathbf{A}}}_{n}^*\right] \\ \bar{\mathbf{Q}}_{n+1}^* &\equiv \alpha \Delta t_n \bar{\mathbf{d}}_{n+1}^* + (1-\alpha)\Delta t_n \bar{\mathbf{d}}_n^* \end{aligned}$$

This results in the general time dependent mathematical adjoint expression

$$\bar{\bar{\mathbf{C}}}_n^* \bar{\phi}_{n+1}^* + \bar{\bar{\mathbf{B}}}_{n+1}^* \bar{\phi}_n^* = \bar{\mathbf{Q}}_n^* \tag{2.10}$$

The matrix operator $\bar{\bar{\mathbf{A}}}_{n+1}^*$ is derived by taking the transpose of $\bar{\bar{\mathbf{A}}}_{n+1}$. Using the definition of this matrix shown previously, this transposed adjoint matrix becomes

$$\bar{\bar{\mathbf{A}}}^T = \begin{bmatrix} \bar{\bar{\mathbf{D}}}_f^T & \bar{\bar{\mathbf{O}}}_c^T \\ \bar{\bar{\mathbf{O}}}_f^T & \bar{\bar{\mathbf{D}}}_c^T \end{bmatrix}$$

with

$$\bar{\bar{\mathbf{D}}}_f^T = \begin{bmatrix} -a_2 & a_2 & & & & & \\ a_2 & b_3 & a_3 & & & & \\ & a_3 & b_4 & a_4 & & & \\ & & & \ddots & & & \\ & & & a_{N_r-2} & b_{N_r-1} & a_{Nr-1} & \\ & & & & a_{N_r-1} & e & \\ & & & & & \ddots & \end{bmatrix}, \quad \bar{\bar{\mathbf{O}}}_c^T = \begin{bmatrix} \vdots & & & & \\ f & & & & \\ & \ddots & & & \\ & & f & & \\ & & & \ddots & \\ & & & & f \end{bmatrix},$$

$$\bar{\bar{\mathbf{D}}}_c^T = \begin{bmatrix} m & k & & & \\ & m & k & & \\ & & & \ddots & \\ & & & & m \end{bmatrix}, \quad \bar{\bar{\mathbf{O}}}_f^T = \begin{bmatrix} \cdots & f & & \\ & & \ddots & \\ & & & f \end{bmatrix}$$

The definitions for the constants shown in the previous matrix are the same as those used for the forward matrix operator $\bar{\bar{\mathbf{A}}}_{n+1}$. Operating on the adjoint solution vector $\bar{\boldsymbol{\phi}}_n^* = \begin{bmatrix} \bar{T}_f^* & \bar{T}_c^* \end{bmatrix}^T$ results in a system of linear equations that can be solved with the given final condition $\bar{T}_f^* = \bar{T}_c^* = 0$.

Examination of Discrete Adjoint Equations as $\Delta r, \Delta z \to 0$

Multiplying the previously defined adjoint operator $\bar{\bar{A}}^*$ by it's solution vector $\bar{T}^* = \begin{bmatrix} T_f^* & T_c^* \end{bmatrix}^T$ results in the following set of equations.

$$a_{i-1}T^*_{f_{i-1,j}} + b_i T^*_{f_i,j} + a_i T^*_{f_{i+1,j}} = Q^*_{i,j} \qquad (1a)$$
$$a_{N_r-1}T^*_{f_{N_r-1,j}} + e{T^*_{f^*_{N_r,j}}}^* + fT^*_{c_j} = Q^*_{N_r,j} \qquad (2a)$$
$$fT^*_{f^*_{N_r,j}} + mT^*_{c_j} + hT^*_{c_{j+1}} = Q^*_{c_j} \qquad (3a)$$
$$fT^*_{f^*_{N_r^*,N_z}} + mT^*_{c_{N_z}} = Q^*_{c_{N_z}} \qquad (4a)$$

Examining equation $1a$, we have the following dicretized relationship

$$a_{i-1}T^*_{f_{i-1,j}} + b_i T^*_{f_i,j} + a_i T^*_{f_{i+1,j}}$$

$$= 2\pi k_f \frac{r_i}{\Delta r} T^*_{f_{i+1,j}} - 2\pi k_f \left(\frac{r_i}{\Delta r} + \frac{r_{i-1}}{\Delta r} \right) T^*_{f_i,j} + 2\pi k_f \frac{r_{i-1}}{\Delta r} T^*_{f_{i-1,j}}$$

$$= 2\pi k_f \left[r_i \frac{T^*_{f_{i+1,j}} - T^*_{f_i,j}}{\Delta r} - r_{i-1} \frac{T^*_{f_i,j} - T^*_{f_{i-1,j}}}{\Delta r} \right]$$

In order to examine this equation as it approaches the continuous or analytic adjoint equation, we operate on the previous expression with $\lim_{\Delta r \to 0}$

$$\lim_{\Delta r \to 0} \left(2\pi k_f \left[r_i \frac{T^*_{f_{i+1,j}} - T^*_{f_{i,j}}}{\Delta r} - r_{i-1} \frac{T^*_{f_{i,j}} - T^*_{f_{i-1,j}}}{\Delta r} \right] \right)$$

$$= 2\pi k_f \left[r \frac{\partial T^*_f}{\partial r} \right]_{r_i}^{r_{i+1}}$$

We then recognize that this expression is equal to

$$k_f \int_{r_i}^{r_{i+1}} dr 2\pi r \left[\frac{1}{r} \frac{\partial}{\partial r} \left(r \frac{\partial T^*_f}{\partial r} \right) \right] = k_f \int_{r_i}^{r_{i+1}} 2\pi r \nabla_r^2 T^*_f$$

Demanding point-wise equality of the energy balance equation implies the term

$$k_f \nabla_r^2 T^*_f$$

which matches the fuel temperature expression in the analytic adjoint.

Performing the same analysis on equation $2a$

$$a_{Nr-1} T^*_{f_{N_r-1,j}} + e T^*_{f^*_{N_r,j}} + f T^*_{c_j}$$

$$= 2\pi k_f \frac{r_{N_r-1}}{\Delta r} T^*_{f_{N_r-1,j}} - \left(2\pi k_f \frac{r_{N_r-1}}{\Delta r} + S_f h_c \right) T^*_{f^*_{N_r}} + 2\pi h_c T^*_{c_j}$$

$$= -2\pi k_f r_{N_r-1} \frac{T^*_{f^*_{N_r,j}} - T^*_{f_{N_r-1,j}}}{\Delta r} + 2\pi r_{N_r} h_c \left(T^*_{c_j} - T^*_{f^*_{N_r,j}} \right)$$

We then impose the following boundary condition

$$-k_f \left. \frac{\partial T^*_f}{\partial r} \right|_{r=R} = h_c \left(T^*_{f^*_{N_r,j}} - T^*_{c_j} \right)$$

resulting in

$$-2\pi k_f r_{N_r-1} \frac{T^*_{f^*_{N_r,j}} - T^*_{f_{N_r-1,j}}}{\Delta r} + 2\pi k_f \left. \frac{\partial T^*_f}{\partial r} \right|_{r=R}$$

We again operate on the previous expression with $\lim_{\Delta r \to 0}$

$$\lim_{\Delta r \to 0} 2\pi r_{N_r} k_f \left[\left. \frac{\partial T_f^*}{\partial r} \right|_{r=R} - r_{N_r - 1} \frac{T^*_{f_{N_r,j}} - T^*_{f_{N_r-1,j}}}{\Delta r} \right]$$

$$= 2\pi k_f \left[r \frac{\partial T_f^*}{\partial r} \right]_{r_{N_r-1}}^{r_{N_r}}$$

which results in

$$-2\pi k_f r_{N_r-1} \frac{T^*_{f_{N_r^*,j}} - T^*_{f_{N_r^*-1,j}}}{\Delta r} + 2_f \left. \frac{\partial T_f^*}{\partial r} \right|_{r=R}$$

Operate on the previous expression with $\lim_{\Delta r \to 0}$

$$\lim_{\Delta r \to 0} \left(-2\pi k_f r_{N_r-1} \frac{T^*_{f_{N_r^*,j}} - T^*_{f_{N_r^*-1,j}}}{\Delta r} + 2_f \left. \frac{\partial T_f^*}{\partial r} \right|_{r=R} \right)$$

$$= 2\pi k_f \left[r \frac{\partial T_f^*}{\partial r} \right]_{r_{N_r-1}}^{r_{N_r}}$$

Recognize that this expression is equal to

$$\int_{r_{N_r-1}}^{r_{N_r}} dr 2\pi r \left[\frac{1}{r} \frac{\partial}{\partial r} \left(r \frac{\partial T_f^*}{\partial r} \right) \right] = k_f \int_{r_{N_r-1}}^{r_{N_r}} dr 2\pi r \nabla_r^2 T_f^*$$

Again, demanding point wise equality of the energy balance term implies the term

$$= k_f \nabla_r^2 T_f^*$$

Examining equation $3a$ and noting that $S_f = 2\pi R$

$$f T^*_{f_{N_r^*,j}} + m T^*_{c_j} + h T^*_{c_{j+1}}$$

$$= S_f h_c T^*_{f_{N_r^*,j}} - \left(h_c S_f - \frac{c_{p_c} \dot{m}_c}{\Delta z} \right) T^*_{c_j} - \frac{c_{p_c} \dot{m}_c}{\Delta z} T^*_{c_{j+1}}$$

$$= -c_{p_c} \dot{m}_c \frac{T^*_{c_{j+1}} - T^*_{c_j}}{\Delta z} + h_c S_f \left(T^*_{f_{N_r^*,j+1}} - T^*_{c_j} \right)$$

We then impose the following source term

$$q''|_{r=R} = h_c \left(T^*_{f_{N_r^*,j}} - T^*_{c_j} \right)$$

Operate on the previous expression with $\lim_{\Delta z \to 0}$

$$\lim_{\Delta z \to 0} \left[-c_{p_c} \dot{m}_c \left(\frac{T^*_{c_{j+1}} - T^*_{c_j}}{\Delta z} \right) + S q'' \right]$$

$$= -c_{p_c} \dot{m}_c \frac{\partial T^*_c}{\partial z} + S \; q''|_{r=R}$$

Performing the limit analysis on equation $4a$

$$f T^*_{f_{N^*_r, N_z}} + m T^*_{c_{N_z}}$$

$$= S_f h_c T^*_{f_{N^*_r, N_z}} - \left(h_c S_f - \frac{c_{p_c} \dot{m}_c}{\Delta z} \right) T^*_{c_{N_z}}$$

$$= c_{pc} \dot{m}_c \left(\frac{T^*_{c_{N_z}}}{\Delta z} \right) + 2\pi R h_c \left(T^*_{f_{N_r, N_z}} - T^*_{c_{N_z}} \right)$$

It is inferred by the structure of the adjoint operator $\bar{\bar{A}}^\dagger$ shown previously that the following boundary conditions also apply:

$$\nabla \; T^\dagger_f \Big|_{r=0} = 0$$

$$T^\dagger_c \Big|_{z=H} = 0$$

From this analysis, we have the following adjoint equations

$$k_f \nabla^2 T^\dagger_f = Q^\dagger_f$$

$$c_{p_c} \dot{m}_c \frac{\partial T^\dagger_c}{\partial z} - \; q'' \big|_{r=R} = Q^\dagger_c$$

with the following boundary conditions

$$\nabla \; T^\dagger_f \Big|_{r=0} = 0 \qquad T^\dagger_c \Big|_{z=H} = 0$$

$$q''\big|^{\dagger}_{r=R} = h_c\left(T_f^{\dagger}\Big|_{r=R} - T_c^{\dagger}\right) = -k_f\left.\frac{\partial T_f^{\dagger}}{\partial r}\right|_{r=R}$$

2.2.2 Analytic Adjoint

An alternative way to derive the adjoint equations is to consider an adjoint problem as derived from the continuous forward equations. This process is briefly described in section 1.3.2 and is now presented in detail for the time dependent forward equations. For this derivation, it was necessary to derive a functional based on the forward operators. Rewrite the forward analytic equations (1.5) - (1.9) as operators on temperature values

$$O_c(\ ) \equiv c_p^c \rho_c A_x \frac{\partial(\ )}{\partial t} + c_p^c \dot{m}_c \frac{\partial(\ )}{\partial z}$$
$$O_f(\ ) \equiv c_p^f \rho_f \frac{\partial(\ )}{\partial t} - k_f \nabla_r^2(\ )$$

$$O_c\left[T_c\right] = -S_f k_f \nabla_r\ T_f|_{r=R}$$
$$O_f\left[T_f\right] = q'''$$

$$h\left(T_f|_{r=R} - T_c\right) = -k_f \nabla_r\ T_f|_{r=R}$$
$$T_c|_{t=0} = T_c^{(o)} \qquad T_c|_{z=0} = T_c^{In}$$
$$T_f|_{t=0} = T_f^{(o)} \qquad \nabla_r\ T_f|_{r=o} = 0$$

The Quantity of Interest associated with the difference between the high fidelity solution and the low fidelity solution is examined. This response is written as

$$\Re \equiv \left\langle \bar{f}_R, \bar{T} - \widetilde{T} \right\rangle_{t,z,r} = \left\langle \bar{T}^{\dagger}, \bar{Q} - \bar{\bar{A}}[\widetilde{T}] \right\rangle + BC + IC + FC$$

After defining the residual, $\bar{r} = \bar{Q} - \bar{\bar{A}}[\widetilde{T}]$, the following expression is produced:

$$\Re = \left\langle \bar{T}^{\dagger}, \bar{r} \right\rangle_{t,z,r} + BC + IC + FC$$

Writing out the forward equations reveals the action of the $\bar{\bar{A}}$ operator for which we seek the adjoint and associated BC, IC, and FC terms. We also scale the coolant equation by $\left[\frac{R^2}{2}\frac{S_f}{R}\right]^{-1} = \left[\frac{1}{\pi R^2}\right]$ anticipating the necessity to relate the fuel and coolant terms with one another. The fuel and coolant equations are then.

$$\left[\tfrac{1}{\pi R^2}\right]\left(c_p^c\rho_c A_x\tfrac{\partial}{\partial t}+c_p^c\dot{m}_c\tfrac{\partial}{\partial z}\right)T_c+\left[\tfrac{1}{\pi R^2}\right]\left(k_f S_f\nabla_r T_f|_R\right)=0$$

$$\left(c_p^f\rho_f\tfrac{\partial}{\partial t}-k_f\nabla_r^2\right)T_f=q'''$$

By demanding that

$$\left\langle\bar{T}^\dagger,\bar{\bar{A}}\bar{T}\right\rangle=\left\langle\bar{\bar{A}}^\dagger\bar{T}^\dagger,\bar{T}\right\rangle$$

for any $\bar{T}$ and $\bar{T}^\dagger$ that satisfies specified BC, IC, and FC, the equations are defined along with the BC, IC, and FC terms. Demanding this holds for any $\bar{T}$ and $\bar{T}^\dagger$ implies point-wise enforcement. The forward equations and their respective boundary and initial conditions are known. To obtain the similar equations for the adjoint problem, the operator must be isolated to operate on the adjoint temperatures in the inner products. The required equations are found by writing the inner products and using integration by parts.

$$\left\langle T_c^\dagger,\left[\tfrac{1}{\pi R^2}\right]c_p^c\rho_c A_x\tfrac{\partial T_c}{\partial t}\right\rangle_{t,z,r}=\left[\tfrac{1}{\pi R^2}\right]c_p^c\rho_c A_x\int_0^R rdr\int_0^H dz\int_0^{t_F}dt\tfrac{\partial T_c}{\partial t}T_c^\dagger$$

$$=\left[\tfrac{1}{\pi R^2}\right]c_p^c\rho_c A_x\int_0^R rdr\int_0^H dz\left[T_c^\dagger T_c\Big|_0^{t_f}-\int_0^{t_F}dt\tfrac{\partial T_c^\dagger}{\partial t}T_c\right]$$

$$=\left[\tfrac{1}{\pi R^2}\right]c_p^c\rho_c A_x\left\langle T_c^\dagger,T_c\right\rangle_{z,r}\Big|_0^{t_F}-\left[\tfrac{1}{\pi R^2}\right]c_p^c\rho_c A_x\left\langle\tfrac{\partial T_c^\dagger}{\partial t},T_c\right\rangle_{t,z,r}$$

The $\left\langle c_p^f\rho_f T_f^\dagger,\frac{\partial T_f}{\partial t}\right\rangle$ and $\left\langle T_c^\dagger,\left[\frac{1}{\pi R^2}\right]c_p^c\dot{m}_c\frac{\partial T_c}{\partial z}\right\rangle$ inner products are developed similarly such that

$$\left\langle T_f^\dagger,c_p^f\rho_f\tfrac{\partial T_f}{\partial t}\right\rangle_{t,z,r}=c_p^f\rho_f\left\langle T_f^\dagger,T_f\right\rangle_{z,r}\Big|_0^{t_F}-c_p^f\rho_f\left\langle\tfrac{\partial T_f^\dagger}{\partial t},T_f\right\rangle_{t,z,r}$$

$$\left\langle T_c^\dagger,\left[\tfrac{1}{\pi R^2}\right]c_p^c\dot{m}_c\tfrac{\partial T_c}{\partial z}\right\rangle_{t,z,r}=\left[\tfrac{1}{\pi R^2}\right]c_p^c\dot{m}_c\left\langle T_c^\dagger,T_c\right\rangle_{t,r}\Big|_0^H-\left[\tfrac{1}{\pi R^2}\right]c_p^c\dot{m}_c\left\langle\tfrac{\partial T_c^\dagger}{\partial z},T_c\right\rangle_{t,z,r}$$

Green's Theorem is applied to $\left\langle T_f^\dagger,-k_f\nabla_r^2T_f\right\rangle$ to obtain

$$\left\langle T_f^\dagger,-k_f\nabla_r^2T_f\right\rangle_{t,z,r}=-k_f\left\langle T_f^\dagger,r\nabla_r T_f-T_f,r\nabla_r T_f^\dagger\right\rangle_{t,z}\Big|_0^R-k_f\left\langle\nabla_r^2T_f^\dagger,T_f\right\rangle_{t,z,r}$$

The resulting BC, IC, and FC terms found in the functional are

$$\left\langle T_c^\dagger, \left[\tfrac{1}{\pi R^2}\right] c_p^c \rho_c T_c \right\rangle_{z,r}\Big|_0^{t_F}, \quad \left\langle T_f^\dagger, c_p^f \rho_f T_f \right\rangle_{z,r}\Big|_0^{t_F}, \quad \left\langle T_c^\dagger, \left[\tfrac{1}{\pi R^2}\right] c_p^c \dot{m}_c T_c \right\rangle_{t,r}\Big|_0^{H},$$
$$-k_f \left\langle T_f^\dagger, r\nabla_r T_f - T_f, r\nabla_r T_f^\dagger \right\rangle_{t,z}\Big|_0^{R}$$

Included in this list of remaining terms is the inner product with $T_c^\dagger$ with the following heat flux term from the coolant equation

$$\left\langle T_c^\dagger, \left[\tfrac{1}{\pi R^2}\right] k_f S_f \nabla_r T_f\big|_R \right\rangle_{t,z,r}$$

Noting that T_c and T_f actually denote $\Delta T_c \equiv T_c - T_c^{(o)}$ and $\Delta T_f \equiv T_f - T_f^{(o)}$, the "natural" boundary and initial conditions for the forward problem are imposed. These conditions are written as

$$T_c|_{z=0} = T_c|_{t=0} = T_f|_{t=0} = 0$$

Additionally, the adjoint final and boundary conditions are free to select and imposed to be the following to remove the BC and FC terms

$$T_c^\dagger\Big|_{z=H} = T_c^\dagger\Big|_{t=t_F} = T_f^\dagger\Big|_{t=t_F} = 0$$

The remaining terms that appear in the functional are as follows:

$$-k_f \left\langle T_f^\dagger, r\nabla_r T_f - T_f, r\nabla_r T_f^\dagger \right\rangle_{t,z}\Big|_0^{R} + \left\langle T_c^\dagger, \left[\tfrac{1}{\pi R^2}\right] k_f S_f \nabla_r T_f\big|_R \right\rangle_{t,z,r}$$

The expression $\left\langle T_f^\dagger, r\nabla_r T_f - T_f, r\nabla_r T_f^\dagger \right\rangle_{t,z}\Big|_{r=0} = 0$ is true due both to symmetry within the geometry of the problem as well as due to the r variable present. The remaining terms

$$-k_f R \left\langle T_f^\dagger, \nabla_r T_f - T_f, \nabla_r T_f^\dagger \right\rangle_{t,z}\Big|_{r=R} + \left\langle T_c^\dagger, \left[\tfrac{1}{\pi R^2}\right] k_f S_f \nabla_r T_f\big|_R \right\rangle_{t,z,r}$$

can be eliminated by first completing the r integration of the second term. This is possible since there is no r dependence of the function's inner product. This produces

$$\left(\tfrac{R^2}{2}\right) \left[\tfrac{1}{\pi R^2}\right] S_f k_f \left\langle T_c^\dagger, \nabla_r T_f \right\rangle_{t,z}\Big|_{r=R} = k_f R \left\langle T_c^\dagger, \nabla_r T_f \right\rangle_{t,z}\Big|_{r=R}$$

This will produce the remaining BC terms in the functional

$$-k_f R \left\langle T_f^\dagger, \nabla_r T_f - T_f, \nabla_r T_f^\dagger \right\rangle_{t,z}\Big|_{r=R} + k_f R \left\langle T_c^\dagger, \nabla_r T_f \right\rangle_{t,z}\Big|_R = 0$$

Next we impose

$$-k_f \nabla_r T_f|_{r=R} = h_c \left(T_f|_{r=R} - T_c \right)$$

which produces the following BC terms in the functional

$$h_c R \left\langle T_f^\dagger, (T_f - T_c) \right\rangle\Big|_{r=R} + k_f R \left\langle T_f, \nabla_r T_f^\dagger \right\rangle_{t,z}\Big|_{r=R} - h_c R \left\langle T_c^\dagger, (T_f - T_c) \right\rangle_{t,z}\Big|_{r=R}$$

$$= R \left\langle T_f, \left[k_f \nabla_r T_f^\dagger + h_c \left(T_f^\dagger - T_c^\dagger \right) \right] \right\rangle_{t,z}\Big|_{r=R} - h_c R \left\langle T_c, \left(T_f^\dagger - T_c^\dagger \right) \right\rangle_{t,z}\Big|_{r=R}$$

To make stationary with respect to T_f, impose

$$-k_f \nabla_r T_f^\dagger\Big|_{r=R} = h_c \left(T_f^\dagger\Big|_{r=R} - T_c^\dagger \right)$$

which eliminates the first term in the remaining functional. For the final term, we use the previously defined BC and return the r dependence to the inner product.

$$-h_c R \left\langle T_c, \left(T_f^\dagger - T_c^\dagger \right) \right\rangle_{t,z}\Big|_{r=R} = \left\langle T_c, \tfrac{2}{R} k_f \, \nabla_r T_f^\dagger\Big|_{r=R} \right\rangle_{t,z,r}$$

Let us define the adjoint heat flux at the pin surface as:

$$q''^\dagger\Big|_{r=R} = -k_f \nabla_r T_f^\dagger\Big|_{r=R} = h_c \left(T_f^\dagger\Big|_{r=R} - T_c^\dagger \right)$$

Gathering up all terms with T_c on one side of the inner product produces the following:

$$\tfrac{-1}{\pi R^2} \left[c_p^c \rho_c A_c \tfrac{\partial(\,)}{\partial t} + c_p^c \dot{m}_c \tfrac{\partial(\,)}{\partial z} \right] T_c^\dagger - \tfrac{2}{R} \, q''^\dagger\Big|_{r=R} = Q_c^\dagger$$

which can be scaled similarly to the forward coolant equation by multiplying through by πR^2.

Doing likewise for T_f produces

$$-\left[c_p^f \rho_f \tfrac{\partial(\,)}{\partial t} + k_f \nabla_r^2(\,) \right] T_f^\dagger = Q_f^\dagger$$

Summarizing the following analytic adjoint operators and previously defined boundary conditions are given by

$$O_c^\dagger(\ ) = -c_p^c \rho_c A_c \frac{\partial(\ )}{\partial t} - c_p^c \dot{m}_c \frac{\partial(\ )}{\partial z}$$
$$O_f^\dagger(\ ) = -\rho_f \frac{\partial(\ )}{\partial t} - k_f \nabla_r^2(\ )$$

$$O_c^\dagger \left[T_c^\dagger\right] = -S_f k_f \nabla_r\, T_f^\dagger\Big|_{r=R} + Q_c^\dagger$$
$$O_f^\dagger \left[T_f^\dagger\right] = Q_f^\dagger$$

F.C. $$T_c^\dagger\Big|_{t=t_F} = \quad T_f^\dagger\Big|_{t=t_F} = 0$$

B.C. $$T_c^\dagger\Big|_{z=H} = 0, \quad \nabla_r\, T_f^\dagger\Big|_{r=0} = 0$$
$$-k_f \nabla_r T_f^\dagger\Big|_{r=R} = h_c \left(T_f^\dagger\Big|_{r=R} - T_c^\dagger\right) = q''^\dagger\Big|_{r=R}$$

These equations are equivalent to the previously presented adjoint equations (1.10) - (1.14). In order to solve these equations, a similar discretization technique to that of the forward high fidelity solution is employed.

2.2.3 Analytic Adjoint Solution

An analytic solution to the adjoint equations was derived in order to help verify mathematical and physical adjoint behavior. Similar to the analytical solution derived for the forward problem, the system is assumed to be at steady state. These steady state adjoint equations as determined by the analytic adjoint problem derivation can be written as

$$-\frac{k_f}{r}\frac{\partial}{\partial r}\left(r\frac{\partial T_f^*}{\partial r}\right) = Q^* \tag{2.11}$$

$$-c_p^c \dot{m}_c \frac{dT_c^*}{dz} - 2\pi R q''^* = 0 \tag{2.12}$$

$$T_c^*|_{z=H} = 0, \quad \frac{\partial T_f^*}{\partial r}\Big|_{r=0} = 0$$

$$-k_f \frac{\partial T_f^*}{\partial r}\Big|_{r=R} = h_c \left(T_f^*|_{r=R} - T_c^*\right) = q''^*|_{r=R}$$

The adjoint source term is defined at the location of interest as

$$Q^* = \frac{1}{2\pi r}\delta\left(r - r_o\right)\delta\left(z - z_o\right)$$

We first examine the problem space for $z_o < z \leq H$. Integrating equation (2.11) from $r' = (0, r)$ with $0 \leq r < R$ and applying the boundary condition at $r = 0$ results in the

following expression for T_f^*:

$$\int_0^r dr' 2\pi r' \left[\frac{-k_f}{r'} \frac{\partial}{\partial r} \left(r' \frac{\partial T_f^*}{\partial r'} \right) = 0 \right]$$

$$r' \frac{\partial T_f^*}{\partial r'} \Big|_0^r = r \frac{\partial T_f^*}{\partial r} = 0$$

$$T_f^*(r,z) = \text{constant in r}$$

Therefore, $q''^*|_{r=R} = -k_f \dfrac{\partial T_f^*}{\partial r}_{r=R} = 0$ for $z_o < z \leq H$. Integrating equation (2.12) from $z' = (z, H)$ with $z_o < z \leq H$ and applying the boundary condition at $z = H$ results in the following expression for T_c^*:

$$\int_z^H dz' \left[-c_p^c \dot{m}_c \frac{dT_c^*}{dz'} \right] = 0$$

$$T_c^*|_z^H = \text{constant}$$

$$T_c^* = 0$$

In order to satisfy the boundary condition at $r = R$, it follows that $T_f^* \Big|_{r=R} = T_c^*$ and thus $T_f^* = 0$ for $z_o < z \leq H$ and all r.

Consider the analytical solution at $z = z_o$. By the previous argument, the adjoint fuel temperature solution for $0 \leq r < r_o$ and $z = z_o$ is

$$T_f^*(r,z)\big|_{z=z_o} = c_o \, f_o(z)|_{z=z_o}$$

where $f_o(z)$ is some function of z. Considering the limit of the solution a distance of $\epsilon << 1$ around r_o, a boundary condition at the $r = r_o$ and $z = z_o$ position is

$$\lim_{\epsilon \to 0} \left[\int_{r_o-\epsilon}^{r_o+\epsilon} -2\pi r dr \frac{k_f}{r} \frac{\partial}{\partial r} \left(r \frac{\partial T_f^*}{\partial r} \right) = \int_{r_o-\epsilon}^{r_o+\epsilon} 2\pi r dr \frac{\delta(r - r_o)\,\delta(z - z_o)}{2\pi r} \right]_{z=z_o}$$

$$\lim_{\epsilon \to 0} \left[-k_f (2\pi r) \left. \frac{\partial T_f^*}{\partial r} \right|_{r_o-\epsilon}^{r_o+\epsilon} = \delta(z - z_o) \right]_{z=z_o}$$

This implies that

$$T_f^*(r,z) = \hat{T}_f^*(r) \delta(z - z_o)$$

Dividing through by $\delta(z - z_o)$ results in the following expression

$$\lim_{\epsilon\to 0}\left[-k_f\left(2\pi r\right)\left.\frac{\partial\hat{T}_f^*}{\partial r}\right|_{r_o-\epsilon}^{r_o+\epsilon}=1\right]_{z=z_o}$$

Noting that $\hat{T}_f^*(r)=c_o$ for $r<r_0$, we can eliminate the derivative at $r_o-\epsilon$ and are left with

$$\lim_{\epsilon\to 0}\left[-k_f\left(2\pi r\right)\left.\frac{\partial\hat{T}_f^*}{\partial r}\right|_{r_o+\epsilon}=1\right]_{z=z_o}$$

which defines a boundary condition.

Integrating the fuel adjoint equation from $r_o+\epsilon$ to r for $r_o<r\leq R$ and using the previously defined boundary condition results in the following:

$$\lim_{\epsilon\to 0}\left[\int_{r_o+\epsilon}^{r}\left(-\frac{k_f}{r'}\frac{\partial}{\partial r'}\left(r'\frac{\partial T_f^*}{\partial r'}\right)\right)2\pi r'dr'\right]_{z=z_o}=0$$

$$\lim_{\epsilon\to 0}\left[-2\pi k_f r'\left.\frac{\partial T_f^*}{\partial r'}\right|_{r_o+\epsilon}^{r}\right]_{z=z_o}=0$$

$$\left.-2\pi k_f r\frac{\partial T_f^*}{\partial r}-1\right|_{z=z_o}=0$$

$$\left.\frac{\partial T_f^*}{\partial r}\right|_{z=z_o}=\frac{1}{r}\left(\frac{-1}{2\pi k_f}\right)$$

which satisfies the BC at $r_o+\epsilon$. The general solution for the above differential equation is

$$\left.T_f^*\right|_{z=z_o}=\left(\tilde{c}_o+\tilde{c}_1\ln r\right)\left.f_1(z)\right|_{z=z_o}$$

with

$$\tilde{c}_1=-\frac{1}{2\pi k_f}$$

The temperature across the interface at r_o is constrained such that

$$\lim_{\epsilon\to 0}\left[T_f^*\left(r_o+\epsilon\,,z\right)=T_f^*\left(r_o-\epsilon,z\right)\right]_{z=z_o}$$

This can be justified due to the fact that integrating the Q^* delta function across r_o at $z=z_o$ produces an expression for the derivative of $\left.T_f^*\right|_{z=z_o}$ that is finite. Since the derivative of $\left.T_f^*\right|_{z=z_o}$ at $r=r_o$ is finite, there can be no jump discontinuity in $\left.T_f^*\right|_{z=z_o}$ at $r=r_o$ and the

previously defined constraint holds. This implies that

$$[f_o(z) = f_1(z) = \delta(z - z_o)]_{z=z_o}$$

Applying the boundary condition for $T_f^*\Big|_{z=z_o}$ at $r = r_o + \epsilon$ results in the following expression for c_o

$$c_o = \frac{-1}{2\pi k_f} \ln r_o + \tilde{c}_o$$

Substituting $T_f^* = \tilde{c}_o + \tilde{c}_1 \ln(r)$ into the pin surface boundary condition at $r = R$ and integrating in the limit about z_o results in the following pin surface relationship

$$-k_f \frac{\tilde{c}_1}{R} = h \left(\tilde{c}_1 \ln R + \tilde{c}_o - \lim_{\epsilon \to 0} \int_{z_o - \epsilon}^{z_o + \epsilon} T_c^*(z) dz \right)$$

The term $\int_{z_o-\epsilon}^{z_o+\epsilon} T_c^*(z)dz = 0$ due to the fact that $T_c^*(z)$ is finite over the interval. Solving for $\tilde{c}_o$

$$\begin{aligned} \tilde{c}_o &= \left(\frac{k_f}{hR} + \ln R \right) \left(\frac{-1}{2\pi k_f} \right) \\ &= \frac{1}{2\pi} \left(\frac{1}{hR} + \frac{1}{k_f} \ln R \right) \end{aligned}$$

Integrating about $z = z_o$ in the limit, the adjoint coolant equation is written as

$$\lim_{\epsilon \to 0} \int_{z_o - \epsilon}^{z_o + \epsilon} \left[-c_p^c \dot{m}_c \frac{dT_c^*(z)}{dz} = 2\pi R q''^* = -2\pi R \frac{1}{2\pi k_f} \frac{k_f}{R} \delta(z - z_o) = \delta(z - z_o) \right]$$

producing

$$\lim_{\epsilon \to 0} T_c^*(z) \Big|_{z-\epsilon}^{z+\epsilon} = -\frac{1}{c_p^c \dot{m}_c}$$

Using the solution for $z > z_o$ renders

$$\lim_{\epsilon \to 0} T_c^*(z - \epsilon) = \frac{1}{c_p^c \dot{m}_c}$$

which is a jump boundary condition for T_c^* at $z = z_o$.

Solving the adjoint coolant equation for $0 \leq z < z_o$ obtains $T_c^*(z) = \tilde{c}_3$, therefore we have for $0 \leq z < z_o$

$$T_c^*(z) = \tilde{c}_3 = \lim_{\epsilon \to 0} T_c^*\left(z_o - \epsilon\right) = \frac{1}{c_p^c \dot{m}_c}$$

As shown for $z > z_o$, there is a solution for the adjoint fuel temperature with $z < z_o$ such that

$$T_f^*\left(r, z\right) = \text{constant in r}$$

Applying the boundary condition and solving for $T_f^*(r, z)$ with $z < z_o$,

$$-k_f \frac{\partial T_f^*}{\partial r}\bigg|_{r=R} = 0 = h_c\left(T_f^*\big|_{r=R} - T_c^*\right)$$

$$T_f^*\left(r, z\right) = T_f^*\big|_{r=R} = \frac{1}{c_p^c \dot{m}_c}$$

Thus the analytical solution for the adjoint coolant and fuel temperatures for a location of interest at $z = z_o$ and $r = r_o$ can be written as

$$T_f^*(r,z) = \begin{cases} 0 & 0 \le r \le R, \quad z_o < z \le H \\ c_o \delta(z - z_o) & 0 \le r < r_o, \quad z = z_o \\ \left(c_o + \tilde{c}_1 \ln\left(\dfrac{r}{r_o}\right)\right)\delta\left(z - z_o\right) & r_o \le r \le R, \quad z = z_o \\ c_1 & 0 \le r \le R, \quad 0 \le z < z_o \end{cases}$$

$$T_c^*(z) = \begin{cases} 0 & z_o < z \le H \\ c_1 & 0 \le z < z_o \end{cases}$$

with

$$\begin{aligned} c_o &= \frac{1}{2\pi}\left(\frac{1}{hR} + \frac{1}{k_f}\ln\left(\frac{R}{r_o}\right)\right) \\ c_1 &= \frac{1}{c_p^c \dot{m}_c} \\ \tilde{c}_1 &= -\frac{1}{2\pi k_f} \end{aligned}$$

This analytic solution only applies to steady state systems with the Q^* defined by Dirac delta functions as noted. In order to analyze the discrete system, we have to change the definition of Q^* to match the discrete adjoint source term.

Physical Error Metric for High and Low Fidelity Solutions

For verification of the physical high fidelity solution, the response function $\Re \equiv \left\langle \bar{f}_R, \bar{T} - \widetilde{\bar{T}} \right\rangle_{z,r}$ is evaluated using the analytic solutions to the steady state adjoint and forward problems. The low fidelity solution is defined to be a constant in both the fuel and coolant regions of the problem space and is written as:

$$\widetilde{T}_f(r,z) = \widetilde{T}_c(z) = b_0$$

This low fidelity analytical solution will hold for the initial condition and all forward boundary conditions if $b_o = T_c(z)|_{z=0}$.

In order to evaluate the error metric, the residual $\bar{r} = A[\widetilde{T}] - Q$ is determined using the previously defined low fidelity solution:

$$\begin{aligned} -\frac{k_f}{r}\frac{\partial}{\partial r}\left(r\frac{\partial}{\partial r}\left(\widetilde{T}_f\right)\right) - q''' &= -\frac{k_f}{r}\frac{\partial}{\partial r}\left(r\frac{\partial}{\partial r}\left(b_o\right)\right) - q''' \\ &= -q''' \end{aligned}$$

$$\begin{aligned} c_p^c \dot{m}_c \frac{d}{dz}\left(\widetilde{T}_c\right) + 2\pi R k_f \left.\frac{\partial \widetilde{T}_f}{\partial r}\right|_{r=R} &= c_p^c \dot{m}_c \frac{d}{dz}\left(b_o\right) - 2\pi R k_f \frac{\partial}{\partial r}\left(b_o\right) \\ &= 0 \end{aligned}$$

The residual vector for the given low fidelity $\widetilde{T}$ solution is therefore

$$\bar{r} = \begin{bmatrix} -q''' & 0 \end{bmatrix}^T$$

The inner product $\left\langle \bar{T}^*, \bar{r} \right\rangle_{z,r}$ should be equal to $\left\langle \bar{Q}^*, \bar{e} \right\rangle_{z,r} = e(r_o, z_o)$. This error term can be written explicitly as

$$\begin{aligned} e(r_o, z_o) &= b_o - T_f(r_o, z_o) \\ = -q''' \frac{R}{2h_c} - \frac{q'''}{4k_f}\left(R^2 - r_o^2\right) - \frac{q'''\pi R^2 z_o}{c_p^c \dot{m}_c} - T_c(0) + b_o \end{aligned}$$

Rewriting $T_f^*(r,z)$ using heaviside step functions

$$T_f^*(r,z) = \left[1 - H\left(z - z_o\right)\right] c_1 + c_o \delta\left(z - z_o\right) + H\left(r - r_o\right) \tilde{c}_1 \ln\left(\frac{r}{r_o}\right) \delta\left(z - z_o\right)$$

evaluating the inner product $\left\langle \bar{T}^*, \bar{r} \right\rangle_{z,r}$

$$\left\langle \bar{T}^*, \bar{r} \right\rangle_{z,r} = \int_0^R 2\pi r dr \int_0^H dz \left[-q''' \left(T_f^*(r,z) \right] \right.$$

$$= -2\pi q''' \left[\int_0^R r dr \int_0^{z_o} dz \; c_1 + \int_0^R r dr \; c_o + \int_{r_o}^R r dr \tilde{c}_1 \ln\left(\frac{r}{r_o}\right) \right]$$

$$= -2\pi q''' \left[\frac{R^2 z_o c_1}{2} + \frac{c_o}{2} R^2 - \frac{\tilde{c}_1}{2} \ln r_o \left(R^2 - r_o^2 \right) + \frac{\tilde{c}_1}{4} \left[R^2 \left(2 \ln R - 1 \right) - r_o^2 \left(2 \ln r_o - 1 \right) \right] \right]$$

Rewriting using the definition of the constants from the analytical adjoint derivation

$$= -2\pi q''' \left[\frac{R^2 z_o}{2 c_p^c \dot{m}_c} - \frac{r_o^2}{4\pi k_f} \ln r_o + \frac{R^2}{2} \left[\frac{1}{2\pi} \left(\frac{1}{h_c R} + \frac{1}{k_f} \ln R \right) \right] \right.$$
$$\left. - \frac{1}{8\pi k_f} \left[R^2 \left(2 \ln R - 1 \right) - r_o^2 \left(2 \ln r_o - 1 \right) \right] \right]$$

$$= -2\pi q''' \left[\frac{R^2 z_o}{2 c_p^c \dot{m}_c} - \cancel{\frac{r_o^2}{4\pi k_f} \ln r_o} + \frac{R}{4\pi h_c} + \cancel{\frac{R^2}{4\pi k_f} \ln R} \right.$$
$$\left. - \cancel{\frac{R^2}{4\pi k_f} \ln R} + \frac{R^2}{8\pi k_f} + \cancel{\frac{r_o^2}{4\pi k_f} \ln r_o} - \frac{r_o^2}{8\pi k_f} \right]$$

$$= -2\pi q''' \left[\frac{R^2 z_o}{2 c_p^c \dot{m}_c} + \frac{R}{4\pi h_c} + \frac{1}{8\pi k_f} \left(R^2 - r_o^2 \right) \right]$$

$$= -\frac{q''' \pi R^2 z_o}{c_p^c \dot{m}_c} - \frac{q''' R}{h_c} - \frac{q'''}{4 k_f} \left(R^2 - r_o^2 \right)$$

setting $b_o = T_c(0)$, we have

$$\left\langle \bar{T}^*, \bar{r} \right\rangle_{z,r} = -\frac{q''' \pi R^2 z_o}{c_p^c \dot{m}_c} - \frac{q''' R}{h_c} - \frac{q'''}{4 k_f} \left(R^2 - r_o^2 \right) = \left\langle \bar{Q}^*, \bar{e} \right\rangle_{z,r}$$

which shows that the analytical adjoint solution in conjunction with the analytic forward solution can exactly calculate the difference between the high and low fidelities at a given location of interest.

Analytic Adjoint Solution Using Discrete Step Function for Q*

In order to apply the analytical adjoint solution to the discretized mathematical problem, a Q^* value was needed that matched the discretized $\bar{Q}^*$ used by the mathematical adjoint. We reconsider the analytic adjoint solution as a Green's Function for a source at r_o, z_o that produces a response at r, z. The analytic adjoint equations are then denoted as follows

$$O_f^*\left(T_f^*\right) = Q_{f,p}^*(r_o, z_o)$$

$$O_c^*\left(T_c^*\right) = 0$$

resulting in the following solution for $T_f^*(r_o, z_o \to r, z)$ and $T_c^*(z_o \to z)$

$$T_f^*(r_o, z_o \to r, z) = \begin{cases} 0 & 0 \le r \le R, \quad z_o < z \le H \\ c_o \delta(z - z_o) & 0 \le r < r_o, \quad z = z_o \\ \left(c_o + \tilde{c}_1 \ln\left(\dfrac{r}{r_o}\right)\right) \delta\left(z - z_o\right) & r_o \le r \le R, \quad z = z_o \\ c_1 & 0 \le r \le R, \quad 0 \le z < z_o \end{cases}$$

$$T_c^*(z_o \to z) = \begin{cases} 0 & z_o < z \le H \\ c_1 & 0 \le z < z_o \end{cases}$$

with

$$\begin{aligned} c_o &= \frac{1}{2\pi}\left(\frac{1}{hR} + \frac{1}{k_f}\ln\left(\frac{R}{r_o}\right)\right) \\ c_1 &= \frac{1}{c_p^c \dot{m}_c} \\ \tilde{c}_1 &= -\frac{1}{2\pi k_f} \end{aligned}$$

Noting that this is a Green's function or solution to the adjoint equations with a unit point source $Q_{f,p}^*(r_o, z_o)$, it is possible to determine an analytical solution using a step function source condition synonymous to the one used by the mathematical adjoint problem using the appropriate convolution. By definition, the discrete mathematical adjoint source is a step function between two discretized radial and axial node locations that are equidistant to a location of interest. This step source can be written as

$$Q_s^*(r_o, z_o) = \begin{cases} \dfrac{1}{\pi\left(r_H^2 - r_L^2\right)(z_H - z_L)} & r_L \le r_o \le r_H, \quad z_L \le z_o \le z_H \\ \\ 0 & \text{otherwise} \end{cases}$$

where r_L, r_H, z_L, z_H are constants as defined by the discretized forward problem. If the discretized error function is defined as $e(r,z)|_{r_L,z_L}^{r_H,z_H} = e(r_o, z_o) = \text{constant}$, then the response of interest is defined as

$$\langle Q_s^*(r_o, z_o) e(r,z) \rangle = \int_0^R 2\pi r dr \int_0^H dz \left(Q_s^*(r_o, z_o) e(r,z)\right)$$

$$= \frac{1}{\pi\left(r_H^2 - r_L^2\right)(z_H - z_L)} \left[\frac{2\pi r^2}{2} z e(r_o, z_o)\right]_{r_L,z_L}^{r_H,z_H} = e(r_o, z_o)$$

which is consistent with evaluating the error metric at location r_o, z_o.

An analytic solution to the adjoint equations with a step function source condition $Q_s^*(r_o, z_o)$ can be found by using the previously determined Green's function and evaluating the following convolution

$$\bar{T}^*(r,z) = \int_0^R 2\pi r_o dr_o \int_0^H dz_o \left(Q_s^*(r_o, z_o) \bar{T}^*(r_o, z_o \to r, z)\right)$$

Rewriting $\bar{T}^*(r_o, z_o \to r, z) = \begin{bmatrix} T_f^*(r_o, z_o \to r, z) & T_c^*(z_o \to z) \end{bmatrix}^T$ and $Q_s^*(r_o, z_o)$ using heaviside step functions results in the following expressions

$$T_f^*(r_o, z_o \to r, z) = \left[1 - H\left(z - z_o\right)\right] c_1 + \left[c_o + H\left(r - r_o\right) \tilde{c}_1 \ln\left(\frac{r}{r_o}\right)\right] \delta\left(z - z_o\right)$$

$$T_c^*(z_o \to z) = \left[1 - H(z - z_o)\right] c_1$$

$$Q_s^*(r_o, z_o) = H(r_o - r_L)[1 - H(r_o - r_H)] H(z_o - z_L)[1 - H(z_o - z_H)] \left[\frac{1}{\pi\left(r_H^2 - r_L^2\right)(z_H - z_L)}\right]$$

Examining each piece of the convolution:

$$\int_0^R 2\pi r_o dr_o \int_0^H dz_o Q_s^*(r_o, z_o) \left[1 - H\left(z - z_o\right)\right] c_1$$

$$= \begin{cases} 0, & z > z_H \\ \int_{r_L}^{r_H} 2\pi r_o dr_o \int_z^{z_H} dz_o \dfrac{c_1}{\pi\left(r_H^2 - r_L^2\right)\left(z_H - z_L\right)}, & z_H \geq z > z_L \\ \int_{r_L}^{r_H} 2\pi r_o dr_o \int_{z_L}^{z_H} dz_o \dfrac{c_1}{\pi\left(r_H^2 - r_L^2\right)\left(z_H - z_L\right)}, & z \leq z_L \end{cases}$$

$$= \begin{cases} 0, & z > z_H \\ \dfrac{\pi\left(r_H^2 - r_L^2\right)\left(z_H - z\right)}{\pi\left(r_H^2 - r_L^2\right)\left(z_H - z_L\right)} c_1 & z_H \geq z > z_L \\ \dfrac{\pi\left(r_H^2 - r_L^2\right)\left(z_H - z_L\right)}{\pi\left(r_H^2 - r_L^2\right)\left(z_H - z_L\right)} c_1 & z \leq z_L \end{cases}$$

$$= \begin{cases} 0, & z > z_H \\ \dfrac{\left(z_H - z\right)}{\left(z_H - z_L\right)} c_1 & z_H \geq z > z_L \\ c_1 & z \leq z_L \end{cases}$$

$$\int_0^R 2\pi r_o dr_o \int_0^H dz_o Q_s^*(r_o, z_o) c_o \delta(z - z_o)$$

$$= \int_{r_L}^{r_H} 2\pi r_o dr_o \int_0^H dz_o \frac{H(z_o - z_L)[1 - H(z_o - z_H)]}{\pi\left(r_H^2 - r_L^2\right)\left(z_H - z_L\right)} c_o \delta(z - z_o)$$

$$= \int_{r_L}^{r_H} 2r_o dr_o \frac{1}{(z_H - z_L)(r_H^2 - r_L^2)} H(z - z_L)\left[1 - H(z - z_H)\right]\left[\tilde{c}_1 \ln r_o + \frac{1}{2\pi}\left(\frac{1}{hR} + \frac{1}{k_f}\ln R\right)\right]$$

$$= \frac{1}{2\pi hR(z_H - z_L)} + \frac{\tilde{c}_1}{(z_H - z_L)(r_H^2 - r_L^2)}\left[r_H^2 \ln\left(\frac{r_H}{R}\right) - \frac{r_H^2}{2} - r_L^2 \ln\left(\frac{r_L}{R}\right) + \frac{r_L^2}{2}\right], \quad z_L \le z \le z_H$$

$$\int_0^R 2\pi r_o dr_o \int_0^H dz_o Q_s^*(r_o, z_o) H\left(r - r_o\right)\tilde{c}_1 \ln\left(\frac{r}{r_o}\right)\delta\left(z - z_o\right)$$

$$= \begin{cases} \int_{r_L}^{r} 2\pi r_o dr_o \int_0^H dz_o \dfrac{H(z_o - z_L)[1 - H(z_o - z_H)]}{\pi\left(r_H^2 - r_L^2\right)(z_H - z_L)}\tilde{c}_1 \ln\left(\dfrac{r}{r_o}\right)\delta\left(z - z_o\right), & r_L \le r < r_H \\ \int_{r_L}^{r_H} 2\pi r_o dr_o \int_0^H dz_o \dfrac{H(z_o - z_L)[1 - H(z_o - z_H)]}{\pi\left(r_H^2 - r_L^2\right)(z_H - z_L)}\tilde{c}_1 \ln\left(\dfrac{r}{r_o}\right)\delta\left(z - z_o\right), & r \ge r_H \end{cases}$$

$$= \begin{cases} \dfrac{H(z - z_L)[1 - H(z - z_H)]}{\left(r_H^2 - r_L^2\right)(z_H - z_L)}\tilde{c}_1\left(-r_L^2 \ln\left(\dfrac{r}{r_L}\right) + \dfrac{r^2 - r_L^2}{2}\right), & r_L \le r < r_H \\ \dfrac{H(z - z_L)[1 - H(z - z_H)]}{\left(r_H^2 - r_L^2\right)(z_H - z_L)}\tilde{c}_1\left(r_H^2 \ln\left(\dfrac{r}{r_H}\right) - r_L^2 \ln\left(\dfrac{r}{r_L}\right) + \dfrac{r_H^2 - r_L^2}{2}\right), & r \ge r_H \end{cases}$$

Therefore, the solution for $\bar{T}^*(r,z)$ using the above definition for $Q_s^*(r_o,z_o)$ is

$$T_f^*(r,z) = \begin{cases} 0 & 0 \le r \le R, \quad z_H < z \le H \\ c_1 & 0 \le r \le R, \quad 0 \le z < z_L \\ \left[\begin{array}{l} \dfrac{(z_H - z)}{(z_H - z_L)} c_1 + \dfrac{1}{2\pi h R (z_H - z_L)} + \\ \\ \dfrac{1}{2\pi k_f (z_H - z_L)\left(r_H^2 - r_L^2\right)} \left(\begin{array}{l} r_H^2 \ln\left(\dfrac{R}{r_H}\right) \\ -r_L^2 \ln\left(\dfrac{R}{r_L}\right) \\ +\dfrac{r_H^2 - r_L^2}{2} \end{array} \right) \end{array} \right] & 0 \le r < r_L, \quad z_L \le z \le z_H \\ \left[\begin{array}{l} \dfrac{(z_H - z)}{(z_H - z_L)} c_1 + \dfrac{1}{2\pi h R (z_H - z_L)} + \\ \\ \dfrac{1}{2\pi k_f (z_H - z_L)\left(r_H^2 - r_L^2\right)} \left(\begin{array}{l} r_H^2 \ln\left(\dfrac{R}{r_H}\right) \\ -r_L^2 \ln\left(\dfrac{R}{r}\right) \\ +\dfrac{r_H^2 - r^2}{2} \end{array} \right) \end{array} \right] & r_L \le r < r_H, \quad z_L \le z \le z_H \\ \dfrac{(z_H - z)}{(z_H - z_L)} c_1 + \\ \dfrac{1}{2\pi h R (z_H - z_L)} + \dfrac{1}{2\pi k_f (z_H - z_L)} \ln\left(\dfrac{R}{r}\right) & r_H \le r \le R, \quad z_L \le z \le z_H \end{cases}$$

$$T_c^*(z) = \begin{cases} 0 & z_H < z \leq H \\ c_1 & 0 \leq z < z_L \\ \dfrac{(z_H - z)}{(z_H - z_L)} c_1 & z_L \leq z \leq z_H \end{cases}$$

This solution is then integrated according to the inner product $\left\langle \bar{T}^*, \bar{r} \right\rangle_{r,z}$ using the same definition for the residual as before in the analytic error metric section with $\tilde{T} = b_o$. Examining the case where $0 \leq r \leq R,\ 0 \leq z < z_L$

$$\int_0^R 2\pi r dr \int_0^{z_L} dz \left[-q''' c_1 \right] = -q''' \pi R^2 z_L c_1$$

Examining the inner product with $0 \leq r < r_L,\ z_L \leq z \leq z_H$

$$\int_0^{r_L} 2\pi r dr \int_{z_L}^{z_H} dz \left[-q''' \left(\frac{(z_H - z)}{(z_H - z_L)} c_1 + \frac{1}{2\pi h R (z_H - z_L)} \right) \right]$$

$$+ \int_0^{r_L} 2\pi r dr \int_{z_L}^{z_H} dz \left[-q''' \left(\frac{r_H^2 \ln\left(\frac{R}{r_H}\right) - r_L^2 \ln\left(\frac{R}{r_L}\right) + \frac{r_H^2 - r_L^2}{2}}{2\pi k_f \left(z_H - z_L\right)\left(r_H^2 - r_L^2\right)} \right) \right]$$

$$= -q''' \left[r_l^2 \pi z_H c_1 - r_L^2 \pi c_1 \frac{z_H + z_L}{2} + \frac{r_L^2}{2hR} \right]$$

$$-q''' r_L^2 \left(\frac{r_H^2 \ln\left(\frac{R}{r_H}\right) - r_L^2 \ln\left(\frac{R}{r_L}\right) + \frac{r_H^2 - r_L^2}{2}}{2k_f \left(r_H^2 - r_L^2\right)} \right)$$

Examining the inner product with $r_L \leq r \leq r_H,\ z_L \leq z \leq z_H$

$$-q''' \left[(r_H^2 - r_L^2)\pi z_H c_1 - (r_H^2 - r_L^2)\pi c_1 \frac{z_H^2 - z_L^2}{2\left(z_H - z_L\right)} + \frac{(r_H^2 - r_L^2)}{2hR} \right]$$

$$+\int_{r_L}^{r_H} 2\pi r dr \int_{z_L}^{z_H} dz \left[-q''' \left(\frac{r_H^2 \ln\left(\frac{R}{r_H}\right) - r_L^2 \ln\left(\frac{R}{r}\right) + \frac{r_H^2 - r^2}{2}}{2\pi k_f \left(z_H - z_L\right)\left(r_H^2 - r_L^2\right)} \right) \right]$$

$$= -q''' \left[(r_H^2 - r_L^2)\pi z_H c_1 - (r_H^2 - r_L^2)\pi c_1 \frac{z_H + z_L}{2} + \frac{(r_H^2 - r_L^2)}{2hR} \right]$$

$$-q''' \left[\frac{r_H^2 \ln\left(\frac{R}{r_H}\right) + \frac{r_H^2}{2}}{2k_f} \right] + \frac{q'''}{8k_f}\left(r_H^2 + r_L^2\right)$$

$$-\frac{q''' r_L^2}{4k_f(r_H^2 - r_L^2)} \left[2r_H^2 \ln\left(\frac{r_H}{R}\right) - 2r_L^2 \ln\left(\frac{r_L}{R}\right) - (r_H^2 - r_L^2) \right]$$

Examining the inner product with $r_H < r \leq R,\ z_L \leq z \leq z_H$

$$-q''' \left[(R^2 - r_H^2)\pi z_H c_1 - (R^2 - r_H^2)\pi c_1 \frac{z_H + z_L}{2} + \frac{(R^2 - r_H^2)}{2hR} \right]$$

$$-q''' \int_{r_H}^{R} 2\pi r dr \int_{z_L}^{z_H} dz \frac{1}{2\pi k_f \left(z_H - z_L\right)} \ln\left(\frac{R}{r}\right)$$

$$= -q''' \left[(R^2 - r_H^2)\pi z_H c_1 - (R^2 - r_H^2)\pi c_1 \frac{z_H + z_L}{2} + \frac{(R^2 - r_H^2)}{2hR} \right]$$

$$-\frac{q'''}{4k_f} \left[2r_H^2 \ln\left(\frac{r_H}{R}\right) + (R^2 - r_H^2) \right]$$

Summing these parts together, we have for $\left\langle \bar{T}^*, \bar{r} \right\rangle_{r,z}$ the expression

$$\left\langle \bar{T}^*, \bar{r} \right\rangle_{r,z} = -q'''\pi R^2 c_1 \frac{(z_H - z_L)}{2} - q''' \frac{R}{2h} + \frac{q'''}{8k_f}\left(r_H^2 + r_L^2 - 2R^2\right)$$

This solution for the analytic adjoint using a step function source was compared with the mathematical and physical adjoint solutions. The comparison can be found in Numerical Results, Chapter 3 of this thesis.

2.2.4 Low Fidelity Adjoint Problem

Initially, the Adaptive Model Refinement project intended to use low fidelity adjoint solution based upon coarsened meshes and adjusted thermal conductivity values as a means of predicting the difference between high and low fidelity models. During numerical testing, this method was shown to lack adequate predictive capability of the quantities of interest. In general, adjoint solutions contain information regarding the local temporal and spatial importance of the residual regarding a specific quantity of interest. The devolution of the mesh from high to low skewed this local importance such that the estimated quantity of interest no longer held pertinent information in regards to the accuracy of the low fidelity model.

Solving for the low fidelity mathematical adjoint is the same as solving for the high fidelity mathematical adjoint using $\widetilde{\bar{\mathbf{A}}}^* = \widetilde{\bar{\mathbf{A}}}^T$ in place of $\bar{\mathbf{A}}^*$. However, in order to evaluate the response $\widetilde{\Re} = \left\langle \widetilde{T}^\dagger, \bar{r} \right\rangle$, the adjoint solution $\widetilde{T}^\dagger$ must be projected onto the high fidelity mesh in order to determine the inner product. This elongation process is non-unique, and a variety of methods were considered to arrive at a low fidelity adjoint solution extrapolated to the high fidelity mesh.

One method considers an additional linear set of equations for the low-fidelity problem. Rewriting the low fidelity equation (2.7)

$$\widetilde{\bar{\mathbf{C}}}_{n+1}\widetilde{\boldsymbol{\phi}}_{n+1} = \widetilde{\bar{\mathbf{B}}}_{n+1}\widetilde{\boldsymbol{\phi}}_n - \widetilde{\mathbf{Q}}_{n+1},$$

we have an additional set of linear equations that project the low fidelity temperatures onto the high fidelity mesh

$$\widetilde{\bar{\mathbf{E}}}\widetilde{\boldsymbol{\phi}}_{n+1} = \bar{\bar{\mathbf{I}}}\widetilde{\boldsymbol{\theta}}_{n+1} \tag{2.13}$$

where $\widetilde{\boldsymbol{\theta}}_{n+1}$ is the low fidelity temperature projected onto the high fidelity mesh and the $\widetilde{\bar{\mathbf{E}}}_{n+1}$ is a $m \times n$ operator with $n > m$ that linearly interpolates the $\widetilde{\boldsymbol{\phi}}_{n+1}$ vector. Writing the block matrix time structure of this problem

$$\begin{bmatrix}
\widetilde{\bar{\mathbf{C}}}_1 & & & & & & & \\
\widetilde{\bar{\mathbf{E}}} & -\bar{\bar{\mathbf{I}}} & & & & & & \\
\widetilde{\bar{\mathbf{B}}}_2 & & \widetilde{\bar{\mathbf{C}}}_2 & & & & & \\
 & & \widetilde{\bar{\mathbf{E}}} & -\bar{\bar{\mathbf{I}}} & & & & \\
 & & & \ddots & & & & \\
 & & & & \widetilde{\bar{\mathbf{B}}}_N & \widetilde{\bar{\mathbf{C}}}_N & & \\
 & & & & & \widetilde{\bar{\mathbf{E}}} & -\bar{\bar{\mathbf{I}}}
\end{bmatrix}
\begin{bmatrix}
\widetilde{\boldsymbol{\phi}}_1 \\ \widetilde{\boldsymbol{\theta}}_1 \\ \widetilde{\boldsymbol{\phi}}_2 \\ \widetilde{\boldsymbol{\theta}}_2 \\ \vdots \\ \widetilde{\boldsymbol{\phi}}_N \\ \widetilde{\boldsymbol{\theta}}_N
\end{bmatrix} =
\begin{bmatrix}
\widetilde{\mathbf{Q}}_1 \\ 0 \\ \widetilde{\mathbf{Q}}_2 \\ 0 \\ \vdots \\ \widetilde{\mathbf{Q}}_N \\ 0
\end{bmatrix}$$

Transposing the matrix operator for the time dependent adjoint equation set and selecting $\widetilde{Q}^*$ as now noted produces

$$\begin{bmatrix} \widetilde{\bar{\mathbf{C}}}_1^* & \widetilde{\bar{\mathbf{E}}}^* & \widetilde{\bar{\mathbf{B}}}_2^* & & & & & \\ & -\bar{\bar{\mathbf{I}}} & & & & & & \\ & & \widetilde{\bar{\mathbf{C}}}_2^* & \widetilde{\bar{\mathbf{E}}}^* & \widetilde{\bar{\mathbf{B}}}_3^* & & & \\ & & & -\bar{\bar{\mathbf{I}}} & & & & \\ & & & \ddots & & & & \\ & & & & & \widetilde{\bar{\mathbf{C}}}_N^* & \widetilde{\bar{\mathbf{E}}}^* & \\ & & & & & & -\bar{\bar{\mathbf{I}}} & \end{bmatrix} \begin{bmatrix} \widetilde{\boldsymbol{\phi}}_1^* \\ \widetilde{\boldsymbol{\theta}}_1^* \\ \widetilde{\boldsymbol{\phi}}_2^* \\ \widetilde{\boldsymbol{\theta}}_2^* \\ \vdots \\ \widetilde{\boldsymbol{\phi}}_N^* \\ \widetilde{\boldsymbol{\theta}}_N^* \end{bmatrix} = \begin{bmatrix} 0 \\ \widetilde{\mathbf{Q}}_1^* \\ 0 \\ \widetilde{\mathbf{Q}}_2^* \\ \vdots \\ 0 \\ \widetilde{\mathbf{Q}}_N^* \end{bmatrix}$$

Note for a single time step, we have the following adjoint matrix equations

$$\widetilde{\bar{\mathbf{C}}}_n^* \widetilde{\boldsymbol{\phi}}_n^* + \widetilde{\bar{\mathbf{E}}}^* \widetilde{\boldsymbol{\theta}}_n^* + \widetilde{\bar{\mathbf{B}}}_{n+1}^* \widetilde{\boldsymbol{\phi}}_{n+1}^* = 0$$

$$-\bar{\bar{\mathbf{I}}} \widetilde{\boldsymbol{\theta}}_n^* = \widetilde{\mathbf{Q}}_n^*$$

where $\bar{\mathbf{Q}}^*$ is the same right hand side as for the mathematical adjoint. The previous system of linear equations reveals that $\widetilde{\boldsymbol{\theta}}_{n+1}^* = -\widetilde{\mathbf{Q}}$ which implies that $\widetilde{\mathbf{Q}}^*$ should be selected equal to $\bar{\mathbf{Q}}^*$. The system then simply solves the low fidelity adjoint problem with $\bar{\mathbf{Q}}^*$ volume weighted to the low fidelity mesh. The resulting expression for $\widetilde{\boldsymbol{\theta}}_{n+1}^*$ will contain no information with regards to the adjoint solution $\widetilde{\boldsymbol{\phi}}_{n+1}^*$, and the resulting response integral is trivial.

Another attempt at arriving at an effective low fidelity adjoint solution used the same operator $\widetilde{\bar{\mathbf{E}}}_{n+1}$ to linearly interpolate the low fidelity adjoint solution onto the high fidelity mesh in a similar fashion to the forward low fidelity problem. This, however, also resulted in response functions that did not accurately describe the differences between the high and low fidelity fuel temperatures.

Chapter 3

Numerical Results

This chapter examines the numerical behavior of the forward and adjoint problems. Various figures and descriptions are given analyzing the forward low and high fidelity solution behaviors as well as adjoint solution behavior. The effectiveness of the physical, mathematical, and analytic adjoint solutions' prediction of the quantity of interest is also investigated in the following chapter.

3.1 Numerical Results for Forward Problem

Figure 3.1 below contains the temperature profile for the steady state solution of the forward problem, equations (2.8) and (2.9), using the high fidelity finite differencing scheme, the low fidelity lumped parameter and finite differencing scheme, and the linear interpolation used to project the low fidelity solution onto the high fidelity geometry. The solutions are shown for a given axial location that is halfway up the height of the fuel pin with a high fidelity ring number of 8 and a low fidelity ring number of 4. Heat generation is assumed constant across the radial direction of the pin at this given axial location.

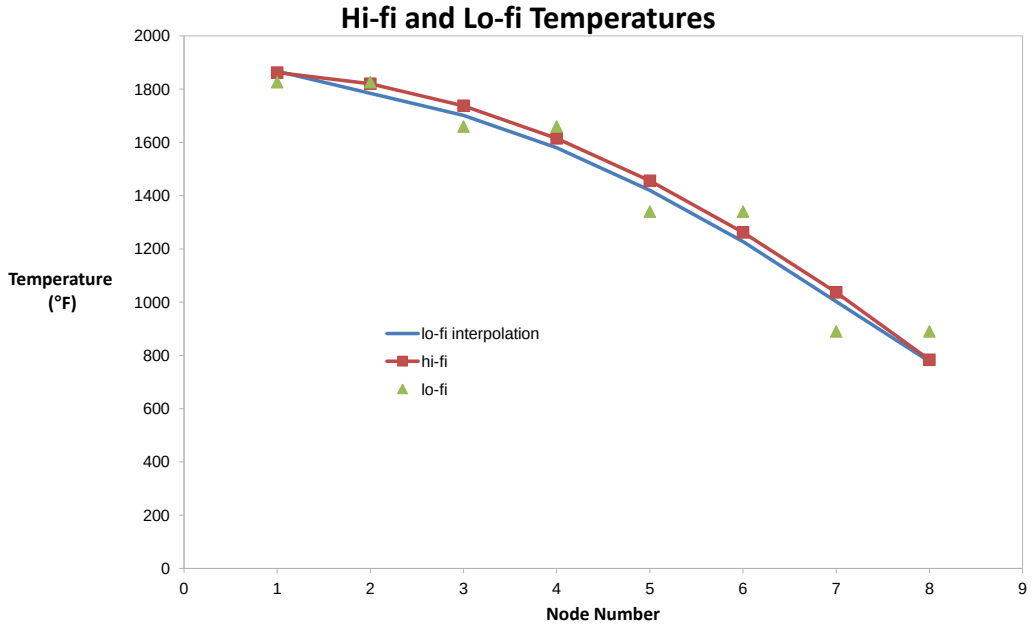

Figure 3.1: **Steady state forward solution as determined by the low fidelity, high fidelity, and low-to-high linear interpolation solution methods**

The red series that represents the high fidelity solution exhibits the quadratic structure that we would expect for a constant heat generation problem. The green series in Figure 3.1 shows the coarsened finite difference model with half as many radial nodes as the high fidelity problem. The adjusted parameters calculated with equation (2.4), when used with the low fidelity problem, will result in exactly the same volume averaged temperatures as the high fidelity problem. The linear interpolation of the low fidelity onto the high fidelity geometry will however contain differences in temperature. The blue line in Figure 3.1 shows the linear interpolation of the low fidelity solution onto the high fidelity mesh. These temperature differences or ΔTs are the quantity of interest for both the steady state and time dependent examples. The differences are noted to be small (2.1% of the largest relative error shown in Figure 3.1). Four linear regions can be seen between the green low fidelity regions, and a small difference between the blue line and the red series can be seen for almost every high fidelity temperature node.

The time dependent forward problem exhibits low fidelity and high fidelity volume averaged temperatures that are not exact. This is due to the fact that the lumped parameters as deter-

mined by equations (2.4) and (2.5) use the steady state forward temperature rather than the time dependent values. Figure 3.2 shows the time dependent behavior at a given axial and radial location within the pin for the low fidelity solution verses the high fidelity solution coarsened to the low fidelity mesh.

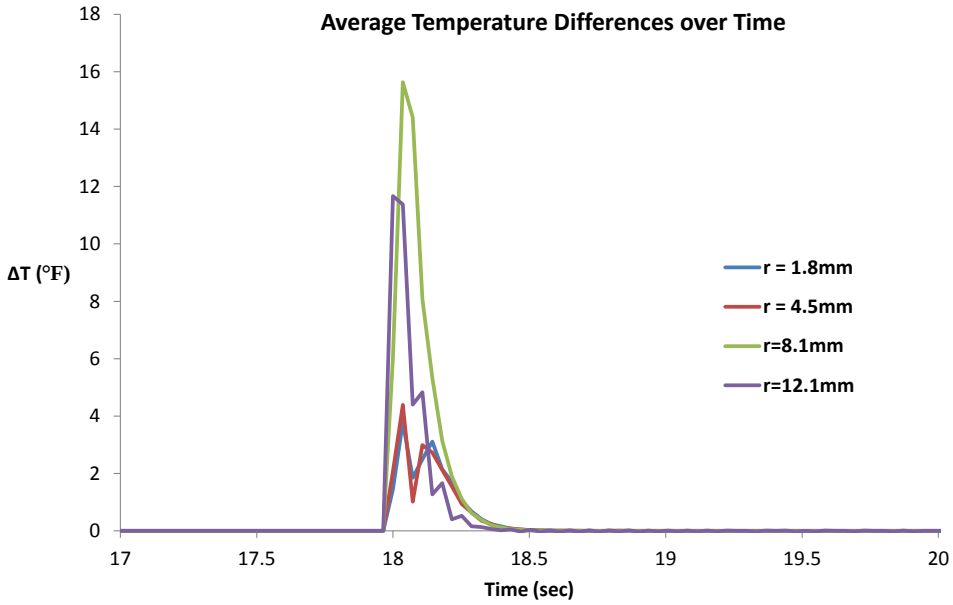

Figure 3.2: **Difference in time dependent hi-fi and low fidelity solution average temperatures at four separate locations of interest**

The results presented in Figure 3.2 correspond to a high fidelity ring number of 8, a low fidelity ring number of 4, and an axial mesh number of 20. The figure shows the ΔT difference between the volume averaged high fidelity solution and the low fidelity solution at each time step. At $t = 0.005$ hrs, the heat generation within the pin is reduced by a factor of 4. Prior to this heat generation step, the k_{eff} and h_{eff} values as determined by equations (2.4) and (2.5) to ensure that the volume averaged high fidelity solution and the low fidelity solution are equal. Once the q''' jump has occurred, the k_{eff} and h_{eff} values for the pseudo-steady state forward problem no longer ensure that $\Delta T = 0$ as one can see from the figure. After the transient has subsided, the difference between the high fidelity volume averaged solution and low fidelity solution return to zero. Each line in Figure 3.2 represents a different low fidelity radial location.

All radial locations correspond to an axial location halfway up the pin.

3.2 Numerical Adjoint Behavior

Using the high fidelity mathematical adjoint for either the time dependent or steady state problem yields the exact value for the quantity of interest at every axial and radial location regardless of the mesh size. The time dependent shape of the mathematical adjoint solution is rather unique given its role as an indicator of the relative influence exerted on the temperature difference at a particular location of interest. Figures 3.3 through 3.5 show the time dependent nature of the high fidelity adjoint.

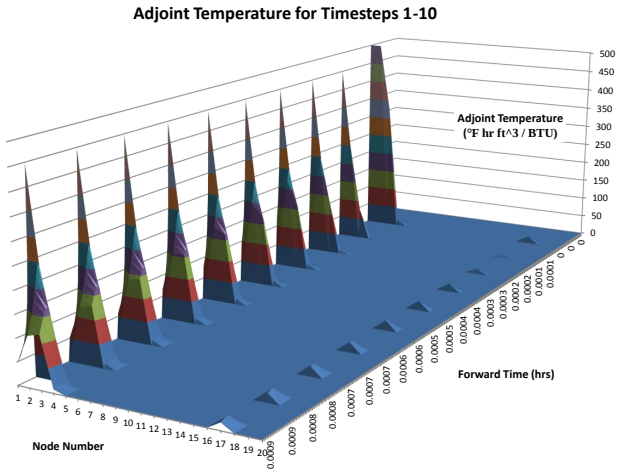

Figure 3.3: **Hi-fi adjoint time dependent solution shape for timesteps 1-10**

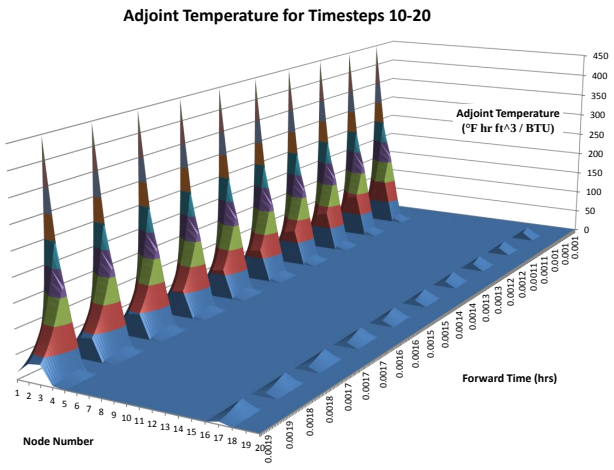

Figure 3.4: **Hi-fi adjoint time dependent solution shape for timesteps 10-20**

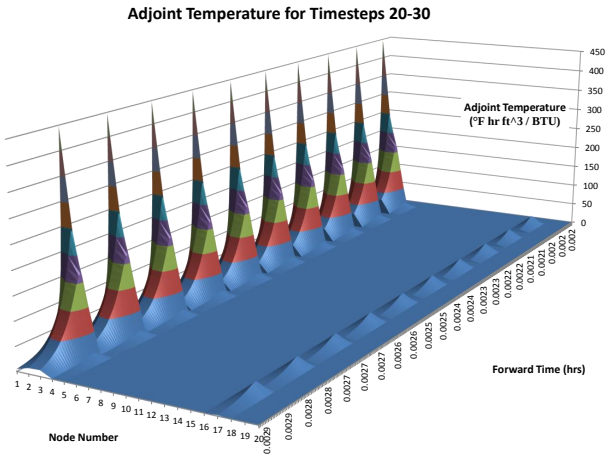

Figure 3.5: **Hi-fi adjoint time dependent solution shape for timesteps 20-30**

Figures 3.3 through 3.5 are for a location of interest at the first radial and first axial node with a ring number of 8 and a radial mesh of 8. The time steps were 0.0001 hours or 0.36 seconds. "Forward time" refers to a fixed Q^* location in time. Both adjoint time and forward time are increasing along the time axis in Figures 3.3 - 3.5 with forward time values listed along the axis. Each adjoint time node contains 30 forward time nodes, since a full temporal and spatial distribution of adjoint values is necessary to calculate the inner product for a given forward

time value. This adjoint time behavior can be seen by observing the T^* shape along the time axis during which the forward time remains constant. Each mathematical adjoint solution will have a given "adjoint time" dependent shape for a constant value of "forward time."

The node number denotes all spatial nodes for every axial and radial location including the axial coolant nodes. Node ordering has the radial values for the first axial location followed by the radial values for the second axial location and so on. Since the first axial mesh is the location of interest, its values are nonzero in the previous figures while the other axial locations are zero with the exception of the coolant values. One can conclude from this that, since there is no axial coupling conduction model for the fuel, other axial mesh locations exhibit no influence on the ΔT quantity of interest. It's also important to note that while the coolant does have some influence, its adjoint solution value is considerably lower than the fuel ring adjoint values.

With the exception of $t = 0.00$, all times steps have the same relative shape with regards to adjoint time. As forward time increases, the location of interest in adjoint time shifts so that more and more of the time dependent adjoint solution shape is revealed. It can be seen that the adjoint solution spikes at the location of interest and then begins to decay away. One can conclude that for a given ΔT, the temperatures at the same time as the examined quantity of interest exhibit the greatest influence on the evaluated metric. Earlier times also exhibit some influence on the quantity of interest, but this influence decays away the farther one is from the time of interest. These figures also demonstrate that future time temperature values have zero influence on a given ΔT.

A time integrated adjoint solution was investigated for several times of interest to better understand the differences between the high fidelity and low fidelity solution shapes. The time integrated adjoints were determined according to the following equation

$$\begin{aligned} T_{hi} - T_{lo} = \Delta T(t_f) &= \int_0^{t_f} dt \int_V d^3r \cdot R(\vec{r}) \cdot T^*(\vec{r}, t) \\ &= \int_V d^3r \cdot R(r, z) \int_0^{t_f} dt \cdot T^*(r, z, t) \\ &= \int_V d^3r \cdot R(r, z) \left\langle T^*(r, z) \right\rangle_{t_f} \end{aligned} \tag{3.1}$$

Because the residuals $R(r, z)$ are assumed to be time independent, equation (3.1) only holds for pseudo-steady state conditions such that q''' is unchanged. Figure 3.6 shows time integrated

$\langle T^*(r,z)\rangle_{t_f}$ values as defined by equation (3.1) for high and low fidelities at three separate t_f times of interest.

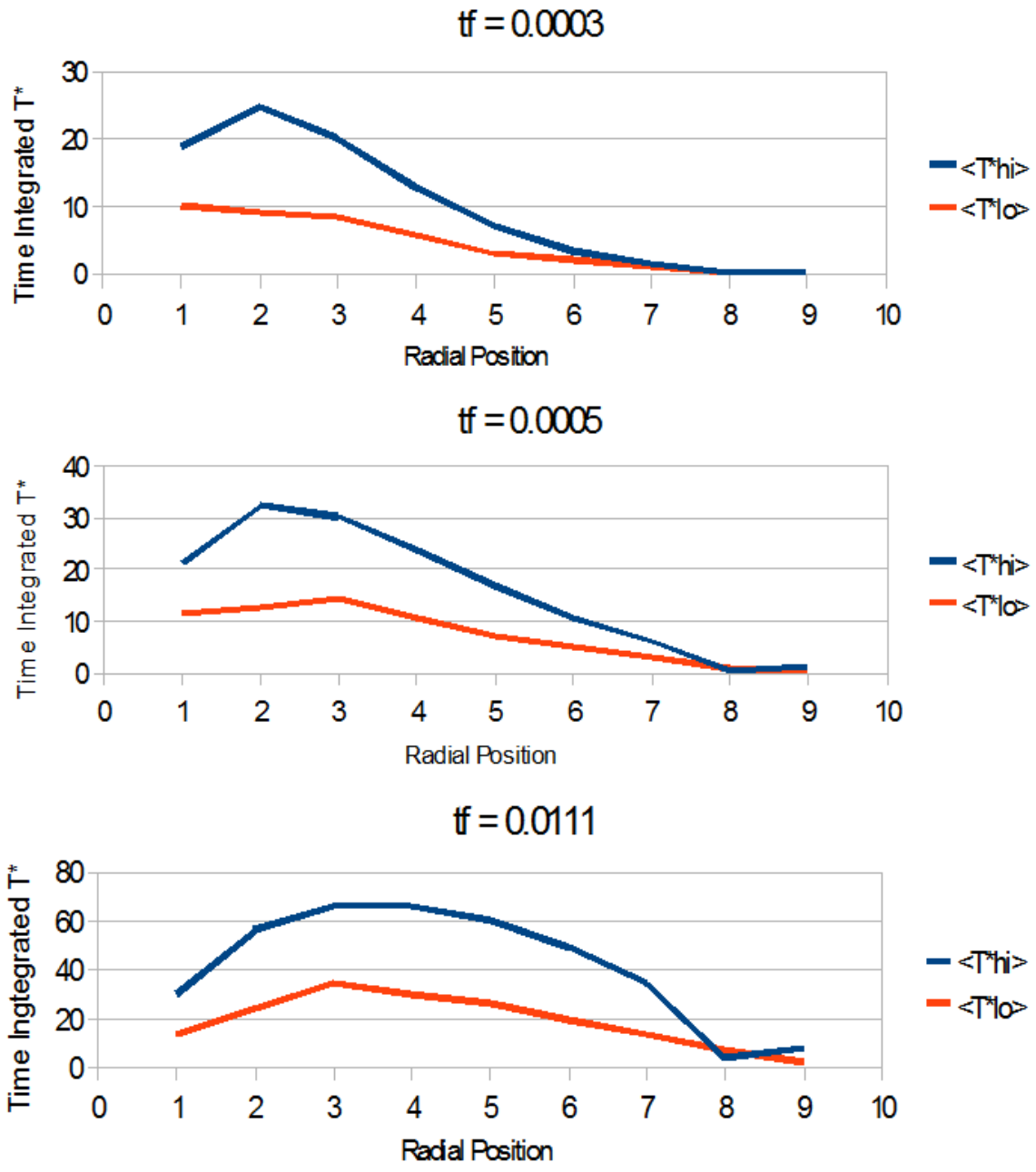

Figure 3.6: **Time integrated T^* for low and high fidelities for given t_f values**

In each case, the location of interest was the centerline radial value and the first axial location or bottom of the fuel pin. The high fidelity ring number was 8 and the low fidelity ring number was 4. There are some similarities between the two adjoint solution shapes, but the low fidelity adjoint is consistently less than the high fidelity adjoint. Since the residuals used in both error metrics are the same, the low fidelity adjoint solution will therefore predict a drastically different response than the high fidelity adjoint solution.

3.3 Numerical Determination of the Quantity of Interest

The following section outlines the various results for the evaluation of a given quantity interest using adjoints. Quantities of interest typically are differences between low-fidelity and high fidelity solutions at a particular location within the fuel pin. It was found that for time dependent problems, the mathematical adjoint predicted perfectly the difference between low and high fidelity problems for either time dependent, steady state, or pseudo-steady state problems at every location of interest within the fuel pin. Initial investigation of the low fidelity adjoint's best estimate of the quantity of interest showed inaccurate approximations, and it was deemed unable to accurately predict the difference between high and low fidelity temperatures in the time dependent problem and steady state problems alike.

Since low fidelity approximations exhibited erratic behavior for the time dependent cases, the problem was simplified to pseudo-steady state cases using constant heat generation and steady state cases with no time dependency whatsoever. Even for these cases, the low fidelity adjoint response does not return accurate approximations of the quantity of interest. The response estimated by the adjoint solutions is the total sum of each adjoint value multiplied by each corresponding nodal residual for a given time step. This residual summation behavior was investigated to gain an understanding of what was occurring during the low fidelity adjoint approximation. Time index in the following figures pertains to both forward time and adjoint reverse time. Each index value corresponds to a fixed location in forward time and all subsequent values in reverse time. Therefore, each "peak" denotes a single location in forward time swept through all adjoint reverse time values. Index values are simply marking the time dependent behavior in both forward and adjoint time. The following figures demonstrate the pseudo-steady state behavior using high and low fidelity adjoint approximations.

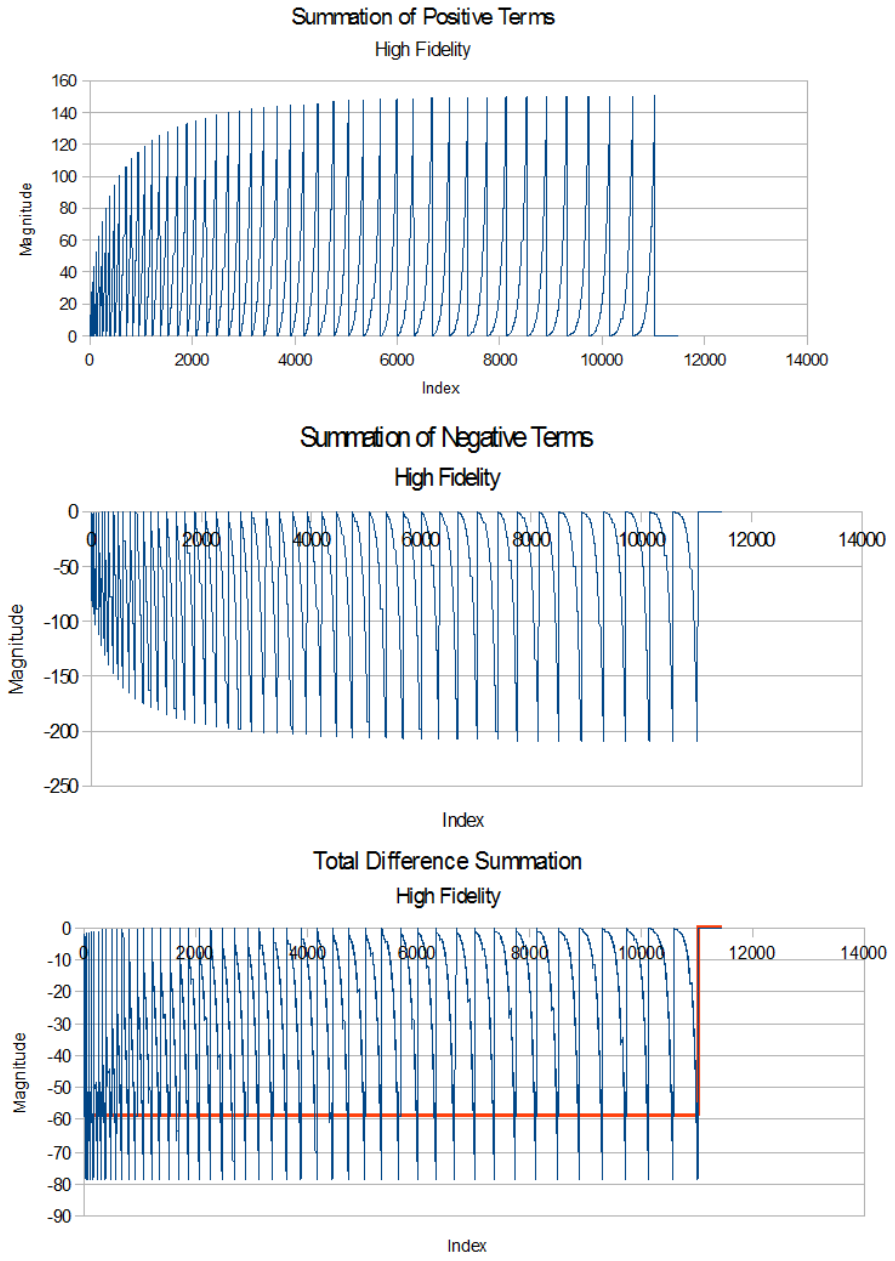

Figure 3.7: **Collection of discretized $\langle T^*_{hi}, r \rangle_{r,z,t}$ positive and negative values as well as their summation and its resulting estimate of the quantity of interest**

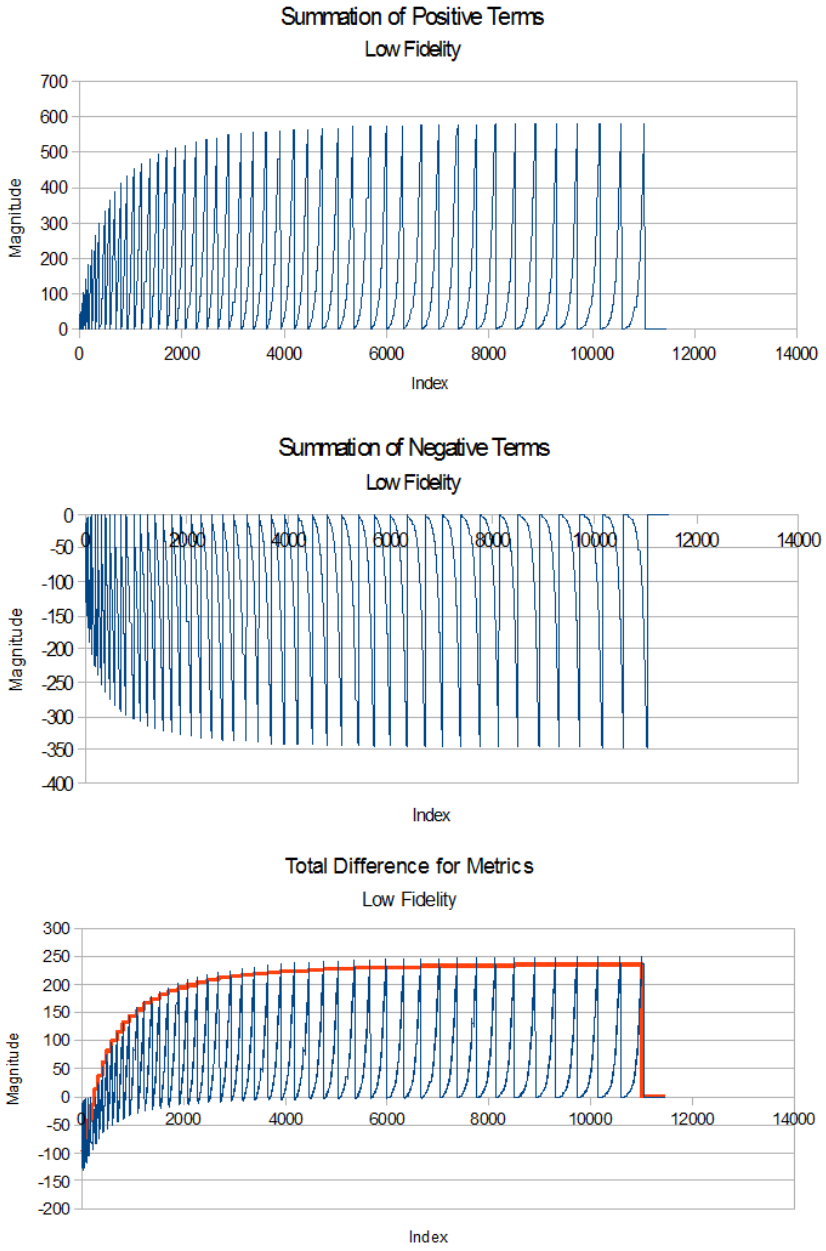

Figure 3.8: **Collection of discretized $\langle T^*_{lo}, r \rangle_{r,z,t}$ positive and negative values as well as their summation and its resulting estimate of the quantity of interest**

The location of interest corresponds to the centerline of the fuel pin and the first axial location. The low fidelity estimate of 248^oF in figure 3.8 is drastically different than the high fidelity's estimate of -59^oF in figure 3.7. The constant value predicted by the high fidelity adjoint is consistent with the constant difference found between the linearly interpolated low fidelity forward problem and the high fidelity forward problem for the pseudo-steady state case. In these figures, the x-axis index denotes the axial and radial node indices along with the time-step index, and the y-axis represents the inner product summation up to a specific index value. Each spike in these figures corresponds to the summation for a specific time of interest. It is interesting to note that although the positive and negative terms approach asymptotic maximum values in figure 3.7, the estimated quantity of interest remains constant. In figure 3.8 however, it takes several time steps for the estimated quantity of interest to reach a constant value. This phenomenon shows the sensitivity of the mathematical adjoint approximation of the quantity of interest and high fidelity mathematical adjoint's ability to predict the quantity of interest regardless of temporal behavior.

In order to verify the low fidelity adjoint, a"low-low" fidelity model was constructed. Comparing the low-fidelity to a "low-low" fidelity is effectively the same as comparing a high fidelity model to a low fidelity model. Therefore, the low fidelity adjoint should predict the exact difference between the low and "low-low" temperature calculations. The low-low fidelity problem considered was a constant temperature equal to the coolant inlet temperature. Figure 3.9 shows the ΔT values as evaluated by the low fidelity adjoint solution and low fidelity $< Q^*, e >$ inner product.

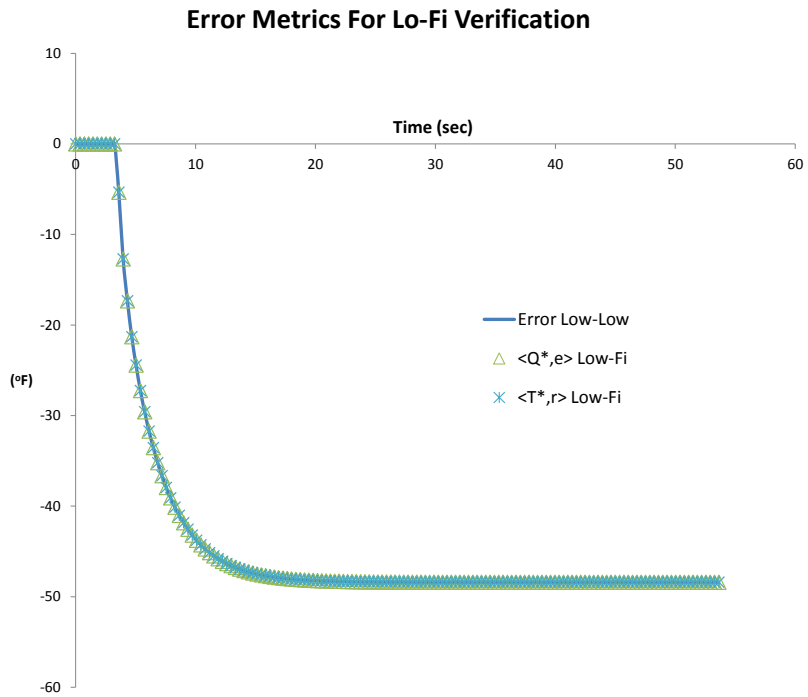

Figure 3.9: **Verification results for the low fidelity adjoint approximation using a steady state "low-low" fidelity solution**

Before the decrease in q''', the low and low-low fidelities are equal to each other and the resulting error metric is zero as seen in figure 3.9. At $t = 0.001$ hours, the low fidelity problem begins to deviate from the pseudo-steady state low-low problem since q''' is decreased at that time. The error metric approximated by the low-fidelity adjoint solution is consistent both with the $\langle Q^*, e \rangle$ inner product and the exact error between the low and low-low fidelity problems. This verifies that the low fidelity adjoint solution is correct and that the linear interpolation of the low fidelity adjoint solution onto the high fidelity spatial mesh is where the significant difference between low and high fidelity response occurs.

Initially, the physical and analytical adjoints showed erratic predictive behavior of the quantity of interest similar to that of the low fidelity adjoint. To contrast the quantity of interest calculated using the three adjoints, the forward problem was further simplified such that the low-fidelity was considered to be a constant temperature throughout the fuel and coolant and set to the coolant inlet temperature. Though completely incorrect, the forward boundary conditions were still satisfied. In this case, the physical and analytical adjoints were found to approximate

the quantity of interest exactly. Figure 3.10 below shows the adjoint solution shapes for three separate radial locations across the same axial location halfway up the fuel pin.

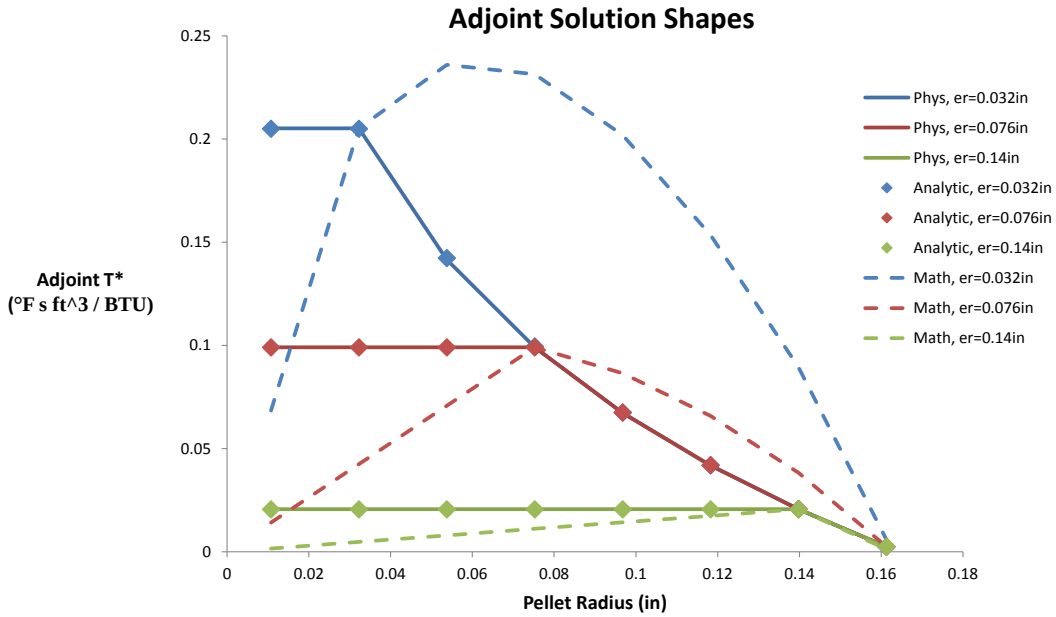

Figure 3.10: **Solution shapes for physical, analytical, and mathematical adjoints for three separate radial locations of interest**

The diamonds, corresponding to the analytical solution, match almost exactly the physical adjoint values. This solution shape has a constant value from the centerline up to the location of interest and decreases logarithmically thereafter. By contrast, the dotted line displays a dissimilar solution shape for the mathematical adjoint solution. At the location of interest it matches the physical and analytical value, but it shows linear and quadratic behavior before and after this radial point. For the case where the quantity of interest is at a radial location of 0.032 inches, the mathematical solution increases quadratically after the location of interest and then begins to diminish. For the other cases, the location of interest is where the maximum adjoint value occurs. Since T^* is a representation of the relative importance of a location with regards to the quantity of interest, figure 3.10 demonstrates that, according to the mathematical adjoint, regions at or after the location of interest are weighted more heavily than other locations. The physical and analytical adjoints, however, suggest that all temperature rings before the loca-

tion of interest are equally weighted and the importance of later rings decreases logarithmically.

Table 3.1 below shows the numerically evaluated quantities of interest corresponding to the same locations as shown previously in figure 3.10. Note that the quantity of interest being evaluated is the difference $T_{lo}(r,z) - T_{hi}$ where $T_{lo} = T_{c,inlet}$.

Table 3.1: **Physical, Analytical, and Mathematical Evaluations of the Quantity of Interest**

Inner Product	**er=0.032in**	**er=0.057in**	**er=0.14in**
$< T^*_{hi}, r >$	-1971.75 ^oF	-1577.39 ^oF	-591.50 ^oF
$< T^*_{phys}, r >$	-1971.75 ^oF	-1577.39 ^oF	-591.50 ^oF
$< T^*_{anylitic}, r >$	-1971.75 ^oF	-1577.39 ^oF	-591.50 ^oF
$< Q^*, e >$	-1971.75 ^oF	-1577.39 ^oF	-591.50 ^oF
$T_{lo} - T_{hi}$	-1971.75 ^oF	-1577.39 ^oF	-591.50 ^oF

As mentioned earlier, the analytical and physical adjoints produce the exact value for the quantity of interest when a constant low fidelity solution is used. The fact that non-constant values for the low fidelity solution result in incorrect analytical and physical adjoint approximations can be attributed to the fact that the residuals as determined by the forward operator are not consistent with those that would be determined using the transpose of the physical adjoint operator. In the case where the low fidelity forward solution is constant, all second order derivatives are equal to zero and the residuals defined by the transposed physical adjoint operator will be equal to the same residuals obtained by the mathematical forward operator.

The low fidelity adjoint mathematical solution shape was also compared to the high fidelity adjoint shape. Figure 3.11 shows the adjoint solution shape for the same locations of interest as in figure 3.10.

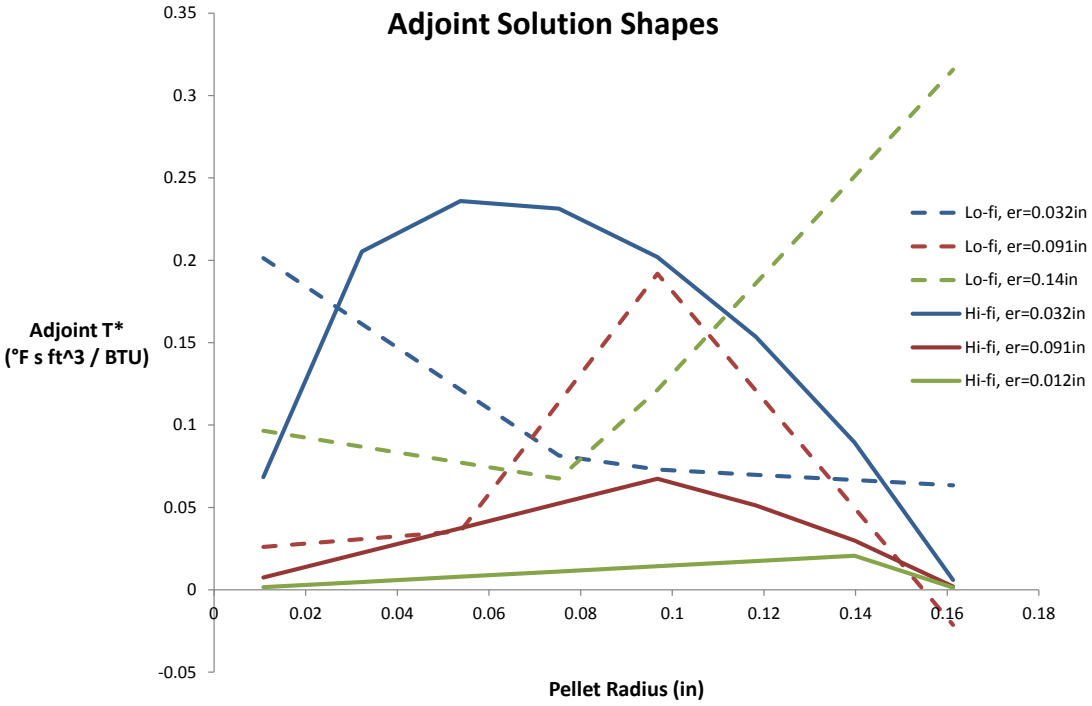

Figure 3.11: **Solution shapes for low fidelity and high fidelity mathematical adjoints for three separate radial locations of interest**

The high fidelity solution shapes in figure 3.11 are the same as previously shown in figure 3.10. The low fidelity solutions represented by the color coded dotted lines show highly erratic behavior with no indication of weighting the appropriate location of interest. Table 3.2 below shows the numerically evaluated quantities of interest corresponding to the same locations as shown previously in figure 3.11. In this case, the evaluated response is the difference between the high fidelity forward solution and the linearly interpolated low fidelity solution.

Table 3.2: **High and Low Fidelity Evaluations of the Quantity of Interest**

Inner Product	**er=0.032in**	**er=0.057in**	**er=0.14in**
$< T^*_{hi}, r >$	-65.73 ^oF	-65.73 ^oF	-41.08 ^oF
$< T^*_{lo}, r >$	213.54 ^oF	-592.54 ^oF	5380.72 ^oF
$< Q^*, e >$	-65.73 ^oF	-65.73 ^oF	-41.08 ^oF
$T_{lo} - T_{hi}$	-65.73 ^oF	-65.73 ^oF	-41.08 ^oF

Again, the mathematical solution approximates the difference exactly while the low fidelity solution exhibits highly erratic behavior inconsistent with an appropriate approximation.

Chapter 4

Conclusions and Future Work

4.1 Conclusion

In all cases, the mathematical adjoint was found to predict exactly the difference between the low fidelity and high fidelity temperatures regardless of whether the problem was time dependent or how the low fidelity temperatures were determined. Investigation of using the low fidelity mathematical adjoint in order to approximate the same QoI showed that low fidelity adjoint solutions were unable to predict quantities within acceptable tolerances. This conclusion was reinforced regardless of time dependence or low fidelity forward problem definition.

The physical and analytical adjoints were found to predict the proper quantities of interest for cases where the residuals obtained using physical and mathematical adjoint operators were consistent; namely, cases where the low fidelity coolant and fuel temperatures were constant. For this scenario, all spatial derivatives, including their discretized approximations, were zero. Although the physical and mathematical adjoint solution shapes varied drastically, the evaluated QoIs were still correct. The evaluation of the analytical adjoint solution provided a benchmark that verified the physical adjoint solution.

Given that the high fidelity adjoint appears to be necessary for the accurate evaluation of specific responses, there need to be adjusted conditions such that it would make sense to use an adjoint approach to support adaptive simulation. Note that the adjoint source term only depends on the QoI and not the forward source term, e.g. power density. This implies that whenever the QoI is to be evaluated, a high fidelity adjoint solution is required. If there are instances where one is interested in obtaining the forward solution for many different forward source terms, there may be a computational advantage of employing the adjoint approach to determine the QoI to judge whether the low fidelity forward solution being employed is suffi-

ciently accurate.

Although the low fidelity adjoint solution does not provide accurate estimations of temperature differences, a conclusion can be drawn with regards to adaptive model refinement. Because the mathematical adjoint gives the exact difference between a given fidelity and all lower fidelities, it can be used to estimate when a given fidelity converges to a higher level of fidelity. In other words, as the difference between a middle fidelity and lower model fidelity decreases, it is conjectured that the difference between the middle fidelity and high fidelity also decreases. This adaptive method can determine when to step up fidelity levels without actually solving for the high fidelity problem and is similar to methods used in adaptive grid refinement.

4.2 Future Work

The complexity of this problem could be increased for further study of the aforementioned low/mid/high fidelity difference estimations. Currently, for basic heat conduction and HEM heat convection, the differences between middle and high fidelities are small. Adding a more complex convection fluids model that includes radial and axial coolant nodes within a given channel could help demonstrate the adaptive model technique investigated in this thesis with more tangible results. Also adding axial coupling with regards to heat conduction could be another model fidelity level worth investigating using adaptive techniques along with varying fuel thermal conductivities with respect to temperature. Future work could also include an expression for the adjoint source, or response function, that results at the high fidelity level from the formulation of low fidelity adjoint equations. It may be possible to computationally derive this response function and could be interesting to contrast it with the true and desired high fidelity response function.

REFERENCES

[1] Jackson, C. J., D. G. Cacuci, and H. B. Finnemann. "Dimensionally Adaptive Neutron Kinetics for Multdimensional Reactor Safety Transients-I: New Features of RELAP5/PANBOX." *Nuclear Science and Engineering* Vol. 131 No. 2, 143-163 (1999).

[2] Jackson, C. J., D. G. Cacuci, and H. B. Finnemann. "Dimensionally Adaptive Neutron Kinetics for Multdimensional Reactor Safety Transients-II: Dimensionally Adaptive Switching Algorithms." *Nuclear Science and Engineering* Vol. 131 No. 2, 164-186 (1999).

[3] Williams, Mark L. "Perturbation Theory for Nuclear Reactor Analysis." *CRC Handbook of Nuclear Reactors Calculations* Vol. 3, 63-188 (1987).

[4] Pironneau, O. "On Optimum Design in Fluid Mechanics." *Journal of Fluid Mechanics* Vol. 64 part 1, 97-110 (1974).

[5] Pupko, V. Y. "Use of Adjoint Functions in Investigations of Heat Conduction and Transfer Processes." *Inzhenerno-Fizicheskii Zhurnal* Vol. 11 No. 2, 242-249 (1966).

[6] Dam, H. van, and J. E. Hoogenboom. "The Adjoint Space in Heat Transport Theory." *International Journal of Heat and Mas Transfer* Vol. 23, 349-353 (1980).

[7] Huang, C. H., and M. N. Ozisik. "Inverse Problem of Determining Unknown Wall Heat Flux in Laminar Flow Through a Parallel Plate Duct." *Numerical Heat Transfer* Part A Vol. 21, 55-70 (1992).

[8] Huang, C., S. Wang. "A Three-Dimensional Inverse Heat Conduction Problem in Estimating Surface Heat Flux by Conjugate Gradient Method." *International Journal of Heat and Mass Transfer*, Vol. 42, 3387-3403 (1999).

[9] *An Optimal Control Approach to A Posteriori Error Estimation in Finite Element Methods.* Institut fur Angewandte Mathematik, Universitat Heidelburg, (2001).

[10] Petersdorff, T. Von, and R. Leis. "Boundary Integral Equations for Mixed Dirichlet, Neumann and Transmission Problems." *Mathematical Methods in the Applied Sciences* Vol. 11, 185-213 (1989).

[11] Carey, V., D. Estep, A. Johansson, M. Larson, and S. Tavener. "Blockwise Adaptivity for Time Dependent Problems Based on Coarse Scale Adjoint Solutions." *SIAM Journal on Scientific Computing* Vol. 342 No. 4, (2010).

[12] Estep, D., S. Tavener, and T. Wildey. "A Posteriori Analysis and Improved Accuracy for an Operator Decomposition Solution of a Conjugate Heat Transfer Problem." *SIAM Journal on Numerical Analysis* Vol. 46 No. 4, 2068-2089 (2008).

[13] Estep, D., V. Ginting, D. Ropp, J. N. Shadid, and S. Tavener. "An A Posteriori - A Priori Analysis of Multiscale Operator Splitting." *Siam Journal on Numerical Analysis* Vol 46 No. 3, 1116-1146 (2008).

[14] Estep, D. M. Pernice, D. Pham, S. Tavener, and H. Wang. "A Posteriori Error Analysis of a Cell-Centered Finite Volume Method for Semilinear Elliptic Problems." *Journal of Computational and Applied Mathematics* Vol. 233, 459-472 (2009).

[15] Estep, D. M. Pernice, D. Pham, S. Tavener, and H. Wang. "A Posteriori Error Analysis for a Cut Cell Finite Volume Method." *Computational Methods in Applied Mechanics and Engineering* Vol. 200, 2768-2781 (2011).

[16] Yen, D. H. Y., J. V. Beck. "Green's Functions for Non-Self-Adjoint Problems in Heat Conduction with Steady Motion." *Journal of Engineering Mathematics* Vol. 57, 115-132 (2007).

[17] Versteeg, H. K., and W. Malalasekera. *An Introduction to Computational Fluid Dynamics: The Finite Volume Method*. Harlow, England: Pearson-Prentice Hall, 2007.

[18] Jarny, Y., M. N. Ozisik, and J. P. Bardon. "A General Optimization Method Using Adjoint Equation for Solving Multidimensional Inverse Heat Conduction." *International Journal of Heat and Mass Transfer* Vol. 34 No. 11, 2911-2919 (1991).

[19] Mesina, G. L.,"Reformulation RELAP5-3D in FORTRAN 95 and Results." *Proceedings of the ASME 2010 Joint US-European Fluids Engineering Summer Meeting and 8th International Conference on Nanochannels Microchannels, and Minichannels* , FEDSM2010-ICNMM2010, Montreal, Quebec, Canada, Aug 1-5, (2010).

[20] Martin, R. P. "TRAC-B thermal-Hydraulic Analysis of the Black Fox Boiling Water Reactor." *National Technical Information Service, 77H-Reactor Engineering and Nuclear Power Plants*. Issue 9318, 1993.

[21] Areva NP Inc, *COBRA-FLX: A Core Thermal-Hydraulics Analysis Code.* ANP-10311NP. pbadupws.nrc.gov, (2010).

[22] Sung, Y., R. L. Oelrich Jr., C. C. Lee, N. Ruiz-Esquide, M. Gambetta, and C. M. Mazufri, "Bechmark of Subchannel Code VIPRE-W with PSBT Void and Temperature Test Data." *Science and Technology of Nuclear Instalations*, Vol. 2012, (2012).

[23] Cardoni, J. N., and Rizwan-uddin. "Nuclear Reactor Multi-Physics Simulations with Coupled MCNP5 and Star-CCM+." *International Conference on Mathematics and Computational Methods Applied to Nuclear Science and Engineering*, (2011).

[24] Christon, M. A., J. Bakosi, M. M. Francois, R. B. Lowrie, R. Nourgaliev. "Multiphase Flow Analysis in Hydra-TH." *Conference: CASL Virtual Roundtable*, (2012).

[25] Sussman, M., A. S. Almgren, J. B. Bell, P. Colella, L. H. Howell and M. L. Welcome., "An adaptive level set approach for incompressible two-phase flows.", *Journal of Computational Physics*, Vol. 148, Issue 1, 81-124 (1999).

[26] Popinet, S. and Zaleski S. "A Front-Tracking Algorithm for the Accurate Representation of Surface Tension." *International Journal of Numerical Methods in Fluids*, Vol. 30 No. 775, (1999).

Section C

Time-dependent GPT Equations for Nodal Diffusion

Derivation for and Solution Verification of the Transient GPT Equations for the 2-Group Neutron Diffusion Equations

Ross Hays
Jaeseok Heo

Department of Nuclear Engineering
North Carolina State University
Raleigh, North Carolina

Theory and Implementation

The adjoint transient problem is useful within the framework of a generalized perturbation theory (GPT) problem for estimating the effect of a given perturbation to the flux or precursor density to a defined inner-product response function. This GPT framework is utilized as the basis for an Adaptive Model Refinement (AMoR) capability. The derivation of the transient adjoint problem requires several steps, described in the paragraphs that follow. This derivation is based upon the time discretized forward, group neutron diffusion equations utilized in the NESTLE computer code. For details on the theory utilized by the NESTLE code, see Reference 1.

The first step in the derivation of the adjoint problem to recast the time discretized forward, group neutron diffusion equations into a form represented by a single matrix operator. Thus these equations:

$$\frac{1}{v_g \Delta t_{n+1}} \phi_g(t_{n+1}) - \vec{\nabla} \cdot D_g \vec{\nabla} \phi_g(t_{n+1}) + \Sigma_{tg} \phi_g(t_{n+1}) = \sum_{g'=1}^{G} \Sigma_{sgg'} \phi_{g'}(t_{n+1}) + (1-\beta) \chi_g^{(P)} \sum_{g'=1}^{G} \nu_{g'} \Sigma_{fg'} \phi_{g'}(t_{n+1}) + \sum_{i=1}^{I^{(D)}} \chi_{gi}^{(D)} \lambda_i C_i(t_{n+1}) + \frac{1}{v_g \Delta t_n} \phi_g(t_n)$$

$$F_{i_n}^0 \sum_{g=1}^{G} \nu_g \Sigma_{fg} \phi_g(t_n) + C_i(t_n) e^{-\lambda_i \Delta t_n} + F_{i_n}^1 \sum_{g=1}^{G} \nu_g \Sigma_{fg} \phi_g(t_{n+1}) - C_i(t_{n+1}) = 0$$

$$F_{i_n}^1 = \frac{\beta_i}{\lambda_i \Delta t_n} \left[\Delta t_n - \frac{1}{\lambda_i} \left(1 - e^{-\lambda_i \Delta t_n} \right) \right]$$

$$F_{i_n}^0 = -F_{i_n}^1 + \frac{\beta_i}{\lambda_i} \left(1 - e^{-\lambda_i \Delta t_n} \right)$$

are transformed into:

$$\begin{bmatrix} \begin{bmatrix} \bar{\bar{I}} & \bar{\bar{0}} \\ \bar{\bar{0}} & \bar{\bar{I}} \end{bmatrix}_0 & & & & & \\ \cdots & \cdots & & & & \\ & \begin{bmatrix} \bar{\bar{B}}_{11} & \bar{\bar{B}}_{12} \\ \bar{\bar{B}}_{21} & \bar{\bar{B}}_{22} \end{bmatrix}_n & \begin{bmatrix} \bar{\bar{A}}_{11} & \bar{\bar{0}} \\ \bar{\bar{A}}_{21} & \bar{\bar{A}}_{22} \end{bmatrix}_n & & & \\ & & \begin{bmatrix} \bar{\bar{B}}_{11} & \bar{\bar{B}}_{12} \\ \bar{\bar{B}}_{21} & \bar{\bar{B}}_{22} \end{bmatrix}_{n+1} & \begin{bmatrix} \bar{\bar{A}}_{11} & \bar{\bar{0}} \\ \bar{\bar{A}}_{21} & \bar{\bar{A}}_{22} \end{bmatrix}_{n+1} & & \\ & & & & \cdots & \end{bmatrix} \begin{bmatrix} \begin{bmatrix} \vec{\phi}_0 \\ \vec{C}_0 \end{bmatrix} \\ \vdots \\ \begin{bmatrix} \vec{\phi}_n \\ \vec{C}_n \end{bmatrix} \\ \begin{bmatrix} \vec{\phi}_{n+1} \\ \vec{C}_{n+1} \end{bmatrix} \\ \vdots \end{bmatrix} = \bar{0}$$

which may be more compactly represented as:

$$A[\Psi] = 0$$

where:

$$\Psi \equiv \left[\left[\vec{\phi}_0, \vec{C}_0\right], \ldots, \left[\vec{\phi}_N, \vec{C}_N\right]\right]^T$$

where $\vec{\phi}_n$ is the vector of flux values for all energy groups and locations at a given timestep, n, and $\vec{C}_n$ likewise denotes the delayed neutron precursor concentrations for all delay groups and spatial locations at timestep n.

Once the transient equation has been cast in this compact form, an error response functional is defined as follows:

$$R = \int_{t_i}^{t_f} dt \int_V d\vec{V} f\left(\vec{r}, t\right) \cdot \Delta\vec{\Psi}\left(\vec{r}, t\right) \equiv \left\langle f, \vec{\Psi} \right\rangle$$

where R is the error response value associated with a user-defined error quantity-of-interest function, $f(\vec{r}, t)$, and a known difference between two solutions, $\Delta\Psi \equiv \hat{\Psi} - \Psi$ (vector notation suppressed for clarity) where the "hated" variable denotes a estimate based upon a lower fidelity model's solution.

Next, define the forward error residual value as follows:

$$A\left[\hat{\psi}\right] = \vec{r}$$

Finally, require that the adjoint solution be the solution of the following equation, where the ad:

$$A^*\left[\psi^*\right] = f$$

The adjoint operator, A^* is calculated through the mathematical transformations required to reproduce the following requirement

$$R = \left\langle f, \Delta\psi \right\rangle = \left\langle A^*\left[\psi^*\right], \hat{\psi} - \psi \right\rangle = \left\langle \psi^*, A\left[\hat{\psi} - \psi\right] \right\rangle = \left\langle \psi^*, A\left[\hat{\psi}\right] \right\rangle = \left\langle \psi^*, \vec{r} \right\rangle$$

This transformation makes use of the initial and boundary conditions of the forward solution and introduces final and boundary conditions on the adjoint solution. This transformation results in an adjoint operator which is the transpose of the forward operator, with the sign of the first-order time derivatives inverted.

$$
\begin{bmatrix}
\cdots & & & & \\
 & \begin{bmatrix} \overline{\overline{B}}_{11}^{+} & \overline{\overline{B}}_{21}^{+} \\ \overline{\overline{B}}_{12}^{+} & \overline{\overline{B}}_{22}^{+} \end{bmatrix}_n & & & \\
 & \begin{bmatrix} \overline{\overline{A}}_{11}^{+} & \overline{\overline{A}}_{21}^{+} \\ \overline{\overline{0}} & \overline{\overline{A}}_{22}^{+} \end{bmatrix}_n & \begin{bmatrix} \overline{\overline{B}}_{11}^{+} & \overline{\overline{B}}_{21}^{+} \\ \overline{\overline{B}}_{12}^{+} & \overline{\overline{B}}_{22}^{+} \end{bmatrix}_{n+1} & & \\
 & & \begin{bmatrix} \overline{\overline{A}}_{11}^{+} & \overline{\overline{A}}_{21}^{+} \\ \overline{\overline{0}} & \overline{\overline{A}}_{22}^{+} \end{bmatrix}_{n+1} & & \\
 & & & \cdots & \begin{bmatrix} \overline{\overline{I}} & \overline{\overline{0}} \\ \overline{\overline{0}} & \overline{\overline{I}} \end{bmatrix}_N
\end{bmatrix}
\begin{bmatrix}
\vdots \\
\begin{bmatrix} \vec{\phi}_n^* \\ \vec{C}_n^* \end{bmatrix} \\
\begin{bmatrix} \vec{\phi}_{n+1}^* \\ \vec{C}_{n+1}^* \end{bmatrix} \\
\vdots \\
\begin{bmatrix} \vec{\phi}_N^* \\ \vec{C}_N^* \end{bmatrix}
\end{bmatrix}
= \vec{0}
$$

which results in the following set of equations

$$
-\frac{1}{v_g \Delta t_n}\phi_g^*\left(t_{n+1}\right) - \vec{\nabla}\cdot D_g \vec{\nabla}\phi_g^*\left(t_{n+1}\right) + \Sigma_{tg}\phi_g^*\left(t_{n+1}\right) = \sum_{g'=1}^{G}\Sigma_{sgg'}\phi_{g'}^*\left(t_{n+1}\right)
$$

$$
+\frac{1}{k_{eff}}\nu_g\Sigma_{fg}\sum_{g'=1}^{G}\left[\sum_{i=1}^{I^{(D)}}\chi_{g'i}^{(D)}\lambda_i F_{i_n}^1 + \left(1-\beta\right)\chi_{g'}^{(P)}\right]\phi_{g'}^*\left(t_{n+1}\right) + \frac{1}{k_{eff}}\nu_g\Sigma_{fg}\sum_{i=1}^{I^{(D)}}F_{i_n}^0 C_i^*\left(t_n\right) +
$$

$$
\frac{1}{k_{eff}}\nu_g\Sigma_{fg}\sum_{i=1}^{I^{(D)}}F_{i_n}^1 C_i^*\left(t_{n+1}\right) + \frac{1}{k_{eff}}\nu_g\Sigma_{fg}\sum_{g'=1}^{G}\sum_{i=1}^{I^{(D)}}\chi_{g'i}^{(D)}\lambda_i F_{i_n}^0\phi_{g'}^*\left(t_n\right) - \frac{1}{v_g\Delta t_n}\phi_g^*\left(t_n\right) + S_{ext,g}^*
$$

$$
C_i^*\left(t_n\right)e^{-\lambda_i\Delta t_n} + e^{-\lambda_i\Delta t_n}\sum_{g'=1}^{G}\chi_{g'i}^{(D)}\lambda_i\phi_{g'}^*\left(t_n\right) - C_i^*\left(t_{n+1}\right) = 0
$$

with final and boundary conditions:

$$
\phi_g^*\left(t_N\right) = 0
$$

$$
C_i^*\left(t_N\right) = 0
$$

$$
\phi_g^*\left(t\right) = 0, C_i^*\left(t\right), t_0 \le t \le t_N, \vec{r} \in \mathrm{d}V
$$

To obtain these final conditions, note that the forward flux and precursor concentrations actually denote the perturbations of these quantities from their initial condition values. Note that the adjoint external source term, $S^*_{ext,g}$ is the quantity-of-interest function, $f(\vec{r},t)$, from before expressed in terms of the discretized energy, space and time mesh. It may also be noted that the adjoint equation is structurally similar to the forward equation; thus many of the methods, and

much of the NESTLE code used to solve the forward equations may also be utilized to solve the adjoint transient with only minor modifications.

Freezing the coupling coefficients correction factors (alias d-tildes) obtained from the forward nodal equations solution using the Nodal Expansion Method (NEM), the adjoint equations are discretized to obtain the nodal balance equations. An inner-outer nested iterative solution approach is then utilized to solve the resulting fixed source equations. This capability has been added to the NESTLE code.In addition, the capability to evaluate the residual, has been added to the NESTLE code.

Verification Tests

Various test cases were executed using NESTLE to verify that the adjoint and residual calculations are being performed correctly. The test case of choice consists of an eigenvalue-initiated null-transient (i.e. steady-state) at 0.01% full power in a standard, 4-loop Westinghouse PWR reactor model with a quarter-core symmetric load of fuel. Thermal-hydraulic feedback is disabled. The number of time-steps was 600, while the size of the timestep was adjusted by decades between 0.0005 seconds and 0.5 seconds. This gives a range of total simulation times between 0.3 and 300 seconds, allowing for the examination of both the effects of timestep size on short-lived precursor groups and the contribution of the long decay tails of the long-lived precursors. The adjoint source term (the QoI for the response, R), was split into two individual responses, referred to simply as Shade 1 and Shade 2. Shade 1 consists of a constant value of 25.0 (arbitrary units) in all flux groups and all spatial nodes at a single specified timestep. Shade 2 consists of a single node -- located at a core location given by indices $ixy=7$, $iz=3$ – with a value of 1.0 for all flux energy groups at a single specified timestep.

Figures 1 through 4 show the adjoint flux and precursor values through time for a single node where the timestep size is adjusted by decades from 0.0005 seconds to 0.5 seconds. In these figures, it can be seen that the adjoint flux values initially decay very quickly (moving backward in time), reflecting the very short-lived influence of prompt neutrons on the quantity of interest. After this initial drop, the adjoint flux values decay at a lower rate, mirroring the decay of the adjoint precursor densities. This reflects the influence of the flux on the production of delayed neutron precursors which have sufficient lifetime to then influence the time of interest for the adjoint source. Furthermore, it can be seen that the adjoint flux and precursor values decay to a constant, non-zero value. This can be attributed to the use of an eigenvalue initiated transient calculation, which has a k_{eff} value of 1.0, causing any change in the initial neutron population to be carried forward to future timesteps.

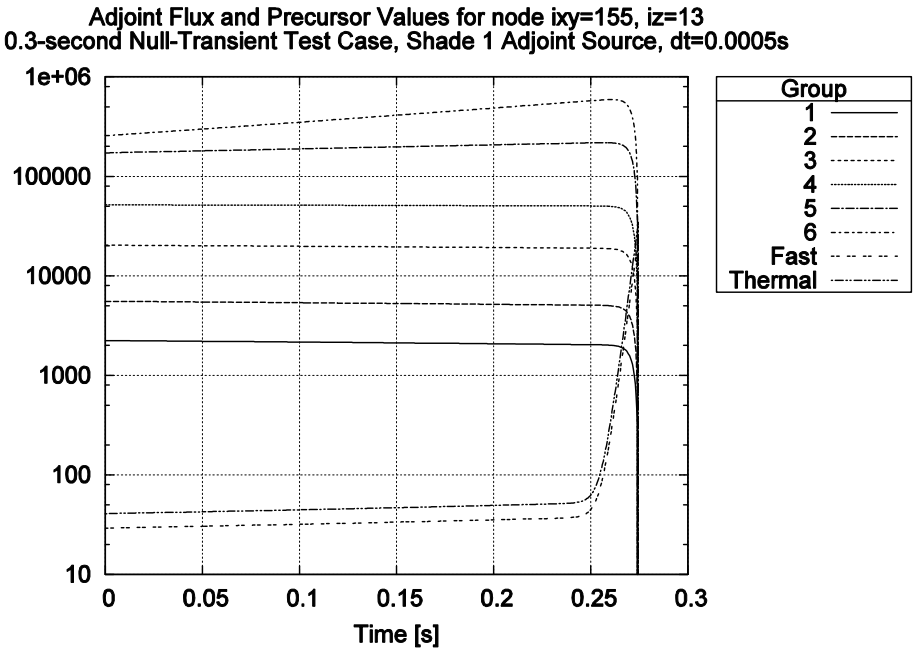

Figure 1: 0.3 Second Null-Transient Test Case Adjoint Solution Values

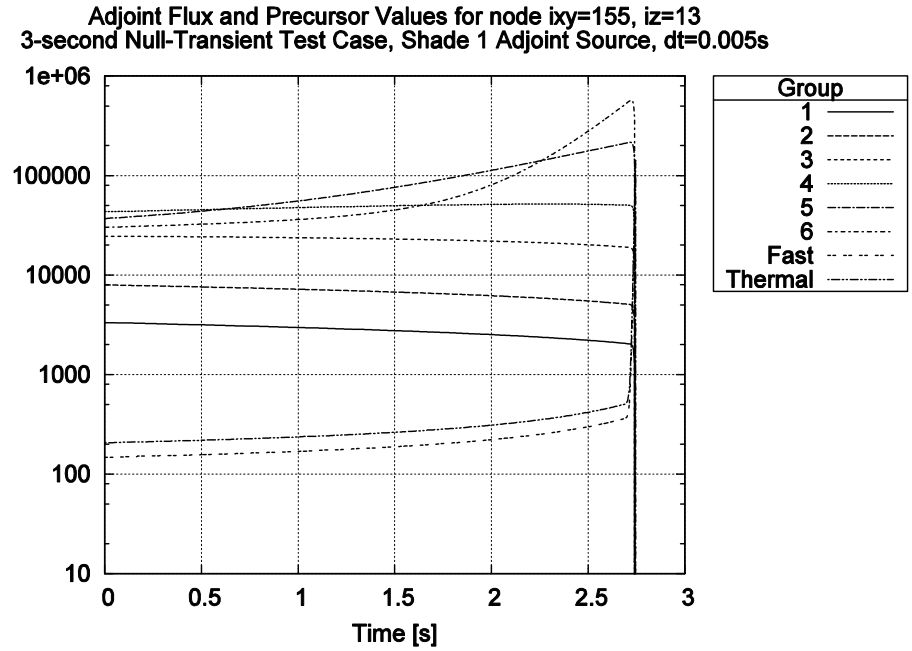

Figure 2: 3 Second Null-Transient Test Case Adjoint Solution Values

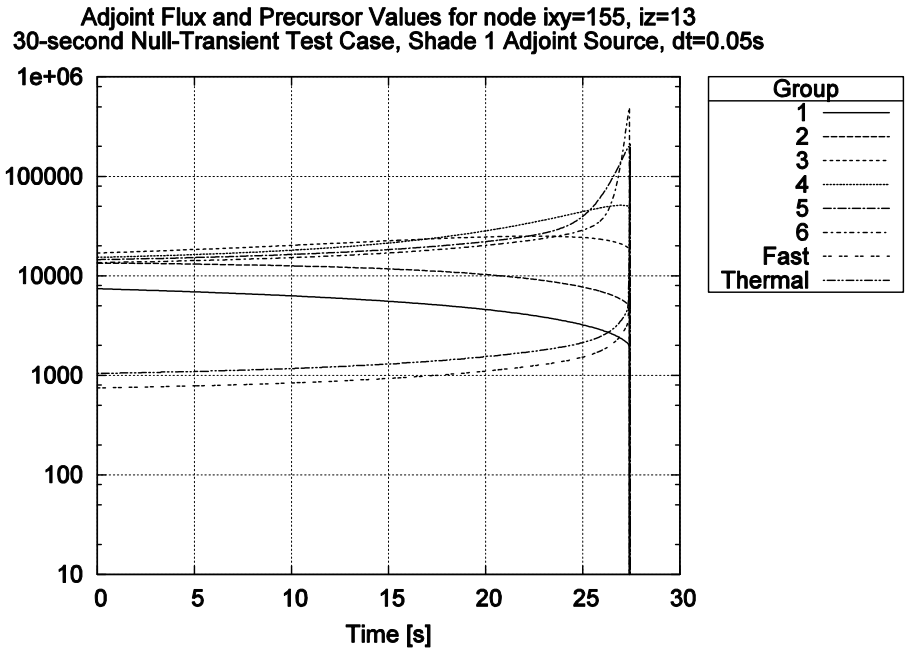

Figure 3: 30 Second Null-Transient Test Case Adjoint Solution Values

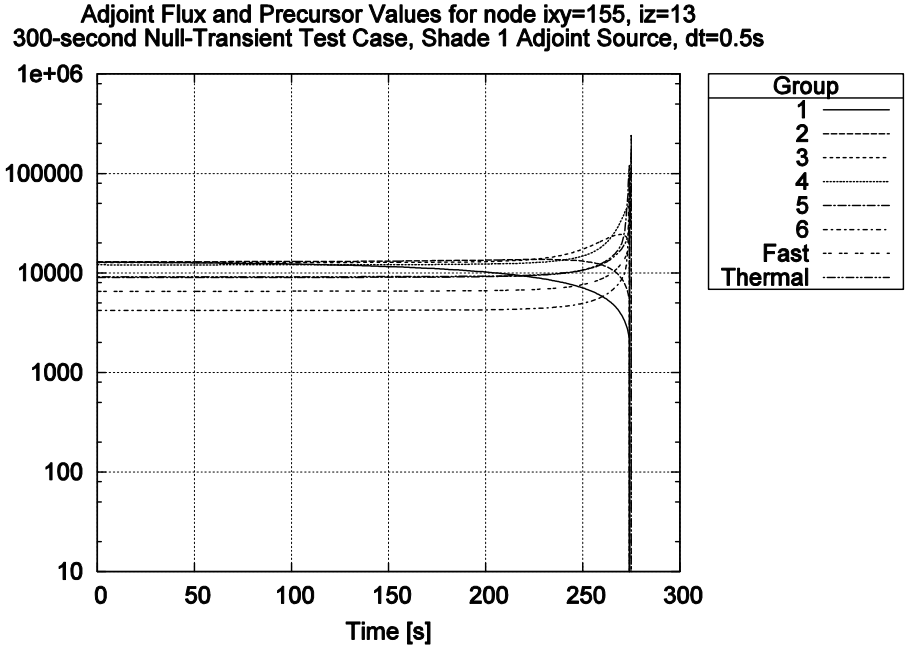

Figure 4: 300 Second Null-Transient Test Case Adjoint Solution Values

To define both the forward and adjoint response calculations, one must choose a time-frame of interest over which the inner-product is to be defined and for which the initial or final conditions will be stated. The forward and adjoint responses are given by the following equations:

$$R_F = <\vec{f}, \Delta\vec{\Psi}> = \int_{t_s}^{t_f}\int_V \vec{f}^T(\vec{x},t)\Delta\vec{\Psi}(\vec{x},t)dVdt$$

$$R_A = <\vec{\Psi}^*, \vec{r}> = \int_{t_s}^{t_f} \int_V \vec{\Psi}^{*T}(\vec{x},t)\vec{r}(\vec{x},t)dVdt$$

The initial or final conditions specified in the derivation of the adjoint impose two constraints on the choice of starting and stopping times. First, at the start time, the natural boundary conditions require that $\Delta\vec{\Psi}(\vec{x},t_s) = 0$ for all $\vec{x}$. This translates into a requirement that the low-fidelity solution evolution begin from a known high-fidelity solution. The adjoint solution likewise has a terminal condition of $\vec{\Psi}^*(\vec{x},t_f) = 0$, which requires that t_f be chosen such that $\vec{f}(\vec{x},t) = 0$ for all $t > t_f$.

The goal is to use the adjoint response formulation to compare the response fidelity of the prolongated point kinetics results to the full NESTLE results. In order to verify the computational results, we will first generate high- and low-fidelity solutions and use them to compare the response values obtained from the forward and adjoint based response equations. For test purposes, define a low-fidelity solution in terms of the high fidelity solution, $\vec{\Psi}(\vec{x},t)$, and a scaling factor, $\alpha(t)$.

$$\tilde{\vec{\Psi}}(\vec{x},t) = \alpha(t)\vec{\Psi}(\vec{x},t)$$

where $\alpha(t) = 1.0$ for $0 < t < 250s$ and $\alpha(t) = \alpha_0$ for $250s < t < 300s$, with separate tests used for α_0 values of 0.2, 1.0, and 1.8. This set of test cases offers two benefits, first it automatically satisfies the initial condition requirements, second, the adjoint response values for the α_0=1.0 case will be attributable to the finite convergence tolerances of the high-fidelity solution, effectively providing an estimate of their contribution to more complicated cases. To further evaluate these effects, each α_0 test case is computed with three different sets of convergence tolerance settings on the high-fidelity forward and adjoint solutions. The convergence settings, termed *Loose*, *Nominal*, and *Tight*, are listed below in Table 1.

Table 1: Convergence Settings

Loose	Nominal	Tight	Criterion	Variable Name
1	1	1	Number of Scattering iterations	NITTH
400	500	1000	Outer iteration limit	KITR
1.0E-05	1.0E-06	5.0E-07	Keff relative error criteria	EPSK
5.0E-05	1.0E-05	1.0E-06	L-2 residual outer iteration norm	EPSOT
3.0E+01	1.0E+01	5.0E+00	L-2 residual norm criteria	EPSRESID
1.0E-01	1.0E-02	1.0E-03	L-infinity error norm criteria	EPSIN
1.0E-02	1.0E-03	1.0E-04	Inner iterations criteria	EPSDET
5	5	5	NEM Update Frequency	NNEM
1.00E-05	1.00E-05	1.00E-06	NEM L-2 Error reduction Factor	EPSNEM

The response values computed using both the forward and adjoint based equations are listed in Table 2. Several important features may be seen. First, a symmetric perturbation in the flux (up or down), produces a nearly symmetric change in the response value. Secondly, as the convergence tolerances are decreased, the forward and adjoint response values appear to converge toward similar values, again displaying the previously noted symmetry. Finally, note that though the $\alpha_0 = 1.0$ adjoint response value is nonzero for all cases, its magnitude remains two to five orders of magnitude below that of the other α_0 cases, and decreases greatly when the tight convergence tolerances are used. Thus, it is expected that unwanted contributions of the high-fidelity solution residual to the computed response value should be relatively minor.

Table 2: Computed Response Values

	$< \vec{f}, \Delta\vec{\Psi} >$		
α_0	Loose	Nominal	Tight
0.2	-9.67172E+12	-9.28002E+12	-9.21589E+12
1	0.00000E+00	0.00000E+00	0.00000E+00
1.8	9.67171E+12	9.28002E+12	9.21589E+12

	$< \vec{\Psi}^*, \vec{r} >$		
α_0	Loose	Nominal	Tight
0.2	-9.79801E+12	-9.26428E+12	-9.26587E+12
1	2.50682E+10	7.82798E+10	-1.43522E+07
1.8	9.84842E+12	9.42084E+12	9.26584E+12

These and other tests completed verify that the GPT time-dependent adjoint solution and the response functional evaluation implemented in the NESTLE code are done correctly.